Coherent structures and impact of the external thermal stratification in a transitional natural convection vertical channel

Martin Thebault

N°d'ordre NNT : 2018LYSE1327

THESE de DOCTORAT DE L'UNIVERSITE DE LYON
opérée au sein de
l'Université Claude Bernard Lyon 1

Ecole Doctorale N° ED 162
(Mécanique, Énergétique, Génie Civil, Acoustique)

Spécialité de doctorat : Thermique, Énergétique, Mécanique des fluides

Soutenue publiquement le 05/12/2018, par :
Martin Thebault

Coherent structures and impact of the external thermal stratification in a transitional natural convection vertical channel

Devant le jury composé de :

Armfield, Steven	Professeur	University of Sydney	Rapporteur
Médale, Marc	Professeur	Aix-Marseille Université	Rapporteur
Podvin, Bérengère	Chargée de Recherche, HDR	CNRS	Examinatrice
Manca, Oronzio	Professeur	University of Campania	Examinateur
Ben Hadid, Hamda	Professeur	UCBL 1	Examinateur
Giroux—Julien, Stéphanie	Maître de Conférences, HDR	UCBL 1	Directrice de thèse
Timchenko, Victoria	Maître de Conférences	UNSW-Sydney	Directrice de thèse
Ménézo, Christophe	Professeur	USMB	Co-directeur
Reizes, John	Professeur Emeritus	UNSW-Sydney	Invité
Xin, Shihe	Professeur	INSA-Lyon	Invité

Thèse préparée dans le cadre d'une cotutelle entre l'Université Claude-Bernard Lyon 1 (laboratoire du CETHIL – UMR 5008) et l'UNSW-Sydney.

UNIVERSITE CLAUDE BERNARD - LYON 1

Président de l'Université	**M. le Professeur Frédéric FLEURY**
Président du Conseil Académique	M. le Professeur Hamda BEN HADID
Vice-président du Conseil d'Administration	M. le Professeur Didier REVEL
Vice-président du Conseil Formation et Vie Universitaire	M. le Professeur Philippe CHEVALIER
Vice-président de la Commission Recherche	M. Fabrice VALLÉE
Directeur Général des Services	M. Alain HELLEU

COMPOSANTES SANTE

Faculté de Médecine Lyon Est – Claude Bernard	Directeur : M. le Professeur J. ETIENNE
Faculté de Médecine et de Maïeutique Lyon Sud – Charles Mérieux	Directeur : Mme la Professeure C. BURILLON
Faculté d'Odontologie	Directeur : M. le Professeur D. BOURGEOIS
Institut des Sciences Pharmaceutiques et Biologiques	Directeur : Mme la Professeure C. VINCIGUERRA
Institut des Sciences et Techniques de la Réadaptation	Directeur : M. le Professeur Y. MATILLON
Département de formation et Centre de Recherche en Biologie Humaine	Directeur : Mme la Professeure A-M. SCHOTT

COMPOSANTES ET DEPARTEMENTS DE SCIENCES ET TECHNOLOGIE

Faculté des Sciences et Technologies	Directeur : M. F. DE MARCHI
Département Biologie	Directeur : M. le Professeur F. THEVENARD
Département Chimie Biochimie	Directeur : Mme C. FELIX
Département GEP	Directeur : M. Hassan HAMMOURI
Département Informatique	Directeur : M. le Professeur S. AKKOUCHE
Département Mathématiques	Directeur : M. le Professeur G. TOMANOV
Département Mécanique	Directeur : M. le Professeur H. BEN HADID
Département Physique	Directeur : M. le Professeur J-C PLENET
UFR Sciences et Techniques des Activités Physiques et Sportives	Directeur : M. Y.VANPOULLE
Observatoire des Sciences de l'Univers de Lyon	Directeur : M. B. GUIDERDONI
Polytech Lyon	Directeur : M. le Professeur E.PERRIN
Ecole Supérieure de Chimie Physique Electronique	Directeur : M. G. PIGNAULT
Institut Universitaire de Technologie de Lyon 1	Directeur : M. le Professeur C. VITON
Ecole Supérieure du Professorat et de l'Education	Directeur : M. le Professeur A. MOUGNIOTTE
Institut de Science Financière et d'Assurances	Directeur : M. N. LEBOISNE

À Jamie, à Pépé, à Mémé Dado.

Acknowledgements - Remerciements

Je voudrais remercier Pr. Ben Hadid, président de mon jury, mes rapporteurs de thèse, Pr Armfield et Pr. Médale ainsi que Mme Podvin, Pr. Manca, qui ont acceptés d'être examinateurs. L'ensemble de leurs commentaires et les discussions que l'on a eu ont grandement contribués à la qualité de ce travail.

Ces trois années de thèse ont été pour moi une expérience immensément riche et formatrice. Je voulais remercier dans un premier temps mes directeurs et superviseurs: Christophe pour sa curiosité et son enthousiasme communicatif ainsi que pour les nombreuses opportunités qui m'ont été ouvertes grâce à lui. Stéphanie pour son encadrement solide et son soutien sans failles dans tous les projets que nous avons suivis. I would also like to thank Victoria for her warm welcome at UNSW and her support, which has helped make this year in Australia an incredible opportunity both on a personal and professional point of view. Finally, I would like to thank John for his extremely useful insights and his generosity. He taught me so many things that will have a crucial impact on the way I will work, and I am very grateful for this.

Cette thèse, bien que portée par un étudiant et ses directeurs est également le fruit de nombreuses interactions et discussions. A ce titre je voudrais grandement remercier Hervé pour les nombreuses conversations que nous avons eues ainsi que son aide pour la mise en place de mes expériences. Merci à Mr Laulagnet pour l'aide et le prêt de matériel acoustique. Merci aux nombreuses personnes qui m'ont permis de mener à bien mes expériences et leur post traitement : Manuel, Yiqin, Serge, Anthony, Eric Matthieu ainsi que toute l'équipe de l'atelier. Parmi les autres personnes que je voudrais remercier pour leur aide sur des points très divers: Yongling, Shihe, Chengwang, Steven, Jeroen...

Je voudrais également remercier Florence, Sophie, Marylin, Nazaré, Mériem, Marion Combe et Elisa pour leur précieuse aide administrative ainsi que pour avoir parfois géré des dossiers complexes essentiels au bon déroulement de ma thèse.

Je voulais aussi grandement remercier Isabelle Schuster, Marion Decquick, Christine Dominjon et plus généralement la KIC InnoEnergy qui m'a permis de suivre des formations d'une rare qualité ainsi que d'effectuer une mobilité confortable grâce à son soutien financier.

I also want to say a warm thank you to Svetlana Tkachenko, "the cluster magician," whose help and knowledge of the UNSW computing facilities as well as the LES codes and methodologies has been of crucial importance for the numerical part of this work. I also want

to thank Oksana Tkachenko who also significantly helped me with the setting of the FLUENT solver. Thanks to Adrian Vieiri for having been such an interesting and involved student. I also have a thought for all the PhD students I met at UNSW, Bac, Shahin, Amin, Benjamin, David and Laetitia. I also want to thanks Julie, Elizabeth and all the GRS team which has always been of great help during my Australian stay.

J'ai une forte pensé pour Gérôme et Camille, mes voisins de chambre avec qui nous avons vécu six mois hors du commun dans la petite maison de 'Papa' Emeric sur Bronte.

Merci également à toute l'équipe du CETHIL, le groupe THEBE et toute l'équipe de doctorants. Je garderai un souvenir indélébile de la superbe ambiance entre les doctorants du CETHIL, Damien Go., Etienne, Aurélia qui m'a fait l'honneur de me désigner "le plus drôle du labo", Adrien dit "LA BATTE", Quenret Moutin, Tiboooo, Loïc Fras-ciné, Damien Glo. AKA la sentinelle du galet, Nicolas Cardinovich, Bus expert en boîte froide confidentielle, Ghady "L'Alpagua Volant" comme on l'appelait chez les scouts, Queen Ju(lie), celle qui rit fort (et on en est bien contents), Kevin, Léon et Benjamin, de la team Stoph, David, Nicolas B., Khriscia, Christophe L., Janett, Naveed, et tous les petits nouveaux qui sont arrivés, Guillaume, Eden, Mathilde, Jean, Sophie, Malak, Chloé, Paul.

Je voulais faire une spéciale dédicace à Eloïse et Rémi, ça a été du pur bonheur de partager votre bureau. Je n'oublierai jamais nos petits dejs au bureau, nos cloches maléfiques ainsi que ces heures de brainstorming pour nos fumiers ou encore nos courses de bateaux. Vous n'êtes pas trop mauvais comme Bretons pour des Nantais.

J'ai une forte pensée pour mes amis, depuis mes amis d'enfance Gaël, Barrois, Lagon, aux copains indéfectibles de la première heure, Pierre et Antoine. Je pense aussi à mes amis qui se reconnaitront: Lille, Grenoble, Paris, Mulhouse, Montpellier, Lyon, Italie, Espagne, Australie!

Enfin je voudrais finir avec ma famille, je pense aux nombreux cousins, cousines, oncles et tantes, Mamie, Pépé, Mémé Mado mais aussi Pépé Charlie bien que je n'ai jamais pu le connaître. Une forte pensée pour mon petit frère Corentin et mes parents qui m'ont toujours soutenu et considéré dans ce que j'entreprenais. J'embrasse ma famille du Sud, Emma, les frangins Jules et Léo ainsi que la petite sœur Elisa. J'embrasse également ma belle famille.

Mes derniers remerciements reviennent à Manon, qui a été un soutien psychologique, émotionnel constant, qui m'a toujours soutenue dans les différents projets jusqu'à m'accompagner en Australie. Manon qui a également relu une grande partie de ces travaux et dont, la qualité d'écriture de cette thèse qui a été soulignée par les différents membres du jury, lui revient en partie.

Abstract

Coherent structures and impact of the external thermal stratification in a transitional natural convection vertical channel

Interest in natural convection in vertical channels has significantly increased over the last several years because of its application in solar energy systems. In natural convective flows, complex coherent structures develop whose the role in heat and mass transfer are not well understood. An experimental and numerical investigation programme was therefore undertaken to investigate the behaviour of such flows. The numerical study is based on Large-Eddy-Simulations of a vertical channel with one side uniformly heated and subjected to random velocity fluctuations at the inlet. Different stages of transitional flow development were identified numerically with two characteristic frequency bands being observed in the flow, near the heated wall. Spectral Proper Orthogonal Decomposition, a method derived from the Proper Orthogonal Decomposition (POD) was also used and shown to be a powerful tool which allows the most energetic modes to be separated accordingly to two characteristic frequency bands found numerically. As result, the contribution of the two families of modes to the near wall turbulent heat transfer and velocity-temperature correlation has been evaluated. Finally, the modes were linked to coherent structures that are observed in instantaneous visualizations of the flow. POD was also performed on experimental measurements showing similarities with the numerically observed structures.

From past experimental studies of similar configurations it was found that large differences in the experimental velocities often occurred for apparently the same conditions. In this work variations of the external thermal stratification have been identified as one possible source of these differences. The influence of external thermal gradients was investigated experimentally and numerically. It is shown that the increase in the positive gradient of the external stratification not only decreases the mass flow rate but also displaces the transition height to a lower location in the channel. As a consequence, as the positive upwards external thermal stratification increases, the flow evolves from a laminar flow to turbulent flow despite the reduction in mass flow rate. Numerical simulations also allow the study of cases of weak and negative thermal stratifications which are difficult to achieve in laboratories.

A theoretical model of the influence of the external thermal stratification on the mass flow rate was also developed. There is an excellent agreement between the theoretical predictions and the experimentally and numerically obtained mass flow rates. This clearly highlights that external temperature distributions are key driving factors and their influence is accurately quantified in this work.

Résumé

Structure cohérente et impact de la stratification thermique extérieure dans un écoulement de convection naturelle de transition dans un canal vertical

L'étude de la convection naturelle en canal vertical à reçu un regain d'intérêt, notamment pour ses applications dans le secteur des énergies solaires. Dans les écoulements de convection naturelle, de nombreuses structures cohérente se développent, dont le rôle dans les transferts de masse et de chaleurs reste aujourd'hui mal connu. Par conséquent une série d'études expérimentales et numériques a été entrepris.

Les études numériques sont basées sur des Simulations aux Grandes Echelles d'un canal vertical dont un des côtés est chauffé uniformément à flux constant et pour lequel une perturbation en vitesse aléatoire est introduite en entrée. Différentes étapes de la transition laminaire-turbulente sont identifiées. De plus, deux bandes de fréquence sont observées en proche paroi chauffée. La Spectral Proper Orthogonal Decomposition, une méthode d'identification dérivée de la méthode Proper Orthogonal Decomposition (POD) a aussi été utilisé et s'est avérée être un puissant outil permettant une très nette séparation spatio-temporelle des modes les plus énergétiques de l'écoulement, en fonction des bandes de fréquence précédemment identifiées. Il devient donc possible d'étudier la contribution de ces modes aux transferts couplés de chaleur et de masse. Une analyse POD des champs de vitesse expérimentaux permet l'identification de similarités avec les structures observées numériquement.

Dans des précédentes études sur la même configuration, de larges différences au niveau de vitesses mesurées ont été rapportées pour des conditions apparemment similaires. Dans ces travaux, les variations du gradient de température extérieur au canal ont été identifiées comme une des sources de ces différences. L'influence du gradient de température externe a donc été étudiée expérimentalement et numériquement. Il est montré qu'une augmentation du gradient positif de température diminue le débit dans le canal mais aussi déplace la transition plus bas dans le canal. Par conséquent quand le gradient de température augmente, l'écoulement évolue d'un écoulement laminaire vers un écoulement transitoire et ceux malgré une diminution de débit. Les études numériques permettent également d'étudier le cas de gradients de température faibles ou négatifs, gradients qui sont difficile à obtenir expérimentalement.

Un modèle théorique de l'influence de la stratification extérieure sur le débit massique induit est aussi développé. L'accord entre les résultats prédits et les résultats expérimentaux et numériques est excellent. Ce dernier point souligne que la stratification thermique est un facteur clé dans ce type d'écoulement et que son influence est précisément quantifiée dans ce travail.

Publication

This thesis is about computational and experimental studies of a transitional natural convection flow. The thesis is based on and contains the following articles which arose from the PhD project.

Journal Papers

- **Thebault, M.**, Reizes, J., Giroux–Julien, S., Timchenko, V. and Ménézo, C. (2018). Impact of external temperature distribution on the convective mass flow rate in a vertical channel – A theoretical and experimental study. *International Journal of Heat and Mass Transfer*, 121:1264-1272

Peer-reviewed Conference Paper

- **Thebault, M.**, Giroux–Julien, S. and Ménézo, C. Modèles d'ordre réduit pour l'analyse et la modélisation de l'effet cheminée et des transferts de chaleur associés - application aux enveloppes ventilées différentiellement chauffées des bâtiments solaires. *Conférence Francophone de l'International Building Performance Simulation Association – IBPSA-France*,Nanterre, France, Mai 2016
- **Thebault, M.**, Giroux–Julien, S. and Ménézo, C. Modèles d'ordre réduit pour l'analyse et la modélisation de l'effet cheminée et des transferts de chaleur associés - application aux enveloppes ventilées des bâtiments solaires ou producteurs d'énergie. *24ème Congrès de la Société Française de Thermique – SFT-24*, Toulouse, France, 30 May - 2 June 2016
- **Thebault, M.**, Giroux–Julien, S., Ménézo, C. and Timchenko, V. Chimney effect analysis for wall thermal flux injection. 6*th Asia-Pacific Forum on Renewable Energy - AFORE 2016*, Nov 2016, Guangzhou, China. 2016.
- **Thebault, M.**, Giroux–Julien, S., Ménézo, C., Timchenko, V. Natural convective flow analysis in vertical channel *International Conference of Heat and Mass Transfer - ICHMT*, Napoli, Italia 2017
- **Thebault, M.**, Giroux–Julien, S., Ménézo, C., Timchenko, V. and Reizes, J. Canal vertical uniformément chauffé soumis à différentes stratifications thermiques extérieures – Etude

expérimentale et numérique. M. *26ème Congrès de la Société Française de Thermique – SFT-26*, Pau, France, 29 May- 1 June 2018

- **Thebault M.**, Giroux–Julien, S., Timchenko, V., Ménézo, C. and Reizes, J. Impact of external temperature distribution on the turbulent and thermal fields in a vertical uniformly heated channel. *Proceedings of the 16th International Heat Transfer Conference, IHTC-16,* August 10-15, 2018, Beijing, China

- Zhao Y., **Thebault M.**, Lei C., Patterson J. C., Giroux–Julien S., Timchenko V. and Ménézo, C. Coherent structures of the K-type transition in natural convection boundary layers: measurements and POD analysis. *Proceedings of the 11th Australasian Heat and Mass Transfer Conference, AHMTC11,* 9-10th July 2018, RMIT University, Melbourne, Australia

Extended Abstract for oral presentations

- Giroux–Julien, S., **Thebault, M.**, Ménézo, C. Unsteady mixed and natural convection in a non-uniformly heated vertical open-ended channel *9th Australian Natural Convection Workshop (9ANCW)* Monash University, Melbourne, Australia, 14-15 December 2015

- **Thebault, M.**, Giroux–Julien, S., Timchenko, V. and Ménézo, C. and Reizes, J. Influence of the external thermal stratification on the velocity and temperature profiles in a uniformly heated vertical channel *10th Australasian Natural Convection Workshop (10ANCW)* Auckland, New Zealand, 30 November - 1 December 2017

- **Thebault, M.**, Giroux–Julien, S., Timchenko, V., Ménézo, C. and Reizes, J. Assessment of decomposition methods for the analysis of transitional natural convection flow in a vertical channel *12th European Fluid Mechanics Conference EFMC12* Vienna, Austria, September 9-13, 2018,

Table of contents

List of figures

List of tables

Nomenclature

Roman Symbols

A	Size of the extended domain (cm)
a	Thermal diffusivity ($m^2\ s^{-1}$)
A_v	Amplitude of the inlet velocity disturbance
A_h	Heated area (m^2)
A_r	Aspect ratio
b	Coefficient of thermal expansion (K^{-1})
C	Spatially integrated temporal covariance matrix - POD
C_p	Specific heat capacity at constant pressure ($kg\ m^2\ K^{-1}\ s^{-2}$)
C_v	Coefficient of the Vreman SGS model
D	Distance between the two wide walls (m)
E	Energy content ($m^2 s^{-2}$)
g	Gravitational acceleration ($m\ s^{-2}$)
Gr	Grashof number $Gr = \frac{gbqL^4}{\nu^2\kappa}$
H	Height of the heated wall (m)
h_c	Non-dimensional location of the maximum $r_{v\theta}$ near the wall
h_e	Non-dimensional location at which growths in T_{min} and V_{max} change
h_T	Non-dimensional location of the first local maximum of temperature at the wall
h_v	Non-dimensional location at which the maximum near-wall velocity is reached)
L	Characteristic length
$\dot{m}$	Mass flow rate ($kg\ s^{-1}$)
N_f	Filter size for the SPOD filtering process
N_t	Number of snapshots

N_x Number of grid points

p pressure (Pa)

Pr Prandtl number $\frac{\nu}{a}$

Pr_{SGS} Coefficient of the Vreman SGS model

q Heat flux (W m^{-2})

$r_{v\theta}$ Coefficient of the v-θ cross-correlation

Ra Rayleigh number $\frac{gbqL^4}{a\nu\kappa}$

R_{air} Specific gas constant of air (m^2 s^{-2} K^{-1})

Ra^* Modified Rayleigh number $Ra \cdot A_r$

Ri Richardson number $\frac{gb\Delta TL}{\nu^2}$

S Filtered spatially integrated temporal covariance matrix - SPOD

S_r Strain rate tensor

S_t Non-dimensional stratification parameter

T Absolute temperature (K)

t Time coordinate (s)

u Velocity component in the x-direction (m/s)

v Velocity component in the y-direction (m/s)

$\mathbf{v}$ Instantaneous velocity vector ((m/s)^3)

w Velocity component in the z-direction (m/s)

w1 PIV field of view $y/H \in [0;0.25]$

w2 PIV field of view $y/H \in [0.25;0.50]$

w3 PIV field of view $y/H \in [0.50 : 0.75]$

w1 PIV field of view $y/H \in [0.75 : 1]$

x x coordinate, horizontal and normal to the heated wall (m)

$\mathbf{x}$ Space coordinate vector (m^3)

y y coordinate, vertical (m)

z z coordinate, horizontal and parallel to the heated wall (m)

Greek Symbols

α Temporal coefficients of the POD modes

β Temporal coefficients of the SPOD modes

ΔT Temperature difference (K)

δ_T Gradient of the linear external thermal stratification (K/m)

η Dynamic viscosity (Pa·s)

η_{SGS} SGS viscosity

γ Scaling factor for the velocity and temperature fluctuating fields (m^2K^{-1})

κ Thermal conductivity (kg m s^{-3} K^{-1})

λ Energy content of the POD modes (m^2s^{-2})

μ Energy content of the SPOD modes (m^2s^{-2})

ν Kinematic viscosity (m^2 s^{-1})

Φ Spatial POD modes

Ψ Spatial SPOD modes

ρ Density (kg/m^3)

σ Stress tensor (kg/m^3)

τ SGS quantity

θ Temperature rise over the reference temperature T_0 (K)

ζ Power coefficient for $Ra = f(\dot{m})$ correlation

Subscripts

0 Reference quantity taken at the inlet height, in the far-field

a Value taken in the far-field atmosphere

eff Effective

f Relative to the flow inside the channel

in Relative to the channel inlet

$inside$ Inside the channel

out Relative to the channel outlet

$outside$ Outside the channel

f Relative to the immediate surrounding of the channel, outside the channel

t Total electrical power

θ θ component of a mode

u u component of a mode

v v component of a mode

w w component of a mode

wall value taken near-wall in chapter 4 and at the wall in chapter 5

$\langle z \rangle$ z-averaging between z/W=0.25 and z/W=0.75

Acronyms / Abbreviations

BIPV Building Integrated Photovoltaic

BISS Building Integrated Solar System

BIST Building Integrated Solar Thermal

BR Bulk region

DFT Discrete Fourier Transform

DMD Dynamic Mode Decomposition

DNS Direct Numerical Simulation

LDV Laser Doppler Velocimetry

LES Large Eddy Simulation

LF Low-frequency

MF Mid-frequency

NCBL Natural convection boundary layer

PGD Proper-Generalized-Decomposition

PIV Particle Image Velocimetry

POD Proper-Orthogonal-Decomposition

PV Photovoltaic

PVT Photovoltaic and Thermal

RANS Reynolds Averaged Navier-Stokes Equations

SGS Subgrid-Scale

SPOD Spectral Proper-Orthogonal-Decomposition

THT Turbulent Heat Transfer

TI Turbulent intensity

UCBL Université Claude Bernard Lyon 1

UNSW University of New South Wales - Sydney

Chapter 1

Introduction

1.1 Motivation

Over the last decade and a half, increasing concerns regarding the environmental issues caused by anthropogenic global warming have spurred a rethinking of the management and methods of producing and of using energy.

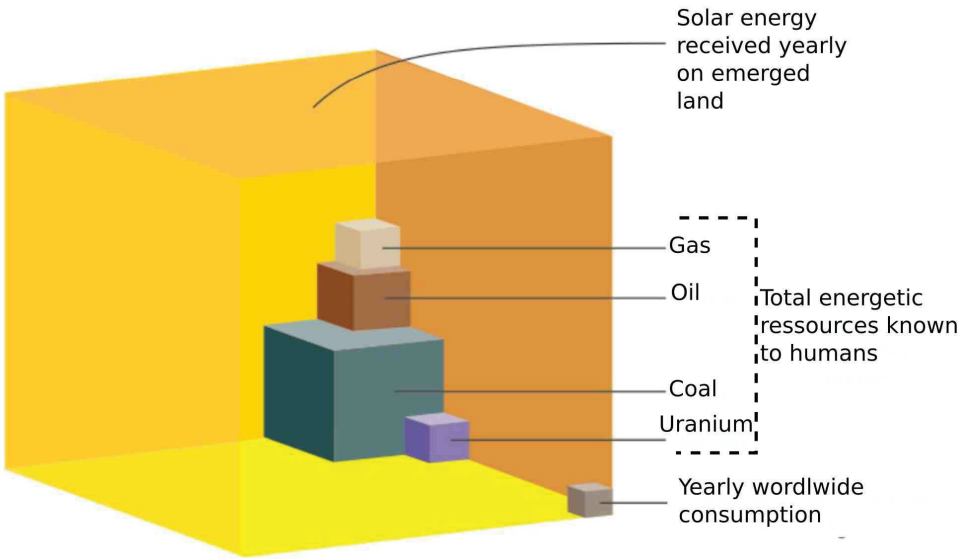

Fig. 1.1 Schematic representation of the different sources of energy available on earth as well as the worldwide consumption. Figure translated from French into English, taken from the work of (negaWatt, 2015).

A schematic representation of the total energy potential of fossil energy as well as the annual solar energy incident on the landmass of the earth, both compared with the total yearly energy consumption is displayed in figure 1.1. This illustration emphasizes the huge potential of solar energy compared with fossil, stocks of which are limited. Further, fossil fuels have significant deleterious environmental cost such as pollution and global warming. Moreover, the daily incident solar energy on the global landmass, is significantly greater than the annual worldwide energy consumption, which was estimated at around 150 000 TWh in 2018 (Enerdata, 2018). Despite its low energy density and its intermittent character, solar energy is spread across the globe. Additionally, progress in term of conversion efficiencies as well as innovations regarding local production and self-consumption, make the harvesting of solar energy one of the most promising solution for the renewable energy age.

The International Energy Agency (IAE, 2017), estimated that the cumulative solar PV capacity reached almost 300 GW and generated over 310 TWh in 2016. It is expected that solar photovoltaic (PV) panels will lead the renewable electricity capacity growth, expanding to a total of around 750 GW in 2022 which is expected to produce of nearly 800 TWh annually. For purposes of comparison, electricity consumption was around 200 TWh in 2017 in Australia and about 470 TWh in France in 2015.

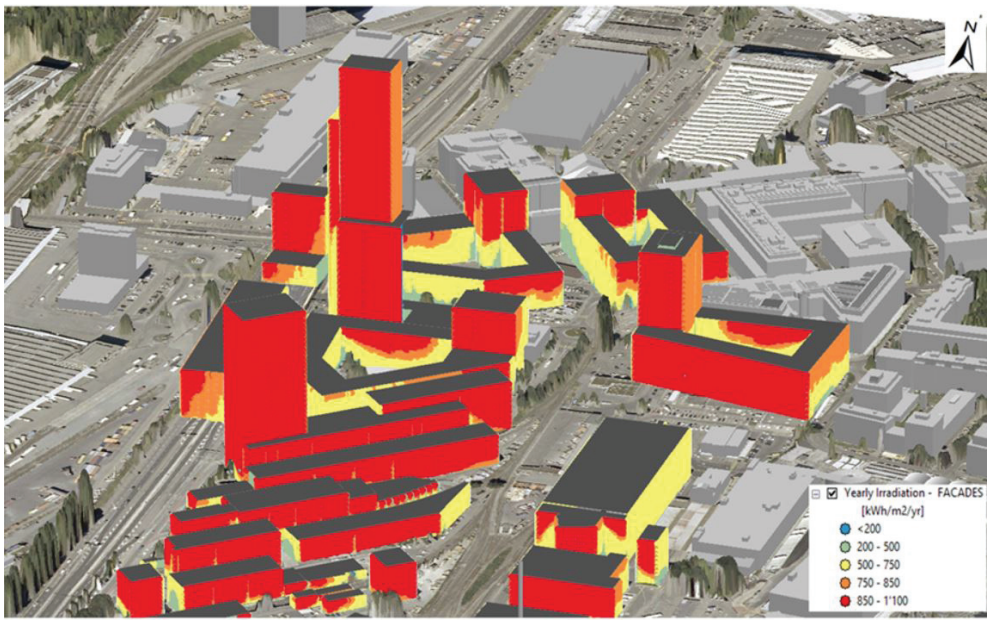

Fig. 1.2 Simulation of the solar potential of vertical surfaces in a district of Geneva. (Desthieux et al., 2018)

Another societal change concerns the rising urbanization worldwide. The New Climate Economy report (The New Climate Economy, 2014), projected that 2/3 of the population will live in urban areas whilst only 1/3 would live in rural regions by 2050; this is the reverse of the situation in 1950. Consequently, urban areas are growing very significantly so that the population density is also becoming much greater in urban areas. As a result, the management of the renewable energy sources in urban areas is one of the core problems to be addressed in the near future.

When an urban area expands, many vertical and horizontal surfaces are created by new buildings, so that an increase in urban density favours the growth of vertical surfaces. Most of the time, these surfaces are not exploited to their full potential. However, it has been demonstrated that these surfaces could collect a significant amount of solar energy as is illustrated in figure 1.2. For that reason, Building Integrated Solar Systems (BISS) technologies have been developed. These systems allow the generation of a local renewable energy, directly on the buildings, without the need of additional land. As a result, the land around the city can be used for other purposes and the energy produced can be used locally, which reduces the costs - both economic and energy - of transport. Finally, if the solarization of cities – defined here as the use of the surfaces of the built environment for the generation of energy - is carried out on a large scale, it would grant urban areas a certain level of autonomy. As far as energy is concerned Among BISS technologies, building integrated solar thermal (BIST) and building integrated photovoltaic arrays (BIPV) have been developed.

BIPV systems collect and convert solar energy into electricity. There is a number of systems being developed which include, hybrid Photovoltaic and Thermal (PVT), also called aero-voltaic

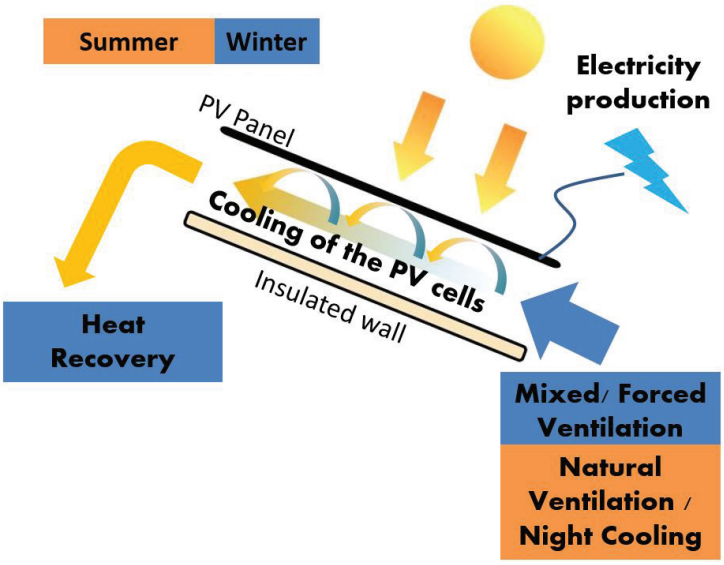

Fig. 1.3 Operating modes of a PVT system

systems such as PV-double skin façades. The working principle of these systems is depicted in figure 1.3. The PV arrays produce electricity, whilst the concomitant, but unwanted thermal heating of the arrays produces natural convective flows in the space between the PV façade and the wall enclosing the building. This phenomenon is sometimes referred to as the stack or chimney effect. This natural ventilation cools the PV arrays, thereby increasing their efficiency (Bloem, 2008), with the supplementary advantage that the heated air flow can also be used for heating or night cooling of the building. BIST systems are only designed for the pre-heating or night cooling of buildings.

For a system to operate without assisted ventilation, one or both of two phenomena are required to generate the necessary flow, namely either wind and/or the chimney effect. These two operating modes can act independently or together depending on the weather conditions. It was shown that usually, when there is wind, the pressure gradient that is generated is much higher than that which would have been generated by pure natural convection (Peuportier, 2016). However, knowledge of natural convective flows in these systems becomes necessary to determine the performance when there is no wind. Indeed in these conditions, the performance of PV systems would likely be reduced because the temperature of the PV cells would rise unless a passive cooling strategy is implemented. This dissertation is focused on a study of cases with no wind so that the cooling airflow is only generated by the chimney effect.

In figure 1.4 solar chimneys, placed on a roof of a public building in the Côtes d'Armor department are presented. These systems use wind depression as well as the temperature difference between the air inside and outside the building to create natural ventilation. The solar

Fig. 1.4 Solar chimneys on the roof of public building in Côtes d'Armor, Brittany, France. Credit: Agence Nicolas Michelin & associés

windows which have been placed at the base of each chimney enhance the chimney effect. A double-skin façade system present on the Surry Hills Library and Community center building is depicted in figure 1.5. In this case it is used for the heating or pre-heating of the air entering the building. The vegetation provides a passive filtering of the contaminants contained in the air.

Examples of BIPV systems are displayed in figure 1.6. The two systems shown in the upper two pictures of figure 1.6 consist of double-skin façades in which PV arrays have been integrated on the outer layer. In these cases the façades play the role of both shading windows and energy producers with the added advantage that the solar cells operate more efficiently because of the cooling airflow between the two façades. The system at the bottom photograph in figure 1.6 is a rooftop hybrid-PV system, which was designed for slightly inclined rooftop, (ADEME project Horizon PV) and which extracts heat from the PV panels by forced convection and uses it for the pre-heating of the warehouse located beneath.

The study of such systems is challenging for several reasons. The flow developing in these systems depends on numerous, coupled and complex phenomena. For example, external factors interfere with their functioning such as relative humidity, the external absolute temperature, external temperature gradient, wind or spatial integration. Moreover, BIPV systems are subject to a wide range of time scales, from the immediate effect of a wind gusts to seasonal changes, as well as a wide range of spatial scales, from the effect of small turbulent structures to the dimensions of a full-scale skyscraper and its surroundings. Finally, when these systems are integrated with full-scale buildings, the flow is likely to be both unsteady and turbulent. For these reasons, different strategies have been used in order to study this flow. Full-scale physical systems have been studied in situ in real-operating conditions (see *e.g.* Saadon et al., 2016).

Fig. 1.5 Vegetalized double-skin façade on the Surry Hills Library and Community center, Surry Hills, Australia Credit: Prodema

However, the complexity of the phenomena and the difficulty of accurately identifying and measuring them make the interpretation of analysis of results rather problematic. Moreover, the number of experiments that can be performed is in general limited. Therefore, laboratory-scale experimental equipment and numerical models have been developed for the study of these systems. The experimental models take the form of channels, the inclination and heating configuration of which can be varied. These models are simplified representations of small PVT systems, which therefore lead to smaller Rayleigh numbers, but they enable more detailed studies of the phenomena possible in better-controlled environment.

Fig. 1.6 BIPV systems, (top left), integrated solar cells on the outer skin of a double skin façade at the Schneider electric building, Grenoble, France, (top right), similar system at the tourism office of Alès, Cévennes, France, (bottom) assisted hybrid thermal-photovoltaic designed with EPC Solaire in the context of the ADEME project Horizon PV

Natural convective flows observed in experimental channels and in numerical simulations of channels of finite sizes often display the following characteristics:

1. The flow undergoes a spatial development during which the velocity and temperature distributions spatially evolve. In the experiments, this spatial development often spreads over several meters. As a consequence, the flow may become spatially developed in the higher part of the channel but the flow is more frequently not spatially fully developed when it reaches the top of the channel. In this case, the spatial development of the flow is of primary importance as it occurs in the entire channel.

2. Despite the efforts made to achieve better control of the environment, its effects on the flow are not well understood, let alone predictable. As for numerical models, the boundary conditions have not yet been properly established. Among different factors, the external thermal stratification has been identified as a potentially highly important parameter on transitional natural convective flows but its impact has not been satisfactorily investigated.

3. These two last points are also closely linked to the flow regimes. Very often, as the fluid travels upwards the flow undergoes a transition from a laminar to a turbulent regime. Since the flow is significantly impacted by the external surrounding conditions, the transition is also expected to result from a strong coupling between the internal development of the flow and the external conditions. Flow structures and especially turbulent structures greatly increase heat transfer rates and for that reason, they must be understood in order to master the heat processes in these systems.

The present work addresses two of the main issues highlighted in the previous points: first, the study of the flow structures in transitional flow and their contribution to the heat transfer rates and then, the effect of some environmental factors and especially of the external thermal stratification on the transitional natural convection flow.

1.2 Thesis objective

The present work was carried out in a context of a PhD cotutelle between the Université Claude Bernard Lyon 1 (UCBL) and the University of New South Wales-Sydney (UNSW). The establishment of this cotutelle was rendered possible by the long and extensive collaboration between the CETHIL laboratory at the UCBL, the LOCIE at University Savoie Mont Blanc and the UNSW Sydney and by a scholarship granted by the French Ministry of Research and Mobility and the financial support of the KIC Inno-Energy.

This study is in the lineage of previous works on a similar configuration during which the experimental apparatus (Sanvicente et al., 2013; Vareilles, 2007), and numerical three-dimensional Large-Eddy-Simulations (LES) simulations (Lau, 2013) were developed. These tools were adapted to the present study and used to gather data.

The flow studied is that of a spatially-developing transitional natural convective flow induced in a vertical channel by one wall uniformly heated at constant heat flux. Note that this work does not involve the first transient stage during which the flow evolves from a stating condition to an established ascendant flow.

The coherent structures of this flow are investigated using classical visualisation methods as well as Proper-Orthogonal-Decomposition (POD) based techniques. To the author's knowledge, it is the first time POD methods have been applied to this sort of flow. These methods give information on the flow structures and their roles in the transitional process that visualisations of instantaneous flow patterns cannot provide. The effect of the external thermal stratification on the flow is then numerically and experimentally studied and a theory is developed in order to predict its impact on the induced mass flow rate.

1.3 Thesis outline

Chapter 2 Past findings are critically reviewed in this Chapter and set the context in which the present study was carried out. The review mainly focuses on the transitional aspect of convective flows and on its interaction with the external environment.

Chapter 3 In this chapter the methodologies adopted in this work are outlined. First, the POD-based methods, namely the snapshot POD and the Spectral POD are introduced. Secondly,

the laboratory, as well as, the experimental apparatus, including the instrumentation used and experimental procedures are described. After, the LES methodology has been detailed and the approach adopted in this work is presented.

Chapter 4 The numerically obtained three-dimensional flow is described and is followed by a POD analysis in order to investigate the coherent structures and their role in the transition. The results of numerical generated data is compared with a POD analysis of experimental results so that the differences and similarities between the experimentally and numerically observed structures are highlighted.

Chapter 5 In the past the transition to turbulence was based on the change in the temperature gradient of the heated wall. This, however, had not been validated. Different indicators of transition are therefore proposed and their relevance for representing changes in the streamwise evolution of the time-averaged quantities of the flow assessed. The effects of the external thermal stratification on the spatially developing transitional natural convective flows are then studied both experimentally and numerically. Finally, the numerical model is used to study the effects of weak and negative stratifications on the flow.

Chapter 6 In order to predict the impact of the external thermal stratification on the convective mass flow rate, a one-dimensional theory was developed. The theoretical predictions are compared to numerical and experimental results.

Conclusion This last chapter summarizes the main conclusions and perspectives that can be drawn from this work.

Chapter 2

Literature review

This chapter presents the natural convection phenomenon and some of the background studies related to the present work. The state of the art associated with natural convection flow in vertical channel is extensive and for that reason, a focus has been made on transitional natural convection flow in channel and the impact of the environmental conditions on it. Furthermore the previous studies of coherent structures relevant for the present work, both in forced and natural convection are also reviewed.

Contents

2.1 Natural convection phenomenon and chimney effect.

2.1.1 Natural convection phenomena

Convective heat transfer is heat transport based on motion of a fluid that transfers heat from one place to another. Usually different types of convection are considered.

- The natural convection, also called free-convection is a motion which is generated from a difference in density. For example, in seas and oceans, a density gradient is caused by a salinity gradient which is at the origin of large-scale motions. Another well-known natural convection phenomenon is linked to the density difference which is inherent to temperature changes within a fluid. Indeed, as the temperature of a fluid rises, its density decreases. A density difference generates an upward force, also called buoyancy, opposing the weight, the magnitude of which, according to the Archimedes's principle, is proportional to the density difference.

- The forced convection occurs when flow convects heat but the density gradient is not at the origin of the motion. External forces such as pressure gradient or far-field velocities are the driving forces.
- Finally mixed convection is a mechanism of heat transport in which both forced convection and natural convection are driving the flow.

Usually the Richardson number (Ri) is used to characterised the different regime of convection. Ri is defined as

$$Ri = \frac{gb\Delta TL}{v^2} \tag{2.1}$$

in which g (m/s^2) is the gravitational acceleration, b (1/K) is the coefficient of thermal expansion ΔT (K) is a characteristic temperature difference between the hot fluid and the cold fluid, L (m) is a characteristic length and v (m/s) is the velocity. The Richardson number represents the importance of the natural convection relative to the forced convection. When $Ri < 1$ the flow convection is considered forced whereas for $Ri >> 1$ the convection is considered natural.

2.1.2 Chimney effect

In natural convection induced by a hot vertical plate, a natural convection boundary layer is generated close to the plate. As the natural convection boundary layer grows, it is fed by flows coming directly from below but also from the side as is illustrated in figure 2.1.

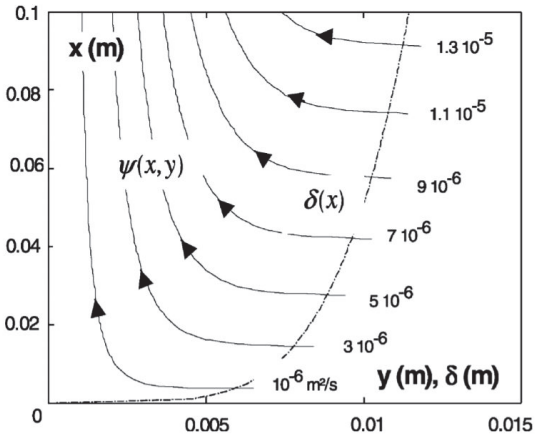

Fig. 2.1 Streamline patterns within the velocity layer at steady state (Polidori et al., 2003).

However, once another wall is placed close enough to the heated wall, then the feeding of the natural convection flow from the side is limited. If the opposite wall is far enough, no great changes are observed on the flow. Nevertheless, once the two walls are close enough the full channel is flowing. This is illustrated in figure 2.2, which comes from the work of Elenbaas

(1942). In his configuration, both walls were uniformly heated. This entrainment effect is called the chimney or the stack effect.

Usually in studies about natural convection, two methods are used in order to heat up the fluid and generate a motion. Either the temperature is imposed or the heat flux is imposed at the walls. Moreover, the usual heating configurations are either a channel which is symmetrically heated on both sides or a channel which is heated on one side, the other side being adiabatic. When imposed temperature boundary conditions are used, it is also possible to generate differentially heated configurations in which the temperature at the walls are different and sometimes opposite. Note some other heating configurations were studied and some of them will be described in the following sections.

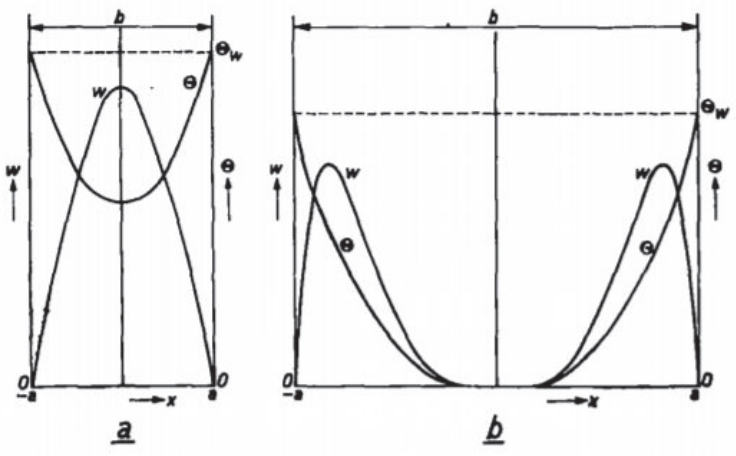

Fig. 2.2 Velocity and thermal profiles in a symmetrically heated channel with (a) narrow gaps and (b) wide gaps (Elenbaas, 1942)

One of the specificity of these flow is that they are open to the external environment. This is probably one of the most important characteristic when it comes to their study. Indeed, the driving forces of the natural convection channel flow are the buoyancy forces themselves and in order to fully understand these flows it is crucial to know what enters and leaves the channel. Experimentally, the difficulty emerges from the actual knowledge of the surrounding and boundary conditions. Indeed some experimental conditions may be extremely hard to measure, and the experimental access to detailed information on the whole surrounding is, for now, barely feasible. The numerical difficulties arise from the failure to accurately know the real surrounding conditions. As a consequence hypothesis and simplifications must be done regarding the boundary conditions which sometimes yield to changes compared to what was experimentally observed.

2.1.3 Conventional non-dimensional numbers

The configuration studied in this dissertation is a vertical channel heated at constant heat flux on one side of the channel. For that reason the non-dimensional number will be expressed in their heat-flux form.

Originally in studies regarding natural convective flow, Gr, the Grashof number was used to quantify the intensity of the turbulent flow.

$$Gr = \frac{gbqL^4}{\nu^2 \kappa} \tag{2.2}$$

where q (W/m^2) is the heat flux, L (m) is a characteristic length and ν is the kinematic viscosity. However in the current literature regarding natural convection the Rayleigh number, Ra, the and the Prandtl number, Pr are more commonly used.

The Prandtl number is defined as

$$Pr = \frac{\nu}{a} \tag{2.3}$$

where a is the thermal diffusivity. It quantifies the ability of the fluid to diffuse momentum by viscous stress relatively to its ability to diffuse heat by thermal diffusivity.

The Rayleigh number Ra, based on the heat flux, is defined as the product of the Grashof number and the Prandtl number and can therefore be expressed as

$$Ra = \frac{gbqL^4}{a\nu\kappa}, \tag{2.4}$$

where a is the thermal diffusivity.

Note that in the literature regarding vertical channels, there are no consensus whether the height or the distance between the two vertical wall should be used to characterise these flow and as a consequence either one or the other can be used. Another solution which has been introduced by Elenbaas (1942) is to introduce the aspect ratio of the channel and to define the modified Rayleigh number, Ra^*, also referred to as the Elenbaas number, defined as

$$Ra^* = Ra \cdot A_r, \tag{2.5}$$

for which the aspect ratio is given by

$$A_r = \frac{D}{H}, \tag{2.6}$$

D (m) being the distance between the two wide vertical walls and H m the channel height.

2.2 Laminar and transitional vertical natural convection flow

In this section, background studies on natural convection flows in vertical channels are presented. The first pioneering studies were reported in the 1940's and were carried out assuming a laminar flow. From that time and up to now, many studies of laminar natural convection flow in vertical channel have done. A brief summary of these studies is presented first.

As a very first approximation, a Rayleigh number of the order of magnitude of 10^9 is considered as the critical Rayleigh number value above which the natural convection flow becomes turbulent. Regarding flows encountered in real systems operating outdoors, the Rayleigh numbers are relatively high and the surrounding environment is not controlled. In these conditions, the flow is very likely to be in a transitional or a turbulent regime. For that reason the main focus of the present dissertation is the study of transitional natural convection, for which interests of the scientific community started in the 80's. A short literature review on this topic is thus proposed in the second part of this section.

Note that complementary literature reviews on natural convection channel flows are to be found in (Lau, 2013; Sanvicente, 2013; Vareilles, 2007) or (Garnier, 2014).

2.2.1 Pioneering studies, correlations and heat transfer enhancement

The first published experimental work on natural convection flow in a vertical channel was conducted by Elenbaas in 1942 (Elenbaas, 1942). The channel was composed of two vertical plates, symmetrically heated at uniform temperature. This study established the dependency of the Nusselt number in relation with the Prandtl and the Grashof numbers.

First analytical solutions were solved numerically in 1962 by Bodoia and Osterle (1962) and later in 1972 by Aung et al. (1972) and Aung (1972). A parabolic model of the Navier-Stokes equations were used for the simulation of the developing flow. Aung et al. (1972) and Aung (1972) respectively addressed the cases of a developing and a fully developed laminar flow. Different heating configurations were studied: symmetrically and asymmetrically heated, for a uniform heat flux or a uniform temperature at the walls. The maximum wall temperature and the Nusselt number were correlated with the Rayleigh number and their results were in good agreements with Elenbaas (1942) experimental results for moderate Rayleigh numbers.

Those pioneering works constitute the basis of numerous works that provided correlations between the maximum wall temperature and heat transfer for different heating configurations (uniform temperature and uniform heat flux) and different aspect ratios and geometries (see *e.g.* Bar-Cohen and Rohsenow, 1984; Khanal and Lei, 2015; Olsson, 2004; Ramakrishna et al., 1982; Rohsenow et al., 1998; Sparrow and Azevedo, 1985)). In its introductive chapter Daverat (2012) provides an exhaustive review of these correlations.

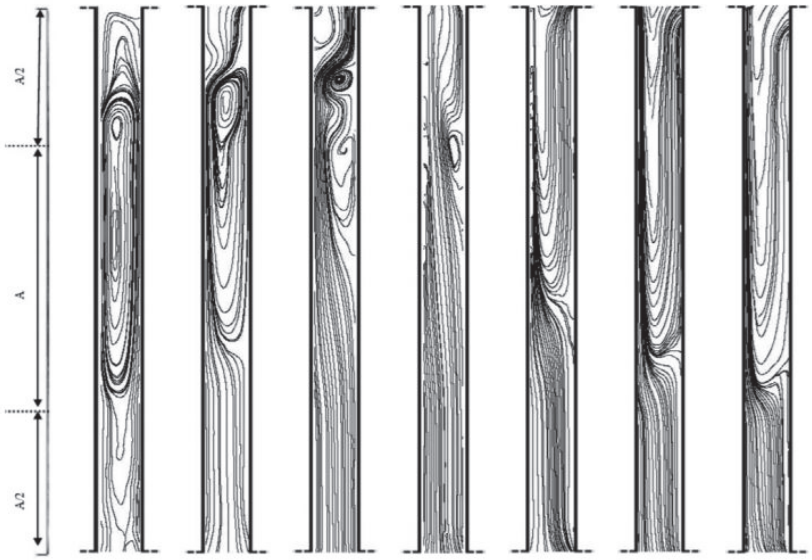

Fig. 2.3 Streamlines of the transient development of the natural convection flow at various time t=60-90-120-180-240-270-300 s. (Polidori et al., 2015)

More recently, and for application purposes different strategies have been successfully developed in order to enhance the heat transfers. Tanda (1997) introduced square ribs in an experimental channel symmetrically heated at uniform temperature. In experimental investigations,Auletta et al. (2001) and Manca et al. (2003) added an inlet adiabatic extension in a channel with uniform heat flux, respectively symmetrically and asymmetrically heated. In a numerical work, Nasri et al. (2015) added an outlet extension for a channel one-sided heated at uniform heat flux.

Another strategy experimentally investigated by Fossa et al. (2008) and Giroux-Julien et al. (2009) and later numerically by Tkachenko et al. (2016) was to modify the spatial distribution of the heat loads which resulted in a decrease of the hot spots temperature and an increase of the mass flow rate.

Laminar flow assumptions enable many relevant analyses. In their paper Khanal and Lei (2014) performed a scaling analysis of the transient and fully developed laminar natural convection flow and developed correlation for the prediction of the heat transfer and the mass flow rates. The transient early-stages of a laminar flow in a uniformly heated channel were investigated experimentally by Polidori et al. (2015) and numerically by Hemmer et al. (2017). The channel was one-sided heated at uniform heat flux. As it can be seen in figure 2.3, the flow goes through complex topological changes including large recirculation zone and significant reversal flows.

Recently Ramalingom et al. (2018) performed a topology optimization problem in order to minimize the pressure drop and maximize the heat transfers. The flow was laminar two-

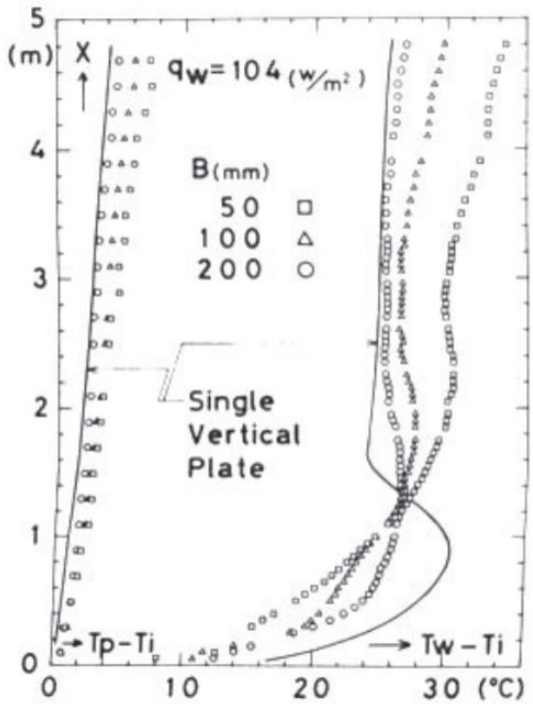

Fig. 2.4 Streamwise evolution of the temperature excess at the walls for various spacing, B, between the walls. (Miyamoto et al., 1986)

dimensional and penalization method was applied within the channel in order to determine whether the zone was considered as fluid or solid.

2.2.2 Transitional natural convection in channel flow

The work of Miyamoto et al. (1986) is one of the first experimental investigations dealing with transitional laminar-turbulent flows in a vertical channel with a uniformly heated wall. The channel was 5 m high and thermocouples and laser doppler velocimetry (LDV) were used to perform temperature and velocity measurements. In this study, a parametric study of the effect of the channel width and the heat input was conducted. In figure 2.4 are depicted the temperature distribution they obtained at the wall for a heat input of 104 W/m^2. In each case, they observed a local maximum of temperature on the heated wall which they associated with the transition to a turbulent flow. A local maximum of temperature at the heated wall has then been observed in numerous configurations (Daverat et al., 2013; Fossa et al., 2008; Sanvicente et al., 2013; Vareilles, 2007). Note that a local maximum of temperature was also observed in the experimental investigations of Brinkworth and Sandberg (2006) in which an air channel uniformly heated was studied. However they attributed it to a temperature loss from radiation directly to the surroundings.

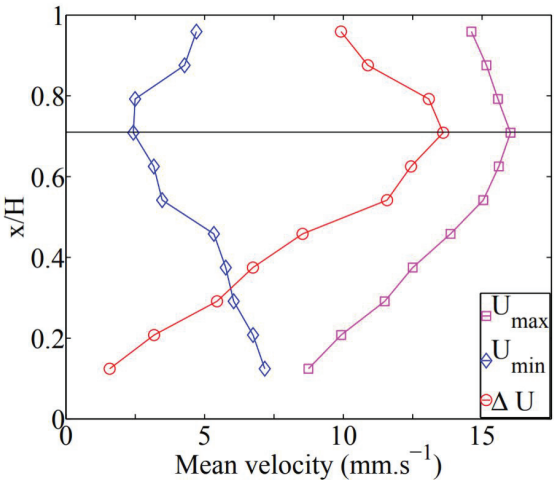

Fig. 2.5 Streamwise evolution of the time-averaged maximum and minimum velocity. The transition is defined here at the height at which their difference start decreasing. (Daverat et al., 2017)

Daverat et al. (2017) conducted an experimental investigation of a water flow contained within a tank. The channel was symmetrically heated at uniform heat flux and simultaneous velocity and temperature measurements were carried within the fluid. As it is depicted in figure 2.5, they used the height at which the velocity difference between, the maximum near wall velocity and, the bulk velocity, as the indicator of transition. In their work, measurements of the velocity and temperature fluctuations showed that the turbulent activity started to rise at a lower location than what was defined as the transition height. Moreover coupled velocity and thermal measurements provided an estimate of the cross-correlation between the wall-normal velocity and the temperature fluctuations, also referred to as turbulent heat transfer. Like the turbulent activity, the turbulent heat transfer also increased lower than the transition height. A transition scenario was thus proposed to explain the transition.

(Li et al., 2017) developed a scaling analysis based on a zonal approach. The zonal partitioning is based on the streamwise location at which transition occurs, then a partitioning based on velocity and thermal boundary layer length is performed independently below and above the transition height. This scaling analysis was validated against the experimental work of Daverat et al. (2017) and provides analytical expressions that can be used in simplified model of the flow.

In parallel numerical investigation have been conducted in order to model this type of flow. Borgers and Akbari (1984) published one of the first numerical study about transitional natural convection channel flow. The channel was symmetrically heated at uniform temperature and they used a simplified two-dimensional code which allowed to switch from a laminar resolution to a turbulent resolution of the flow once a certain transition criteria was reached. The code was then used to provide correlations for the Nusselt number.

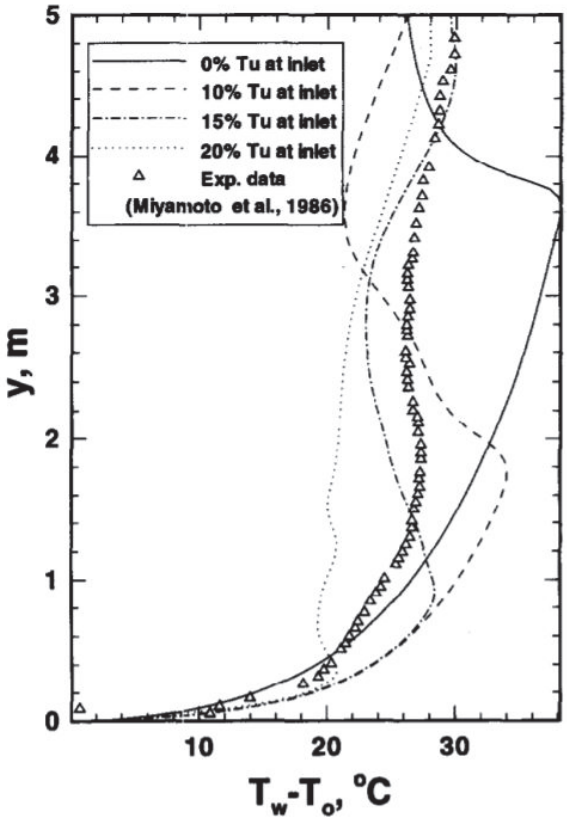

Fig. 2.6 Temperature distribution at the heated wall. The lines represent numerical RANS results obtained for different turbulent intensity levels at the inlet and the triangle are the experimental data of Miyamoto et al. (1986). (Fedorov and Viskanta, 1997)

In a two-dimensional numerical study, Fedorov and Viskanta (1997) used a steady-state Reynolds-Averaged-Navier-Stokes (RANS) solver to model a configuration similar to the experimental work of Miyamoto et al. (1986). They used different levels of turbulent intensity at the inlet of the channel and compared their results to those of Miyamoto et al. (1986). They obtained good quantitative agreement with the time-averaged velocities in the channel. Regarding the temperature distribution, which are displayed in figure 2.6, the agreement was considered the best with a turbulent intensity of 15 %. However there were still strong differences between the experiment and numerical results: the temperature growth in the lower region were very distinct, and the local maximum of temperature, considered as an indicator of the transition turbulence, was predicted significantly lower numerically than what was observed by Miyamoto et al. (1986).

Some years later Yilmaz and Fraser (2007) and Yilmaz and Gilchrist (2007) performed experimental-numerical confrontations respectively in a uniform temperature and a uniform heat flux channel. These numerical study were steady-state, two-dimensional RANS modelling. They used different turbulence models and their own experimental measurements and managed

to obtain fairly good time-averaged representation of the experimentally observed flow. But once again the same differences with the prediction of the temperature at the wall were observed.

More recently, Lau et al. (2011) investigated the same configuration using this time a three-dimensional Large-Eddy-Simulation (LES) solver for which he assessed different subgrid-scale models. Two SGS models were used, namely the Smagorinsky (1963) and the Vreman (2004) SGS models. It appears that the experimental temperature distribution at the heated wall of Miyamoto et al. (1986) was very well captured by the LES model using the Vreman SGS.

As was demonstrated by Fedorov and Viskanta (1997) and Yilmaz and Gilchrist (2007) in studies using RANS models and by Lau et al. (2012b) and Tkachenko et al. (2016) in LES investigations, the turbulent intensity level at the entrance of the channel proved sometimes crucial in order to obtain a fairly good representation of the mean and turbulent quantities of the flow. Moreover Lau et al. (2012b) and Tkachenko et al. (2016) observed that the introduction of a disturbance also increases the occurrence of intermittent velocity and thermal flow structures, especially near the heated-wall.

These last observations raise two major questions regarding the study of transitional natural convection. What is the effect of the surrounding conditions on the transitional flow? What are the velocity and thermal structures observed and how to study their impact on the flow? Therefore, in the following sections, some content on the impact of the surroundings on the flow behaviour will be introduced. Then some ways of studying unsteady flow structures will be described.

2.3 Effect of the boundaries on the natural convection flow in the open-ended channel

As mentioned above, one of the crucial points with natural convection flows in channel is that they are self-driven open flow, which make them very sensitive to all the surrounding conditions.

Experimentally, when these system operate in real-condition (see *e.g.* Saadon et al., 2016) there is no control and very weak knowledge of the external surroundings. Furthermore outdoor conditions can be extremely complex. For that reason different experimental strategies have been adopted in order to better control these conditions. The most basic approach consist of an apparatus placed in large laboratory room (see *e.g.* Miyamoto et al., 1986). These apparatus are subject to less external disturbances than what a system operating outdoor would. Nevertheless numerous sources of disturbance are still present in a laboratory room, from the heat of an electronic device to the velocity disturbance from a computer fan. In some cases screens or heavy curtains have been used in order to reduce these external sources (Fossa et al., 2008; Manca et al., 2003) but they are not sufficient to isolate the channel.

To better control the sources of disturbance, some experimental apparatus are enclosed within a cavity build for that purpose (see *e.g.* Daverat, 2012). By this aim the sources of

disturbances are better known. However these cavities are usually smaller than what a large laboratory room could be and therefore the effect of the cavity size on the flow must be evaluated. One of the first study which investigates the effect of the cavity size on the channel flow was done by O'Meara and Poulikakos (1987). In their experiment they conducted studies on the effect of the distance of each of the cavity walls on the laminar flow and concluded that the ceiling had the greatest negative impact on the cooling process.

In spite of the efforts which are made in order to reduce the effect of the surroundings on the channel flow, experimental channel will always be contained within an ambient in which more or less complex disturbances occur. It is thus crucial for numerical and theoretical studies to adequately model the boundary conditions of such configurations. To that aim, two main strategies have been adopted over the past years which Garnier (2014) referred to as implicit and explicit approaches.

The **implicit approach** consists in considering the channel and its surrounding. Most of the time the channel is modelled within a closed or opened cavity. Kheireddine et al. (1997) investigated a laminar two-dimensional flow within a cavity with free pressure boundary conditions and concluded on the importance of having these boundaries as far as possible from the channel for it not to affect the flow.

Garnier (2014) investigated an unsteady laminar two-dimensional channel flow in closed cavities of various sizes. The channel generates velocity and thermal structures which are exhausted from the channel in the upper region of the cavity (see figure 2.7). As long as these structures remain high enough above the channel exit, they do not interact with the channel. However, once the simulation run for a sufficient time, these structures will progressively create thermal and pressure stratifications which, when they start to reach the channel top opening, modify the flow in the channel. Garnier (2014) therefore defined a characteristic time, that depends on the cavity size and the heat injected, and for which the channel flow remains undisturbed by the external conditions. A similar study have been carried out by Zoubir (2014). The implicit approach remains a very cost-computing method.

The **explicit approach** consists in truncating the computational domain in order to only simulate the channel flow. An usual approach consists in considering the whole channel and modelling the inlet and outlet boundary conditions. In this case, the choice of the velocity, the pressure and the temperature boundary conditions are crucial. Different study attempted to better model these boundary conditions which some of them will be more specifically addressed in the following paragraphs. A benchmark study of Desrayaud et al. (2013) proposed reference solutions for different set of boundary conditions.

An alternative approach has been proposed by Naylor et al. (1991). In their numerical study, an half-disk, depicted in figure 2.8 have been added to the computational domain below the inlet. The flow can develop freely in this region and therefore the effect of the boundary on the channel flow is reduced. Manca et al. (1994) defined an I-type configuration illustrated in

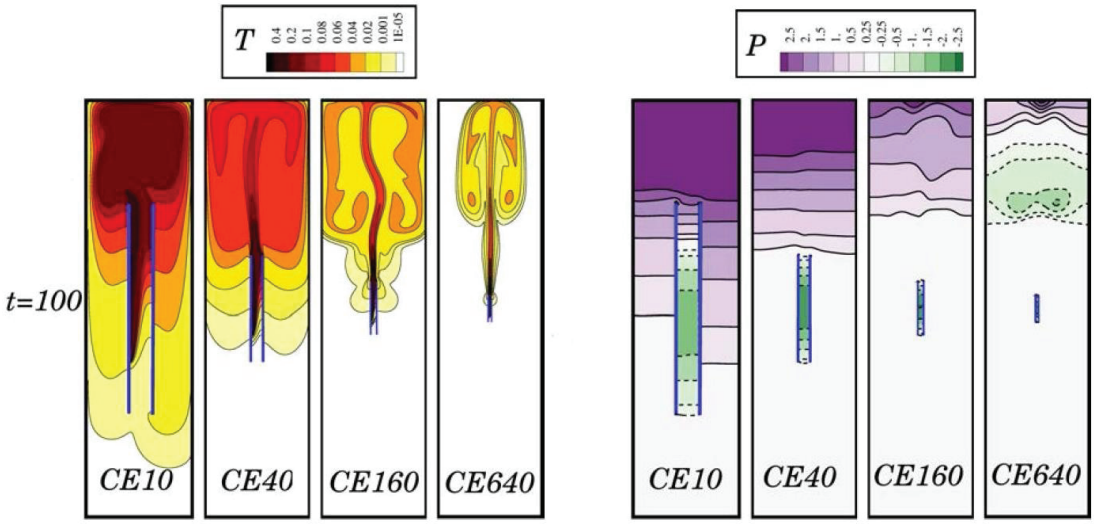

Fig. 2.7 Temperature (left) and dynamic pressure (right) distributions after 100 s for various cavity size. The two blue lines represent the channel walls. The height of these walls remains constant but the size of the cavity significantly increases from CE10 to CE640. (Garnier, 2014)

figure 2.9 for which additional domain where considered below the inlet and above the outlet of the channel. This approach has been successfully used in numerical/experimental comparison by Lau et al. (2012a) or Tkachenko et al. (2016). Note that even if the boundary conditions at the channel inlet and outlet are less constrained than for usual explicit approaches, the adequate modelling of the open boundary conditions remains a crucial point. Moreover, contrary to implicit approaches, this approach does not consider interaction between the exhausting flow and the entering flow.

The attempts to isolate the channel from all the external disturbances are relevant for studies in which very clean properties of the flow need to be observed. However, from the perspective of the application purposes, these flows are expected to be subject to very complex structures and therefore, the impact and effect of the surrounding conditions on the flow must be studied. As a consequence having external non-controlled source of disturbance, when they can be measured and monitored, represent a great opportunity for the study of these systems. The following sections propose a short review of the effect of the surroundings on the flow behaviour.

2.3.1 Inlet disturbances

In experimental studies the entrained flow is always disturbed to some extent. One of the perturbation sources may come from the channel entrance shape. Indeed a sharp leading edge generates disturbances and recirculating zone. In an experimental study of a transitional flow, Katoh et al. (1991) changed the sharp entrance shape of their channel by a smoother bell-shaped entry. They observed a significant decrease of the inlet disturbance and a displacement of the transition location higher in the channel. Similar entrance shape are used in other vertical

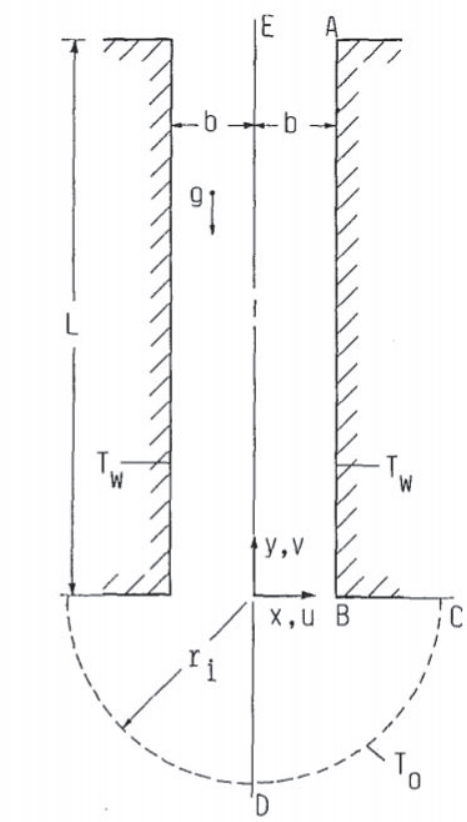

Fig. 2.8 Computational domain of (Naylor et al., 1991)

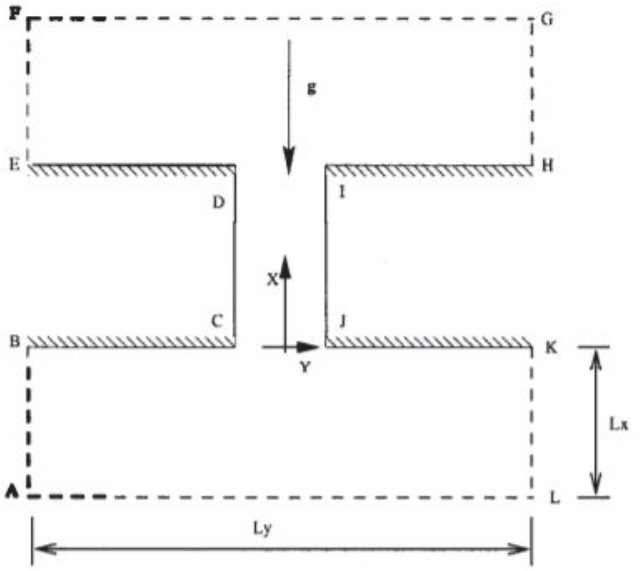

Fig. 2.9 I-type computational domain. (Campo et al., 1999)

channel apparatus (see *e.g.* Daverat et al., 2013; Dupont et al., 2013). Similar conclusion were obtained by Vareilles (2007) when he introduced bevelled entrance edges. Sometimes an adiabatic zone is also placed at the inlet, which provides some space for the fluid to develop before approaching the heated area (see *e.g.* Fossa et al., 2008; Ospir et al., 2012).

Despite the precautions that can be taken at the inlet to smooth the entrance of the flow in the channel, the presence of a high inlet disturbance level was still often reported. Sanvicente et al. (2013) performed PIV measurements in a transitional natural convection channel and measured turbulent intensity around 25% in the entrance region. Daverat et al. (2013) reported turbulent intensity up to 35 % at the inlet of a water channel with isoflux conditions. The inlet disturbance is known to have a significant effect on the transitional flow behaviour. For example, as was mentioned in the previous section, in numerical investigation, the inlet turbulent intensity significantly changes the time-averaged flow behaviour (see *e.g.* (Fedorov and Viskanta, 1997; Giroux-Julien et al., 2009; Lau, 2013)).

2.3.2 Effect of the dynamic conditions

The impact of the pressure boundary conditions on the channel flow had been underestimated for a long time, probably because it was very difficult to measure. As the channel flow is an open flow, it had often been assumed that the pressure at the inlet and outlet boundaries could be approximated as being equal to the static pressure outside the channel in the still ambient.

In 1981 Dalbert et al. (1981) introduced a pressure drop at the inlet, following the Bernoulli law. The numerical results appeared to be different than for the cases without a pressure drop and showed better agreements with the analytical solution of a fully developed flow obtained by Aung (1972).

Garnier (2014) used an implicit approach to propose reference cases for the laminar modelling of velocity and pressure at the inlet and outlet boundaries. In experimental-numerical confrontation Zoubir (2014) and Brangeon et al. (2015) studied the influence of different dynamic boundary conditions. The benchmark study (Desrayaud et al., 2013) highlighted the similarity and differences obtained by different research team modelling the same case.

2.3.3 Flow reversals

In 1984, Sparrow et al. (1984) first reported the existence of a reverse flow at the outlet of the channel. The configuration was a vertical channel heated on one-side at uniform temperature. Since that time a great number of studies mentioned or studied the reverse flow phenomenon.

Dupont et al. (2013) distinguished the cases of a permanent reverse flow, an intermittent reverse flow and the absence of reverse flow. Then a classification of the outlet flow in these categories was proposed depending on the Rayleigh number and the aspect ratio of the channel.

An experimental laminar study of Polidori et al. (2015) studied the early transient stage of the reversal flow. They described a succession of complex structures that occur at the outlet of a channel asymmetrically heated.

More recently, an experimental study of Li et al. (2018) (same apparatus as Daverat (2012)) showed the occurrence of a dramatic change in the flow behaviour. The flow was reported to change from a classical channel flow to a single plate flow. They attributed these changes to a strong reversal flow induced by large scale circulations occurring in the water tank containing the channel.

The reverse flow introduces fluid from the outlet which may have different temperature than the inlet fluid. Moreover when there is a reversal flow, it reduces the area from which the flow can exit the channel and therefore because of the mass conservation, it accelerates this flow. As a consequence it creates shear in the higher region of the channel. If this reverse flow is intermittent it can also create strong unsteadiness.

2.3.4 Effect of the external temperature distribution

Another external factor which induces strong changes on the flow behaviour is the external thermal stratification.

The impact of the ambient temperature conditions on natural convection has been known for some time and has been extensively studied in the cases of heated vertical plates. In 1967 Cheesewright (1967) first developed similarity solution for steady laminar natural convective flows adjacent to vertical isothermal plate in non-uniform ambient temperatures. His work started after he noticed significant differences between analytical models and experimental measurements which he attributed to the external thermal stratification.

Another pioneering experimental and theoretical study of Jaluria and Gebhart (1974a) investigated the effect of external thermal stratification on a natural convection flow induced by a uniformly heated vertical plate. They used a stratification factor J that they obtained by similarity analysis and which quantify the stratification strength. Among over observations they showed that as the external thermal stratification was increasing the velocity was decreasing as shown in figure 2.10. They reasoned that this was caused by the fact that as the ambient temperature increases downstream, the temperature difference between the local ambient temperature at a particular elevation and the temperature of the upward moving fluid in the boundary layer at the same elevation is less than it would have been if the ambient temperature had been uniform, with the result that a reduced buoyancy led to lower induced velocities.

However, only a few studies were carried out on its impact in the case of a vertical channel uniformly heated. Regarding the previous numerical works, the impact of the ambient temperature distribution was observed in some cases in which the channel was modelled as enclosed in an adiabatic closed cavity initially at uniform temperature. Because of the heat injection

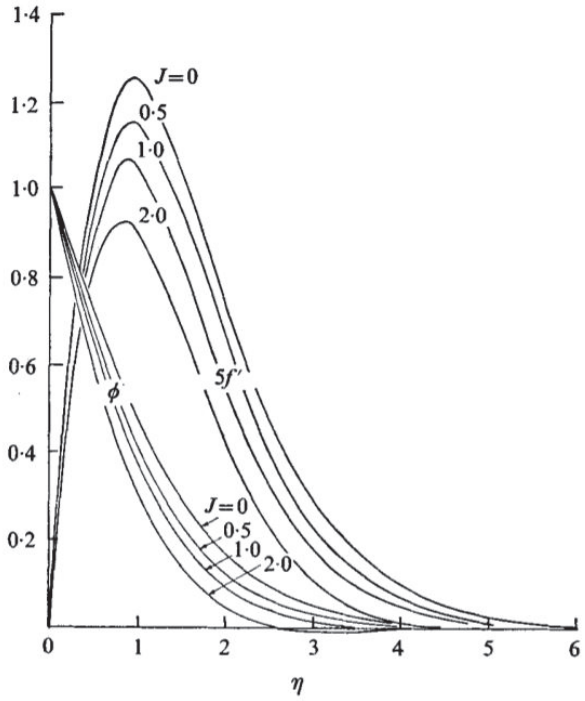

Fig. 2.10 Influence of the external thermal stratification, J on the temperature and velocity distributions. (Jaluria and Gebhart, 1974a)

in the channel, the top of the cavity became progressively thermally stratified and once the developing thermal stratification reached the top of the channel, the velocity in the channel decreased (Garnier, 2014; Hemmer et al., 2016; Zoubir, 2014). More recently the impact of thermal stratification was explicitly studied in a recent laminar two-dimensional numerical investigation by Ramalingom et al. (2017) which confirmed the previous observations.

Experimentally the impact of the temperature gradient had been known for many years though not specifically investigated. Haaf et al. (1983) in a pilot project on a solar chimney, underlined and recorded its "favourable or unfavourable effect".

Daverat et al. (2011) highlighted, in a symmetrically heated water channel, the strong influence of the external thermal stratification on the velocity and thermal fields of the flow. A figure taken from their paper is presented in figure 2.11.

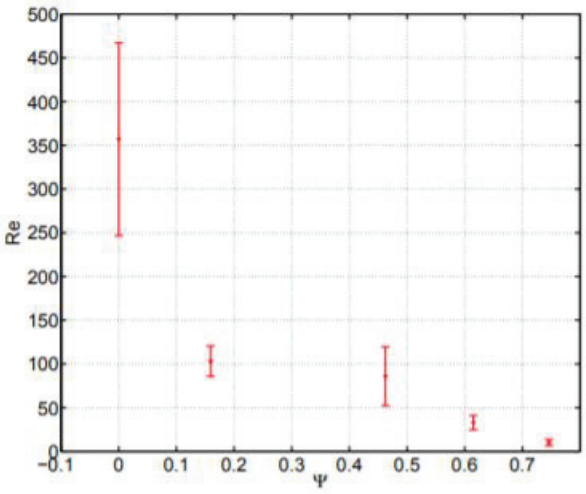

Fig. 2.11 Evolution of the Reynolds number with the external thermal stratification (In this figure Ψ is a stratification parameter proportional to the external thermal stratification). (Daverat et al., 2011)

They observed thermal stratifications up to 9 K/m for a fixed heat input of 190 W/m^2. The external thermal stratification significantly impacted the flow behaviour. Moreover they reported that for external stratification higher than 2 K/m, the channel was not flowing full at the inlet. Instead two independent boundary layer flows developed on the heated walls.

However, in the great majority of the experimental studies, when the external thermal stratification is mentioned, it is not considered as one of the influential factor under study. Either its impact is assumed to be neglectible (Sanvicente et al., 2013), or the measurements are done before the surrounding atmosphere becomes stratified, or they are carried out under a constant external thermal stratification (Polidori et al., 2015). Sometime an active cooling system is used in order to keep the ambient temperature uniform (Daverat et al., 2017; Li et al., 2018), but it requires extreme caution in order not to disturb the flow.

The impact of the external thermal stratification on the transition of the natural convection flow, was investigated experimentally and theoretically in the case of an isoflux vertical plate by Jaluria and Gebhart (1974b). They observed that as the surrounding thermal stratification increased, the transition height was displaced at a higher location. As to uniformly heated vertical channels, no studies explicitly analysed the effects of the thermal stratification on the transitional behaviour. However, it can be seen in the experimental work of Daverat et al. (2011) that, when they plotted the wall temperature relative to the temperature of the ambient fluid at the same height, a maximum was reached and was displaced lower in the channel as the external thermal stratification increased. This result could suggest a displacement of the transition to turbulent flows lower in the channel as the external thermal stratification increased.

2.3.5 Radiation

The consideration of radiation in the context of natural convection in vertical channels is also of great importance and numerous experimental and numerical works investigate its effect.

The effect of radiations in these types of configuration can be split in two major aspects which are, the amount of energy exchanged by radiation between walls and the openings as well as the effect of radiation on the flow itself as a participative media.

Exchanged of energy by radiations between the walls were observed in numerous experimental studies in which only one wall was heated at uniform heat flux. It was observed that the unheated wall as well as the fluid near it were hotter than the fluid temperature in the middle of the channel, only direct radiation between the walls could have provided this heating. Many examples of this sort can be observed in the experimental measurements of Miyamoto et al. (1986), Webb and Hill (1989) Sandberg and Moshfegh (1996), Fossa et al. (2008) or Sanvicente (2013); Vareilles (2007).

Carpenter et al. (1976) is one of the first numerical study which included the effect of radiation in vertical channel. The flow was laminar and asymmetrically heated at uniform heat flux. It was noticed that the heat exchanged between the wall as well as the heat exchange through the open ends of the channel could considerably reduce the maximum temperature at the wall.

Different approachs have been developed in order to study the effect of radiation, from the first order which only consider radiation between the surfaces (see *e.g.* Carpenter et al. (1976), Lau (2013) Ramalingom et al. (2017)). Other modelling of the radiation including the participative media have been developed, the literature of which have been summarized by Tkachenko (2018). Furthermore, in her PhD dissertation she used a discrete ordinates model for radiation transport and considered humid air which is a participative medium. She demonstrated that depending on the in the context of transitional vertical channel flow, the effect of radiation heat transfer between the walls is tremendous. The time-averaged and instantaneous features of the flow were also altered, to lesser extent, by its relative humidity.

2.4 Study of intermittent structures and techniques for their analysis

2.4.1 Identification of coherent structures

Fig. 2.12 Popular paintings in which turbulent structures are depicted (left) *Studies of Water passing Obstacles and falling* by Leonard Da Vinci - (right) *The Star Night* by Van Gogh

In order to paraphrase George (2017),flow structures have always been observed and everyone could distinguish a flow in which movements are present from a still flow. Painters, poets, writers and scientists have drawn and described such structures over the centuries and two well-known representations of turbulent structures can be seen in figure 2.12. However, until today no-one can claim to have discovered a perfect way to identify and quantify these structures.

The identification, definition and study of large-scale organised structures, also sometimes referred to as coherent structures, has been one of the main topics in turbulence investigations for the past decades. Many methods of identification, definition and characterisation of these structures were proposed over the past years (see e.g. the reviews of Cantwell, 1981; Jiménez, 2018).

Instantaneous visualizations of the structures

The most basic visualisations can be obtained by plotting instantaneous components of the flow or vorticity fields, but these methods are very qualitative and, as a consequence, finer methods were developed in order to attempt to define unambiguously these structures. These methods are generally based on the identification of spatial regions in which the vorticity tensor, the strain rate tensor and the velocity gradients respect some criteria.

Three of the most famous of these methods are: The $Q-criterion$ (Hunt et al., 1988), defined as the region with a positive second invariant of the velocity tensor, the $\Delta-criterion$ (Chong et al., 1990) which identify the region in which the vorticity strain tensor are dominated

by the rotation tensor, or the $\lambda^2 - criterion$ (Jeong and Hussain, 1995) which is based on the finding of pressure minima inherent to the vortices. Other method, referred to as Lagrangian methods, uses a lagrangian approach to identify vortex (see *e.g.* the $M - criterion$ (Haller, 2005)). A detailed presentation of these methods may be found in (Haller, 2005; Kolář, 2007) or (Holmén, 2012)).

These methods proved to be very efficient in the identification of vortical structures such as eddies, hairpin vortices or the λ structures of the transitional flow. However, they present two drawbacks. First of all, they identify structures in instantaneous visualisations of the flow. As a consequence the structures represented are a subjective choice and the role that these structures may play in the long term is difficult to appreciate. Moreover, these methods focus on the identification of vortices which indeed represent a great part of the flow structures. However some structures such as the long streamwise streaks observed in some wall-bounded transitional flow are not vortical Wu and Moin (2009). These methods are thus unable to identify them. As a consequence, other approaches were developed in parallel in order to identify structures inherent to a flow.

Decomposition methods

Decomposition methods were developed and used with the main purpose to decompose a physical field into physical modes. Those modes, depending on the way they are obtained, can be studied for their physical meaning but can also be used to build a reduced-order model. A reduced-order model enables a drastic reduction of the state variables leading to a fast, accurate and precise model.

The basic idea of these methods is to re-write a physical field $P(x,t)$, x being the spatial coordinate and t the temporal coordinate, as a decomposition of spatial modes ϕ and temporal modes a. There are many different decomposition methods and two families can be distinguished. The *a posteriori* and the *a priori* methods.

A priori methods need a mathematical formulation of the problem from which modes are extracted, based on different methods. Stability analysis can thus be considered as an *a priori* method. Many *a priori* methods were developed as for instance the Proper Generalized Decomposition (PGD) (Chinesta et al., 2014) which builds modes based on an iterative process or the Branch Eigenmode Decomposition (Quemener et al., 2007) which decomposes the flow according to the branch modes. On the one hand, these methods present the advantage that no detailed dataset are necessary. On the other hand, it is necessary to know with precision the physical formulation of the problem. Indeed, a biased formulation of the problem will lead to biased results.

A posteriori methods are based on the decomposition of a pre-existing dataset of a time and space physical field observation. The data can either come from experimental measurements or from numerical simulations. A decomposition of this dataset is done in order to extract modes

according to various criteria. Because of this, the sample on which the decomposition is done is of great importance and needs to be chosen so that all the physical behaviours of interest can be captured. One of the most famous of these methods is the Proper-Orthogonal-Decomposition (POD) first formulated in the turbulence field by (Lumley, 1967). This method decomposes the flow based on an energetic criterion. However, one of the first *a posteriori* method which was developed is the Direct Fourier Transform (DFT) (see e.g. (Lesieur, 2008)). Spatial-DFT applied to flow fields extract spatial modes associated to single frequencies. One can cite the Dynamic Mode Decomposition (DMD) (Schmid, 2010) which decomposes the flow in dynamic modes composed of a spatial component associated with a spatial growth, a decay rate and a proper frequency. These methods have the advantage of being extremely robust because, as long as there is data, they can be applied and will provide modal decomposition. However, because a detailed dataset is required, they can be more costly than *a priori* methods.

POD-based methods

One of the more promising methods for identifying turbulent structures is the POD. This method has been used in many different fields from biology to social sciences and signal processing or fluid mechanics. Depending on the fields of interest it is known under different names such as Principal Component Analysis, Karhumen-Loève Decomposition, Singular Value Decomposition. These methods are inspired from a statistical method the origin of which was attributed to Pearson (1901). In 1967, Lumley (1967) first formulated POD for the study of coherent structures in turbulence researches. Indeed, the POD decomposes the flow according to an energetic criterion. To that extent, large-scale coherent structures with significant energetic content can be extracted from the flow.

According to the review of Berkooz et al. (1993) and the retrospective of George (2017), the use of POD evolved in two main directions: the construction of reduced-order models (see e.g. Aubry et al., 1988) and the identification of coherent structures (see e.g. Glauser and George, 1987). POD was originally applied to velocity fields, however its use was extended to other fluctuating fields such as the temperature field in the case of a cavity flow (Lumley and Poje, 1997; Podvin and Le Quéré, 2001; Podvin and Sergent, 2015), and thermally driven rotating flow (Hasan and Sanghi, 2007) and to the pressure field in the case of a turbulent jet (Arndt et al., 1997) and the flow past an airfoil (Ribeiro and Wolf, 2017).

Since Lumley first proposed his formulation of POD, many extensions have been developed and adapted in order to improve the decomposition results for particular flow configurations. One such extension is the Spectral Proper Orthogonal Decomposition (SPOD) method recently developed by Sieber et al. (2016). It should be noted that, in the literature, two methods were referred to as SPOD, and Sieber et al. (2017) clarify the relation between them by separating the time-domain SPOD Sieber et al. (2016) and the frequency-domain SPOD (Taira et al., 2017; Towne et al., 2018). Sieber et al. (2017) claim that the fundamental difference between these

methods lies in the way the space-time correlation matrix of the fluctuating fields is treated before solving the eigenvalue problem. The frequency-domain SPOD of Towne et al. (2018) share some features with DFT and DMD in the sense that it identify spatial modes associated with a single frequency. On the other hand, the time-domain SPOD developed by Sieber et al. (2016) bridges the gap between the classical POD and pure Fourier decomposition methods of studying fluctuating fields (Noack, 2016) thereby enabling, in some cases, an improvement of the identification of coherent structures associated with characteristic frequency bands (Ribeiro and Wolf, 2017; Sieber et al., 2016; Stöhr et al., 2017).

2.4.2 Coherent structures in vertical natural convection flows

Spatially developing natural convection in a vertical channel is a complex multifaceted flow affected by many parameters. Despite the natural convection is generated by an entirely different mechanism from shear or pressure-driven flows, many of the same phenomena act within the developing boundary layer, particularly in the vicinity of the wall. To that extent, the intermittent structures inherent to natural convection flows in a vertical channel may be related to all these flows.

Transitional wall-bounded externally driven flows

Transitional wall-bounded flows, and particularly zero-pressure-gradient boundary layer transitions are commonly divided into two different classes of transition: the natural transition and the bypass transition.

The natural transition -the literature about this was well summarised by Sayadi et al. (2013)- is triggered by small-amplitude background disturbances. In this case, Tollmien-Schlichting two-dimensional waves are amplified until three-dimensional secondary instabilities develop and form at one point turbulent spots populated with coherent hairpin vortices. These spots finally merge into a fully turbulent flow downstream. Rempfer and Fasel (1994) and Sayadi et al. (2014) respectively used POD and DMD in order to provides insight of the role of the flow structures as well as a reduced-order representation of the natural transitional flow.

The bypass transition -the scenari of which were reviewed by Zaki (2013)- occurs when a disturbance of significant amplitude is introduced in the initial flow. In this case, non-linear mechanisms lead to a faster route to turbulence which bypass the instabilities observed in the case of natural transition. In bypass transition, the laminar region is populated by near-wall elongated streamwise velocity streaks similar as those observed in figure 2.13 (see e.g. Klebanoff et al., 1962; Kline et al., 1967; Wu and Moin, 2009). These streaks are also present in the transition region. Moreover turbulent spots, populated with hairpin vortices, arise from near wall Λ structures (Wu and Moin, 2009). Finally the turbulent spots merge into a turbulent boundary

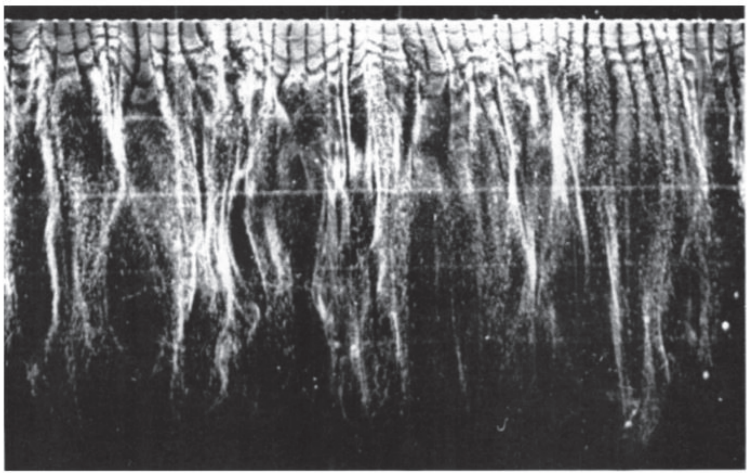

Fig. 2.13 First experimental visualization of velocity streaks of the by-pass transition, using smoke. (Kline et al., 1967)

layer densely populated with coherent vortices (Hack and Moin, 2018; Jeong et al., 1997; Wu and Moin, 2009).

The large-scale structures present in the bypass transition transport passive scalars so that streamwise velocity fluctuations and the scalar field fluctuations are strongly correlated near-wall (see e.g. Abe and Antonia, 2009; Kim and Moin, 1989; Pirozzoli et al., 2016; Wu and Moin, 2010; Wu et al., 2017). As a consequence the temperature field has sometimes been used as a tracer to observe these structures experimentally (see e.g. Atta and Helland, 1980; Chen and Blackwelder, 1978).

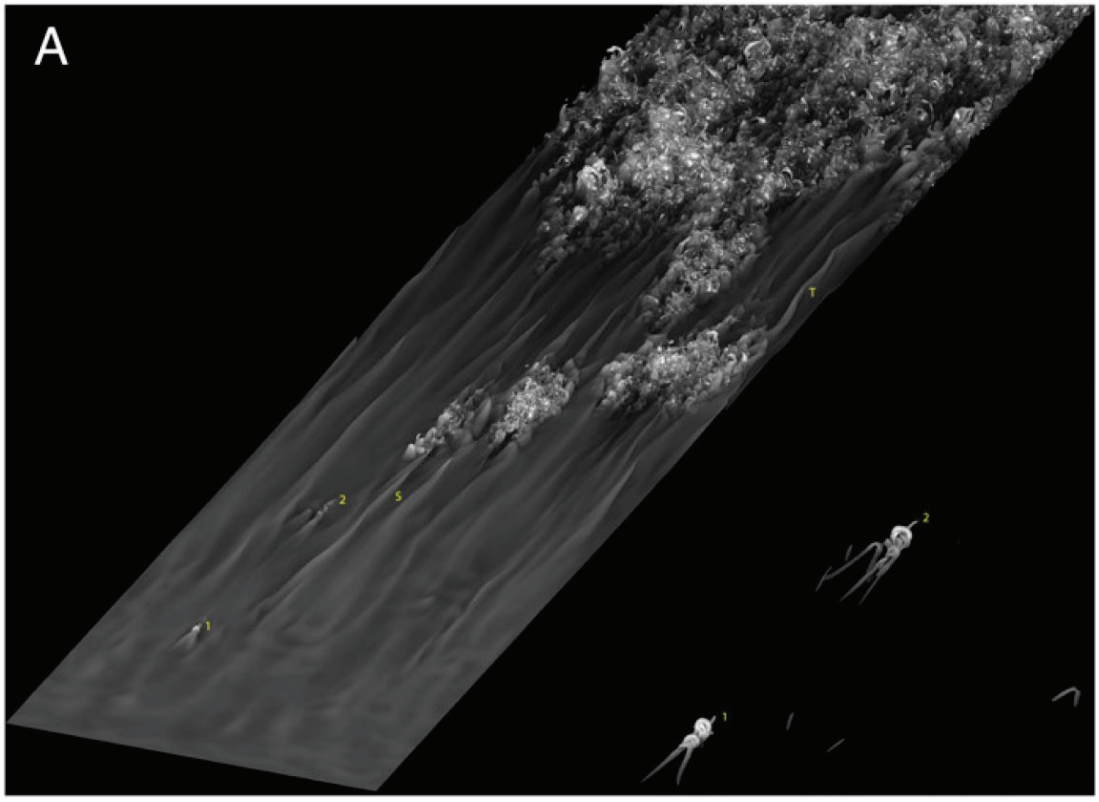

Fig. 2.14 Isocontours of temperature used to visualize the structures of the by-pass transition modelled by DNS. (Wu et al., 2017)

Turbulent natural convection

The study of instantaneous structures in the case of natural convection has not received much attention. The most often described structures are hairpin vortices, also referred to as arch-shaped vortex tubes and have been observed in the cases of turbulent natural convection flow over a vertical plate (Nakao et al., 2017) and in a vertical channel (Pallares et al., 2010), both configurations having isothermal boundaries. Pallares et al. (2010) described in detail these vortices and showed that they generate large heat transfer fluctuations at the wall. They also noted that contrary to turbulent wall bounded forced convection, the wall shear stress and the wall heat transfer were not correlated in turbulent natural convection. In a inclined channel configuration, heated from below, Ferahta et al. (2012) reported rolls that were generated at the heated wall and that were increasing the mixing with the cold fluid located above.

Ng et al. (2017) numerically studied the case of the ultimate regime in vertical natural convection flow. They obtained it in a channel in which the walls were differentially maintained at a constant temperature, with a streamwise periodic boundary condition and at high Rayleigh number. They observed correlated velocity and thermal streaks which they compared to the streaks observed in wall-bounded forced convection described above. All these structures were

observed in the case of spatially-developed flow but none of them focused on the transition to turbulence.

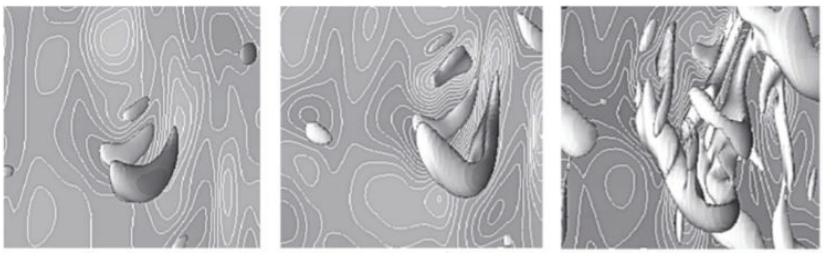

Fig. 2.15 Evolution of an hairpin vortex generated by a transitional natural convection flow. Structures are visualised using the Q-criterion. (Abramov et al., 2014)

Transitional natural convection

Transitional natural convection has been even less addressed. Zhao et al. (2013) studied the resonance of natural convection boundary layer over a isothermal vertical plate and numerically observed the organised Λ-shaped vortices, characteristic of K-type and H-type controlled transition (Zhao et al., 2017) that they obtained by introducing a disturbance at the resonant frequency of the boundary layer.

Abramov et al. (2014) described the appearance of the hairpin vortical structures depicted in figure 2.15, similar to those described by Pallares et al. (2010), that they observed in a transitional natural convection flow over a vertical plate in which they introduced homogeneous isotropic turbulence. However, despite a brief description of the transitional stage, the work then focused on the flow and thermal field statistics once the flow was considered fully turbulent. As a result, no previous studies identified and characterised the structures that can be observed in a spatially developing transitional vertical natural convection channel flow.

2.5 Previous results of Sanvicente (2013) and Lau (2013): emerging issues

The present work continues previous studies of natural convection flow in vertical channel, one mainly experimental carried by Sanvicente (2013) and another mainly numerical by Lau (2013). These works focused on the study of natural convection flow in vertical channel.

Sanvicente (2013) performed PIV measurements in an air channel and contributed to the experimental characterisation of the heat transfer in the channel for different varying parameters such as the inclination of the channel, the channel width or the heat input. A very detailed description of the experimental apparatus and the PIV methodology can be found in the Sanvicente PhD dissertation (Sanvicente, 2013). Her velocity measurements were carried out in five vertical two-dimensional planes of $100 \times 200\,\mathrm{mm}^2$, located at different y. Each

measurement sessions consisted of 8000 snapshots sampled at 11 Hz providing a dataset of about 12 min. This sampling time was chosen as it proved to provide reliable statistics of the flow (Sanvicente et al., 2013).

Lau (2013) developed an in-house LES code in which the Vreman SGS model (Vreman, 2004), adapted to transitional low-turbulence natural convection flow, was included. This code was first validated against the experimental data of Miyamoto et al. (1986) and was also used to perform numerical-experimental confrontation with the experimental measurements of (Sanvicente, 2013).

2.5.1 Repeatability

One of the issue raised by (Sanvicente, 2013) was the issue of repeatability. Indeed it was observed that, for a same injected heat flux, repeatability was difficult to achieve in a non-controlled environment. This is illustrated in figure 2.16 which shows that the temperature profiles at the wall and the streamwise velocity profiles are subject to repeatability issues. And yet, no attempt to explain the origin of this repeatability was offered. Moreover, only a limited amount of data about the surrounding environment was available so that it was not possible to determine whether a parameter of the environment may have caused these variations.

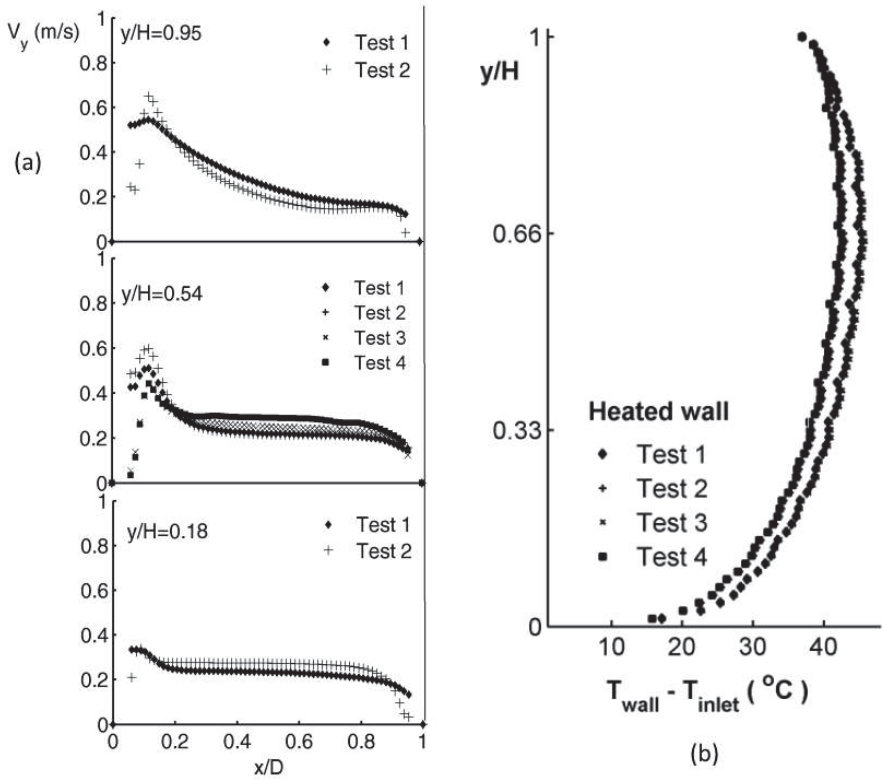

Fig. 2.16 Performed tests under the same injected flux conditions:(a) Streamwise velocity at different streamwise location, (b) wall temperature profiles (Sanvicente, 2013)

2.5.2 Description of the instantaneous structures of the flow

Preliminary frequency analyses were conducted by Sanvicente (2013) on the streamwise velocity component, near the heated wall. As can be seen in figure 2.17, no clear dominating frequency was identified but instead, a low-frequency band in the range [0.03-0.67 Hz] was observed. It was suggested that these frequencies were related to instability and intermittent structures of the boundary layer flow.

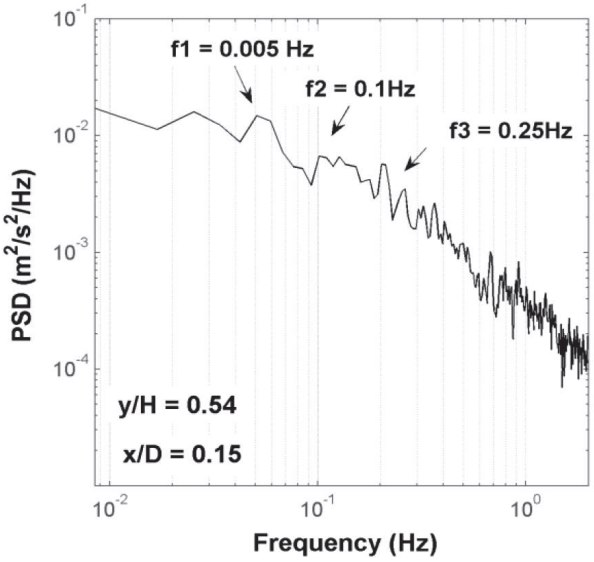

Fig. 2.17 Frequency analysis of the streamwise velocity at $y/H = 0.54$ for $x/D = 0.15$ (Sanvicente, 2013)

It was also observed that the flow was strongly unsteady with many coherent intermittent structures being present. Some of these structures were qualitatively described (Lau, 2013; Sanvicente et al., 2013). Instantaneous coloured isotherms of temperature have been plotted by Lau (2013) in figure 2.18. Experimentally, no detailed temperature fields are available, however the PIV measurements of (Sanvicente, 2013) allows the observation of plume-like velocity structures as plotted in figure 2.19. More detailed descriptions of the structures that were observed in the experiments and in the numerical results can be found in (Lau, 2013; Sanvicente, 2013). However, except for some Fourier analyses such as presented in figure 2.17, it stands that all the descriptions made relied on instantaneous visualization of the flow. Either the velocity or thermal fields were directly plotted. Other quantities such as the vorticity or the Q-criterion were used to display the coherent velocity and thermal structures. As mentioned in section 2.4.1, one of the main drawbacks of these representations is that they represent the flow at one instant and, consequently, it may be difficult to assess how representative such structures may be compared to the others.

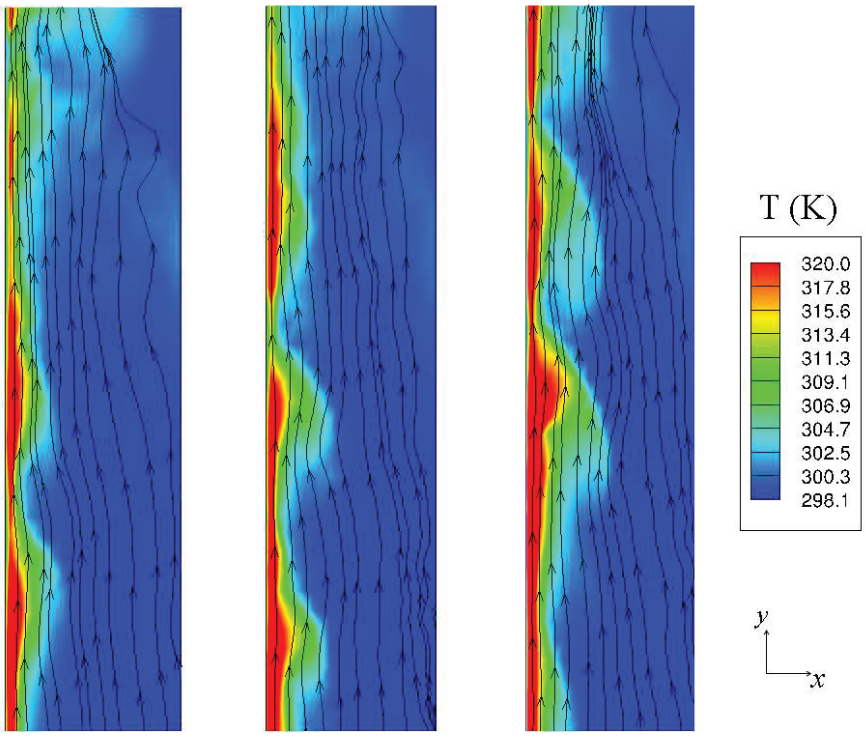

Fig. 2.18 Computed instantaneous isotherm at three randomly chosen times, together with streamlines in the section $0.65 < y/H < 0.85$ of the channel. (Lau, 2013)

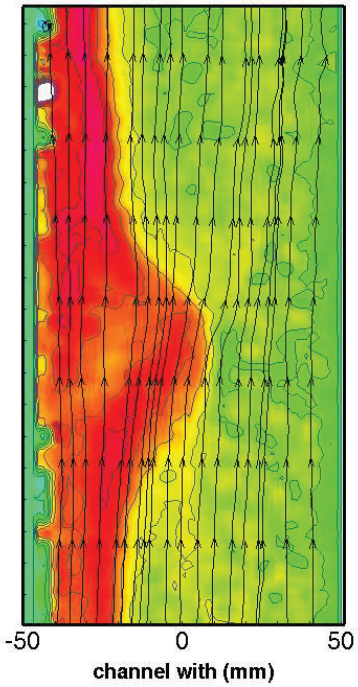

Fig. 2.19 Instantaneous visualisation of the velocity field obtained using PIV in a vertical plan normal to the heated wall. Measurements made at mid height of the channel. The field of view is approximately 18 cm high for 10 cm wide. Sanvicente (2013)

In order to better characterize and describe the structures that have been observed, Proper-Orthogonal-Decomposition based methods will be used as an analytical tool in this thesis. However, in order to do so, it is necessary to collect data set based on which the decomposition can be performed

2.5.3 Pre-existing data

In their respective works (Sanvicente, 2013) and (Lau, 2013) had collected experimental and numerical data. Some of this data has been used in the present work to perform preliminary observations but there were certain limitations which have emerged from existing data.

Regarding the available experimental data of Sanvicente (2013), the limitations are as follows:

- The analysis of the structures and their evolution is in part limited by the size of the PIV field of view which was 200 mm$\times$ 100 mm.
- The PIV measurement areas do not cover the whole height of the channel so that it is not possible to obtain a complete view of the channel which limits analysis of the evolution of the structures.

As to the available numerical data of Lau (2013), except for some very short sequences, no data samples were long enough to statistically investigate the effect of coherent structures.

For these reasons additional data needs to be collected for further investigation. In the present work, both experimental and numerical data will be collected. Indeed, experimentally obtained velocities provide information of the real structures which develop in this type of flow. However the observations obtained are often reduced to two-dimensional plans of limited size. Furthermore other physical fields such as the pressure and temperature fields are very difficult to measure. Numerically generated data present the opposite advantages and drawbacks. Numerical methods can provide complete three-dimensional velocity and thermal fields. However the adequate modelling of the flow is a crucial question in numerical study and every phenomenon which is numerically observed should be confronted to experimental observations to confirm its validity.

Chapter 3

Methodology

In order to address the problematic raised in the previous chapters, data need to be first collected. In the present dissertation both experimental and numerical data are used. This chapter presents the methodology adopted to collect and study the data. In the first section, the POD and the SPOD of Sieber et al. (2016), are presented. Then the experimental apparatus is presented followed by the numerical model, used to collect data. Finally the thought of process which guided the main works of this dissertation is exposed.

During these studies it was also attempted to disturb the flow using acoustic disturbance. However no clear results of the impact of the acoustic disturbance on the flow were observed, for that reason and for clarity purposes, the details of these experiments have been presented in appendix A.

Contents

3.1 Proper Orthogonal Decomposition and Spectral Proper Orthogonal Decomposition methodologies

3.1.1 Fluctuating fields and velocity-temperature coupling

Let t be the time coordinate and $\mathbf{x} = (x, y, z)$ the space coordinate vector. $T(\mathbf{x}, t)$ is the absolute instantaneous temperature and $\mathbf{u}(\mathbf{x}, t) = (u(\mathbf{x}, t), v(\mathbf{x}, t), w(\mathbf{x}, t))$ is the vector of instantaneous velocities obtained through the numerical simulations. Rather than the absolute instantaneous temperature, the temperature rise above the reference temperature T_0, $\theta(\mathbf{x}, t)$ is preferably used in the remainder of the paper.

The POD is commonly performed on physical fields from which the temporal mean was removed. Consequently the instantaneous fields are separated into a time-averaged component, $\overline{\mathbf{u}}(\mathbf{x})$ and $\overline{\theta}(\mathbf{x})$, and a fluctuation part, $\mathbf{u}'(\mathbf{x}, t)$ and $\theta'(\mathbf{x}, t)$,

$$\mathbf{u}(\mathbf{x}, t) = \overline{\mathbf{u}}(\mathbf{x}) + \mathbf{u}'(\mathbf{x}, t), \tag{3.1}$$

and

$$\theta(\mathbf{x}, t) = \overline{\theta}(\mathbf{x}) + \theta'(\mathbf{x}, t). \tag{3.2}$$

In the literature, two methods have been adopted in order to consider the temperature field in the POD analysis. One consists in using a separate representation for the fluctuating velocity and thermal fields (see e.g. Jing et al., 2003; Park et al., 2004). This approach provided a good representation of the flow dynamics in the case of a natural convection flow in a cavity. However the aim of the present paper is to extract and identify coupled velocity and temperature structures which is the reason for employing a mixed-representation in this work. This representation has been used by Lumley and Poje (1997), Podvin and Le Quéré (2001), Hasan and Sanghi (2007), Bailon-Cuba and Schumacher (2011) and Podvin and Sergent (2012, 2015). It consists in linking and scaling the contribution of the temperature fluctuation with the fluctuating kinetic energy. A scaling factor γ is thus calculated by

$$\int_{all\,space} \overline{u'u' + v'v' + w'w'} \mathrm{d}\mathbf{x} = \gamma \int_{all\,space} \overline{\theta'\theta'} \mathrm{d}\mathbf{x}, \tag{3.3}$$

to evaluate the coupling.

3.1.2 Snapshot Proper Orthogonal Decomposition

The POD method relies on the decomposition of the fluctuating fields as a superposition of spatial modes, called here POD modes, associated with temporal coefficients and amplitudes. In the case of a discrete dataset, in time and space, such as that generated by numerical models, the snapshot-POD developed by Sirovich (1987) is commonly used because of its particularly robust and adapted formulation. In the remainder of the dissertation, the snapshot-POD method is referred to as POD method.

Let N_t be the number of snapshots and N_x the domain size *i.e.* the number of grid points. The POD modes are calculated from the spatially integrated temporal covariance matrix of the dataset, $\boldsymbol{C}$ whose elements are defined at the respective times t_i and t_j ($(i,j) \in [\![1;N_t]\!]^2$) by

$$C_{i,j} = \frac{1}{N_t} \langle \mathbf{u}'(\mathbf{x},t_i), \mathbf{u}'(\mathbf{x},t_j) \rangle. \tag{3.4}$$

The inner product $\langle .,. \rangle$ is the L^2 inner product

$$\langle \mathbf{u}'(t_i), \mathbf{u}'(t_j) \rangle = \int_{all\,space} u'(\mathbf{x},t_i)u'(\mathbf{x},t_j) + v'(\mathbf{x},t_i)v'(\mathbf{x},t_j) + w'(\mathbf{x},t_i)w'(\mathbf{x},t_j) \mathrm{d}\mathbf{x}. \tag{3.5}$$

In order to consider the temperature field, as mentioned above, the elements of the covariance matrix C become

$$C_{i,j} = \frac{1}{N_t} \left(\langle \mathbf{u}'(\mathbf{x},t_i), \mathbf{u}'(\mathbf{x},t_j) \rangle + \langle \theta'(\mathbf{x},t_i), \theta'(\mathbf{x},t_j) \rangle \right). \tag{3.6}$$

The temporal coefficients of the POD modes are obtained by solving the eigenproblem associated with $\boldsymbol{C}$,

$$\boldsymbol{C}\alpha = \lambda\alpha. \tag{3.7}$$

α are the eigenvectors and λ the eigenvalues. $\boldsymbol{C}$ is symmetric semi-definite positive, therefore its eigenvalues are positive. λ_k is the eigenvalue associated with the k-ith mode and represent its energetic weight. The eigenvalues are classified by magnitude so that

$$\lambda_1 \geq \lambda_2 \geq \cdots \geq \lambda_{N_t} \geq 0. \tag{3.8}$$

Each eigenvector $\alpha_k(t)$ of α is the temporal coefficient of the k-ith mode. It describes the temporal evolution of the k-ith POD mode over the N_t time steps. They are orthogonal and scaled with the energy so that $\overline{\alpha_i(t)\alpha_j(t)} = \lambda_i\delta_{ij}$. The POD spatial modes $\phi_k = (\phi_{u,k}, \phi_{v,k}, \phi_{w,k}, \phi_{\theta,k})$ are then calculated as follows

$$\phi_{\mathbf{u},k}(\mathbf{x}) = \frac{1}{N_t\lambda_k}\sum_{n=1}^{N_t}\alpha_k(t_n)\mathbf{u}'(\mathbf{x},t_n), \tag{3.9}$$

and

$$\phi_{\theta,k}(\mathbf{x}) = \frac{\sqrt{\gamma}}{N_t\lambda_k}\sum_{n=1}^{N_t}\alpha_k(t_n)\theta'(\mathbf{x},t_n). \tag{3.10}$$

For more information about the properties of the POD decomposition, see Holmes et al. (1996).

3.1.3 Spectral Proper Orthogonal Decomposition

SPOD is an alternative method to the POD and was recently proposed and fully detailed by Sieber et al. (2016). By definition, the POD decomposition is energetically optimal, so that a maximum of the fluctuating energy is captured in a minimum of modes. The SPOD decomposition offers to progressively decrease the optimal energetic decomposition of pure POD by increasing the harmonic correlation of the temporal coefficient associated with each SPOD modes (Noack, 2016). Moreover, when the harmonic correlation of the modes is increased at its maximum, the modes becomes the modes that would be obtained by DFT of the flow. The main characteristics of the SPOD, being used in the present dissertation, are summarized in this section.

SPOD modes are obtained by applying a filter to the covariance matrix $\boldsymbol{C}$ computed for POD. The elements of the filtered covariance matrix $\boldsymbol{S}$ are then

$$S_{i,j} = \frac{1}{2N_f+1}\sum_{k=-N_f}^{k=N_f}\omega_k C_{i+k,j+k}, \tag{3.11}$$

where N_f is the filter size and ω_k are the elements of a weight function. Sieber et al. (2016) suggest using either a box filter or a Gaussian mask for the weight function. In the remainder of this work, this last option has been used as it enables a smoother filtering of the covariance

matrix (Sieber et al., 2016). The choice of the filter size is important and depends on the flow configuration; it is further discussed for the present study in section 4.4. The covariance matrix $\boldsymbol{C}$ is a $N_t \times N_t$ matrix. It should be noted that unless $N_f = 0$, in which case SPOD becomes POD, some values of the filtered covariance matrix are not defined near the boundaries. One of the methods proposed by Sieber et al. (2016) facing this situation is to assume periodic boundary conditions of the covariance matrix so that for example if $i+k > N_t$, then $C_{i+k,j+k} = C_{i+k-N_t,j+k}$.

Once S is calculated, the method is the same as for POD but is now applied to the filtered covariance matrix S. The problem now becomes

$$S\beta = \mu\beta, \tag{3.12}$$

and β and μ are respectively the eigenvectors and eigenvalues of $\boldsymbol{S}$. As with the eigenvectors obtained by POD, $\overline{\beta_i(t)\beta_j(t)} = \mu_i\delta_{ij}$.

The SPOD spatial modes $\psi_k = (\psi_{u,k}, \psi_{v,k}, \psi_{w,k}, \psi_{\theta,k})$ are then calculated as follows

$$\psi_{\mathbf{u},k}(\mathbf{x}) = \frac{1}{N_t\mu_k}\sum_{n=1}^{N_t}\beta_k(t_n)\mathbf{u}'(\mathbf{x},t_n), \tag{3.13}$$

and

$$\psi_{\theta,k}(\mathbf{x}) = \frac{\sqrt{\gamma}}{N_t\mu_k}\sum_{n=1}^{N_t}\beta_k(t_n)\theta'(\mathbf{x},t_n). \tag{3.14}$$

The spatial modes are orthonormal by construction, namely, $\langle\psi_i, \psi_j\rangle = \delta_{ij}$.

Pure Fourier modes are obtained for periodic boundary condition of the covariance matrix, if a box filter of the same size as the number of snapshot is applied or if a Gaussian filter of infinite size is applied.

3.2 Data collection: Experimental device and details of the experiments

3.2.1 Experimental apparatus

The experimental channel and the coordinate system are presented in figure 3.1. This channel had been initially build by Vareilles (2007) during its PhD thesis and a very detailed description of the apparatus is available in its manuscript. He also characterized the thermal properties of the apparatus. Some changes and improvements on the apparatus were made by Sanvicente (2013). She conducted the first PIV measurements in the channel and provided a very complete description of the PIV methodology for that configuration. This section presents the apparatus and some additional features that were implemented for the present study.

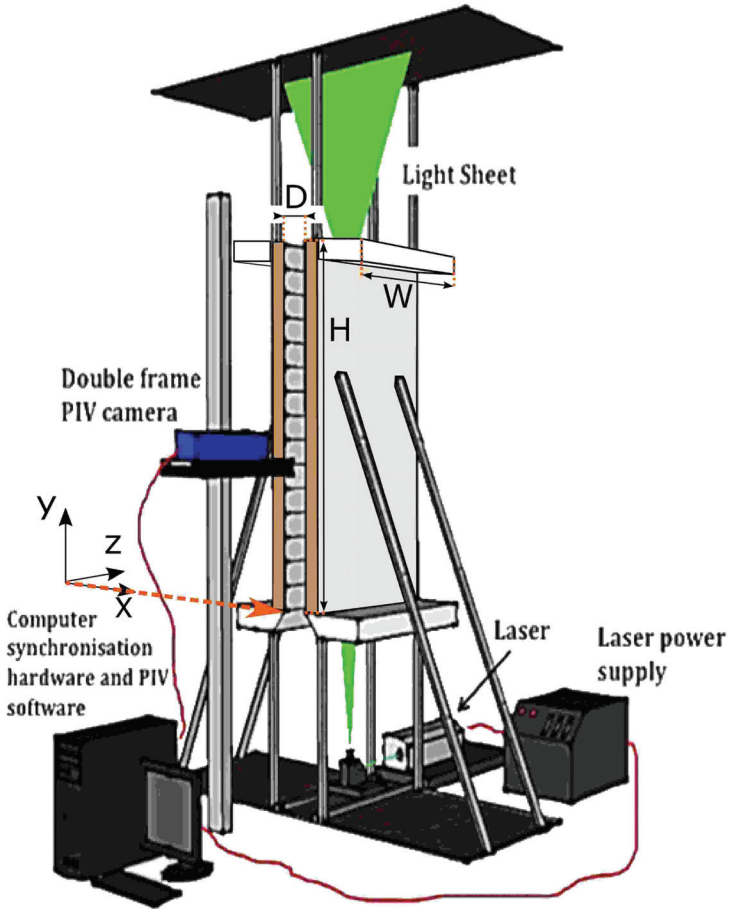

Fig. 3.1 Scheme of the experimental apparatus and coordinate system.

The configuration studied here is a channel composed of two parallel vertical walls of dimensions $H = 1.50$ m high $W = 0.70$ m wide and $D = 0.10$ m apart. They are insulated by 12 cm thick insulating polyurethane blocks of thermal conductivity 0.027 W/mK, embedded in wooden frame. The channel is closed on both lateral sides by two vertical Plexiglas sheets to avoid lateral infiltration of air and allow optical access to the channel. The inside surface of each of the wide channel walls is covered by 15 independently controlled stainless steel foil heaters, each 10 cm wide, 50 μ m thick and 70 cm long. The emissivity of the foils is 0.092 and the thermal conductivity is 13 W/mK. The leading edges of the two wide plates have 30° chamfers at the inlet in order to guide the fluid and reduce inlet turbulence.

The experimental apparatus is located in a 6.6 m high, 4.6 m wide and 7.0 m long laboratory; in the basement of the CETHIL laboratory in Lyon, France. In the channel entrance is located at 0.75 m from the floor and a 0.70 m $\times$ 1 m artificial ceiling was placed 75 cm above the channel outlet. This type of geometry was defined by Manca et al. (1994) as an I-type geometry. This geometry configuration was designed in order to have the same boundary condition above and below the channel. Moreover when it comes to numerically model this configuration,

the presence of these wall allows to reduce the size of the computational domain and thereby reducing the memory requirements and the CPU time needed for numerical simulations.

3.2.2 Temperature measurements

Wall temperatures For the temperature acquisition at the wall, 75 thermocouples were placed along the vertical mid-plane line z/W=0.5 in which z is defined in figure 3.1. The thermocouples were placed inside the insulation and in intimate contact with the heated foil. This arrangement gives five vertical measurement points per foil and prevents thermocouples intruding into the flow region. Additional thermocouples were positioned in the insulation so as to evaluate heat losses.

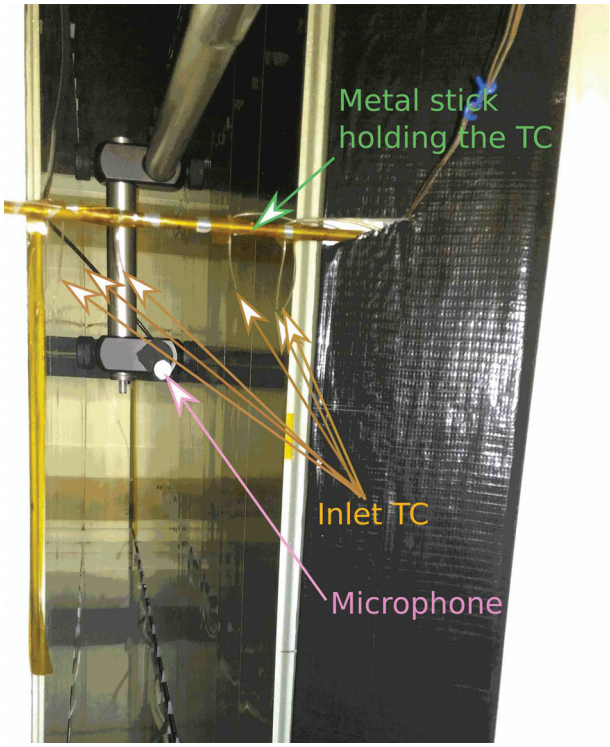

Fig. 3.2 Inlet thermocouples, picture taken from below the channel.

Inlet temperatures Six thermocouples were located across the inlet of the channel in order to obtain the mid-plane inlet temperature profile. These thermocouples were taped to a thin metal stick of 4 mm diameter. The stick was placed at approximately 3 cm from the laser sheet and the thermocouples at around 5 mm from the laser sheet. The location of these TC can be seen in figure 3.2 which is a picture of the inside of the channel taken from below the channel. On this picture, presence of a microphone can also be noted[1].

[1]This microphone is present on the picture because at that time, tests to characterize an acoustic disturbance were being carried. As mentioned in the introduction of this chapter, more details and outcomes of the experiments

Regarding the inlet temperature, some tests were carried and it appeared that the time-averaged inlet temperature profiles was mostly uniform. A very slightly higher temperature, of less than 0.5 K was measured very close to the heated wall. Once the characterisation of the inlet temperature was finished, the inlet thermocouples were removed to limit there potential disturbance on the flow.

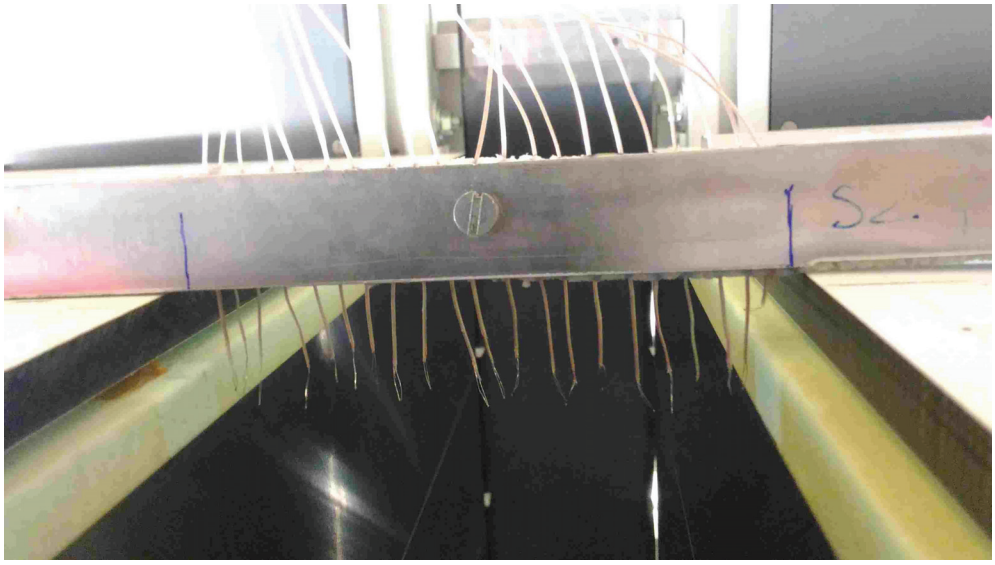

Fig. 3.3 Pictures of the outlet thermocouples

Outlet temperatures Twenty thermocouples were located just above the outlet in the mid-plan z/W=0.5. The thermocouple were originally spaced by 2.5 mm near the wall and every 5 mm in the middle. Because it was not possible to exactly respect the spacing between the thermocouples, their exact locations were therefore obtained *a posteriori* from pictures as the one displayed in figure 3.3. All the inlet and outlet thermocouples were standard K-types thermocouples made from 120 μm wire.

Temperatures in the room Ambient thermal conditions were evaluated with five K-types 200 μm thermocouples located at 0.1; 0.7; 1.3; 1.7 and 2.3 m from the floor on the same vertical pole, 1.5 m from the channel. The ambient vertical temperature gradient, δ_T (K/m) was then defined as the slope of the linear regression of these measurements.

All thermocouples were calibrated individually in a constant temperature water bath before being installed. The calibration procedure is given by Sanvicente (2013). Thermocouples measurement uncertainty was evaluated as $\pm$0.05 K. The temperature acquisition rate was 10 Hz.

carried with an acoustic disturbance are presented in appendix A. However when PIV measurements were done, the microphone was removed to not disturb the flow

3.2.3 Velocity flow field measurement

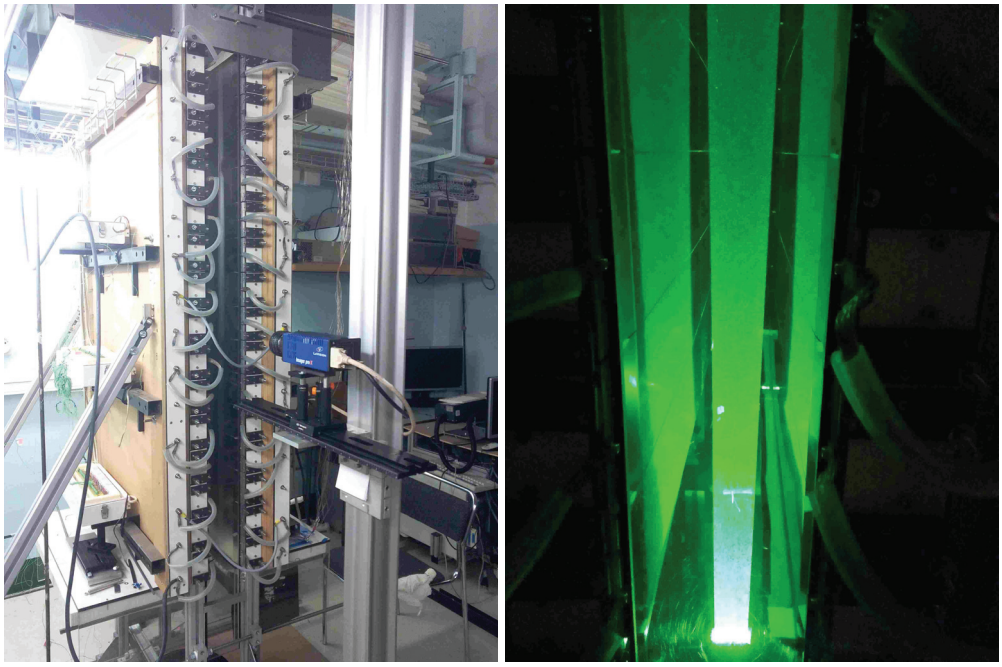

(a) Channel and PIV camera (b) Laser sheet

Fig. 3.4 Pictures of the experimental apparatus

Velocity fields on the centre plane, z/W=0.5, were obtained with the Particle Image Velocimetry (PIV) method. The apparatus and methodology had already been described and characterized in details by Sanvicente et al. (2013) and main features are summarized below. The main difference with the devices used by Sanvicente (2013) are than the camera used for the present study had a greater resolution which allowed to obtain a larger field of view.

The PIV system was composed of a pulsed Nd: YAG laser emitting at 532 nm, a standard set of lenses to get sheets was used and a Charge-Coupled Device camera employed for image acquisition. The image recording was done with a resolution of 540×2048 pixels. The acquisition window corresponded to a section of the flow to a 100 mm wide by 380 mm high area. This field of view covers a quarter of the channel height and thereby allows to cover the whole height of the channel with only four measurements. The different heights at which PIV measurements were performed, namely, w1,w2,w3,w4 which corresponds respectively to the 1st, 2nd 3rd and 4th quarters of the channel have been represented in figure 3.5.

Experiments were conducted by seeding the flow with droplets of silicon oil Di-Ethyl-Hexyl-Sebacat. The generated particles have a diameter smaller than 1 μm and a density of 912 kg/m^2 and have sufficient light scattering capability as well as a minimal slip between the fluid and the particle (Sanvicente, 2013). The standard double frame PIV method was used in which the two images were acquired 1 ms apart. This time has been set so that particles did not moved by

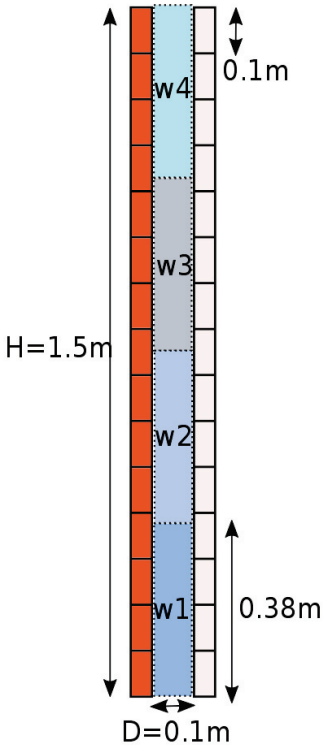

Fig. 3.5 PIV fields of views at z/W=0.5

more than 1/4 of the interrogation window between the two frames. The acquisition frequency employed was 10 Hz.

Raw image were post-processed using PIVlab (Thielicke and Stamhuis, 2014), a toolbox developed in the Matlab environment. Cross correlation technique was used so as to obtain a snapshot of the velocity vector field. Data analysis was then done using in-house sub-routines in Matlab.

During each measurement session, 8000 double images were acquired, which correspond to a measurement period of 14 min. This measurement period provides a reliable average of the main quantities of the flow (Sanvicente et al., 2013). The systematic errors, related to the laser, the seeding procedure, the camera calibration and the post processing were estimated at ± 0.015 m/s.

3.2.4 Experimental conditions and external thermal stratification

The experimental procedure for a measurement session had been described in details by Vareilles (2007) and Sanvicente (2013). Before each measurement the channel was operated at the nominal power for four hours in order to ensure thermal steady conditions inside the walls. All

temperature and velocity measurements devices needed to be warmed up and were also switched on some times before being used.

Indoor temperatures were not controlled and allowed to evolve freely. Indeed, an active control of them would introduce perturbations of temperature and velocity fields. Unfortunately there were parasitic heat sources and velocity disturbances in the room such as the laser power supply and the PIV computer. In order to minimize their impact on the flow they had been placed as far as possible from the channel.

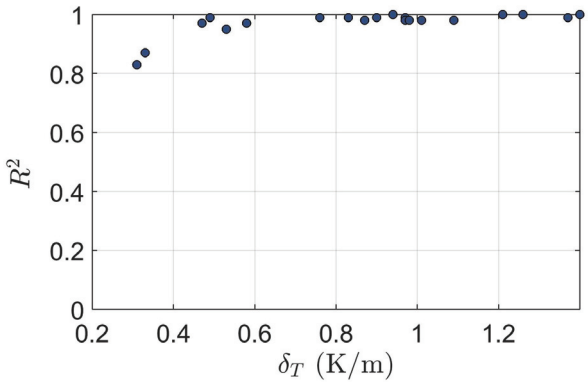

Fig. 3.6 Coefficient of determination, R^2 of the temperature gradients δ_T

For the great majority of the cases the room temperature distribution could be approximated by a linear distribution with a coefficient of determination R^2, greater than 0.95. The external thermal stratification is thus characterised by the gradient of the approximate linear temperature distribution outside the channel, referred as δ_T (K/m). δ_T is positive if the temperature increases upwards and negative if it decreases. The coefficient of determinations of the thermal gradients are plotted in figure 3.6.

It was observed that for the present measurements, the temperature gradient in the laboratory increased by 0.01 K/m per hour during the operating periods. Similar observations were made by Vareilles (2007) on the same apparatus. Since the measurements took approximately a quarter-of-an-hour, the temperature gradient in the room was constant during the measurement period.

The average temperature change in the room during one measurement is ± 0.1 K. Because this change was also small, conditions could still be assumed to remain constant during the measurement period. During the whole test period, the ambient room temperature ranged between 16 and 24 °C which induce neglectible changes in the fluid transport properties.

3.2.5 Repeatability - Impact of the external thermal stratification

One major issue which arose from the measurements is directly observable in figure 3.7. In this figure are plotted, time averaged streamwise velocities at $y/H = 0.25$ and the heated wall

temperatures, obtained during three different measuring sessions for the same injected power of 100 W. Measurements of session 1 were carried out the 13^{th} of October 2016, those of session 2 were obtained the 20^{th} of October and those of session 3 the 24^{th} of November 2016. It appears that there is a significant changes between the sessions, the differences in velocities between session 1 and session 3 reaches up to 70 %.

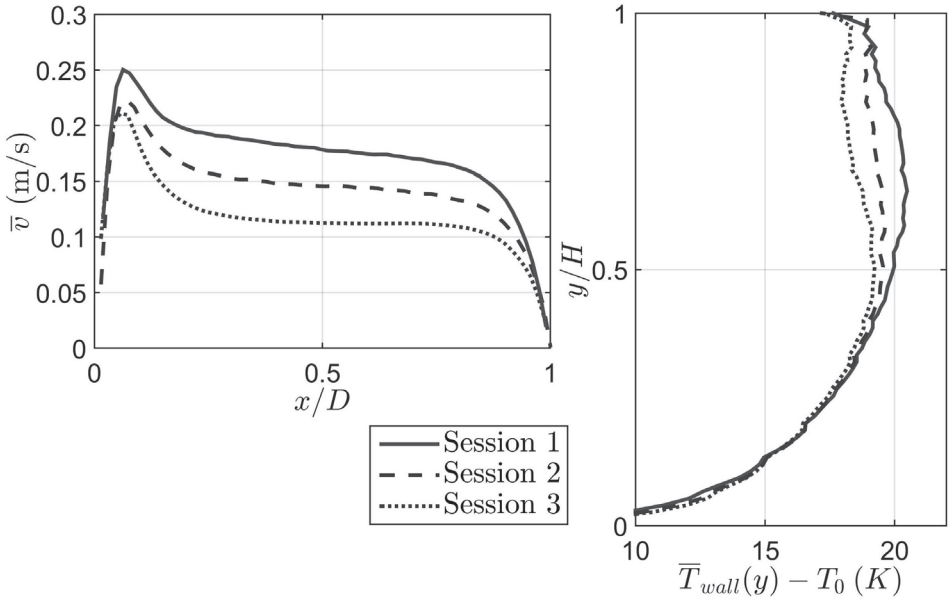

Fig. 3.7 Time-average streamwise velocities plotted at $y/H = 0.25$ and time-averaged wall temperatures corresponding to three measurement sessions

For PIV measurements, the sources of uncertainties and repeatability issues are multiple. First of all, in our case the PIV system is used for different application within the laboratory and therefore cannot be integrated on the present channel once for all.

For the present study, the PIV devices were implemented based on the configuration of the previous measurement campaign of Sanvicente (2013). However, the positioning of the different elements (camera, location of the laser, location of the computers, location of the channel itself etc $\cdots$) may have changed since Sanvicente's measurements which could be a source of difference with her measurements.

Once the PIV devices were installed, then, the different systematic settings are another source of uncertainty. In her PhD manuscript, (Sanvicente, 2013) performed a complete systematic uncertainty analysis and came up with a uncertainty level of around 0.015 m/s. This uncertainty level represents more than 10% of the time-averaged velocity level of session 2 plotted in figure 3.7 but can, in no way, explain the differences observed between session 1 and session 2.

The evolution of the surrounding conditions was thus carefully inspected in order to better understand their impact on the flow. In order to do so, the humidity and temperature of the room were recorded. Humidity was measured at one location outside the channel at approximately one

meter from the floor while ambient temperatures were measured at different locations outside the channel which allows to obtain the temperature distribution within the room.

The relative humidity in the room ranged between 25 % and 60 %. The reference temperature in the room, measured at the inlet level of the channel, far from the channel ranged between 16 °C and 24 °C. However, it was not possible to correlate one of these factor with the changes observed.

The external thermal stratification was thus observed closely. This time it was found that it was extremely well correlated with the changes in the time averaged velocities and with the temperature changes at the wall. Regarding the figure 3.7 the external thermal stratification were respectively of $\delta_T = 0.49$ K/m, $\delta_T = 0.83$ K/m and $\delta_T = 1.09$ K/m.

3.2.6 Impact of the external velocity disturbances

In spite of the efforts made to limit the presence of external disturbance, many structures were observed entering the channel. A brief discussion on the effect of these structures on the flow is proposed in appendix B.

3.2.7 Measurement campaign

Once the measurement devices were operational, the experimental campaign started. It lasted for three months between the 7 October to the 8 December 2016. A total of around 130 measurement sessions of 15 min each have been recorded which represents nearly 32 hours of recording. To store this data, nearly 3 TB were required. Note that not all this data have been used for the present work as a great part of it were obtained attempting to disturb the flow with an acoustic disturbance (see appendix A). Other tests with staggered heating configurations and partial obstructions of the inlet flow were also done but not presented in this dissertation.

3.3 Data collection: Numerical model

By definition, RANS methods are not able to model intermittent structures so that only LES or DNS could have been used for the present analysis. DNS requires a very fine mesh and a very small time step, which would have required very large computing resources, both to perform the calculations and to store the data. Given that POD decomposition requires an amount of data sufficiently large to capture repetitive patterns of the flow dynamics, DNS would have been too costly in terms of computing resources for the present analysis. Moreover, data generated with an LES code yields results which are sufficient for the accurate prediction of the most energetic modes as these involve large eddies which are correctly simulated. For all these reasons LES methodology was used rather than DNS.

First the computational domain is introduced, then the governing equations, the subgrid model developed by Vreman (2004) and adapted to natural convection by Lau et al. (2012c,d), and the LES method are introduced. Finally the different solvers and numerical methods are presented.

3.3.1 Computational domain and general boundary conditions

The computational domain is illustrated in figure 3.8. Based on the I-type geometry defined by Manca et al. (1994), two extended domains were added to the upper and lower ends of the channel for the entrained and exhausted flow to be appropriately simulated as was done in the work of Lau et al. (2012b). The top boundary is 0.75 m from the channel outlet and corresponds to the artificial ceiling present in the experimental apparatus and was modelled as a wall condition. A uniform heat flux as imposed at the heated wall. The unheated wall is either adiabatic except when specified otherwise. All the walls of the domain, plotted by a thick plain black line, were defined as adiabatic walls.

Pressure, temperature and inlet disturbances were specified at the open boundaries. In this dissertation, different sorts of boundary conditions were applied depending on the cases studied. The details of the boundary conditions will thus be provided in the introductory parts of each of the concerned chapter.

3.3.2 Large eddy simulation and Vreman subgrid scale model

In LES, the flow is separated into large and small scales based on a spatial filtering. The filter size is commonly assumed to be equal to the size of the computational grid. The large scale motions are directly simulated whereas a SGS model is used to evaluate the effects of flow structures smaller than the filter size used in the simulations.

The grid-filtering operation is defined for a physical quantity φ as

$$\overline{\varphi}(\mathbf{x},t) = \int_{\mho} \omega(\mathbf{x}-\mathbf{x}')\varphi(\mathbf{x}',t)d\mathbf{x}' \tag{3.15}$$

in which $\mho$ is the computational domain, ω is a normalized filter function, defined here as a box filter, of width Δ.

Because in natural convection, the changes in density can be significant, it is common to adopt a modified approach for the filtering of the Navier-Stokes equations, commonly called the Favre-filtering, defined as

$$\widetilde{\varphi}(\mathbf{x},t) = \frac{\overline{\rho\varphi(\mathbf{x},t)}}{\overline{\rho}} \tag{3.16}$$

in which the operator $\sim$ indicates the Favre-filtered quantity.

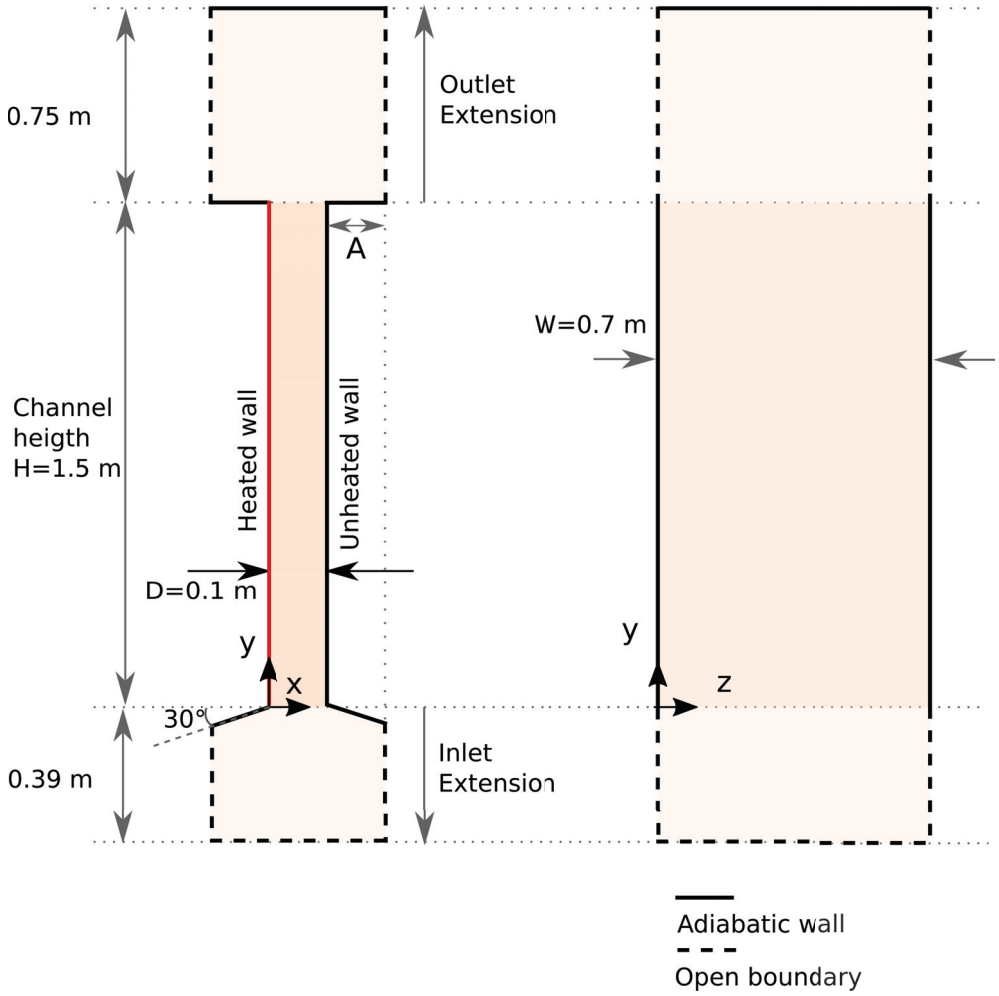

Fig. 3.8 Scheme of the computational domain

The instantaneous variable can now be expressed as

$$\varphi(\mathbf{x},t) = \widetilde{\varphi}(\mathbf{x},t) + \varphi''(\mathbf{x},t), \tag{3.17}$$

in which $\widetilde{\varphi}(\mathbf{x},t)$ represents the quantity that will be directly calculated whereas $\varphi''(\mathbf{x},t)$ represents the part of the component, smaller than the grid filter width, that will be modelled by the SGS.

The resulting set of conservation equations for a buoyancy-driven flow at low-Mach-number using Favre averaging and the Einstein summation convention may be written as :
conservation of mass,

$$\frac{\partial \overline{\rho}}{\partial t} + \frac{\partial (\overline{\rho}\widetilde{u_i})}{\partial x_i} = 0, \tag{3.18}$$

conservation of momentum,

$$\frac{\partial\left(\overline{\rho}\widetilde{u}_j\right)}{\partial t}+\frac{\partial\left(\overline{\rho}\widetilde{u}_i\widetilde{u}_j\right)}{\partial x_i}=-\frac{\partial\overline{p}}{\partial x_j}+\frac{\partial\widetilde{\sigma}_{ij}}{\partial x_i}+\frac{\partial\tau_{u_iu_j}}{\partial x_i}+(\overline{\rho}-\rho_0)g_j, \tag{3.19}$$

and conservation of energy,

$$\frac{\partial\left(\overline{\rho}C_p\widetilde{T}\right)}{\partial t}+\frac{\partial\left(\overline{\rho}C_p\widetilde{u}_i\widetilde{T}\right)}{\partial x_i}=\frac{\partial}{\partial x_i}\left(\kappa\frac{\partial\widetilde{T}}{\partial x_i}\right)+\frac{\partial\left(C_p\tau_{u_iT}\right)}{\partial x_i}. \tag{3.20}$$

$\widetilde{u}_i$ are the filtered Cartesian velocity components, ρ_0 is the reference density at the reference temperature T_0. $\overline{\rho}$ and $\widetilde{T}$ are respectively the filtered density and the filtered temperature, $\overline{p}$ is the filtered dynamic pressure, κ is the thermal conductivity, and C_p is the specific heat capacity at constant pressure. $\widetilde{\sigma}_{ij}$ is the filtered stress tensor which can be written, under the Stokes assumption as

$$\widetilde{\sigma}_{ij}=2\eta\left(\widetilde{Sr}_{ij}-\widetilde{Sr}_{kk}\delta_{ij}\right), \tag{3.21}$$

where $\widetilde{Sr}_{ij}$ is the strain rate tensor, η the dynamic viscosity and δ_{ij} is the Kronecker delta,

$$\widetilde{Sr}_{ij}=\frac{1}{2}\left(\frac{\partial\widetilde{u}_i}{\partial\widetilde{x}_j}+\frac{\partial\widetilde{u}_j}{\partial\widetilde{x}_i}\right). \tag{3.22}$$

The dynamic viscosity η is calculated using the Sutherland's law:

$$\eta=18.27\times10^{-6}\frac{291.15+\Lambda}{T+\Lambda}\left(\frac{T}{291.15}\right)^{3/2} \tag{3.23}$$

in which Λ is a constant that depends of the gas and can be evaluated at $\Lambda=110.56$ for air at moderate temperature and pressure.

The effect the non-simulated small-scale structures is represented by the SGS stress tensor $\tau_{u_iu_j}$ and the SGS heat flux vector τ_{u_iT} in equations 3.19 and 3.20. The Vreman SGS model (Vreman, 2004) adapted to transition flows with low turbulence level is used in this work. It has been shown that in natural convection problem in cavities (Lau et al., 2012c) and channel flows (Lau et al., 2012b, 2011, 2012d), this SGS model yields better agreement with experiment than the Smagorinsky SGS model Smagorinsky (1963).

The subgrid Reynolds stresses and turbulent heat fluxes are represented in the modified Vreman SGS model as

$$\tau_{u_iu_j}=-2\eta_{sgs}\left(\widetilde{Sr}_{ij}-\frac{1}{3}\widetilde{Sr}_{kk}\delta_{ij}\right), \tag{3.24}$$

and

$$\tau_{u_iT}=\frac{\eta_{sgs}}{Pr_{sgs}}\frac{\partial\widetilde{T}}{\partial x_i} \tag{3.25}$$

in which η_{sgs} is the SGS viscosity model proposed by Vreman (2004), namely,

$$\eta_{sgs} = \overline{\rho} C_v \sqrt{\frac{B_d}{c_{ij} c_{ij}}}, \tag{3.26}$$

and Pr_{sgs} and C_v are coefficients of the SGS model and $c_{ij} = \partial \widetilde{u}_j / \partial x_i$, $B_d = \widetilde{d}_{11}\widetilde{d}_{11} - \widetilde{d}_{12}^2 + \widetilde{d}_{11}\widetilde{d}_{33} - \widetilde{d}_{13}^2 + \widetilde{d}_{32}\widetilde{d}_{33} - \widetilde{d}_{23}^2$ and $\widetilde{d}_{ij} = \Delta_m^2 c_{mi} c_{mj}$, Δ_m being the filter width in the m direction. As suggested by Vreman (2004), C_v and Pr_{sgs} were set to 0.1 and 0.4 respectively. In the remainder of this work, only filtered quantities are considered and the symbols $\sim$ and $-$ will not be used for the sake of clarity. The derivation of the LES approach the implementation of the Vreman SGS model and its validation for this flow configuration are presented in detail in the work of Lau (2013).

3.3.3 Solvers and numerical methods

Lau (2013)'s in-house LES solver

In the present work two different solvers and numerical methods have been used. The first solver is an in-house code developed and validated by Lau (2013).

The filtered equations were discretised using a finite volume formulation. A fourth-order central differencing scheme was applied to approximate the convective terms of the control volume whilst a second-order central differencing scheme was used for the diffusion terms and other spatial derivatives. The solution was advanced in time using an explicit two-step predictor-corrector approach, the time step was 10^{-3} s which yielded to a maximum Courant Friedrichs Lewy number of 0.35.

The detailed derivation, and implementation of the numerical method may be found in (Lau, 2013). This solver have been validated against experimental data for various configuration such as a cavity flow (Lau et al., 2012c) or the channel flow of Miyamoto et al. (1986), (Lau et al., 2011, 2012d). More recently, Li et al. (2015) compared the LES results using Vreman-Lau SGS and the experimental results of Miyamoto et al. (1986) with their own DNS results. Both LES and DNS were able to accurately predict the time averaged velocities and turbulent intensity in the high part of the channel (no comparison were shown at lower levels). The LES even provided more accurate prediction of the time averaged excess wall temperature which Li et al. (2015) explained by differences in the boundary conditions. However both the LES and DNS could accurately predicts the height at which transition was triggered which is one of the most crucial point in the present dissertation.

The solver of Lau (2013) is an in-house code in which all the parameters and equations are explicitly known. For these reasons it has been used for the finer studies involving the study of coherent structures. However the main drawback of this code was that, at that time, it could not

perform parallel calculations. As a consequence the code was run on a single node and several months of computation were needed to obtain long sequences of the flow.

The grid of the channel itself is composed of $48 \times 328 \times 78$ elements respectively in the x, y and z directions. Based on the scaling analysis developed by Armfield et al. (2007), the thermal boundary layer thickness scale is in the order of $\delta \sim y/Ra(y)^{1/5}$, which, in this case make that two to three points lie within the boundary layer. The mesh used was validated in (Lau, 2013).

FLUENT LES solver

The second solver used is a FLUENT-based solver in which the Vreman SGS model had been implemented. It was possible to parallelize the calculation with this solver, and therefore it has been used for studies implying great amount of cases. A second order discretisation was used for the spatial derivatives. A SIMPLE scheme was used for the pressure-velocity coupling and the solution was advanced using a bounded second order implicit scheme. The time step was 10^{-2} s.

The numerical methods used in FLUENT are not as accurate as those used in the in-house code of (Lau, 2013). Moreover it is not possible to access the details of the codes. For these reasons this solver is preferably used to obtain time averaged and turbulence statistics. The geometry and the mesh were generated using ANSYS DesignModeler and the a mesh independence study was carried out and is be presented in chapter 5.

3.4 Cases studied

Three values of Rayleigh numbers have been investigated. They correspond to the three injected electrical powers Q_t (W), 100, 230 and 500 W used in the experiments. The subscript t indicates the total injected electrical power.

The heated foils have a uniform electrical energy heat flux supplied on one side of the channel. Sanvicente (2013) and Vareilles (2007), who used the same channel, estimated that around 5% of the supplied electrical power was lost by conduction through the insulation and by radiation directly to the surroundings. The net heat input, Q (W) transferred to the flowing fluid, was then calculated by subtracting the estimate of these losses from the total electrical power Q_t. In order to have the same heat injected in the channel numerically and experimentally, the net heat injected in the channel numerically corresponds to Q. The resulting main parameters are listed in table 3.1.

These Rayleigh numbers have been chosen because they are similar to those that had been used in the previous study of (Lau, 2013; Sanvicente, 2013; Vareilles, 2007). They represent a range of Rayleigh that would be obtained if such systems were working in real outdoor operating conditions. Moreover transition was observed at these Rayleigh numbers.

Table 3.1 Summary of the cases studied

Cases	100 W	230 W	500 W
Ra	$Ra = 1.5 \times 10^{12}$	$Ra = 3.5 \times 10^{12}$	$Ra = 7.5 \times 10^{12}$
Electrical power Q_t (W)	100	230	500
Net heat input Q (W)	95	219	475
Net heat flux q (W/m^2)	90	208	452

Despite the fact that experimental and numerical data had already been collected on the same experimental apparatus and using the same code. In the remainder of this dissertation this data will not be used. Except for some cases, explicitly mentioned, all the plots and work presented have been obtained from the experimental and numerical data that were collected by the author himself.

3.5 Research opportunities and thought process

This work was carried out thanks to a cotutelle between UCBL and UNSW. In that context experimental resources were available at the UCBL while the numerical resources were located at the UNSW. This section gives a chronological presentation of the steps which led to this work.

As mentioned in the introduction, the aim of this work is to study the effects of the surroundings on the channel flow and more especially on the intermittency and unsteadiness of the flow that were described in previous works. The use of decomposition was identified as a promising tool to perform this analysis.

This Ph.D. work therefore started with the identification of adapted decomposition methods for this flow configuration and preliminary observations were made on available experimental data. In parallel, study of the literature suggested the possibility to trigger intrinsic characteristics of the flow.

Once these first preliminary steps were done, a new experimental campaign began and more adequate measurements were achieved. A wider observation of the structures was achieved by the enlarging of the PIV field of view. To better characterise the environmental conditions, accurate measurements of the external thermal ambiance and of the humidity were made possible. Finally, in order to trigger some of the intrinsic behaviours of this flow, acoustic perturbations were introduced (see appendix A).

For material (availability of the PIV devices) as well as schedule reasons (mobility at the UNSW), an intensive measurement campaign of three months was carried out, and simultaneously some post-processing of the data collected was done. The effect of the controlled acoustic

disturbances on the time-averaged quantities of the flow proved extremely difficult to assess because of large problems of repeatability which made the study of the impact of a disturbance on the flow almost impossible (see appendix A). After the investigation of the surroundings, these repeatability problems appeared to be mainly caused by changes of the external thermal stratification. For that reason, the study of the effects of controlled disturbances was postponed and the focus shifted to the theoretical, experimental and numerical characterisation of the effect of the external thermal stratification on the flow.

Chapter 4

Identification of coherent structures using POD-based method in a transitional natural convection flow, spatially developing in a vertical channel

Numerical simulations were performed of a spatially developing transitional flow in a vertical channel with one side uniformly heated and subjected to random velocity fluctuations at the inlet. The in-house LES numerical solver which was developed and validated by Lau (2013) and the POD-based decomposition methods described in the previous chapters were used in order to simulate and study the three-dimensional flow dynamic and the coherent structures. In this chapter no stratification of the ambient atmosphere have been considered so that in all the numerical results δ_T=0 K/m. This chapter is mainly numerical but POD analysis is also performed on experimental velocity fields obtained by PIV.

Contents

4.1 Introduction

In this study, numerically generated flow fields are described in the case of three-dimensional spatially-developing transitional natural convective flows induced by a uniform heat flux on one side in a vertical air channel of finite height. The in-house LES code in which the Vreman SGS model had been implemented (Lau et al., 2012c,d) was used to simulate the flow. The generation of an artificial stochastic velocity fluctuation at the inlet allows the triggering of the transition to turbulence within the channel, at locations similar to those experimentally recorded (Lau et al., 2012b).

Three values of Rayleigh number for which transition from laminar to turbulent flow have been previously observed numerically and experimentally (Lau et al., 2012b; Sanvicente et al., 2013) are investigated, namely, $Ra = 1.5 \times 10^{12}$, $Ra = 3.5 \times 10^{12}$, $Ra = 7.5 \times 10^{12}$. They correspond to total electrical power of 100, 230 and 500 W at the hot wall (see table 3.1 for the summary of the case studied).

The flow is first characterised by a three-dimensional mapping of its mean streamwise velocity and temperature fields, as well as the near wall temperatures and characteristic frequencies. Then the differences in the decomposition of the velocity and temperature fluctuating fields, which depend on whether POD or SPOD is employed, are discussed. SPOD proves to be able to achieve a spatio-temporal distinction of the most energetic modes into two categories. The cross-correlation between the streamwise velocity and the temperature as well as the turbulent heat transfer rate of each of the mode categories are then examined. The modes are then matched with actual coherent structures observed in the instantaneous visualisations of the flow.

Finally POD method is also applied to experimental data obtained by PIV. The modes are described and used to analyse different flow behaviours. Moreover some potential similarities between the experimentally and numerically observed structures are presented. Finally PIV measurements performed over the whole channel allow to perform a complete representation of the POD modes.

4.2 Computational details

4.2.1 Boundary conditions

At the adiabatic walls in figure 3.8, no-slip conditions was applied together with a zero temperature gradient normal to these walls. At the open-boundaries, similar to Gresho (1991), a stress-free boundary condition has been implemented as

$$\nabla \cdot (\tilde{\sigma}_{ij} + \overline{p}\delta_{ij}) = 0 \tag{4.1}$$

where $\tilde{\sigma}_{ij}$ is the stress tensor depicted in equation (3.19).

To take into account the impact of external disturbances, the method adopted in the present numerical simulations is to generate a disturbance in the inflow. Based on previous LES numerical investigations of Lau et al. (2012b) and Tkachenko et al. (2016) performed on the same configuration, the three components of the inlet velocity are disturbed at the lower boundaries of the computational domain with the following relation

$$\mathbf{u}^*_{in} = \mathbf{u}_{in} + A_v \varepsilon, \tag{4.2}$$

in which $\mathbf{u}_{in}$ is the vector of velocities, at any point of the inlet boundary of the computational domain, as calculated at the end of the n^{th} time step. The symbol * refers to the velocity at the same point to be used at the beginning of the $(n+1)^{th}$ time step. ε is a pseudo-random number between $[-1;1]$ independently generated for each time step at each point of the lower boundaries open to the atmosphere and A_v is the amplitude of the disturbance. $A_v = 0.005$ m/s, corresponds on average to 25% of the velocity at the inlet of the channel itself. This is in the

same order of magnitude as the inlet velocity disturbance that would be obtained from the inlet turbulence kinetic energy value that Fedorov and Viskanta (1997) needed in their calculations to get agreement with experiment. As mentionned in the introduction, Sanvicente (2013) and Daverat et al. (2013) respectively reported experimental inlet turbulent intensity of 25% and 35%.

4.2.2 Effect of a stochastic noise on the flow structures

It was observed by Lau (2013) and Tkachenko et al. (2016) in LES investigations that the introduction of a numerical stochastic noise also modified the intermittent behaviour of the flow. However in their study, the flow visualisations were often in a two-dimensional vertical plan, normal to the heated wall.

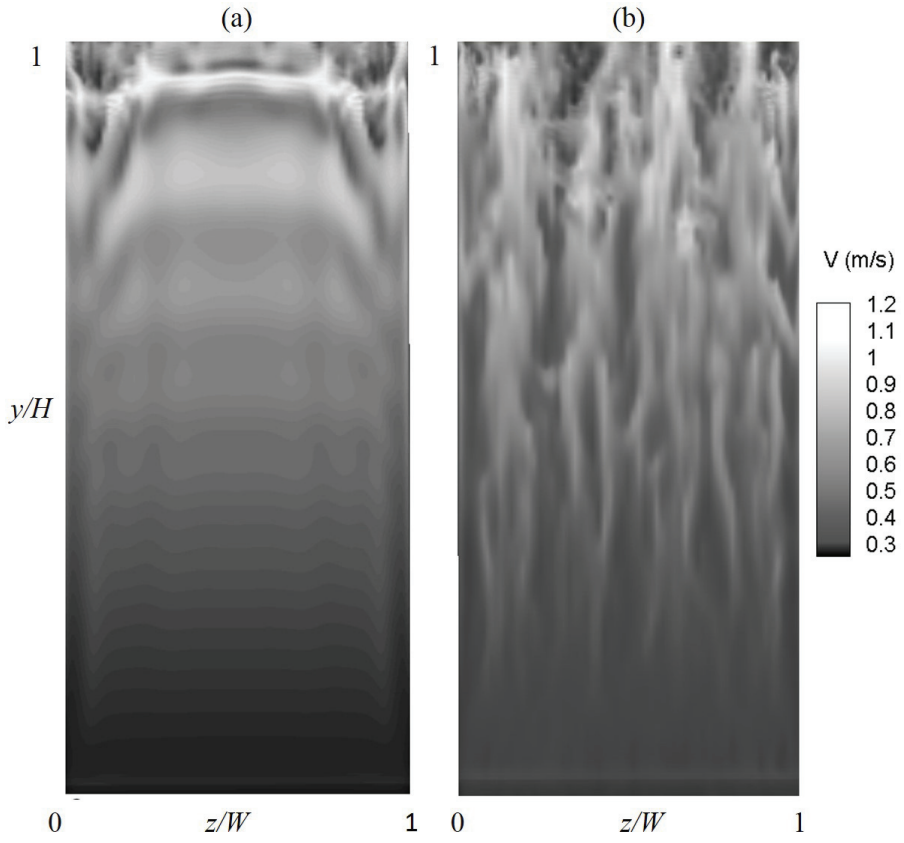

Fig. 4.1 Instantaneous visualisation of the streamwise velocity plotted in a plan parallel to the heated wall at z/W=0.1. (a) No perturbations of the inlet velocity, (b) with perturbations.

In figure 4.1 two instantaneous visualizations of the streamwise velocity have been plotted near the heated wall, in the velocity boundary layer. The same heat was injected and these plots were obtained after the same time had elapsed. In figure 4.1 (a), the velocity field was not disturbed at the inlet whereas in figure 4.1 (b), a stochastic noise was introduced at the inlet. The flow regime on the left is laminar and the streamwise oscillation are the first appearance of the

Tollmien-Schlichting waves, characteristics of the first stages of transition in classical transition. The flow structures on the right are drastically different and present features more similar to those of the bypass transition despite that, to the author knowledge, no case of buoyancy driven bypass transition have been explicitly reported in the literature yet. In the remainder of this dissertation a perturbation was introduced in all the numerical simulations.

4.2.3 Initialization and statistical convergence

The flow was initialized with the last set of results obtained by Lau et al. (2012b) which corresponded to the flow field after 80 s passed. Considering the turnover time $\mathscr{T}$ defined here as

$$\mathscr{T} = \frac{V_{in}}{H} \tag{4.3}$$

which represent the time for the whole fluid in the channel to be replaced if it were flowing at the time and spaced averaged inlet velocity V_{in} m/s. Then 80 s represents 7 to 15$\mathscr{T}$ depending on the Rayleigh number. During this time Lau et al. (2012b) recorded at least 30 repetitions of large-scale ejection and therefore assumed a meaningful statistical convergence.

In the present dissertation collection of the data and averaging for the statistics were started from the the last set of results of Lau et al. (2012b). The sampling at 0.1 s intervals was started at the first iteration after restarting the simulation. The total length of the resulting datasets was of 80 s which represents 800 snapshots. Finally, only the data within the channel itself are stored in the present work.

4.3 Flow and thermal fields spatial development

The spatially-developing transitional air flow induced by natural convection in a vertical channel heated on one side is presented in this section at $Ra = 3.5 \times 10^{12}$. A numerical-experimental comparison on this configuration and for this Rayleigh number was made by Lau et al. (2012b). In their study they focused on the time averaged streamwise velocity, wall temperature, Nusselt numbers and some turbulent statistics in the mid-plan of the channel at z/W=0.5.

In this section, the three-dimensional numerical flow is described and time-domain Fourrier transform are performed at different levels in the flow.

4.3.1 Mean temperatures and velocities at $Ra = 3.5 \times 10^{12}$

In transitional vertical channel flow at constant heat flux injected on one side, it is usual to consider the height at which the wall temperature reaches a local maximum as an indicator of the zone where transition from laminar to turbulent flow occurs (Fedorov and Viskanta, 1997; Lau et al., 2012b,d; Miyamoto et al., 1986). In the remainder of the present chapter, this height

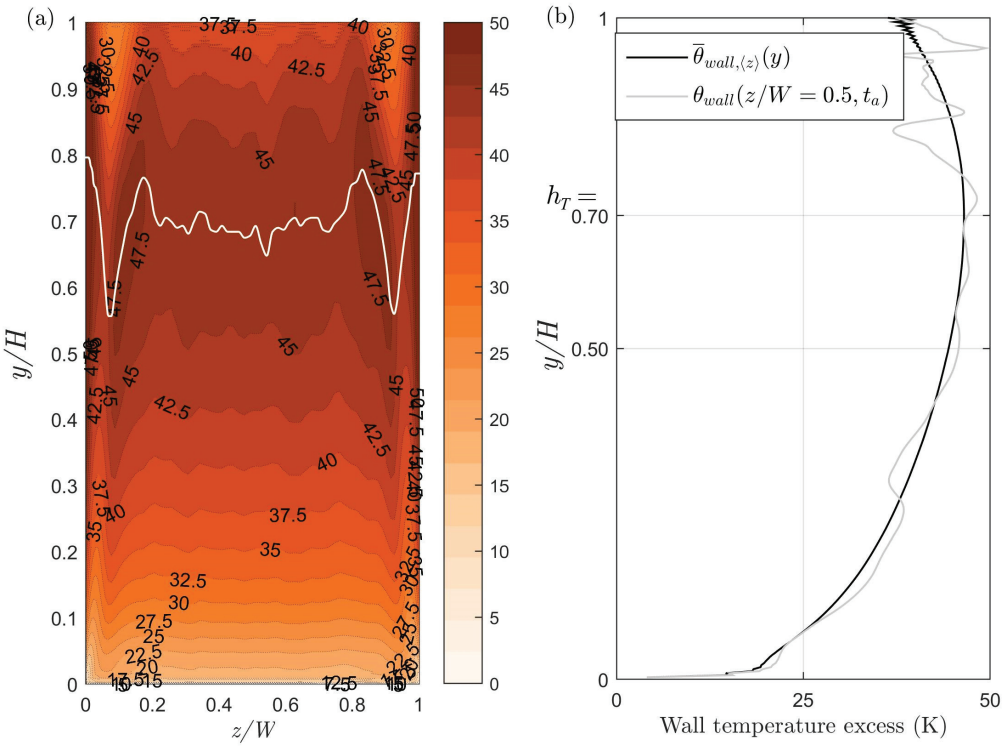

Fig. 4.2 Time-averaged temperature at the heated wall at $Ra = 3.5 \times 10^{12}$ (a) near-wall plan $\overline{\theta}_{wall}(y,z)$, the plain white line corresponds to the transition height (b) Black line, near-wall, z-averaged $\overline{\theta}_{wall,\langle z\rangle}(y)$. Light line, instantaneous near-wall temperature at z/W=0.5 and at an arbitrary time t_a

will be called the transition height and will be noted in its non-dimensional form h_T, the scaling factor being the height of the channel, H.

The near-wall time-averaged temperature rise of the heated wall, $\overline{\theta}_{wall}$, is plotted in figure 4.2, the subscript *wall* referring to a quantity that is taken at the first grid point from the hot wall that is at $x/D = 0.01$. In figure 4.2(a), the location of the transition height is plotted as a plain white line. It can be seen that the lateral walls induce a local peak and valley in the temperature distribution. However the temperature distributions between $z/W = 0.25$ and $z/W = 0.75$ are fairly uniform in the z direction. In that region, transition remains around $h_T = 0.70 \pm 0.02$.

Because the temperature distributions in that area are fairly uniform in the z direction, and for a better appreciation of the temperature distribution, the z-spatial averaging between $z/W = 0.25$ and $z/W = 0.75$ is defined and indicated by the subscript $\langle z\rangle$. The mean temperature, $\overline{\theta}_{wall\langle z\rangle}$, plotted in figure 4.2(b), has a very high gradient in the first, lower, part of the channel but its slope decreases and the temperature finally reaches a local maximum at $h_T = 0.70$.

Time-averaged streamwise velocity profiles coloured by the local time-averaged temperature are plotted at y/H of 0.05, 0.33, 0.66, 0.95 in figure 4.3. In the bulk of the flow near the entrance, $y/H = 0.05$, the velocity profile is almost uniform, and the thermal boundary layer is

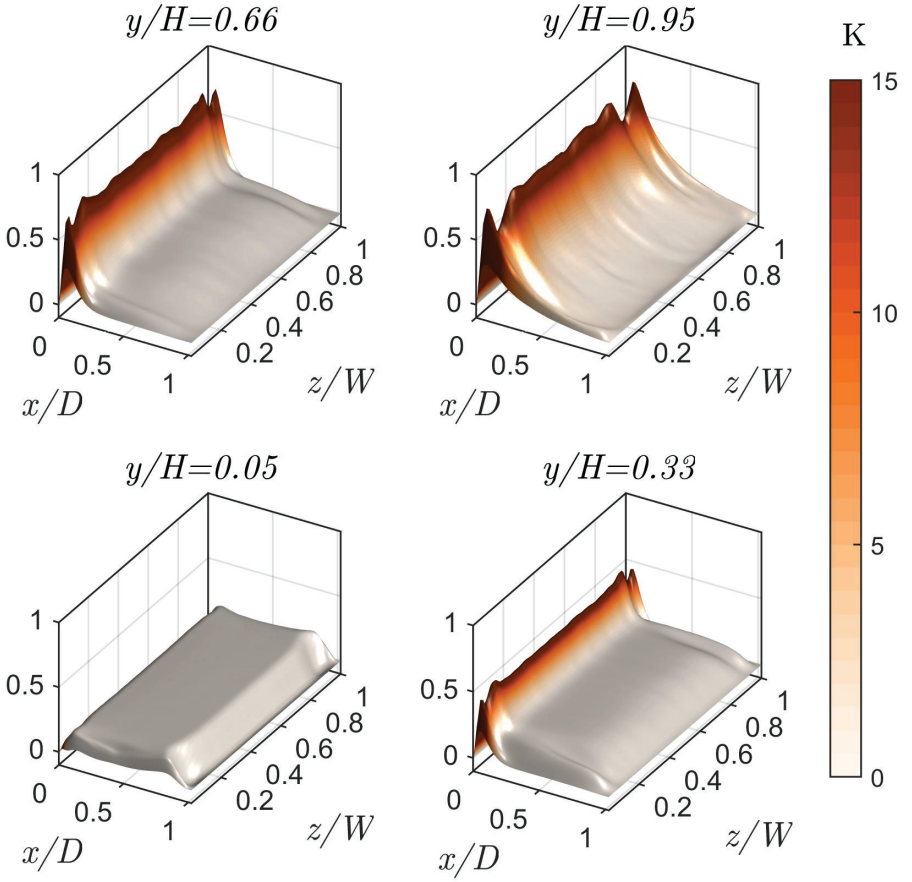

Fig. 4.3 Time-averaged streamwise velocity $\overline{v}$ coloured by the local time-averaged temperature $\overline{\theta}$ at $Ra = 3.5 \times 10^{12}$ and different height $y/H = 0.05$, $y/H = 0.33$, $y/H = 0.66$, $y/H = 0.95$. The colorbar on the right indicates the temperature scale.

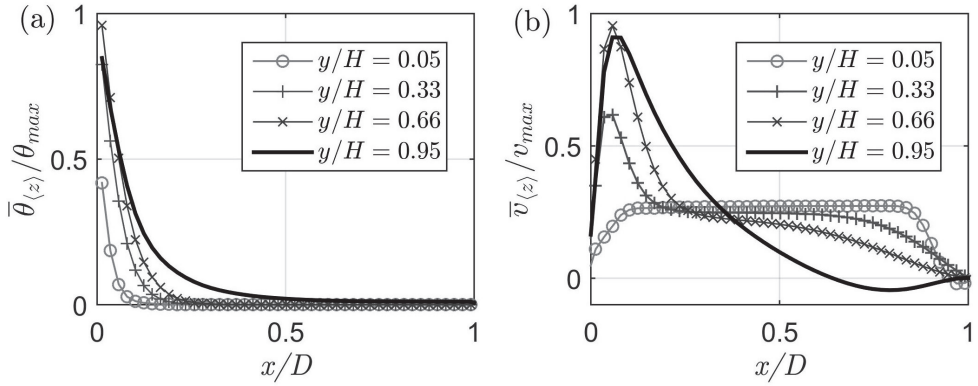

Fig. 4.4 Time and z-spaced averaged (a) temperature $\overline{\theta}_{\langle z\rangle}/\theta_{max}$ and (b) streamwise velocity $\overline{v}_{\langle z\rangle}/v_{max}$ at $Ra = 3.5 \times 10^{12}$ $y/H = 0.05$, $y/H = 0.33$, $y/H = 0.66$, $y/H = 0.95$.

just beginning to develop. Further up in the channel, as can be seen at heights $y/H = 0.33$ and $y/H = 0.66$, the thermal boundary layer has grown inducing a much higher buoyancy-driven velocity near the heated wall, which is concomitant with a decreasing velocity in the bulk flow. However the high temperature fluid does not mix with the bulk flow which remains at inlet temperature. This indicates that little turbulent activity exists in the flow up to $y/H = 0.66$. Finally at $y/H = 0.95$, the velocity and thermal boundary layers are wider and the maximum velocity and temperature decrease. This indicates that the transition to turbulent flow, expected at around $y/H = 0.70$ as discussed above, has started. Because of the complex interaction with the lateral side walls, assumed to be adiabatic, the mean velocity boundary layer on the hot wall has a peak and valley shape in the vicinity of these walls, similar to the mean temperature figure 4.2(a). Moreover, as for the mean wall temperature figure 4.2(a) the mean temperature and mean velocity profiles are nearly uniform in the z-direction between $z/W = 0.25$ and $z/W = 0.75$. As a consequence, $\overline{\theta}_{\langle z \rangle}/\theta_{max}$ and $\overline{v}_{\langle z \rangle}/v_{max}$ were plotted in figure 4.4 which allows a better visualisation of the flow development in that region. The subscript *max* indicates the maximum values of $\overline{\theta}_{\langle z \rangle}$ and $\overline{v}_{\langle z \rangle}$ which are respectively of $\theta_{max} = 47°\text{C}$ and $v_{max} = 0.67\,\text{m/s}$. It can be seen that at $y/H = 0.95$ there is a negative velocity near the unheated wall which is due to a reverse flow at the outlet.

Note that in figure 4.3 especially in the top-right figure there are bright white patches due to the glare of the rendering.

4.3.2 Fourier analysis at $Ra = 3.5 \times 10^{12}$

In figure 4.5, the streamwise evolution of the frequency spectrum obtained by Discrete Fourier Transform (DFT) of the fluctuating components of the velocity near the heated wall, $x/D = 0.05$, on the centreline, $z/W = 0.5$, are presented at discrete values of $y/H = 0.20, 0.39, 0.79, 0.94$. Different scales have been used for each of the velocity components at the various heights to generate a better image for visualisation purposes. Two frequency bands are particularly well defined in the streamwise component of the flow, v', at $y/H = 0.79$. In this spectrum, a low-frequency (LF) band ranging between 0.0125 Hz to 1.2 Hz and a medium frequency (MF) band starting at 1.2 Hz, are visible. The MF band is evaluated to range between 1.2 Hz and 3.5 Hz. The LF band is shared by all the velocity components at $y/H = 0.20$ whilst the MF band is particularly pronounced in the higher part of the channel in w', the spanwise component of velocity.

It should be noted in figures 4.3 and 4.2 respectively that, even in the central region of the channel, there are weak spatial oscillations of the temperature distribution in the z-direction and some 'folds' in the velocity distribution. These oscillations suggest that the strict statistical convergence was not reached. However, given the frequencies of interest identified in figure 4.5, the statistical convergence for the associated phenomena can be assumed to have been achieved.

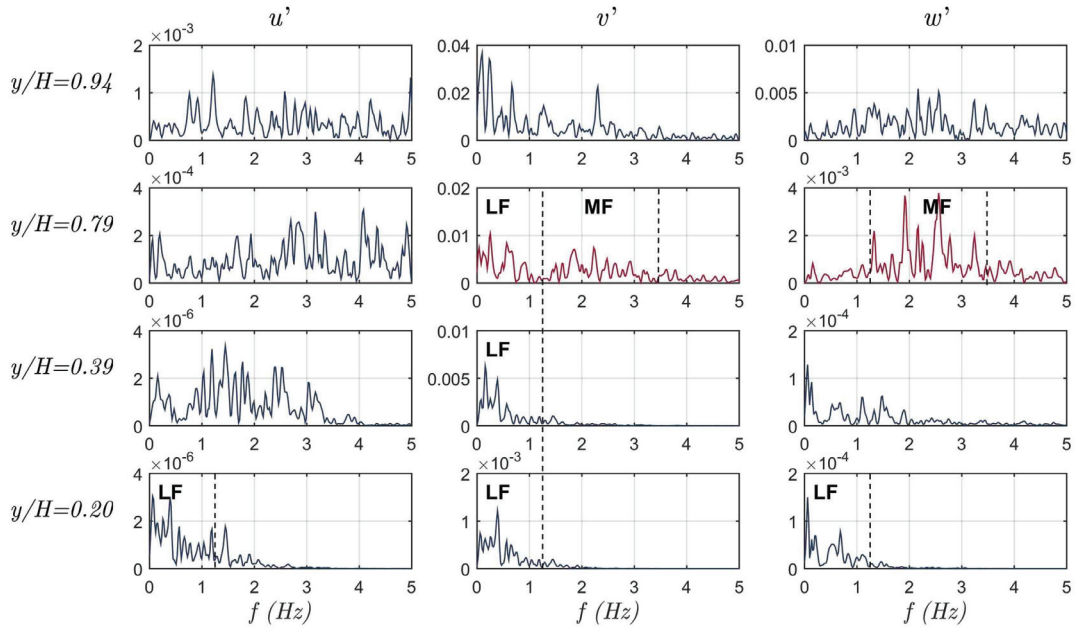

Fig. 4.5 Frequency spectrum of the velocity components, from left to right, u' v' and w', in the centreline close to the heated wall at $x/D = 0.05$, $z/W = 0.5$ at different y/H locations from bottom to top (a)-(d) $y/H = 0.20, 0.39, 0.79, 0.94$. The dashed lines separate the LF and MF frequency bands.

The phenomena associated with frequencies around the lowest detectable frequency of 0.0125Hz are beyond the scope of this study.

Now that the mean fields have been described and the characteristic frequencies of the flow identified, instantaneous structures of the flow are analysed using POD-based methods. To that aim the ability of POD and SPOD to capture the behaviour of the flow in that configuration is evaluated.

4.4 Assessment of the POD and SPOD decomposition at $Ra = 3.5 \times 10^{12}$

As mentioned in section 3.3, one of the SPOD key parameter is the filter size N_f that is applied to the correlation matrix C, before the eigenproblem is solved. A suitable filter size has to be determined in order to identify modes that could not have been identified with the POD method. Many examples of this were presented by Sieber et al. (2016) or Ribeiro and Wolf (2017).

The SPOD decomposition is no longer optimal as far as the energetic decomposition is concerned (Noack, 2016), and as the filter size increases, the energy of the most energetic modes is re-distributed amongst the less energetic modes. At $Ra = 3.5 \times 10^{12}$, a filter size $N_f = 20$ allows the SPOD to extract modes with marked distinct behaviours. This demarcation could not

be achieved with a smaller filter size and $N_f \geq 20$ only flattens the energy distribution without yielding a better distinction. The frequency content of the temporal coefficients associated with each mode is plotted in figure 4.6 for POD and SPOD decompositions. The frequency content of the POD and the SPOD modes respectively corresponds to the DFT of the POD temporal coefficients α (3.7) and of the SPOD temporal coefficients β (3.12). The temporal coefficients were scaled by the eigenvalues in order to compare the amplitude of their DFT on the same colour scale. In both cases, the characteristic frequencies increase with the order of the modes. This result is usual for POD and SPOD analysis since higher order modes generally represent smaller energetic structures with lower energetic contribution and higher frequencies.

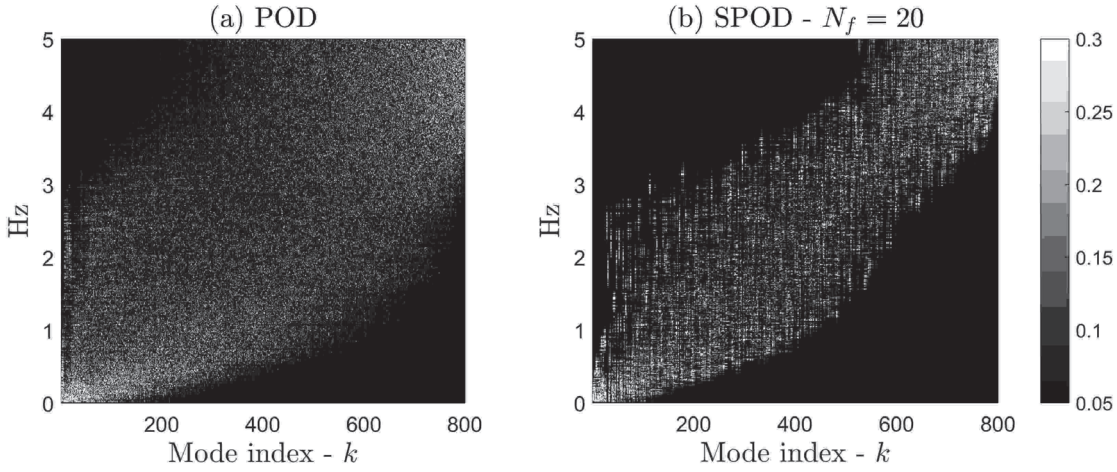

Fig. 4.6 DFT of the scaled temporal coefficients (a) $\alpha_k/\sqrt{\lambda_k}$ for POD, (b) $\beta_k/\sqrt{\mu_k}$ for SPOD decomposition with $N_f = 20$, at $Ra = 3.5 \times 10^{12}$.

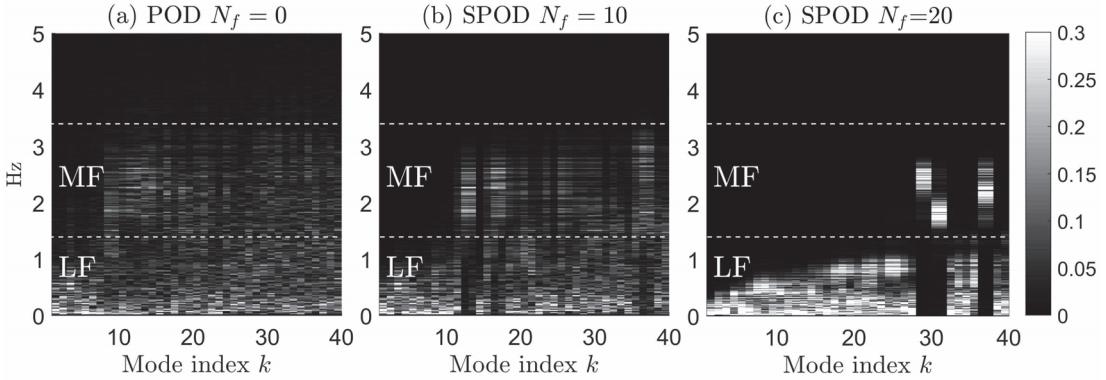

Fig. 4.7 DFT of the scaled temporal coefficients of the first 40 modes (a) $\alpha_k/\sqrt{\lambda_k}$ for POD, (b) $\beta_k/\sqrt{\mu_k}$ for SPOD decomposition with $N_f = 20$, at $Ra = 3.5 \times 10^{12}$.

A magnified view of the spectral densities of the first 40 modes for both decomposition methods is presented in figure 4.7. The LF and MF frequency band ranges, identified in section 4.3.1, are represented by the dashed lines. In the case of the POD modes, in figure 4.7(a), the temporal coefficients contain a wide range of frequencies. In figure 4.7(b) SPOD was

applied with a filter size of $N_f = 10$, each temporal coefficient is associated with a lesser range of frequencies. However, it is clearly noticed, in figure 4.7(c), that the SPOD decomposition, with a filter size of $N_f = 20$ sorted the first 40 modes into two categories based on their spectral content. The first type has frequencies contained in the LF-frequency bands while the second type in the MF-frequency band. This demarcation could not be achieved with a smaller filter size and $N_f > 20$ only flattens the energy distribution without yielding a better distinction.

The use of the SPOD approach allows the first 40 modes to be unambiguously identified as belonging to either the LF or the MF types; therefore, they will be referred to as LF and MF modes.

The differences between POD and SPOD spatial modes as well as the effect of the filter size can be observed in figure 4.8. The structures observed in these modes are the core study of the remaining of this chapter, and will be studied in details in the following sections. At this point, the aim of this figure is only to briefly illustrate the sorting of the modes which was made based on the LF and MF bands. In figure 4.8 (a) a section of $\phi_{v,16}$, a POD modes which contains both LF and MF is plotted at $x/D = 0.05$. The structures observed are rather complex with long streamwise structures alternating in the z-direction as well as smaller structures alternating in the y-direction. The SPOD modes $\psi_{v,27}$, $\psi_{v,28}$, obtained with the filter size of N_f=20, are depicted in figure 4.8 (c). They correspond to modes which the temporal coefficients respectively have a clear LF and MF band (figure 4.7). In comparison with the POD mode, the structures observed in these SPOD modes look clearer and not mixed up. In figure 4.8 (b) is depicted a SPOD mode, obtained with a smaller filter size of N_f=10, which mainly contains MF frequencies but still have some of the LF frequencies as well as patterns in between those of $\phi_{v,16}$ and $\psi_{v,28}$ obtained with N_f=20.

The relative energy content $E_{POD}(k)$ and $E_{SPOD}(k)$ of the eigenvalues (λ equation (3.7) for POD and μ equation (3.12) for SPOD) associated with the 40 most energetic POD and SPOD modes are plotted in figure 4.9. They are defined as $E_{POD}(k) = \lambda_k / E_{tot}$ and $E_{SPOD}(k) = \mu_k / E_{tot}$ for POD and SPOD, where

$$E_{tot} = \sum_{k=1}^{k=N_t} \lambda_k = \sum_{k=1}^{k=N_t} \mu_k. \tag{4.4}$$

Except for modes 5-6, the 20 first SPOD modes are less energetic than their corresponding POD modes. However, after mode 32 the SPOD modes become more energetic than POD modes. The cumulated energy contents of the first 40 POD and SPOD modes represents respectively 35% and 32% of the total energy (4.4).

In this flow configuration, the SPOD can be used to decompose the dynamic of the flow into modes, the most energetic of which are associated with clearly delineated frequency spectra, belonging either to the LF or the MF frequency ranges identified in section 4.3.1. The increase in the harmonic coherence of these modes comes with a low loss in the energy captured compared to POD modes. For this reason, SPOD will be used in order to analyse the flow dynamics.

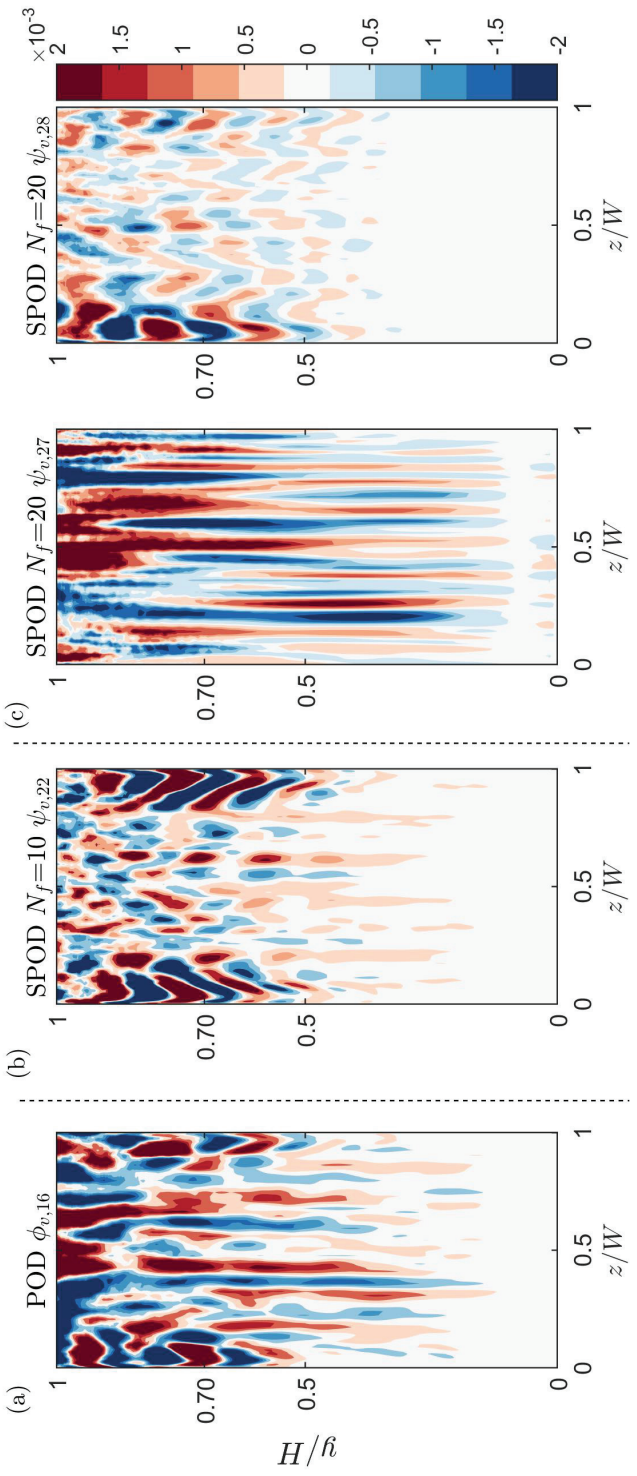

Fig. 4.8 Spatial modes for different filter size (a) POD, N_f=0 $\phi_{v,16}$, (b) SPOD, N_f=15 $\psi_{v,22}$ and (c) SPOD, $N_f = 20$ $\psi_{v,27}$ and $\psi_{v,28}$.

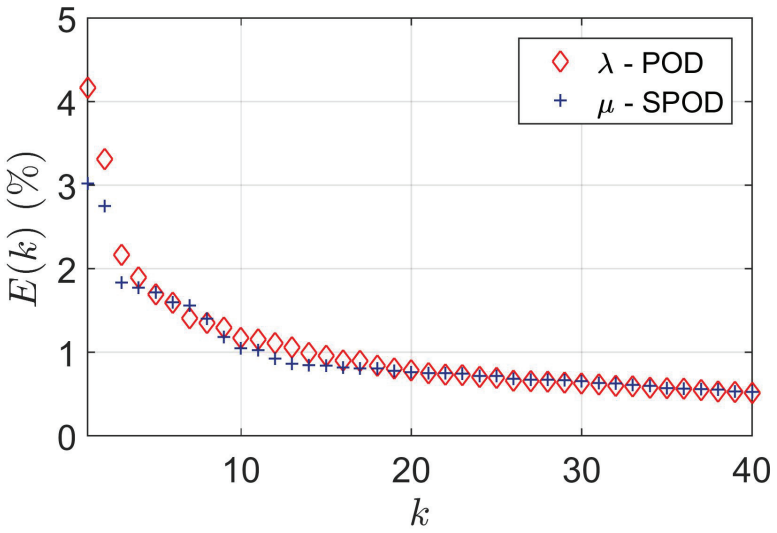

Fig. 4.9 Relative energy content of the first 40 POD and SPOD modes at $Ra = 3.5 \times 10^{12}$.

4.5 Generalisation and extension to $Ra = 1.5 \times 10^{12}$ and $Ra = 7.5 \times 10^{12}$

As stated above, numerical results were also obtained for two other Rayleigh numbers of $Ra = 1.5 \times 10^{12}$ and $Ra = 7.5 \times 10^{12}$. Similar behaviours of the mean and fluctuating fields are observed for these cases with changes in the location of the maximum temperature on the wall, in the characteristic frequency bands, in the time-averaged velocities and in the temperature distributions on the heated wall. The assessment of the decomposition method to be employed for each of the Rayleigh numbers was performed in the same way as that used above for $Ra = 3.5 \times 10^{12}$. The use of a filter size $N_f = 15$ allowed the LF and MF modes to be distinguished in the case of $Ra = 1.5 \times 10^{12}$ whereas a filter size $N_f = 25$ is necessary to clearly separate the frequency bands at $Ra = 7.5 \times 10^{12}$.

Table 4.1 Characteristic of the flow and of the SPOD decomposition

Ra	$Ra = 1.5 \times 10^{12}$	$Ra = 3.5 \times 10^{12}$	$Ra = 7.5 \times 10^{12}$
Number of snapshots, N_t	800	800	800
Averaged inlet velocity in m/s	0.13	0.20	0.30
Transition height, h_T	0.87	0.70	0.65
LF-band in Hz	0.0125-1.0	0.0125-1.2	0.0125-1.7
MF-band in Hz	1.0-2.5	1.2-3.2	1.7-4
γ (3.3)	1.8×10^{-3}	9.8×10^{-4}	4.8×10^{-4}
Filter size, N_f	15	20	25

The SPOD relative energy content associated with the modes for each Rayleigh number is plotted in figure 4.10. The energy is more evenly distributed among the modes at higher

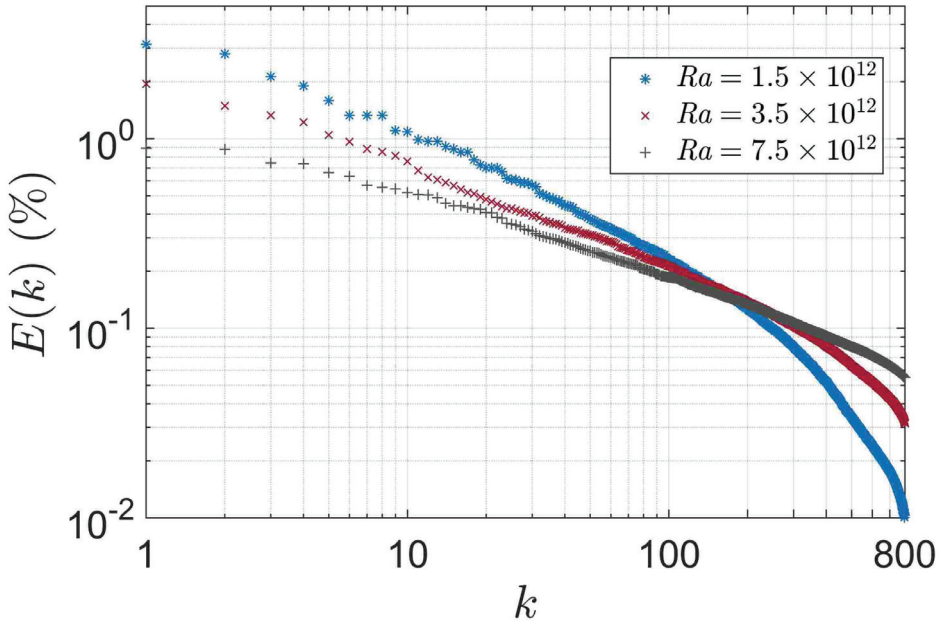

Fig. 4.10 Relative energy content of the 800 modes at $Ra = 1.5 \times 10^{12}$, $Ra = 3.5 \times 10^{12}$ and $Ra = 7.5 \times 10^{12}$.

Rayleigh numbers which is due to an increase in the complexity of the flow structures. It is interesting to observe that there is a change in the energy decreases for $Ra = 1.5 \times 10^{12}$ at around k =200. This change may indicate a new step in the convergence of the method and could be used as a criterion to build reduced-order-model. Note that after closer examination of the three curves it can be observed that they do not cross at the exact same point as could be thought in figure 4.10

The characteristics of the flow as well as the SPOD decomposition parameters for the three Rayleigh numbers are summarized in table 4.1. The LF and MF bands are wider and shifter at higher frequencies as the Rayleigh number increases. Moreover the ratio between the turbulent kinetic energy and the mean of the temperature fluctuations squared, represented by γ in equation (3.3), decreases as the Rayleigh number increases. This suggests that, in the present configuration, as the Rayleigh number increases, the kinetic energy in the whole channel increases less than the square of the temperature fluctuations.

4.6 Description of the LF and MF modes

In this section, the SPOD analysis is used to extract the coherent structures associated with the LF and MF modes, the main focus being on the structures that develop near the heated wall. One representative mode of each of the LF and MF family, identified with the SPOD are described at

$Ra = 3.5 \times 10^{12}$. The analysis is then extended to the other two Rayleigh numbers for which similarities and differences are highlighted.

4.6.1 At $Ra = 3.5 \times 10^{12}$

Low frequency modes, streak modes

A three-dimensional representation of the first LF-mode, ψ_1, is plotted in figure 4.11. Two isosurfaces of the v-component of the mode 1, denoted $\psi_{v,1}$, of amplitudes -0.0005, +0.0005 are plotted. These isosurfaces are coloured by the local value of the temperature-component, denoted $\psi_{\theta,1}$. Organised elongated streamwise velocity streaks are observed close to the heated wall ($x/D = 0$). The uniform colour of each streak shows that they correspond to coherent thermal streaks. The streaks more or less retain the same shape up to the transition height at $h_T = 0.70$ where they start to break up. In the bulk region, below h_T, no isosurface of $\psi_{v,1}$ at the selected amplitude are present which signifies a low activity. Finally coherent structures of pure velocity are also seen near the unheated wall ($x/D = 1$). These structures interact and merge with the streaks above the transition height.

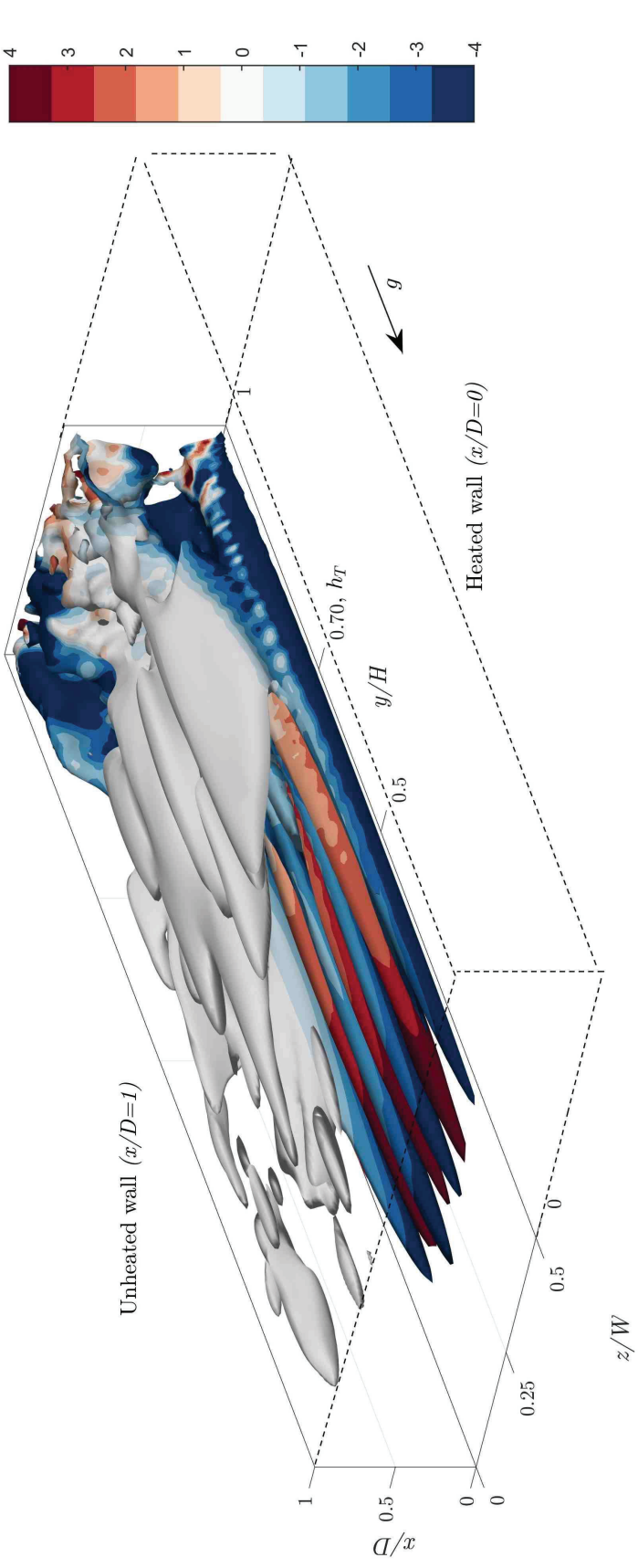

Fig. 4.11 Positive and negative isosurfaces of $\psi_{v,1}$ coloured by the local value of $\psi_{\theta,1}$. Due to the presence of structures close to each of the walls, only half of the channel is presented for a better visualisation, between $z/W = 0$ and $z/W = 0.5$. The scale in the x-direction is double that in the other two directions.

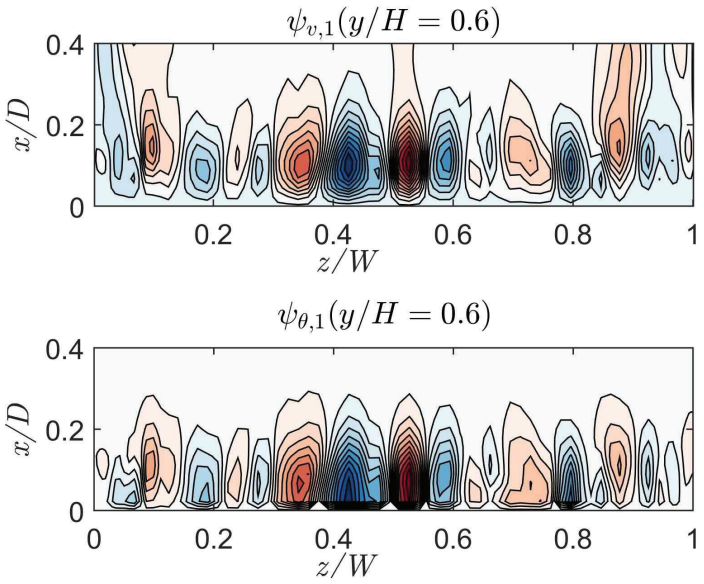

Fig. 4.12 Countours of $\psi_{v,1}$(left) and $\psi_{\theta,1}$(right) equally spaced between -0.001 and 0.001 at $y/H = 0.6$.

Figure 4.12 displays a section of $\psi_{v,1}$ and $\psi_{\theta,1}$ at y/H=0.6 on which it appears that positive and negative streaks of $\psi_{v,1}$ correspond to positive and negative streaks of $\psi_{\theta,1}$.

Negative and positive isosurfaces of amplitudes -0.0001 (blue) and 0.0001 (red) of the x and z components of mode 1 $\psi_{u,1}$ and $\psi_{w,1}$ are presented in figure 4.13. Only few of the isolated $\psi_{u,1}$ and $\psi_{w,1}$ isosurfaces appear below the transition height, which means that the x and z components contribute little to ψ_1. The streaks observed in $\psi_{v,1}$ are not affected by any x or z components, at least below h_T, which suggests that they are not vortical structures but only alternatively accelerated and decelerated thermal-velocity corridors. Near the unheated wall, the white patches represent velocity structures at inlet temperature.

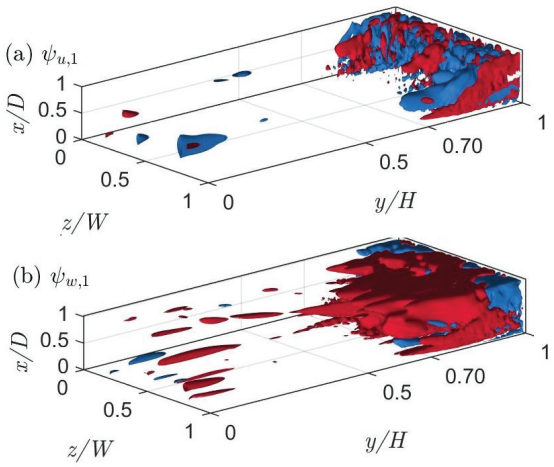

Fig. 4.13 Positive (red) and negative (blue) isosurfaces of the (a) $\psi_{u,1}$ (b) $\psi_{w,1}$. The scale in the x-direction is double that in the other two directions.

In order to assess the organisation of the structures near the heated wall, figure 4.14 displays a section of the v-component of the first four LF-modes at $x/D = 0.05$. They all are composed of well organised streamwise oriented streaks with similar spanwise wavelengths between 0.08 and 0.12 m. The spatial organisations of these four modes start to disintegrate above the transition height with growth, decay and merging of the streaks, although some streaks in the $\psi_{v,3}$ and the $\psi_{v,4}$ modes exhibit minor variations in the streamwise direction below the transition height.

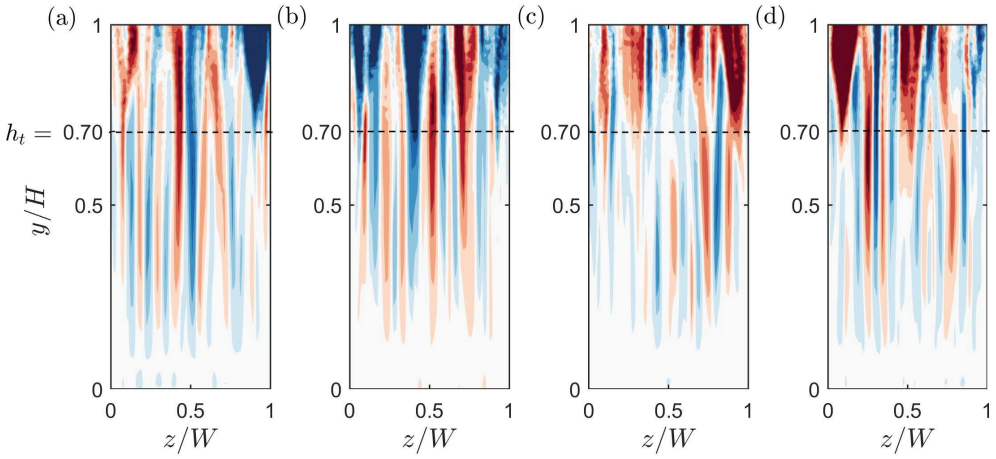

Fig. 4.14 Colour plots of (a) $\psi_{v,1}$, (b) $\psi_{v,2}$, (c) $\psi_{v,3}$ and (d) $\psi_{v,4}$ in the section $x/D = 0.05$. The colour scale ranges from -0.001 (blue) to 0.001(red).

The remaining LF-modes among the first 40 modes (figure 4.7) exhibit a similar spatial behaviour to those of figure 4.14. They are all composed of elongated correlated velocity and thermal streamwise streaks, with only minor contributions from the x and z components.

Medium frequency modes, v-shaped modes

The components of most energetic MF mode, ψ_{28}, are displayed in figures 4.15-4.16. Two isosurfaces of $\psi_{v,28}$, of amplitudes -0.0005, +0.0005, coloured by the local value of $\psi_{\theta,28}$ are plotted on Figure 4.15. This mode is composed of staggered structures showing "V" or "Λ" shape patterns. While the structures remain very close to the heated wall in the low and mid sections of the channel, they progressively grow and expand to occupy the whole channel depth (x-direction) as they travel upstream. Positive and negative isosurfaces of $\psi_{v,28}$ approximately correspond to positive and negative structures of $\psi_{\theta,28}$.

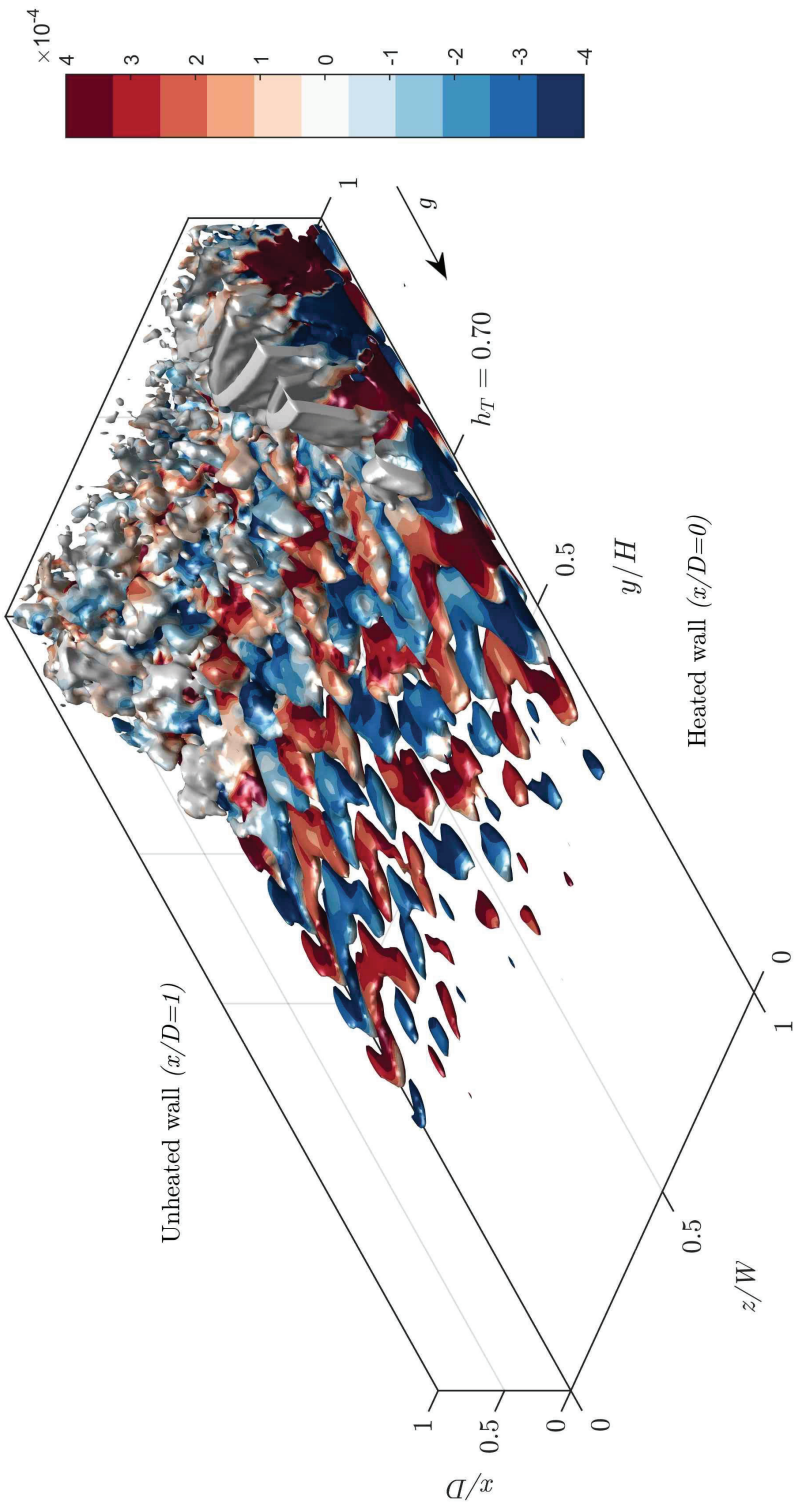

Fig. 4.15 Positive and negative isosurfaces of $\psi_{v,28}$ coloured by the local value of $\psi_{\theta,28}$. The scale in the x-direction is double that in the other two directions.

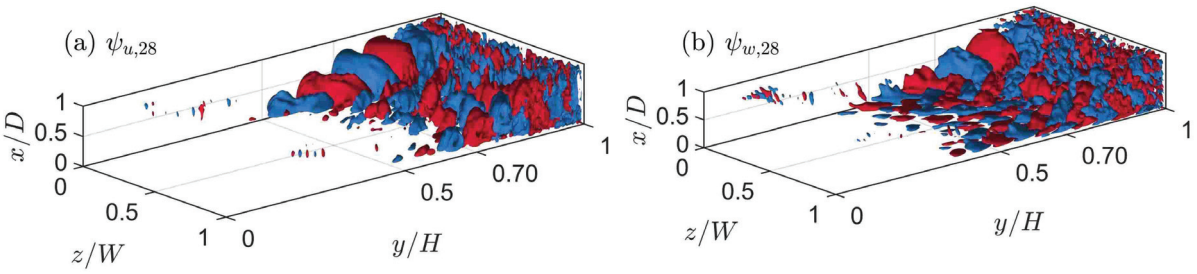

Fig. 4.16 Positive and negative isosurfaces $\psi_{v,28}$ coloured by the local value of $\psi_{\theta,28}$. The scale in the x-direction is double that in the other two directions.

Negative and positive isosurfaces of amplitudes -0.0001 (blue) and 0.0001 (red) $\psi_{u,28}$ and $\psi_{w,28}$ are plotted in figure 4.16. Unlike the LF modes, ψ_{28} contains a significant contribution from its u and w components near the heated wall, below the transition height, which indicates a strong vortical content of these structures.

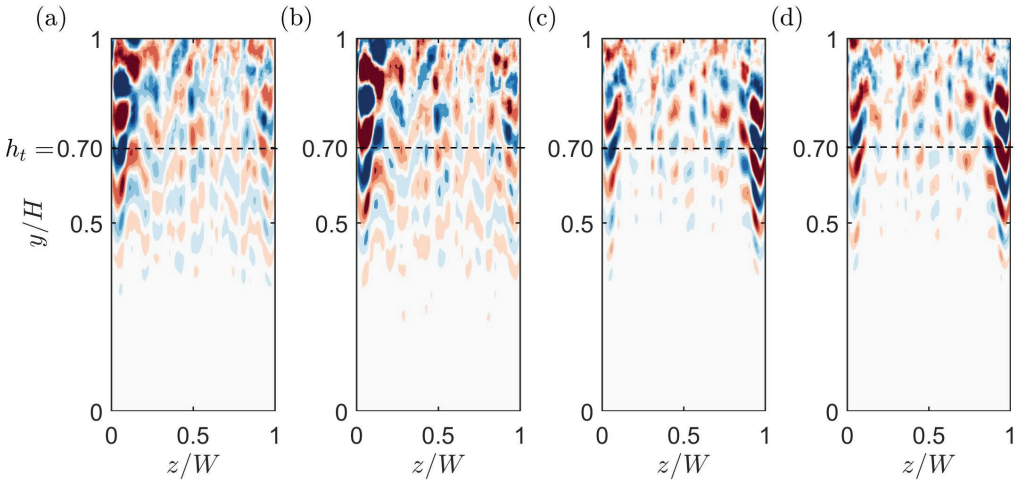

Fig. 4.17 Colour plots of (a) $\psi_{v,28}$, (b) $\psi_{v,29}$, (c) $\psi_{v,30}$ and (d) $\psi_{v,31}$ in the section $x/D = 0.05$. The colour scale ranges from -0.001 (blue) to 0.001(red).

Figure 4.17 displays a section of the first four MF-modes at $x/D = 0.05$. These modes all represent structures similar to those of ψ_{28}. The structures are better defined close to the lateral walls. The spanwise size of the structures may be in part constrained by the lateral confinement. In the streamwise direction, the wavelengths of the structures range between 0.20 and 0.30 m. It can be seen that these modes form two pairs, modes 28-29 and modes 30-31. The modes within the pairs represents the same structures shifted in the streamwise direction by a quarter of the streamwise wavelength. The coupling of these pairs of mode is further confirmed in figure 4.18 by their phase diagrams (a) $\beta_{29}(\beta_{28})$ and (b) $\beta_{31}(\beta_{30})$. The circular shape observed is characteristic of coupled modes, and reflects an oscillating process of the structures.

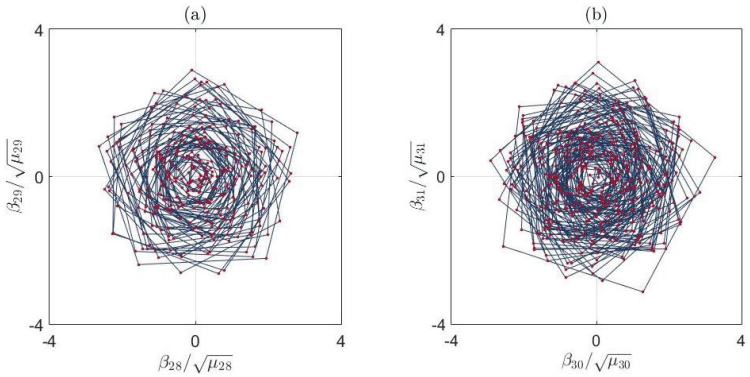

Fig. 4.18 Phase diagram of (a) $\beta_{29}(\beta_{28})$ and (b) $\beta_{31}(\beta_{30})$.

4.6.2 At $Ra = 1.5 \times 10^{12}$ and $Ra = 7.5 \times 10^{12}$

The main similarities and differences of the LF and MF modes at $Ra = 1.5 \times 10^{12}$ and at $Ra = 7.5 \times 10^{12}$ are discussed in this section. The streamwise component of the two first LF-modes at $x/D = 0.05$ are plotted in figure 4.19(a-b) at $Ra = 1.5 \times 10^{12}$ and (e-f) at $Ra = 7.5 \times 10^{12}$. The streamwise component of the two first MF-modes at $x/D = 0.05$ is plotted in figure 4.19 at (c) – (d) $Ra = 1.5 \times 10^{12}$ and at (g) – (h) $Ra = 7.5 \times 10^{12}$. Their corresponding temporal coefficients are displayed in figure 4.20.

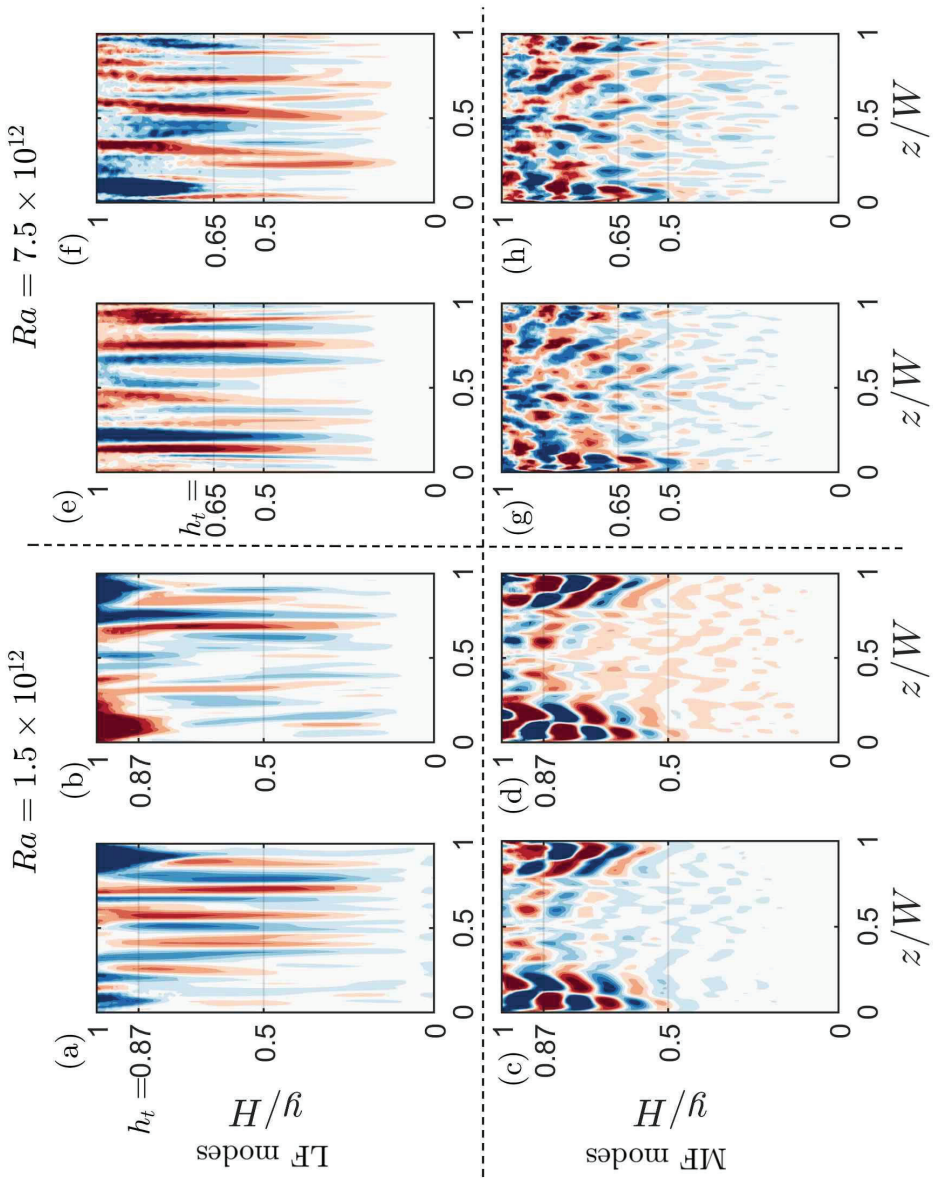

Fig. 4.19 v-component in the section $x/D = 0.05$ of the two first LF-modes $\Psi_{v,1}$ and $\Psi_{v,2}$ (a-b) at $Ra = 1.5 \times 10^{12}$ and at (e-f) at $Ra = 7.5 \times 10^{12}$ as well as the two first MF- modes (c-d) $\Psi_{v,8}$ and $\Psi_{v,9}$ at $Ra = 1.5 \times 10^{12}$ and (g-h) $\Psi_{v,77}$ and $\Psi_{v,78}$ at $Ra = 7.5 \times 10^{12}$. The colour scale ranges from -0.001 (blue) to 0.001(red).

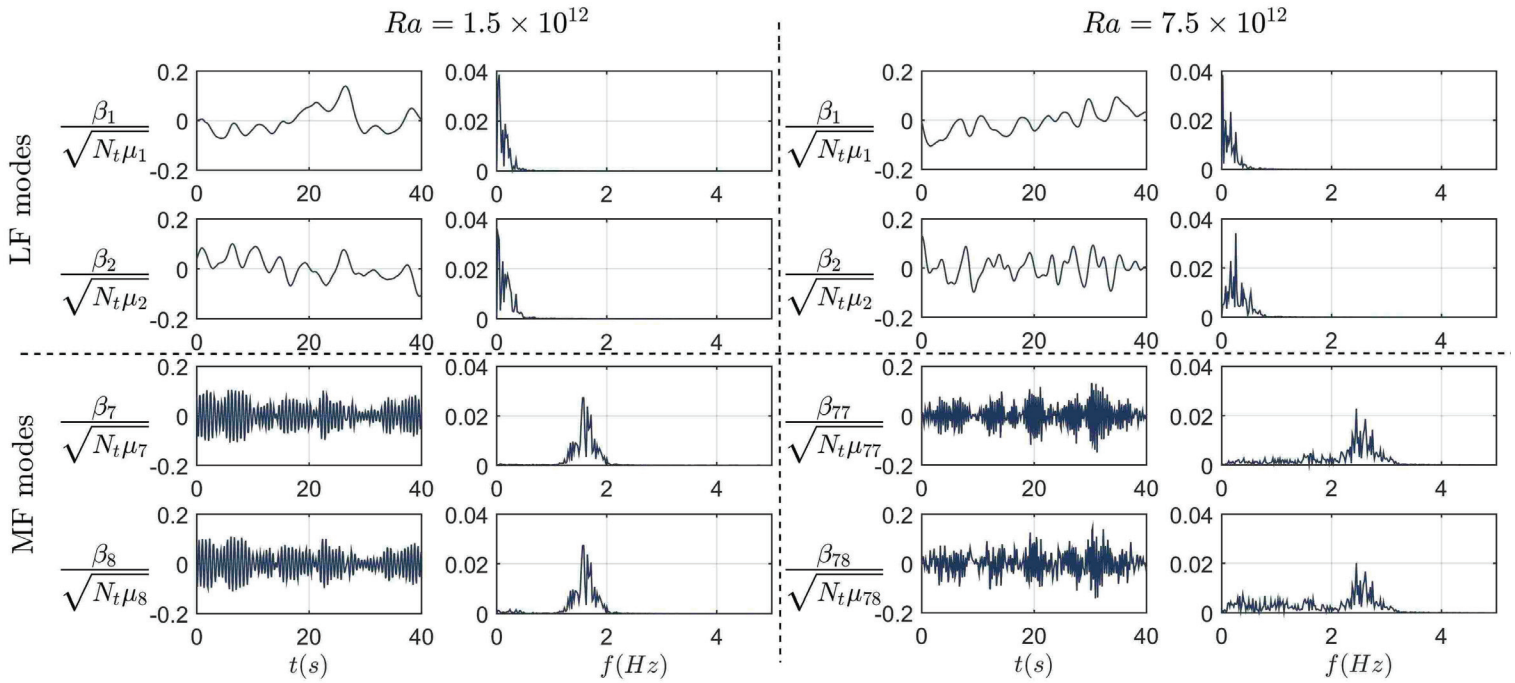

Fig. 4.20 Time coefficients $\beta_k(t)/\sqrt{N_t \mu_k}$ and corresponding spectral contents of the two first LF-modes and MF-modes at $Ra = 1.5 \times 10^{12}$ and at $Ra = 7.5 \times 10^{12}$.

Similarly to $Ra = 3.5 \times 10^{12}$, the streaks of the LF-modes remain well organised up to the transition height which is located at respectively $h_T = 0.87$ at $Ra = 1.5 \times 10^{12}$ and $h_T = 0.65$ at $Ra = 7.5 \times 10^{12}$ (see table 4.1). The wavelengths of the spanwise organisation of the streaks are in the same order of magnitude between 0.08 and 0.12 m for the three Rayleigh numbers. The v-patterns of the MF-modes at $Ra = 1.5 \times 10^{12}$ are well-defined close to the lateral walls and weaker in the z-bulk region of the channel. Regarding the MF-modes at $Ra = 7.5 \times 10^{12}$, the structures are not as well organised as for the two lower Rayleigh numbers. In general, as the Rayleigh number increases, the structures identified by the MF-modes get smaller.

Regarding the temporal coefficients plotted in figure 4.20, the same clear distinction between the low and medium frequency bands of the modes is observed. Similarly to $Ra = 3.5 \times 10^{12}$, the MF-modes for the two other Rayleigh numbers also come by pairs.

Thus far, two great families of modes have been identified for the three investigated Rayleigh numbers showing similar temporal and spatial organisation. While at the three Rayleigh numbers, the first LF-modes remains the most energetic modes, the order (based on the energy content) of the first pair of MF-modes gets higher as the Rayleigh number increases. The first MF-modes pair is respectively ranked (7,8) and (76,77) at $Ra = 1.5 \times 10^{12}$ and $Ra = 7.5 \times 10^{12}$. Thereby their relative energetic contribution in the flow realisation is getting lower, as a consequence of the increase in the flow complexity.

In the next section, a physical interpretation of the structures represented by the LF and MF modes is proposed. Moreover, their contributions to the coupled velocity and thermal fields is discussed.

4.7 Physical interpretation of the mode contribution

4.7.1 Coupled velocity and thermal fields

In order to better understand the role of the LF and MF-modes in the heat transfer at the wall, their contribution is studied separately. Indeed, by construction, the temporal coefficients associated with the SPOD modes are orthogonal so that the time averaged coupled velocity and thermal fields can be decomposed as the sum of the contributions of each SPOD mode. It follows that

$$\overline{u'\theta'} = \frac{1}{\sqrt{\gamma}} \sum_{k=1}^{N_t} \mu_k \psi_{u,k} \psi_{\theta,k}, \tag{4.5}$$

and

$$\overline{v'\theta'} = \frac{1}{\sqrt{\gamma}} \sum_{k=1}^{N_t} \mu_k \psi_{v,k} \psi_{\theta,k}. \tag{4.6}$$

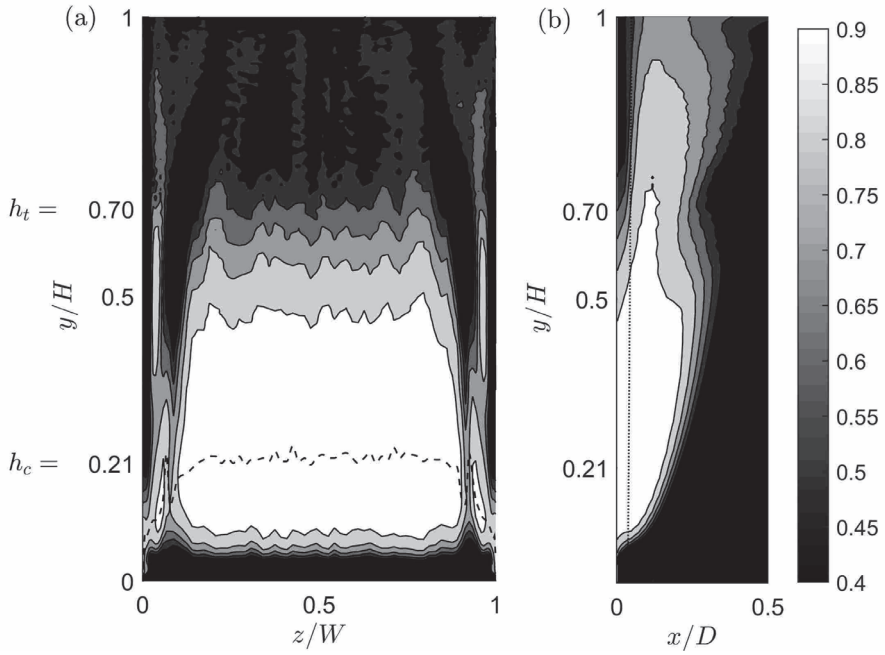

Fig. 4.21 (a) Near-wall v-θ correlation, $r_{v\theta,wall}(y,z)$ and (b) z-averaged v-θ correlation, $r_{v\theta,\langle z\rangle}(x,y)$. $Ra = 3.5 \times 10^{12}$

v-θ cross-correlation

As mentioned in the general introduction chapter 3, the near-wall streamwise velocity and temperature fields are highly correlated in forced convection flow (Abe and Antonia, 2009; Pirozzoli et al., 2016; Wu and Moin, 2010) whereas it is not the case in vertical turbulent natural convection (Pallares et al., 2010). To study this effect the cross-correlation between the streamwise velocity fluctuations and the temperature fluctuations, referred to as the v-θ correlation, is defined here at each location $\mathbf{x}$ by the correlation coefficient $r_{v\theta}(\mathbf{x})$ and is calculated as follow

$$r_{v\theta}(\mathbf{x}) = \left(\frac{\overline{v'\theta'}}{\sqrt{\overline{v'^2}\,\overline{\theta'^2}}} \right)(\mathbf{x}). \tag{4.7}$$

Equation (4.6) allows decomposing equation (4.7) into the contribution of each mode to the total v-θ correlation. Thus equation (4.7) can be written as

$$r_{v\theta}(\mathbf{x}) = \left(\frac{1}{\sqrt{\gamma\,\overline{v'^2}\,\overline{\theta'^2}}} \sum_{k=1}^{N_t} \mu_k \psi_{v,k} \psi_{\theta,k} \right)(\mathbf{x}). \tag{4.8}$$

In order to assess how the LF and the MF modes (identified figure 4.7) contribute to the v-θ correlation, their contributions to $r_{v\theta}(\mathbf{x})$, namely, $r_{LF}(\mathbf{x})$ and $r_{MF}(\mathbf{x})$ are calculated with $k \in$ LF modes and $k \in$ MF modes respectively.

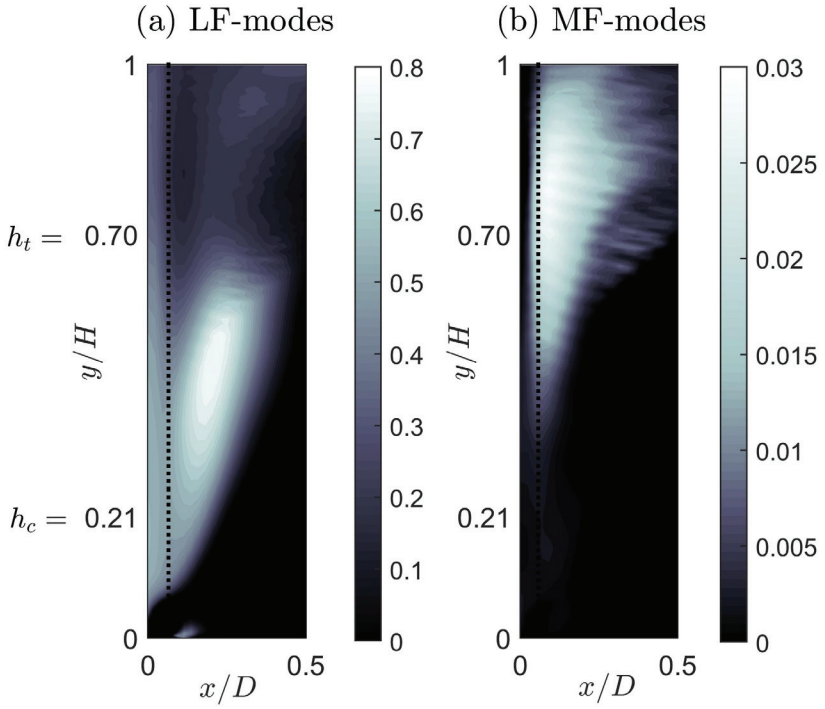

Fig. 4.22 (a) LF-modes contribution to the z-averaged v-θ correlation, $r_{LF,\langle z\rangle}(x)$ (b) MF-modes contribution to the z-averaged v-θ correlation $r_{MF,\langle z\rangle}(x)$. $Ra = 3.5 \times 10^{12}$.

The near-wall v-θ correlation, $r_{v\theta,wall}(y,z)$, at $Ra = 3.5 \times 10^{12}$ is plotted in figure 4.21(a) with the dashed line indicating the height at which the maximum value of this correlation, around 0.98, is reached. In the remainder of the present chapter, this height will be noted in its non-dimensional form h_c. It can be seen that near-wall, $r_{v\theta}(\mathbf{x})$ becomes significant with a value higher than 0.5 starting from $y/H = 0.07$. It reaches its maximum at approximately $h_c = 0.21$ and then starts to decrease. As shown by the contours of $r_{v\theta,\langle z\rangle}(x,y)$ in figure 4.21(b), this behaviour is particularly marked close to the hot wall and a dotted line have been plotted at $x/D = 0.05$ to highlight it. Figure 4.22(a) and figure 4.22(b) respectively plot $r_{LF,\langle z\rangle}(x)$, the z-averaged contribution of the LF-modes to the correlation coefficient and $r_{MF,\langle z\rangle}(x)$, the z-averaged contribution of the MF-modes to the correlation coefficient. Similarly to figure 4.21(b), the dotted line plots $x/D = 0.05$. It appears that the LF-modes contribution is high near the wall whereas it is not the case for the MF-modes. Further away from the hot wall, past approximately $x/D = 0.05$, the LF-modes contribution decreases in the higher part of the channel, whereas the MF-modes contribution keeps increasing from approximately $h_c = 0.21$.

The same behaviour is observed for the two other Rayleigh numbers with the correlation coefficient reaching its maximum at $h_c = 0.18$ for $Ra = 1.5 \times 10^{12}$ and $h_c = 0.23$ for $Ra = 7.5 \times 10^{12}$.

Turbulent Heat Transfer

One of the explanations for the decrease in the near wall v-θ correlation could be the intensification of the turbulent heat transfer (THT) normal to the wall. These transfers are characteristic of hot fluid that travels normal to the heated wall. The THT is defined at each coordinate by $\overline{u'\theta'}(\mathbf{x})$. Semi-log diagrams in figure 4.23 show the streamwise evolution of the near-wall, z-averaged THT $\overline{u'\theta'}_{wall,\langle z\rangle}(y)$ for the three Rayleigh numbers.

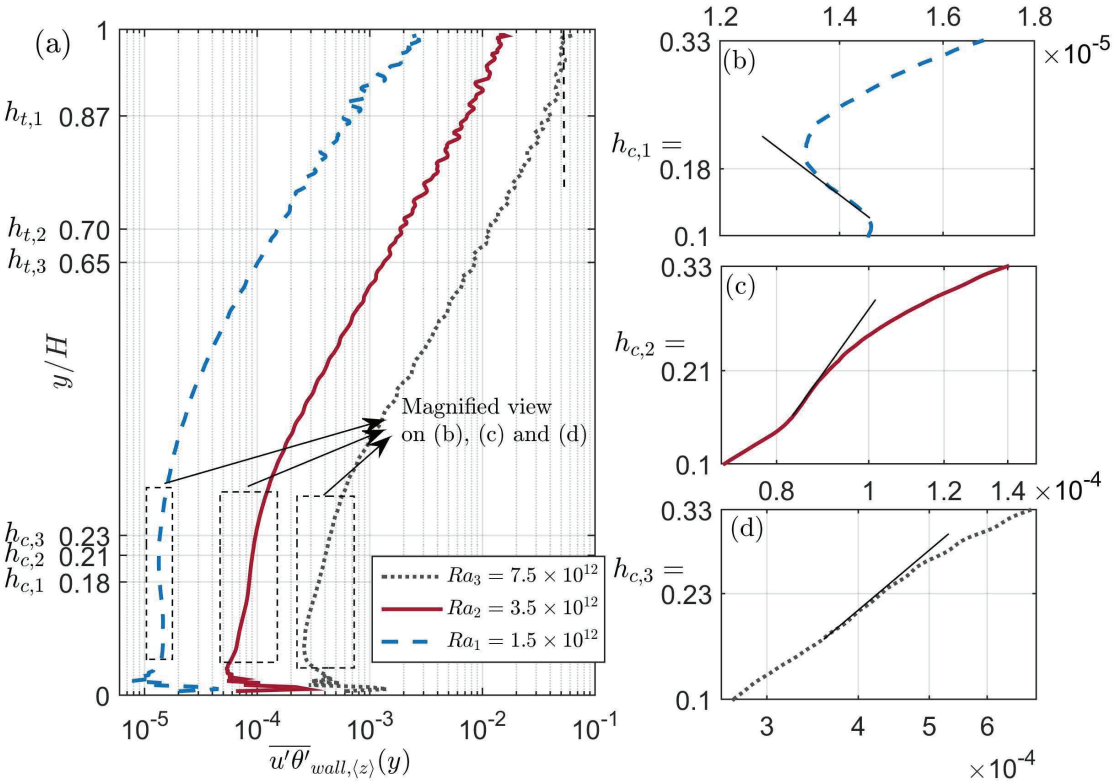

Fig. 4.23 THT $\overline{u'\theta'}_{wall,\langle z\rangle}(y)$, blue dashed line $Ra = 1.5 \times 10^{12}$, plain red line $Ra = 3.5 \times 10^{12}$ and gray dotted line $Ra = 7.5 \times 10^{12}$. Magnified views between $y/H = 0.1$ and $y/H = 0.33$ at (b) $Ra = 1.5 \times 10^{12}$, (b) $Ra = 3.5 \times 10^{12}$ and (d) $Ra = 7.5 \times 10^{12}$. Plain straight line are plotted on the magnified views in order to emphasize changes in the THT growth changes.

As can be seen in figure 4.23(a), directly after the entrance, there is a peak which quickly vanishes. This is due to the entrance effect which has been observed and described in many configurations (see e.g. Katoh et al., 1991; Sanvicente et al., 2013). Then the THT generally increases up to the exit of the channel. At $Ra = 1.5 \times 10^{12}$ the THT drops in the lower part of the channel, which may be due to a slight relaminarisation of the flow as was previously observed (Sanvicente et al., 2013). At $Ra = 3.5 \times 10^{12}$, the THT growth slightly decreases in the higher part of the channel. This behaviour is more pronounced at $Ra = 7.5 \times 10^{12}$ where the THT reaches an asymptotic value in the higher part of the channel (highlighted by a thin dashed line in figure 4.23(a)). The near-wall THT growth does not seem to be altered around the transition height, except for some oscillations. However, it is clear on the magnified views

(figure 4.23(b-d)) that the height at which the maximum near-wall v-θ correlation is reached, h_c, also corresponds to an increase in the THT growth at the wall.

The role of the modes on the THT behaviour is investigated using the decomposition equation (4.5). The contributions of the first LF and MF modes, among the first 40 modes, are respectively calculated as

$$\overline{u'\theta'}_{LF} = \frac{1}{N_t} \sum_{k=LF modes} \mu_k \psi_{u,k} \psi_{\theta,k}, \tag{4.9}$$

and

$$\overline{u'\theta'}_{MF} = \frac{1}{N_t} \sum_{k=MF modes} \mu_k \psi_{u,k} \psi_{\theta,k}, \tag{4.10}$$

and have been plotted on a semi-log diagram in figure 4.24 for the case of $Ra = 3.5 \times 10^{12}$. This figure demonstrates that, unlike the LF-modes, the MF-modes contribute to the near wall THT growth rate change at $h_c = 0.21$.

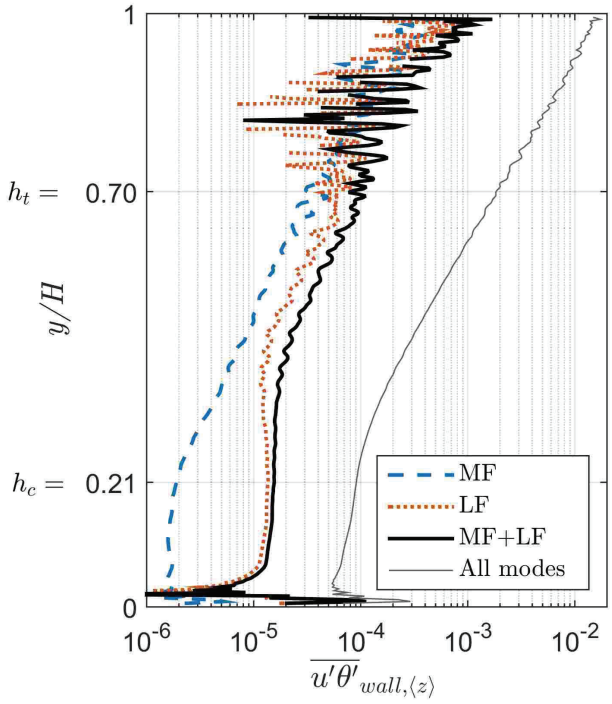

Fig. 4.24 Contribution of the LF and the MF modes to the total near wall THT at $Ra = 3.5 \times 10^{12}$. The dashed blue line plots the contribution of the MF modes $\overline{u'\theta'}_{MF,wall,\langle z\rangle}$, the orange dotted line corresponds to the LF modes $\overline{u'\theta'}_{LF,wall,\langle z\rangle}$, the plain thick black line plots the contribution of the first 40 modes $\overline{u'\theta'}_{wall,\langle z\rangle,LF+MF}$, and the plain thin grey line plots the contribution of all the modes.

It is thus possible to conclude that the decrease of the near wall v-θ correlation starts concomitantly with an increase of the THT growth at the hot wall. These changes are in part due

to the appearance of structures, identified by the MF-modes which play a role in the near-wall THT growth, before the transition height. These structures extract heat normal to the wall, increasing the THT and thus resulting in a poor v-θ correlation near-wall for $x/D \lesssim 0.05$ as observed in figure 4.22(b). Once these coupled velocity and thermal structures are far enough from the wall, they are convected downstream, which results in a growth of the v-θ correlation away from the wall.

These results suggest that despite the relative low energetic content of the MF-modes, they have a notable role in the flow dynamic, especially in the evolution of the coupled velocity and thermal quantities.

4.7.2 Physical description of the transitional flow

As mentioned in the introduction, one of the main purposes of POD-based methods is the identification of coherent structures in turbulent flow. Indeed, flow structures can directly be observed locally by plotting dynamic or thermal instantaneous quantities. However, if these structures have a strong intermittent behaviour, it may be difficult to quantify and analyse their contribution to the flow dynamic over a long period of time. To overcome this limitation, POD-based methods were developed. Reciprocally, the structures obtained by POD sometimes remain hard to interpret when regarding corresponding instantaneous coherent structures that are actually observed in the flow.

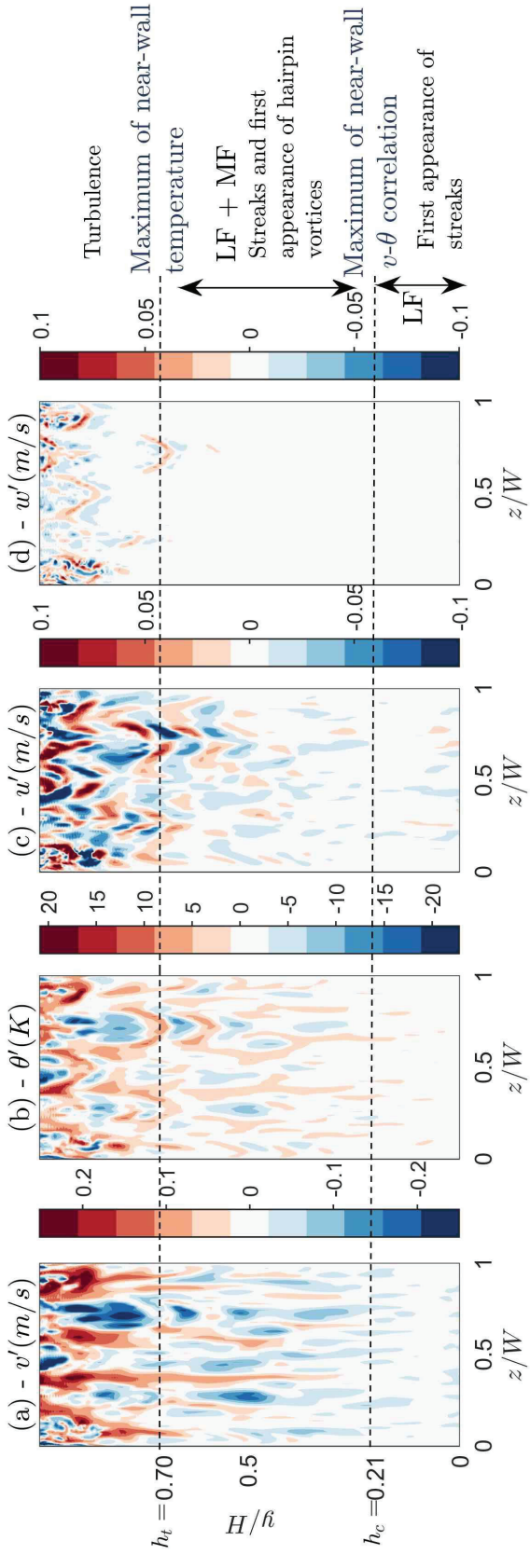

Fig. 4.25 Instantaneous visualisation of the fluctuating velocity component of the flow and indicators of the near wall dynamic and transition stages changes (a)v',(b)θ',(c)w',(d)u'.

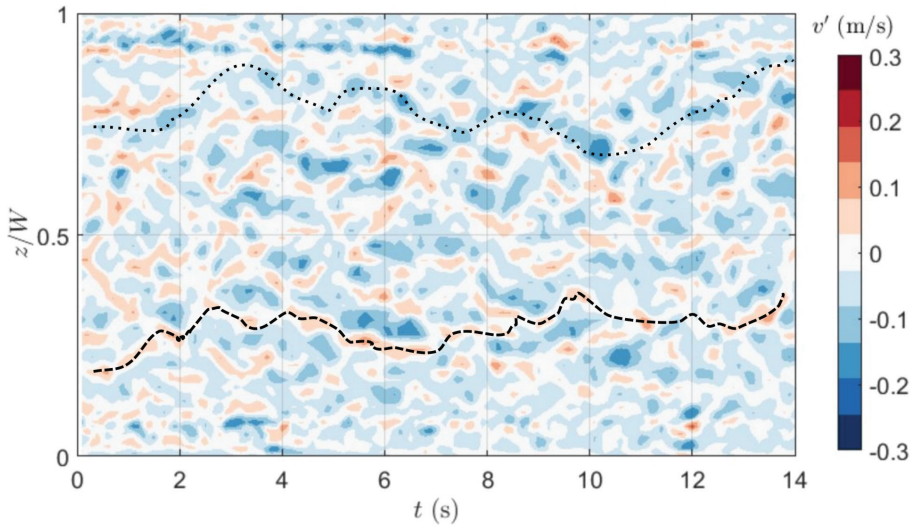

Fig. 4.26 Streamwise instantaneous velocity v' evolution, plotted at y/H=0.5 and x/D=0.1. The dashed line indicate the z-displacement of a high velocity streak and the dotted line, a low velocity streak.

Instantaneous contours of the fluctuating components of the flow at $Ra = 3.5 \times 10^{12}$, were plotted at $x/D = 0.1$ in figure 4.25. It can be noticed that the streamwise velocity streaks are the most common structures appearing in the lower part of the channel. These streaks remains close to the heated wall and moves in the z-direction, sometimes a streak disappear or appear or it degenerates into finer scale structures. A dashed line and a dotted line respectively track the displacement of a high and a low velocity streak.

These streaks are the dominant structures where the low-frequency modes are dominant (see figures 4.5,4.14). Moreover, as is shown by figure 4.25(c-d), the streaks do not present any particular vortical content. Thereby they can be associated with the coherent streaks identified by the LF-modes.

Further up, but still below the transition height, long streamwise streaks are still present, however, some v-shaped structures start to appear. A v-shaped structure can be observed at this particular time around $y/H = 0.6$ and $z/W = 0.7$. This structure has been plotted in figure 4.27 using the Q-criterion (Hunt et al., 1988).

These structures, often referred to as hairpin structures, have been observed and described in the case of natural convection flow for the configurations of an heated vertical plate by Abramov et al. (2014) and for a heated vertical channel by Pallares et al. (2010). They are composed of a head and two elongated legs. Unlike hairpin structures in a forced convection channel flow in which the bulk flow velocity is higher than the near-wall velocity, in natural convection flow, the head of the hairpin structure is convected from a high speed region near wall to a lower speed region in the bulk flow so that the head is lagging behind the legs. As can be seen on the instantaneous wall temperature distribution in figure 4.27, the hairpin structures extract heat

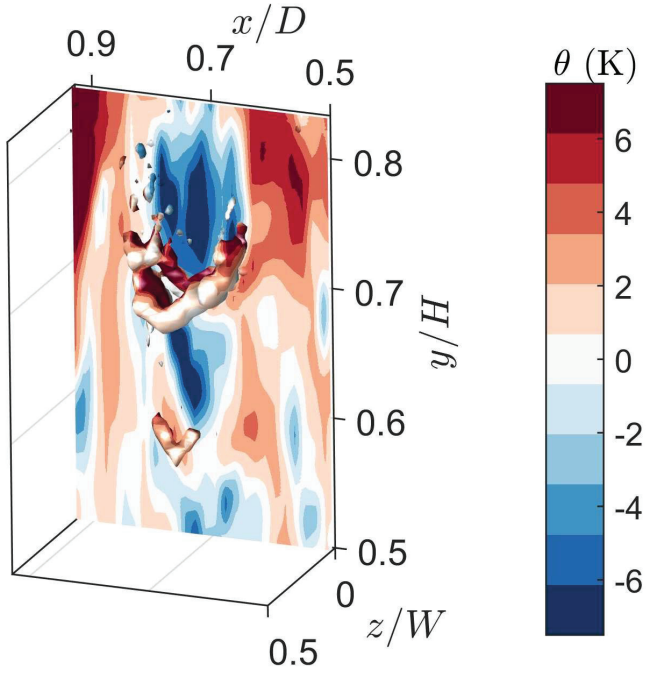

Fig. 4.27 Isocountour of Q coloured by the local temperature θ'. The wall temperature distribution is plotted as well.

from the wall, transporting hot fluid into the bulk flow and leaving a cold region at the wall where they have been ejected from. Thereby they are likely to play a significant role in the THT. Their appearance and amplification is concomitant with the appearance and growth of the medium frequency band observed in figure 4.5. Therefore these structures can be related to the MF modes.

By summarising the different points highlighted above, a description of the development of the near-wall instantaneous structures in the case of a spatially-developing transitional natural convection flow in a vertical one side uniformly heated channel is proposed.

In figure 4.25 three regions are delimited by the height at which the maximum near-wall v-θ correlation and the height at which maximum near-wall temperature are reached. Very low in the channel, three-dimensional elongated streamwise structures develop. These structures are correlated with the temperature distribution as high and low speed streaks correspond respectively to hot and cold streaks. In the meanwhile the correlation between the temperature and the streamwise velocity increases until it reaches a maximum at $h_c = 0.21$. From there on, three-dimensional structures characterised by v-shaped patterns, a strong vortical content, and a MF characteristic band start to appear. As these structures grow and become more frequent downstream they transport hot fluid from the wall into the bulk flow. As a consequence, the near-wall v-θ correlation decreases and the near-wall THT rate increases. During all this early stage of transition, the temperature at the wall keeps increasing up to $h_T = 0.70$. From this point on, the flow transits to turbulence, the spatial coherence of the streak degenerates and the

ejection of structures from the wall becomes more frequent. Note that the coherent velocity structures encountered in this natural convection transition scenario are analogous in many ways to those that appear in the bypass transition scenario (for the cases of zero-pressure gradient boundary layer flows (see e.g. Wu and Moin, 2009; Zaki, 2013) or forced convection (Wu and Moin, 2010)) mentioned in the introduction. Given that in zero-pressure gradient boundary layer flows and for similar inlet disturbance levels as those employed here, the by-pass transition would have been triggered, it can then be supposed that the transition here is a by-pass transition. The example of $Ra = 3.5 \times 10^{12}$ was taken but the same processes occur at $Ra = 1.5 \times 10^{12}$ and $Ra = 7.5 \times 10^{12}$.

4.8 Partial Conclusion on the numerical investigation

A spatially-developing three-dimensional transitional natural convection flow in a vertical uniformly heated channel, was modelled by Large-Eddy-Simulation at three Rayleigh numbers $Ra = 1.5 \times 10^{12}$, $Ra = 3.5 \times 10^{12}$ and $Ra = 7.5 \times 10^{12}$ with an in-house code using the Vreman SGS model. In order to take into account external disturbances inherent to this configuration, a random perturbation has been added to the velocity calculated at the lower boundaries of the computational domain. The results are detailed for the intermediate Rayleigh number $Ra = 3.5 \times 10^{12}$ and extended afterwards to both other Rayleigh numbers.

The flow is first described and characterised by its time-averaged velocities, its time-averaged temperatures and its frequencies near the hot wall. The transition height is defined here as the height at which the maximum temperature is reached immediately near the hot wall. Two marked frequency bands, named Low-Frequency (LF between 0.0125 and 1.2 Hz at $Ra = 3.5 \times 10^{12}$) and Medium-Frequency (MF between 1.2 and 3.5 Hz at $Ra = 3.5 \times 10^{12}$) bands have been highlighted by performing DFT at different locations near the heated wall. In order to link these frequency bands to the development and the behaviour of the natural convection flow, POD and time-domain SPOD have been applied to the velocity and the thermal fields. For that specific configuration, it has been shown that the modes obtained by SPOD can be identified to the LF and MF frequency bands. Named respectively the LF and the MF modes, they have drastically different spatial organisation:

-The LF modes corresponds to streak-like modes and are characterised by streamwise elongated velocity structures alternating in the spanwise direction forming hot-high-velocity and cold-low-velocity streaks.

-The MF-modes are less energetic than the first LF-modes and correspond to v-shaped staggered structures with strong vortical contents. As was shown by phase diagrams, the MF-modes come in pairs, which describes an oscillating process.

The LF and MF modes remains spatially well defined and organised at least up to the transition height where they start to break up.

The contribution of each family of modes to the coupled velocity and thermal fields has then been investigated through the v-θ correlation and $\overline{u'\theta'}$, the turbulent heat transfer normal to the wall (THT). It has been shown that near-wall the maximum v-θ correlation, around 0.98, is reached lower than the transition height. From that point on, the v-θ correlation decreases concomitantly with an increase in the growth of the near wall THT. The modal decomposition allows to conclude that:

-The streaks of the LF modes contribute to the high near-wall v-θ correlation at least up to the transition height.

-The structures identified by the MF-modes extract heat from the wall to the bulk region, which contributes to the decrease of the near-wall v-θ correlation and the increase in the THT growth that is observed near-wall. Once these structures have been ejected from the wall, they convect hot structures downstream which results in an increase of their contribution to the v-θ correlation away from the wall.

Finally, the LF and MF modes were matched with instantaneous coherent structures observed in the instantaneous visualizations. Their contributions to the global transitional process and more specifically to the early stages of this process were analysed. In the lower part of the channel, elongated streamwise streaks associated to a strong near-wall v-θ correlation are amplified until it reaches a maximum. This height could be considered as an indicator of an early stage of transition to turbulence. From there, the v-θ correlation decreases concomitantly with an increase in the growth of the near-wall THT $\overline{u'\theta'}$. These changes are in part driven by v-shapes structures which start to appear, grow and extract heat from the wall to the bulk region. Above the height at which the maximum wall temperature is reached, all the structures start degenerating in finer scales. This attests that the near wall maximum temperature at the heated wall is here a relevant indicator of the location at which the flow becomes turbulent.

4.9 POD analysis on experimental data of a transitional natural convection flow

In what follows POD analysis is performed on experimentally collected velocity fields. In the first subsection 4.9.1, data that had been collected by Sanvicente (2013) were used. In the following subsection, POD is applied to data that were collected during this work by the author himself which covers the whole channel height. The cases presented here corresponds to those of a uniform heating on one side of the wall at two heat flux of $Ra = 3.5 \times 10^{12}$ and $Ra = 7.5 \times 10^{12}$.

4.9.1 Preliminary POD analysis at $Ra = 7.5 \times 10^{12}$

As was mentioned in section 2.5, the field of views of the measurements of Sanvicente (2013) were of size $100 \times 200\,\mathrm{mm}^2$, the sampling frequency of 11 Hz and the sampling length of 8000 snapshots. In this subsection the field of view is located between y/H=[0.45 ; 0.60], the Rayleigh number is $Ra = 7.5 \times 10^{12}$ and the height at which the maximum temperature at the wall was reached, h_T, was reported at around $y/H = 0.65$.

POD analysis

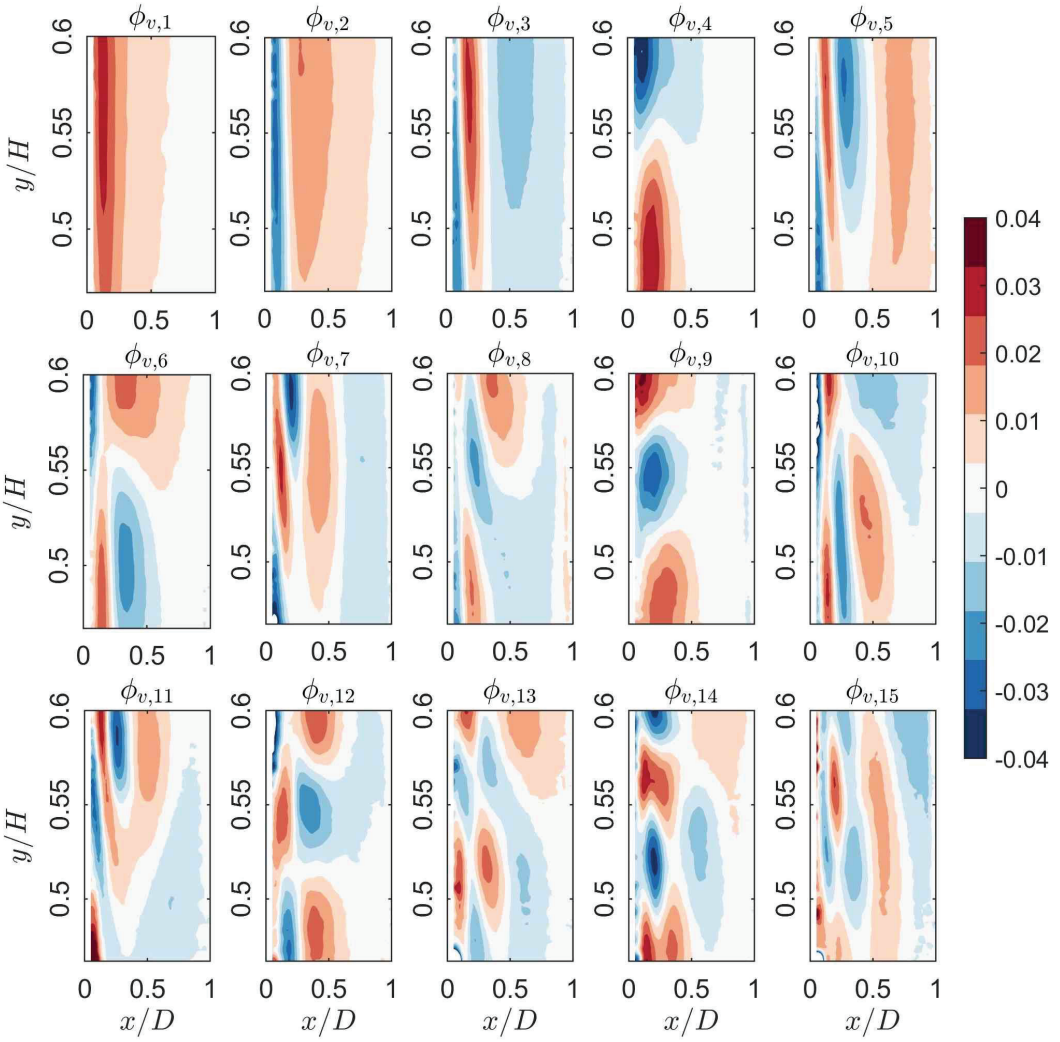

Fig. 4.28 Streamwise components of modes 1 to 18 at y/H=0.54 and $Ra = 7.5 \times 10^{12}$. The red and blue contours respectively represent positive and negative contours of the POD modes.

The streamwise component of the 15 first streamwise POD modes at $Ra = 7.5 \times 10^{12}$ are plotted in figure 4.28 at y/H=0.54.

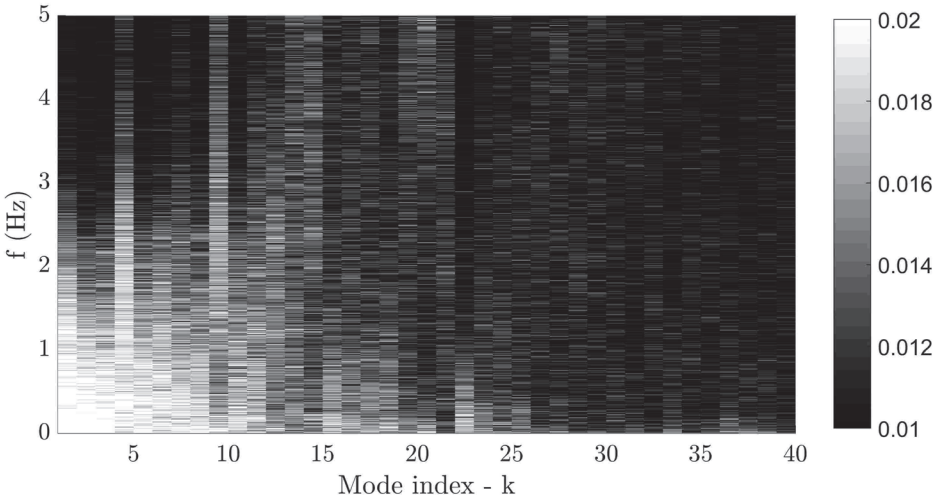

Fig. 4.29 DFT of the scaled temporal coefficients of the first 50 modes $\alpha_k/\sqrt{\lambda_k}$ at $Ra = 7.5 \times 10^{12}$. The color scale indicates the amplitude of the DFT.

The three first modes, do not exhibit major streamwise variations. Moreover they mainly represent structures that are located close to the heated wall. Mode 4 is the first mode with a phase changing in the streamwise direction. Then the structures identified by the modes have more complex shapes. However some of these modes have similar spatial organisations. It is the case of modes 4, 9 and 14 which represent a phase changing in the streamwise directions with different streamwise wavelength. Modes 5, and 12 may represents z-vortical structures with respectively 0, 1 and 2 phase changes in the streamwise direction. Modes 5 and 10 could be seen as layers of counter rotative vortical structures. Another interesting features is the inclination of the structures in some of the modes, such as 5, 7, 8, 11, which angles with the heated wall ranges between 6 ° and 10 °. The inclination of the structures have often been reported as a characteristic of near-wall turbulent structures (see *e.g.* Jiménez (2018) for forced convection and Pallares et al. (2010) or Abramov et al. (2014) for natural convection.

The DFT of the temporal coefficients of the first 40 modes have been plotted in figure 4.29. This figure provides a quick overview of the characteristic frequencies associated with each modes. Apart from mode 4 which characteristic frequencies ranges from 0 to approximately 2.2 Hz, the most energetic modes up to mode 8 have low characteristic frequencies, below 1 Hz. From mode 8 the frequency signals of the modes are richer and more spread.

For a better visualization of the frequency content of the first 15 modes, their distribution have been plotted in figure 4.30. As was noted previously a low characteristic frequency band is present in almost all the modes displayed. Note that this low frequency band can, in some cases such as modes 3 or 5, be split in two, the lowest band stopping at 0.2 Hz and the second ranging between 0.25 Hz and 0.5 Hz approximately. However none of these frequency clearly dominates. Higher frequency band, in the range of [0.8 Hz;3 Hz] can be clearly observed in the temporal coefficient of mode 9, 11, or 12.

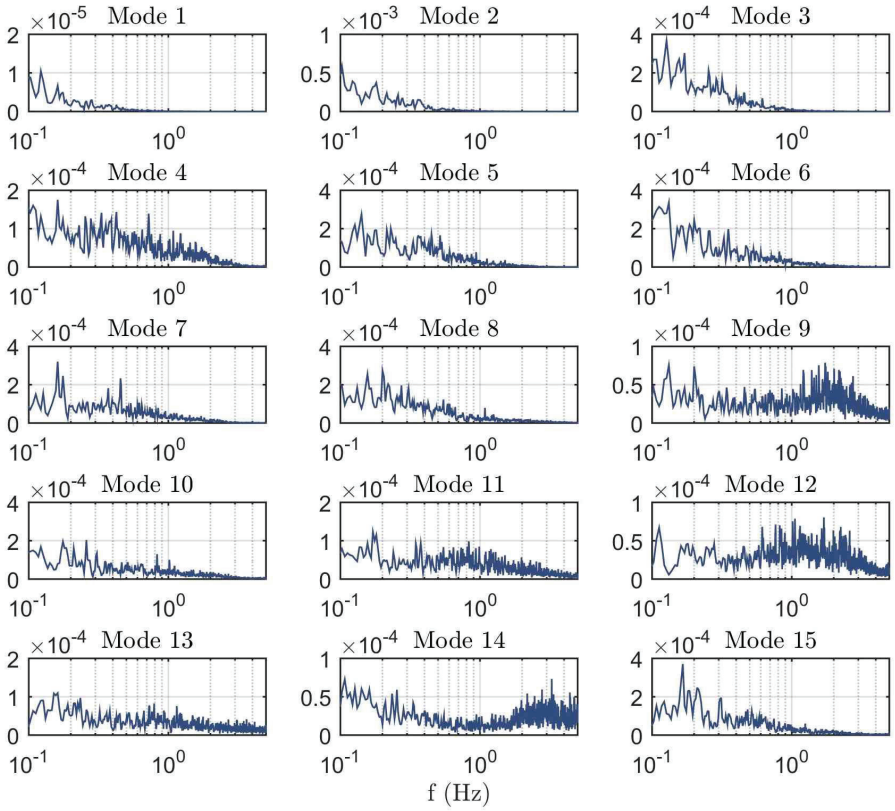

Fig. 4.30 DFT of the scaled temporal coefficients $\alpha_k/\sqrt{\lambda_k}$ of the 15 first experimental POD modes $Ra = 7.5 \times 10^{12}$

In the light of the POD analysis that was conducted on numerical data, these low-frequency and mid-frequency bands observed in the experimental modes directly echo with those associated with the numerical modes (respectively 0.0125-1.7 Hz and 1.7-4 Hz for the LF and MF bands at this Rayleigh number). Furthermore the experimental modes 1 2 3 5 6 have a low frequency band and are mainly streamwise oriented. These modes could thus corresponds to the LF-modes numerically obtained and described in section 4.6.1. Similarly the mid-frequency experimental modes such as modes 9 and 14 corresponds to structures with a spanwise phase changing which could be affiliated to the MF-modes numerically obtained and described in section 4.6.1.

Intermittent experimental flow

In this section, a physical interpretation of the role of the mode is proposed. By simple observations the flow, two representative behaviours can be clearly distinguished, a weakly disturbed flow and a strongly disturbed flow. The weakly disturbed flow is represented by instantaneous visualizations of the fluctuating velocities in figure 4.31. In that case the can be seen as a pseudo-steady flow with some weak unsteadiness which remain spatially well-defined, located near the heated wall and which are almost uniform in the streamwise direction. The flow depicted in figure 4.32 corresponds to the strongly disturbed flow which has a more complex

behaviour and for which numerous and diverse structures are observed. Such a distinction can be criticized because it is not based on any objective criteria, but for the great majority of the cases, the distinction between these two regimes is clear.

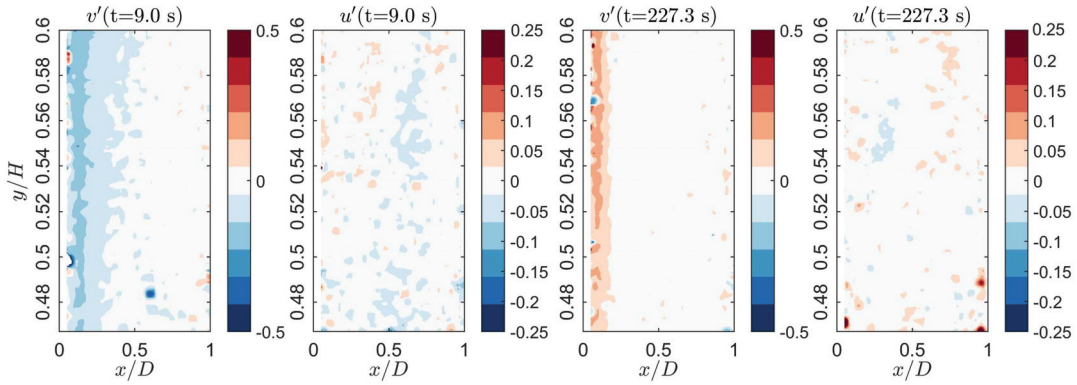

Fig. 4.31 Instantaneous visualisations of the streamwise and wall-normal fluctuating velocity components of the flow obtained by PIV at y/H=0.54, $Ra = 7.5 \times 10^{12}$, weakly disturbed flow.

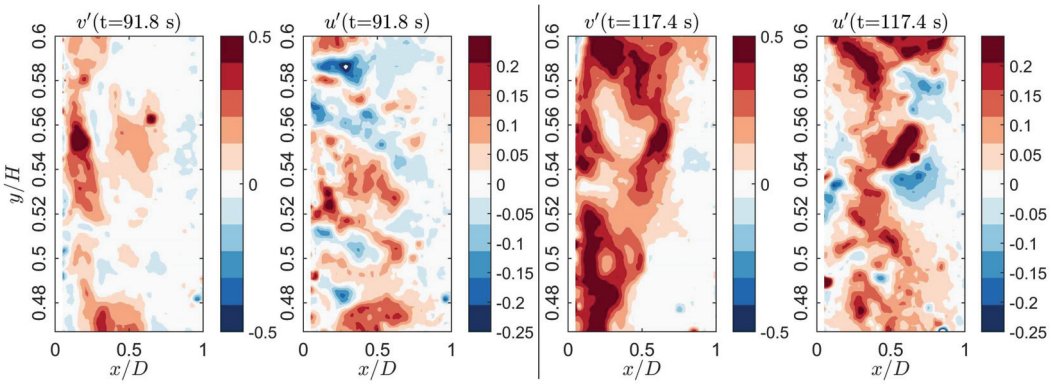

Fig. 4.32 Instantaneous visualisations of the streamwise and wall-normal fluctuating velocity components of the flow obtained by PIV at y/H=0.54, $Ra = 7.5 \times 10^{12}$, strongly disturbed flow.

The weakly disturbed flow is composed of a velocity field, similar to a time-averaged flow field, (Mode 1) which amplitudes is modulated in time. Moreover this flow is subjected to slight modulations of the streamwise velocity in the wall-normal direction.

The absolute value of the scaled temporal coefficients of modes 1 to 40 have been plotted in figure 4.33. The time spawned represent the period from 140 s to 180 s. This period was chosen because both a weakly disturbed and a strongly disturbed flow were successively observed. The amplitude of the scaled temporal coefficients is given by the color scale. The time-averaged field was removed and therefore, the temporal coefficients represent fluctuating components and have a zero time-averaged value.

The temporal coefficients of the first three modes are sometimes synchronised. Moreover their variations are rather slow with characteristic times around the second. The temporal

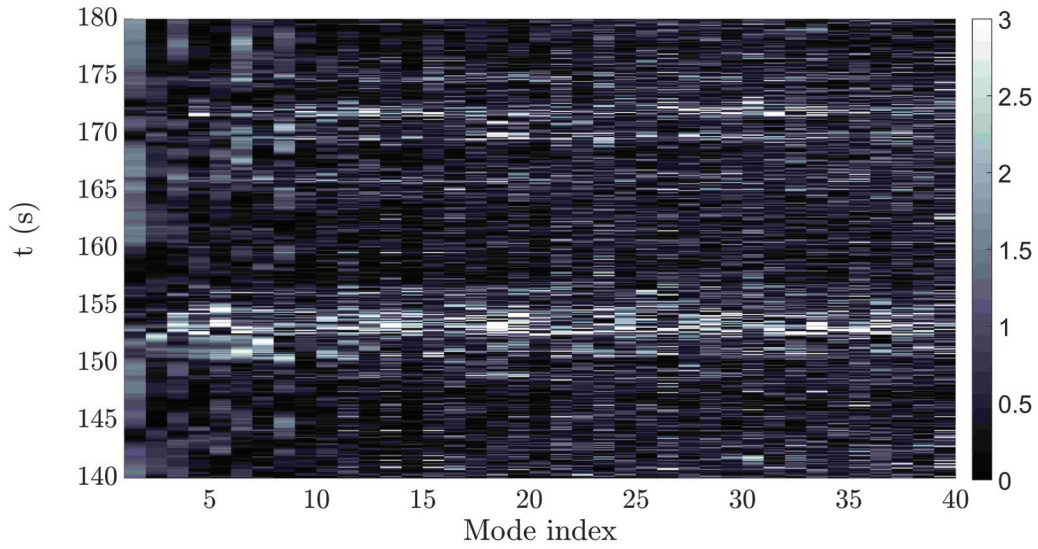

Fig. 4.33 Scaled temporal coefficients of the first 40 modes, $\alpha_k/\sqrt{\lambda_k}$

coefficients of the higher order modes rather have the opposite behaviour. Indeed these less energetic modes are solicited in a more impulsive way and over short periods. This figure also allow to observe the two major behaviours of the flow defined above. The weakly disturbed flow occurred in the range t=[140 s;150 s], t=[155 s;162 s], and t=[175 s;180 s], the activity of the modes is low during these periods. During the strongly disturbed periods, the modes are highly solicited such as during the periods t=[150 s;155 s] and around t=165 s, and t=171 s.

The weakly disturbed flow can be obtained in great part by adding mode 2, mode 3 and mode 4 to mode 1, indeed these modes have a quasi-uniform distribution across the field of view in the streamwise direction which is not the case of the other modes. This can be further confirmed given the weak temporal solicitation of the other modes during the calm period. However modes 1 to 4 are not able to represent the flow when it is strongly disturbed, and in that case many more modes are therefore required.

4.9.2 Complete representation of the POD decomposition of the flow at $Ra = 3.5 \times 10^{12}$

In this section a reconstitution of the POD modes at $Ra = 3.5 \times 10^{12}$ is presented on the entire channel height. PIV measurements were carried out for all the 4 windows (w1, w2, w3 and w4, see figure 3.5) and POD decomposition is performed at each window. In figures 4.36 and 4.37 the 20^{th} first experimental modes obtained at each window have been plotted over the whole height of the channel.

The full-mode n is constituted of the n^{th} partial-modes obtained at each windows, w1, w2, w3 and w4. For this reconstitution, repeatability due to the external thermal stratification

has been minimized[1]. In the present experimental case, $h_T \simeq 0.47$ is lower than what was observed by Sanvicente (2013) for a similar heat input. This difference is likely to the change in the external thermal stratification and is addressed in details in the next chapter. One of the consequence is that in these experimental results, the higher half (w3 and w4) of the channel is turbulent whereas in the numerical results presented above, only the higher quarter of the channel was turbulent at this Rayleigh number.

There are no connections between the partial-modes which can be observed at the junction of each window at y/H=0.25, y/H=0.50, y/H=0.75. The modes that would be obtained if the PIV measurements were performed on the entire channel at once (and not split in four windows) would be expected to be different from the reconstitution obtained here. However in some cases, modes obtained at two separate windows are very well connected. Such examples are, w1 and w2 for modes 1, 2, 3, 7, 8, w2 and w3 for modes 3,4 and 6 or w3 and w4 for mode 4, 6, 7, 11, 12, 13.

Below h_T, long streamwise structures are observed near wall such as in mode 1, mode 2 or in w1 of mode 3 or mode 13. These structures may corresponds to the streaks observed numerically. Indeed, a two-dimensional projection of a streak in the mid-section would yield to a similar representation. Some modes such as mode 6 or mode 14 in w2 may be representative of the MF-modes numerically identified as they represent structures slightly tilted which alternate in the streamwise direction. In general the modes obtained above h_T exhibit smaller and more complex structures.

Because the flow is spatially developing, the modes observed at w1, w2 and w3 are different. However, the modes obtained at w3 and w4 are sometimes very similar such as for the modes 1, 2, 3, 4, 7, 13, 14 or 15 at w3 and w4 for examples. This suggests that similar structures are observed in these windows and thus that the flow in the higher part of the channel start to be spatially developed.

The energy content of the first 20 modes are displayed in figures 4.34 and 4.35. In figure 4.34 the energy of each mode obtained at each window is scaled by the total fluctuating energy of w4, E_{w4} which is respectively 1.1, 2.9, 3.3 times higher than E_{w3}, E_{w2} and E_{w1}. It appears that the energy distribution is somehow similar for the modes obtained below the transition, at w1 and w2 and above the transition, at w3 and w4. The total fluctuating energy above the transition is 3 times higher than below the transition. In figure 4.35 the energy of each mode is scaled by the total fluctuating energy of the corresponding window E_{w_j}, $j = 1,2,3$ and 4. The first modes

[1] In order to minimize the differences that would result from changes in the external thermal gradients, the records at w2, w3, w4 were obtained the same day. As was mentioned in section 3.2, the external thermal stratification change during one measurement (15 min approximately) was too low to be measured. However, much more time was needed in order to displace the camera from one window to the other and to operate to all the calibration settings before being able to measure again. During these periods, the external thermal stratification increased from $\delta_T = 1.38$ K/m to $\delta_T = 1.39$ K/m. The wall temperature distribution remained almost identical, with local differences below 3%, and h_T remained at the same level, around y/H=0.48. The measurements at w1 were carried out the following day. The thermal stratification was of $\delta_T = 1.40$ K/m and the temperature at the wall were very close to those observed the day before, the transition height was moved at h_T=0.47.

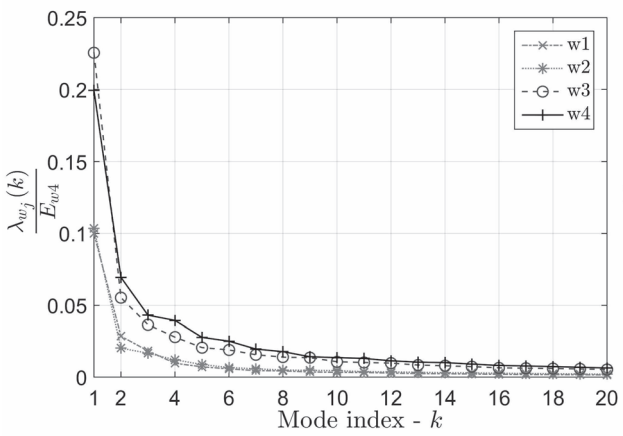

Fig. 4.34 Absolute energy distribution of the first 20 POD modes scaled by E_{w4}.

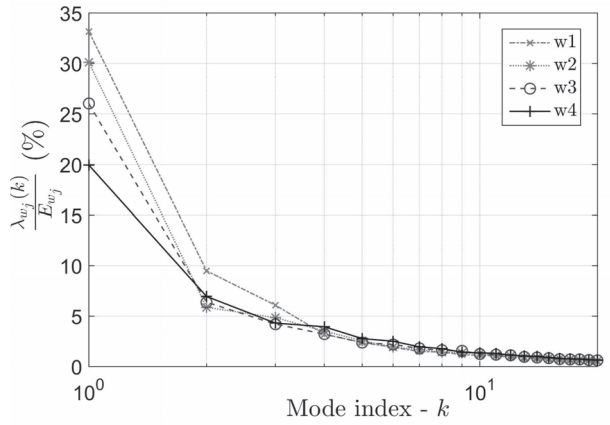

Fig. 4.35 Relative energy distribution of the first 20 POD modes (%)

is always highly energetic and represents between 20 to 35% of the total relative fluctuating energy. It is more likely for this mode to represent some changes in the mean flow rather than actual highly energetic coherent structures. Then the convergence is relatively slow and the 20 first modes respectively represents 69, 63, 59 and 56% of the total fluctuating energy at w1, w2, w3 and w4.

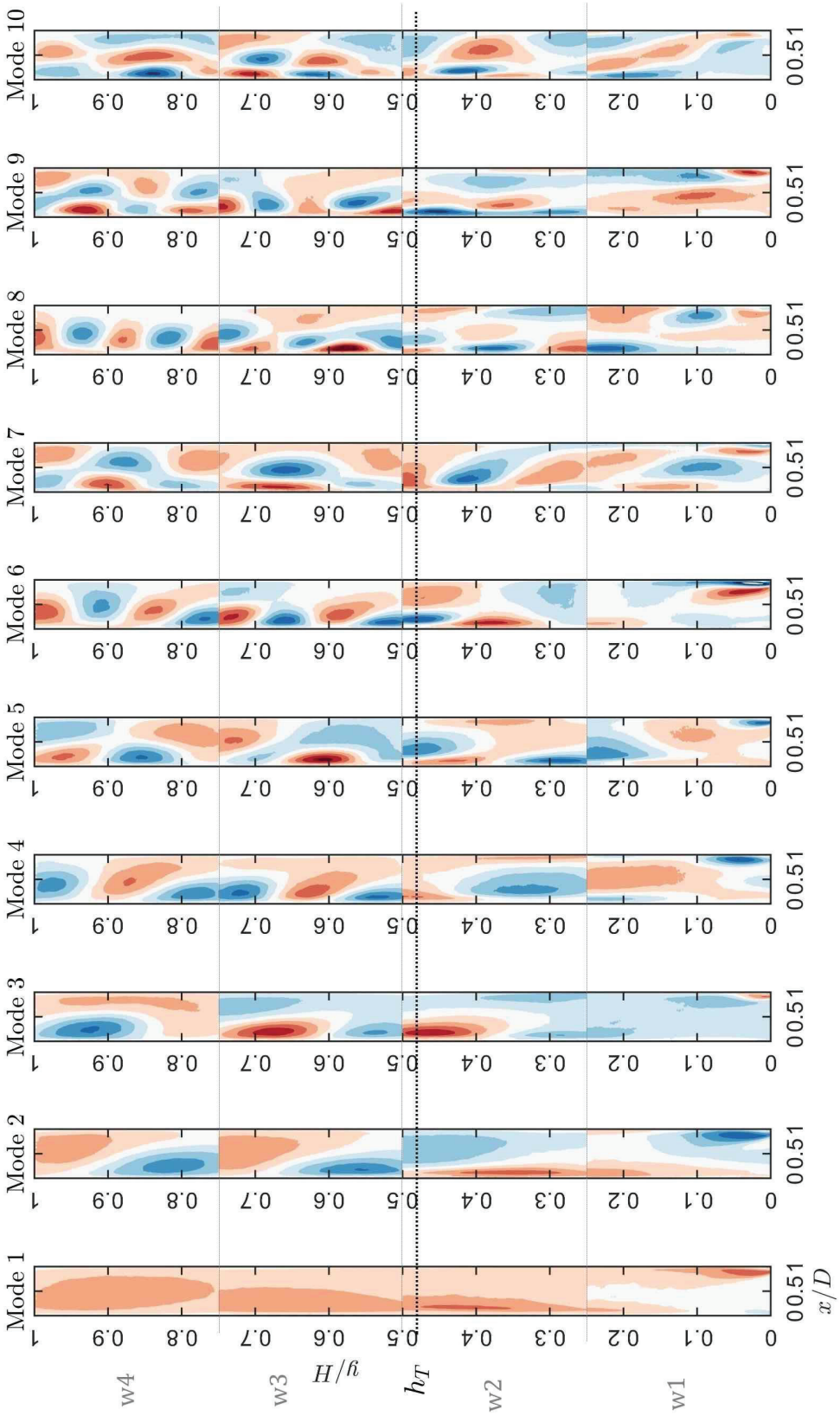

Fig. 4.36 Experimental reconstitution of the POD Modes 1 to 10 for $Ra = 3.5 \times 10^{12}$.

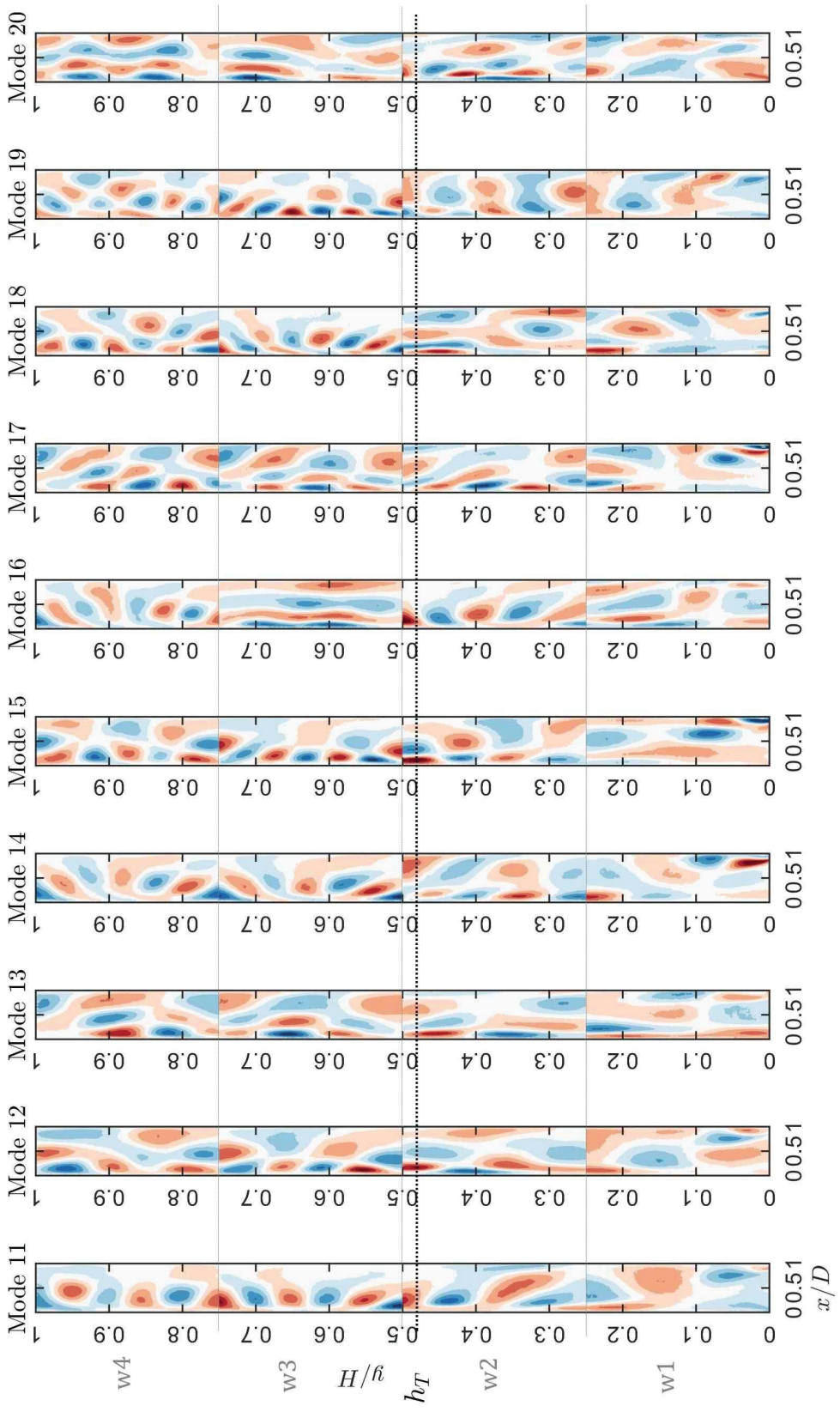

Fig. 4.37 Experimental reconstitution of the POD Modes 11 to 20 for $Ra = 3.5 \times 10^{12}$.

4.9.3 Partial conclusion on the experimental investigation

POD analysis have been applied to velocity measurements obtained by PIV. Experimentally two pronounced flow behaviour were observed, a calm flow for which only few modes can capture the dynamic, and strongly disturbed flow, for which much more modes are required. In a second time a complete reconstitution of POD modes on the whole channel height provides some insight on the flow development and the structures encountered at different stages of the transition spatially developing flow. It appears that the total fluctuating kinetic energy above the transition height h_T is up to 3 times higher than below it.

Finally two particular types of modes, namely long streamwise oriented structures with a low-frequency band and streamwise alternating structures with medium frequency band are also observed experimentally and may be related to the LF and MF modes observed numerically. A proper scaling analysis would be necessary to confirm this last point.

The structures observed experimentally are expected to be more complex than those observed numerically because the inlet and outlet conditions are more complex as well. Indeed, additionally to the structures inherent to the channel flow (which may corresponds to the numerically observed structures described above), there is also the presence of the large structures in the room that are entrained inside the channel and that strongly impact the flow, as was discussed in appendix C, figure B.1.

Chapter 5

Indicators and processes of transition in a vertical channel flow under external thermal stratification

As was mentioned in the previous chapters, sections 3.2.5 and This chapter presents an experimental and numerical investigation of a spatially developing transitional flow in a vertical channel with one side uniformly heated, subjected to random velocity fluctuations at the inlet and to various external thermal stratifications. Transition indicators are first defined and the transitional spatial flow development is then presented. Experimental and numerical comparisons are then carried out and explanation of the transition mechanism are then proposed. Finally the numerical model is used to study negative stratifications of temperature.

Contents

5.1 Introduction

The objective of the present chapter is to study the effects of the external thermal stratification on a three-dimensional spatially-developing transitional natural convective flows induced by a uniform heat flux on one side in a vertical air channel of finite height. Experimental velocities and temperatures are obtained respectively using PIV and thermocouples. The FLUENT solver in which the Vreman SGS model have been implemented as user defined function was used to simulate the flow (see section 3.3.3). The generation of an artificial stochastic velocity fluctuation at the inlet controls the triggering of the transition to turbulence within the channel.

The two cases under investigation are the cases of 100 W and 230 W because a great amount of experimental data were collected for these heat inputs. These cases corresponds respectively to the Rayleigh numbers of $Ra = 1.5 \times 10^{12}$ and $Ra = 3.5 \times 10^{12}$ and to the net injected heat flux of $q = 90$ W/m^2 and $q = 208$ W/m^2. The case of $Ra = 7.5 \times 10^{12}$ was not investigated given that very limited experimental data were collected at that Rayleigh number.

First of all the numerical results are used to define transition indicators and a new indicator is proposed. Then the streamwise evolution of the time-averaged velocities and temperature are described. The effect of the external thermal stratification on the flow behaviour is then studied

using both the experimental and numerical results. The numerical model is then used to study the effect of weak and negative stratifications on the flow, that is the temperature gradient is negative upwards, are difficult to obtain in a non-controlled experimental room, but are common within the first few dozen of metres of the atmosphere.

5.2 Boundary conditions and grid validation

In this study, the impact of different external thermal stratifications on the flow behaviour is studied. As a consequence a lot of different cases needed to be simulated and therefore the calculations needed to be run in parallel. However, as mentioned in section 3.3.3 the in-house numerical code that was used in the previous chapter could only run on one node and as a result would have been to slow. Thus another solver, for which parallel computation is possible have been used. For the present study, a FLUENT solver have been used. The method, namely LES method with the Vreman SGS model remains the same but the mesh, the boundary conditions and the numerical methods were changed. As a consequence some preliminary tests were made in order to validate grid independence of the results.

The computational domain is the same as was used before (figure 3.8). However a new parameter, the horizontal size of the extended domain A is introduced.

5.2.1 Boundary conditions

Linear thermal and pressure stratification

Similarly to what was observed experimentally (section 3.2.4), the ambient temperature, far-field, is considered to have a linear distribution so that at any height in the surrounding ambient atmosphere,

$$T_a(y) = T_0 + (y - y_0)\,\delta_T, \tag{5.1}$$

The subscript a refers to a quantity taken in the atmosphere far-field. δ_T (K/m) is the temperature lapse rate in the ambient room. As mentioned in 3.2.4, δ_T is positive if the temperature increases upwards and negative if it decreases. The ambient atmosphere is considered as a still, single phase ideal gas so that the ideal gas law and the hydrodynamic stability law can be applied viz,

$$p_a = \rho R_{air} T_a, \tag{5.2}$$

$$\frac{dp_a}{dy} = -\rho g. \tag{5.3}$$

By substituting equation (5.1) in equation (5.2) and then substituting ρ in equation (5.3) and integrating, it follows that the hydrostatic pressure follows the exponential law

$$p_a(y) = p_0 \left(1 + \frac{\delta_T}{T_0}(y - y_0)\right)^{\left(\frac{-g}{R_{air}\delta_T}\right)}. \tag{5.4}$$

In the CFD-code these temperature and pressure distributions are applied at the open boundaries of the computational domain using a user-defined function. The stratified temperature equation (5.1) is the temperature of the fluid entering the open boundaries.

Inlet noise

As mentioned earlier, the introduction of a disturbance of the velocity field at the inlet is necessary in numerical works in order to obtain at least qualitative agreement between numerical and experimental measurements (Fedorov and Viskanta, 1997; Lau et al., 2012b; Tkachenko et al., 2016). To that end, the environmental noise in the room is modelled here as a disturbance of the velocity components generated at the inlet by the Spectral Synthesizer method, based on the work of Smirnov et al. (2001) and implemented in FLUENT. This method generates a random spatial and temporal coherent noise at the inlet and is one of the most commonly-used method to synthesize disturbed inlet conditions for LES simulations (Tabor and Baba-Ahmadi, 2010). As can be seen in figure 5.1 this method provides a fair representation of the inlet turbulent intensity experimentally recorded.

Radiation between the walls

The numerical model used here do not consider the radiation with the air and the surfaces. However as mentioned in the introduction, section 2.3.5, in order to achieve better agreements between numerical and experimental results, radiation must be considered. As was showed in the numerical study of Tkachenko (2018), the effect of the radiation between the walls is significantly higher than these of the radiation with the air as a participative media, even considering the case of an air saturated with water-vapour. Moreover, experimentally, no correlation between the relative humidity in the room and the temperature/velocities in the channel could be observed (see section 3.2.5). For these reasons only the radiations between the surfaces was considered and the air was as non-participative.

Using the radiosity model and considering a non-participative media, Sanvicente (2013), evaluated, that for this configuration approximately 10% of the total net heat injected in the channel is transmitted by radiation to the wall facing the heated wall. As a consequence, in the numerical model the total heat flux injected in the channel follows the same distribution, namely, 90% on the heated wall and 10% on the facing wall. This approach constitute the simplest approximation to take into account the weak heating by radiation received from the non actively heated plate.

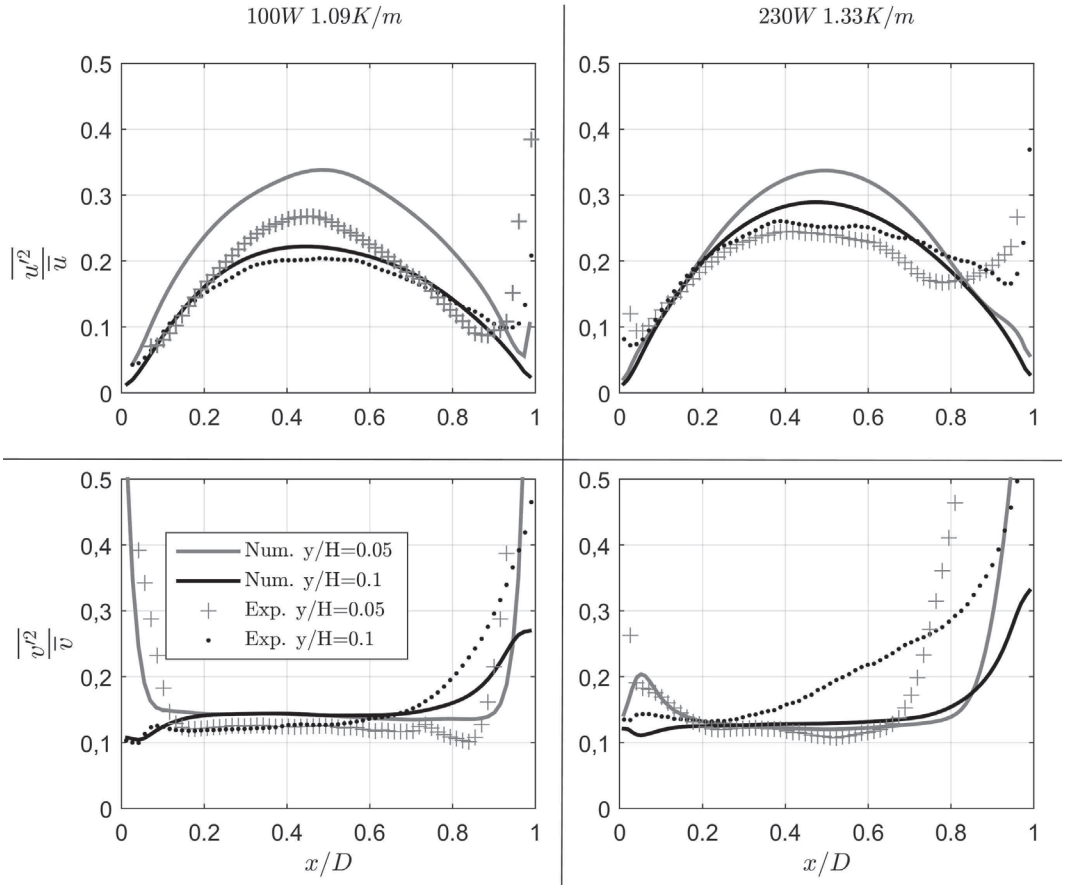

Fig. 5.1 Experimental and numerical streamwise and wall-normal turbulent intensities in the inlet region of the channel. Solid lines, numerical data, dotted lines, experimental data.

In the experimental configuration, only one wall is directly heated by Joule effect, and the facing wall is heated "passively" by radiation; therefore these walls are referred to as the heated wall and the unheated wall. The same nomenclature is adopted for the walls in the numerical model.

5.2.2 Mesh and domain size studies

The flow is initialized with zero initial velocity and a uniform temperature of T_0 within the channel. From the first few iterations, complex structures are seen and approximately 20 to 30 s are needed in order to obtain an established ascendant flow. From there on, the 10 s-moving averaged of the mass flow rate have maximum differences of about 30%. Averaging for the flow statistics was only commenced after 100 s had elapsed.

Depending on the external thermal stratification, the duration of the sampling period, in order to obtain statistical convergence of the mean values below 1%, was different. For no stratification cases *i.e.* $\delta_T = 0$ K/m, 50 s usually provides excellent statistical convergence.

However, as the thermal stratification increases, up to 100 s may be necessary to achieve the same convergence rate.

The mesh convergence was conducted at $Ra = 3.5 \times 10^{12}$ and with an external thermal gradient of 0.72 K/m which represents one of the intermediate thermal stratification experimentally observed. Four different meshes were used, a very coarse mesh (VCM) a coarse mesh (CM) an intermediate mesh (IM) and a fine mesh (FM). Details of the meshes can be found in table 5.1.

Table 5.1 Mesh characteristics within the channel itself

Name	Elements in $x \times y \times z$	Number of elements
VCM	55×135×65	500K
CM	60×165×80	800K
IM	75×240×85	1500K
FM	90×300×85	2300K

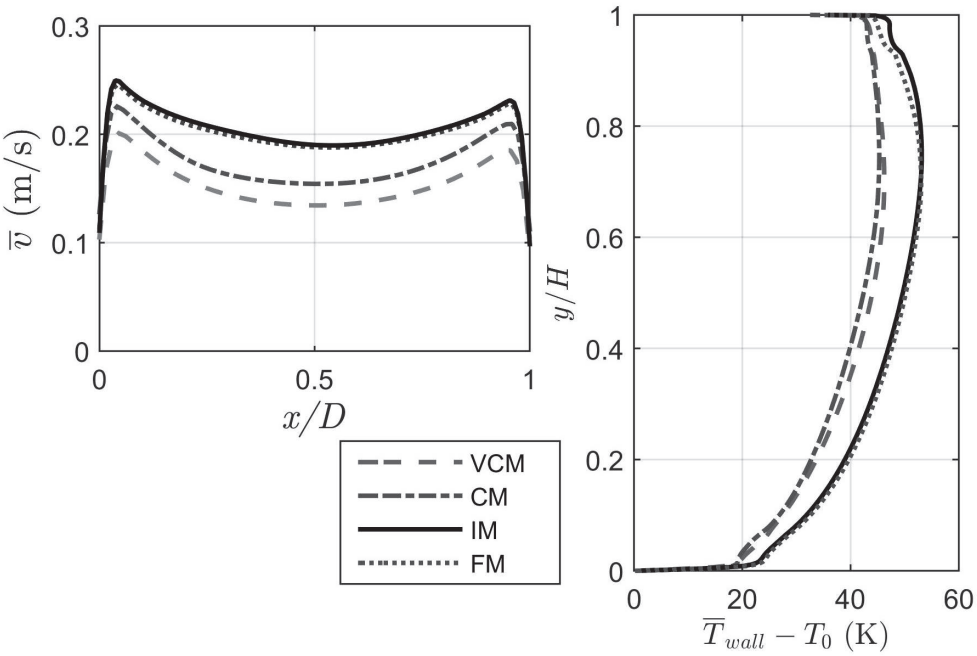

Fig. 5.2 Time-averaged velocity and wall-temperature distributions as a function of the mesh size

As is shown in figure 5.2, there are very small differences in the time-averaged velocity profiles between the IM and the FM; being differences below 1%. The temperature profiles at the wall are also very similar for these two meshes with differences below 1% except at the very top of the channel where it reaches 4%. Multiplying the number of elements by 1.8 has almost no effect on the time averaged quantities. Therefore the IM was considered satisfactory for the present study.

Now that the mesh has been validated, the influence of the inlet and outlet extensions sizes is briefly discussed. The sizes of the extended domains are progressively increased by modifying

the size of A on both sides of the channel, as is shown in figure 5.3. Four sizes were studied, D_0, the initial extended domain corresponds to $A = 7cm$, then D_1, D_2 and D_3 respectively corresponds to A values of 14, 21 and 28 cm. The mesh remains unchanged in the channel and in the initial extended domain D_0 and additional cells are added in the extensions.

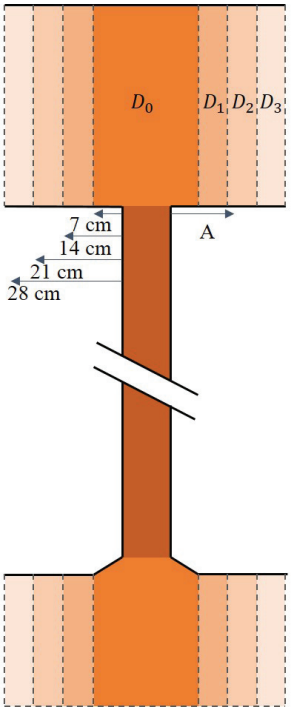

Fig. 5.3 Representation of the different computational domains for various sizes of A. Thick black line represents walls and dashed lines represents open boundaries.

As may be seen in figure 5.4, the size of the extended domain have an impact on the mass flow rate. However, the changes in the mass flow rate remains below 4% between D_1 and D_2 at $Ra = 1.5 \times 10^{12}$ and is almost unchanged between D_2 and D_3 at $Ra = 3.5 \times 10^{12}$ case. This is the reason for choosing domain D_1 for $Ra = 1.5 \times 10^{12}$ and D_2 for $Ra = 3.5 \times 10^{12}$.

5.3 Indicators of transition and time averaged quantities

As previously mentioned, the temperatures will be expressed as the temperature rise above the reference temperature T_0 and noted θ.

$$\theta = T - T_0 \tag{5.5}$$

For each case, the reference temperature is defined as the temperature at the height of the inlet level, far from the channel. When needed the air properties are taken at T_0. In the numerical simulations $T_0 = 293.15$ K.

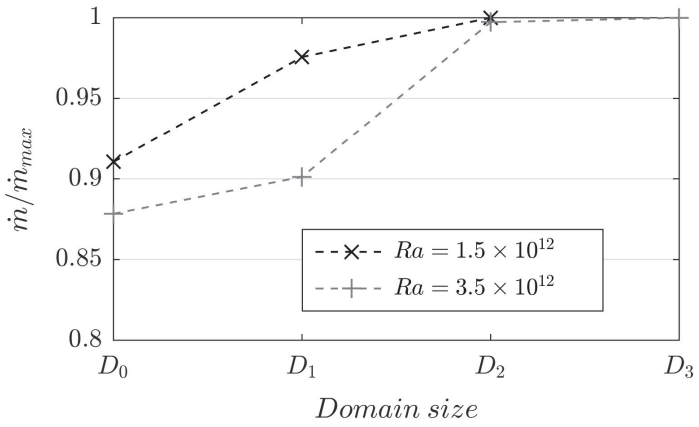

Fig. 5.4 Influence of the extended domain size on the mass flow rate variation.

As mentioned in section 3.2.4 the external thermal gradients that occurred naturally in the laboratory were not controlled. They ranged from 0.49 K/m to 1.14 K/m and 0.31 K/m to 1.40 K/m at $Ra = 1.5 \times 10^{12}$ and $Ra = 3.5 \times 10^{12}$ respectively. The same range of δ_T was studied numerically.

In this section, numerical velocity and thermal fields are studied in order to better understand the transitional process in a channel flow configuration within an thermally stratified atmosphere. To that end, the numerical model corresponding to the case $Ra = 1.5 \times 10^{12}$, $\delta_T = 1.09$ K/m is used. It corresponds to one of the highest stratification reached at $Ra = 1.5 \times 10^{12}$ in the experimental tests.

Note that the analysis is focused on the velocity and temperature components in the mid-section z/W=0.5. This choice was made given that present experimental data as is the great majority of the data in the literature are discussed in this section.

5.3.1 Definition of transition indicators

As mentioned in the previous chapter, in studies dedicated to natural convection in uniformly heated vertical channels, it is common to use the first local maximum of temperature at the heated-wall in order to localize the transition region. One of the reason was the ease of obtaining measurements of the temperature distribution on the heated wall compared with velocity measurements in the fluid. However, in the literature, other indicators have been used. This is the case of Daverat et al. (2017), who, in a uniformly ans symmetrically heated water channel, defined the transition height as the streamwise location at which the difference between the peak velocity and the bulk flow velocity starts decreasing. Given that the transitional region is spread over a distance, it is possible for different local indicators to take place within it.

To assess the relevance of different indicators of transition, the streamwise evolution of different time-averaged velocity and thermal quantities, have been plotted in figure 5.5 for

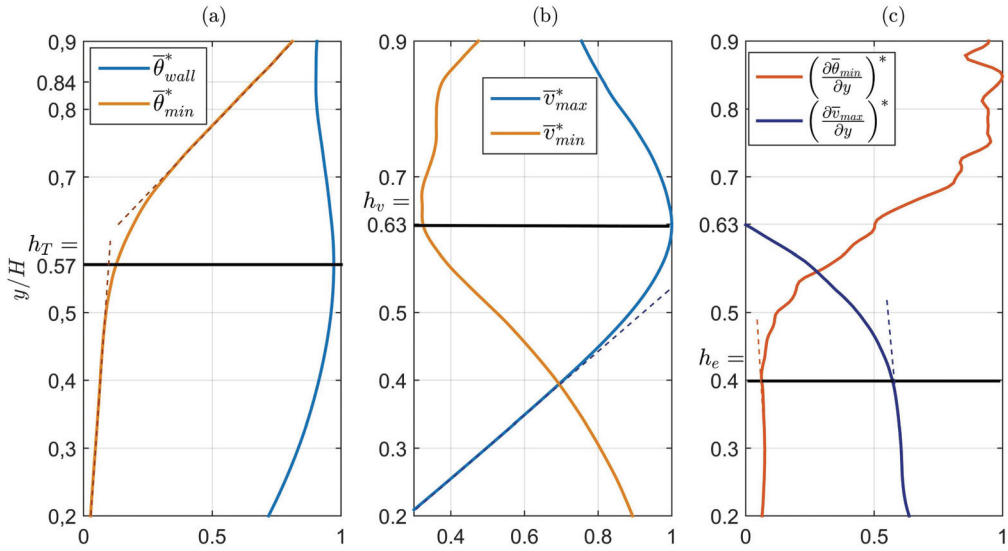

Fig. 5.5 Streamwise evolution of (a) $\overline{\theta}^*_{wall}$ and $\overline{\theta}^*_{min}$, (b) $\overline{v}^*_{max}$ and $\overline{v}^*_{min}$ and (c) $(\partial \theta_{min}/\partial y)^*$ and $(\partial v_{max}/\partial y)^*$. Thin dashed lines have been plotted to indicate linear trends or significant changes in the quantities growth. $Ra = 1.5 \times 10^{12}$

$Ra = 1.5 \times 10^{12}$. The overline indicates a time-averaged quantity. All the quantities have been scaled with their maximum streamwise value for visualization purposes. The scaled quantities are indicated by the superscript *.

In figure 5.5 (a) have been plotted the streamwise evolution of the minimum temperature in the fluid and the wall temperature. The temperature at the wall $\overline{\theta}^*_{wall}$ increases from the beginning of the channel and reached a local maximum at approximately $h_T = 0.57$, where h_T was defined in the previous chapter as the non-dimensional height at which the first local maximum of the wall temperature is reached. Slightly higher, at approximately $y/H = 0.84$, $\overline{\theta}^*_{wall}$ reaches a local minimum, then the wall temperature increases until the end of the channel. Regarding $\overline{\theta}^*_{min}$ the minimum temperature in the fluid, it rises slowly and almost linearly from approximately $y/H = 0.2$ to $y/H = 0.5$. This increase of temperature is mainly due to conduction and diffusion heat transfers which dominate in this region. Just before $y/H = 0.5$, the growth of $\overline{\theta}^*_{min}$ changes and $\overline{\theta}^*_{min}$ starts to significantly increase. From $y/H = 0.75$ $\overline{\theta}^*_{min}$ evolves linearly with a higher growth rate than in the lower part of the channel. Thin dashed lines have been plotted to indicate this evolution. The variation of $\overline{\theta}^*_{min}$ suggests that some of the transition phenomenon appear to have started lower than h_T.

The streamwise evolution of the maximum and minimum velocities are plotted in figure 5.5 (b). In the lower part of the channel $\overline{v}^*_{min}$ keeps decreasing while $\overline{v}^*_{max}$ increases almost linearly from $y/H = 0.2$ to $y/H = 0.4$. $\overline{v}^*_{max}$ reaches a peak at $y/H = 0.63$ and $\overline{v}^*_{min}$ reaches its minimum slightly higher. The height at which $\overline{v}^*_{max}$ is reached will be referred to in its non-dimensional form as h_v. h_v is similar to the indicators used by Daverat et al. (2017) at the only difference that in the experimental measurements of Daverat et al. (2017) it was mentioned

that $\overline{v}^*_{max}$ and $\overline{v}^*_{min}$ variations were inverted at the same height. This difference could be explained by the spatial discretization of their experimental velocity measurements which was larger than the one numerically achieved in the present work. Given the proximity between the height of the maximum of $\overline{v}^*_{max}$ and the height of the minimum of $\overline{v}^*_{min}$, it is possible for the difference to not have been detected.

The fact that there are changes in the growth of $\overline{\theta}^*_{min}$ and $\overline{v}^*_{max}$ lower than h_T and h_v suggests that some transition phenomenon may have started at lower levels. Thus, in figure 5.5 (c) the streamwise evolution of their y-variation, respectively $\left(\partial\overline{\theta}_{min}/\partial y\right)^*$, and $(\partial\overline{v}_{max}/\partial y)^*$ are plotted. From $y/H = 0.2$ to $y/H \simeq 0.4$, $\left(\partial\overline{\theta}_{min}/\partial y\right)^*$ remains relatively constant and after $y/H \simeq 0.4$ it increases. This height corresponds to the area from which $\overline{\theta}^*_{min}$ growth rates change (see figure 5.5 (a)). Then from $y/H \simeq 0.75$, $\left(\partial\overline{\theta}_{min}/\partial y\right)^*$ remains relatively constant despite some oscillations.

$(\partial\overline{v}_{max}/\partial y)^*$ decreases from $y/H = 0.2$, however its variation is very small until approximately $y/H \simeq 0.4$. From there, there is a change in the gradient of $(\partial\overline{v}_{max}/\partial y)^*$ decrease. It is interesting to note that the changes in $\left(\partial\overline{\theta}_{min}/\partial y\right)^*$, and $(\partial\overline{v}_{max}/\partial y)^*$ variations occur in the same area, evaluated around $h_e = 0.4$.

This phenomenon can be explained by the development of turbulent transfers normal to the wall. Indeed, given that the wall is uniformly heated, as the flow develops, the fluid near-the wall heats up and as a consequence its velocity increases as well. However, at one point, this increase of velocity is limited by the shear from the wall and from the velocity difference between the peak velocity and the bulk flow. Consequently the streamwise convective heat transfer is limited as well. However, in order to keep dissipating heat from the wall, other transfer processes must be taking place. As a result, wall-normal heat transfers may start to increase. These transfers, convect heat and mass from the wall region into the bulk region. They may be the cause of the changes of $\left(\partial\overline{\theta}_{min}/\partial y\right)^*$, and $(\partial\overline{v}_{max}/\partial y)^*$ at $y/H = 0.4$. This hypothesis can be partly confirmed by the experiments of Daverat et al. (2017) in which they observed an increase of the turbulent heat transfer $\overline{u'\theta'}$ lower than h_T and h_v. As a consequence h_e could also be considered as an indicator of the early stages of transition.

5.3.2 Evolution of the temperature and velocity profiles at $Ra = 1.5 \times 10^{12}$ with 1.09 K/m

Streamwise velocity and temperature profiles of the numerical results at $\delta_T = 1.09$ K/m are plotted at different streamwise heights in figures 5.6 and 5.7. As was observed in the previous section, velocity and temperature changes in the flow do not occur at the same heights. To that extent h_T will be considered as the transition indicator for the temperature profiles and h_v for the velocity profiles. Two color sets are used in each figure. The blue/purple set are used for the profiles plotted below the transition indicators and the orange/red color set are used for the profiles plotted above it.

The velocity profiles figure 5.6 are characteristic of a velocity distribution obtained in a channel heated on one side. At the entrance the velocity profile is almost flat. Then as the altitude increases and up to h_v, a high-velocity region close to the heated wall develops and the velocity in the bulk region decreases. The velocity peak near the heated wall is due to the heat transfer which heats up the fluids and generates a local high velocity buoyancy-driven region. In the bulk region, the flow is mainly driven by entrainment and shear from the high velocity region near the heated wall. As the flow goes upward, and before transition occurs, a certain region of the flow, near the heated wall will be accelerated whereas the remaining of the flow will see its velocity decrease because of mass conservation. Based on that Li et al. (2017) proposed to define these two regions depending on the sign of the velocity gradient $\partial\overline{v}/\partial y$. The region where $\partial\overline{v}/\partial y > 0$ corresponds to the accelerating buoyant region and will be referred to as the Natural Convection Boundary Layer (NCBL), and the region where $\partial\overline{v}/\partial y < 0$, which corresponds to the decelerating region, is referred to as the Bulk Region (BR).

This distinction is only relevant until the height h_v is reached given that, from there the near wall velocity tends to decrease and the bulk velocity to increase. This is also the reason why the clear distinction between the NCBL and the BR is no longer possible in the upper part of the channel.

Note that close to the unheated wall a secondary high-velocity region also develops due to the slight heating by radiation on this wall. However the main focus will be on the main NCBL and the BR flow.

It can be seen in figure 5.7 that the hot fluid remains close to the hot wall in what is clearly the thermal boundary layer, below h_T. Whilst there is a slight increase in the temperature of the bulk region, it remains essentially at inlet temperature. Then, above h_T, the wall temperature decreases. It also appears that h_T is a fair indicator of the height from which the temperature in the bulk region start to significantly increase.

The streamwise evolution of the turbulent intensity profiles at $z/W = 0.5$, $TI(u)$, $TI(v)$ and $TI(T)$ are plotted in figure 5.8 (a) (b) and (c) respectively. The turbulent intensity is respectively defined for the velocity components and the temperature by:

$$TI(u) = \frac{\sqrt{\overline{u'^2}}}{\sqrt{\overline{u}^2 + \overline{v}^2}} \tag{5.6}$$

and

$$TI(T) = \frac{\sqrt{\overline{T'^2}}}{\sqrt{\overline{(T)}^2}}. \tag{5.7}$$

$TI(u)$ is high at the entrance of the channel and its maximum is reached in the center of the channel. Then the flow is calming and $TI(u)$ progressively decreases and remains at his lowest values from approximately $y/H = 0.23$ to h_e. During this decrease, the peak is displaced

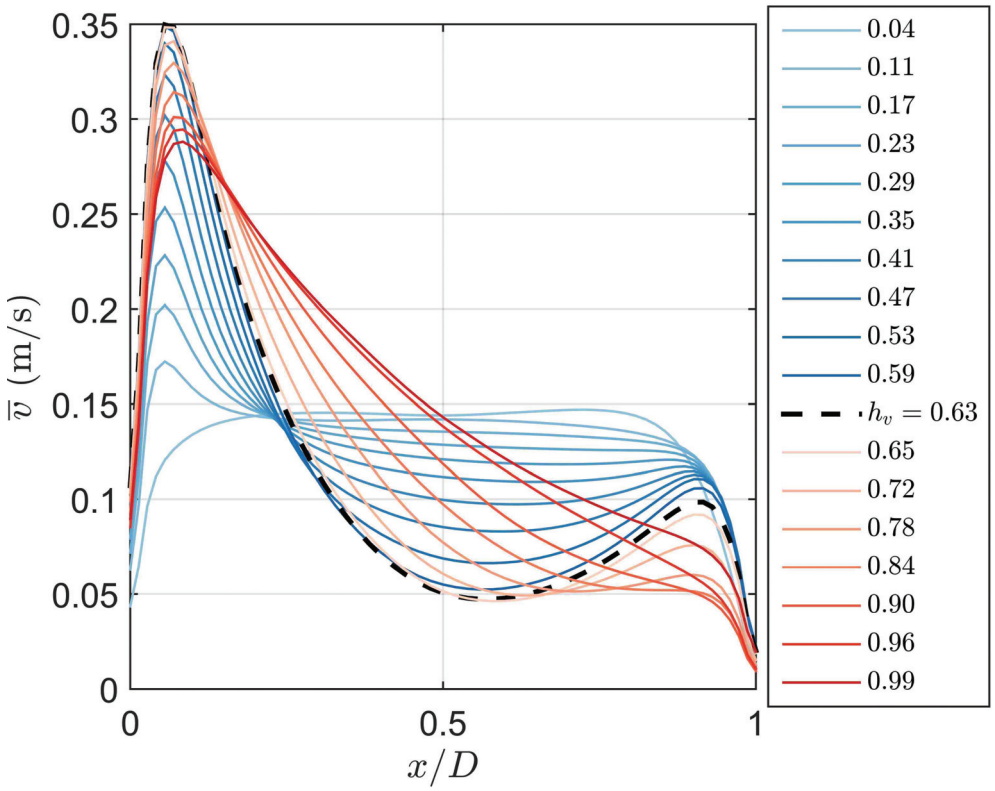

Fig. 5.6 Velocity profiles at $z/W = 0.5$ at $Ra = 1.5 \times 10^{12}$ with 1.09 K/m, the thick dashed line plots the velocity profiles at h_v

from $x/D = 0.5$ to $x/D = 0.4$. From this point $TI(u)$ increases considerably and reaches its maximum around $y/H = 0.72$ while the peak x-location is displaced around $x/D = 0.6$. Above this level, the $TI(u)$ profiles undergo another change with the maximum $TI(u)$ decreasing and being displaced toward the unheated wall. It should be noted that despite the fact that h_e does not capture the profiles at which $TI(u)$ is minimum, it correctly indicates the height from which $TI(u)$ increases. Moreover in this case, h_T and h_v, respectively plotted by a thin dashed black and gray line, do not seem to be the frontier of any particular changes.

$TI(v)$, plotted in figure 5.8 (b), keeps increasing from the inlet of the channel to approximately $y/h = 0.65$. From this point, similarly to $TI(u)$, the maximum $TI(v)$ decreases and is shifted toward the unheated wall. In this case h_e also seems to be at the frontier of a change in the $TI(v)$ distribution as from there the peak is moved to the center of the channel and $TI(v)$ is considerably increased. In this case h_T does not seem to correspond to any particular changes, but h_v is very close to the height at which the maximum $TI(v)$ is reached.

Finally $TI(T)$, in figure 5.8 (c), generally increases from the inlet of the channel to $y/h = 0.84$, height above which it remains approximately the same. The maximum $TI(T)$ occurs at the heated wall from y/H=0.04 to approximately y/H=0.23. Above this level, and up to h_e, $TI(T)$ at the wall remains constant but the maximum $TI(T)$ is displaced to $x/D = 0.07$. Then from h_e $TI(T)$ increases at all x-location but the peak remains around $x/D = 0.07$ at least up to

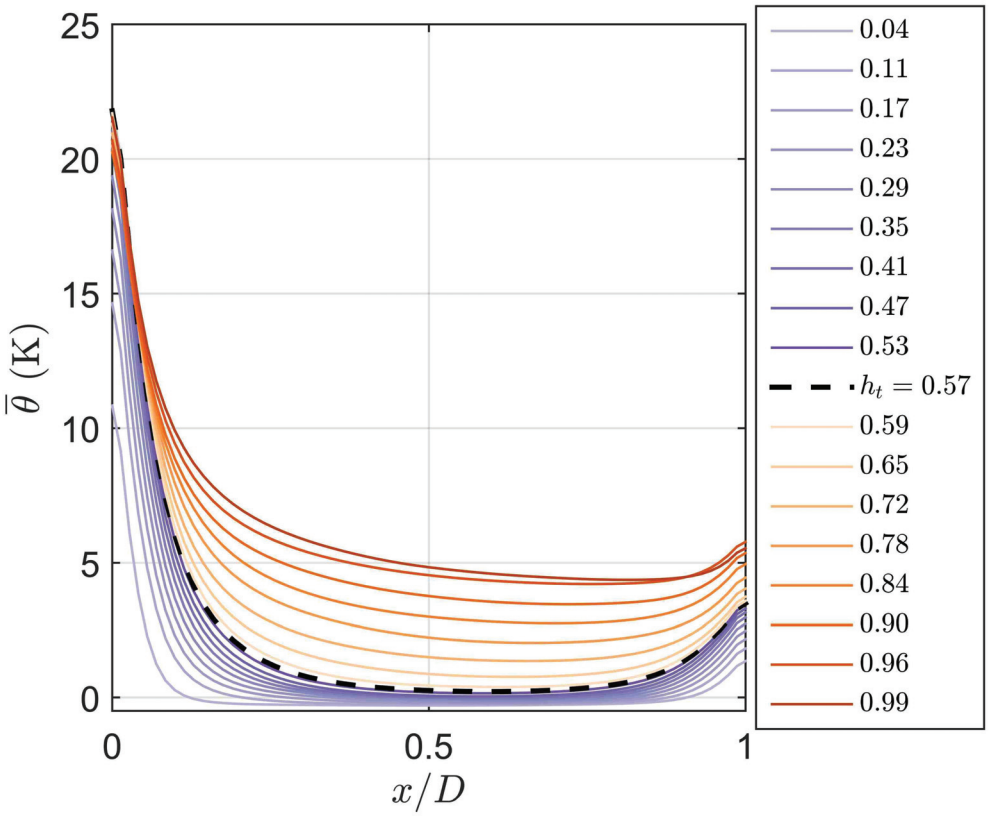

Fig. 5.7 Temperature profiles at $z/W = 0.5$ at $Ra = 1.5 \times 10^{12}$ with 1.09 K/m, the thick dashed line plots the velocity profiles at h_T

$y/H = 0.65$. Then the maximum $TI(T)$ moves back to the wall. In this case h_e clearly indicates the location from which $TI(T)$ at the wall start rising again.

From these profiles it follows that h_e can be adopted to indicate the changes in the TIs. h_T and h_v are respectively legitimate indicators of the thermal and the velocity changes occurring during the boundary layer transitional process. Furthermore the significant changes observed on the time-averaged quantities, as well as on the intermittent structures (see chapter 4) suggest that h_T and h_v corresponds to the late stages or to the end of the transition.

5.3.3 Summary of the transition indicators

A summary of the different transition indicators considered in this chapter as well as in the previous chapter are presented in table 5.2. h_T has been widely used in the literature and indicates well the time-averaged temperature changes occurring at the wall and within the flow during the transitional process. h_V indicates better the changes in the time-averaged velocity behaviour. As was mentioned in chapter 4, the appearance of the turbulent coherent structures was significant above h_T. Given the close spatial proximity between h_T and h_v, both these indicators are considered as indicators of the late stages of transition.

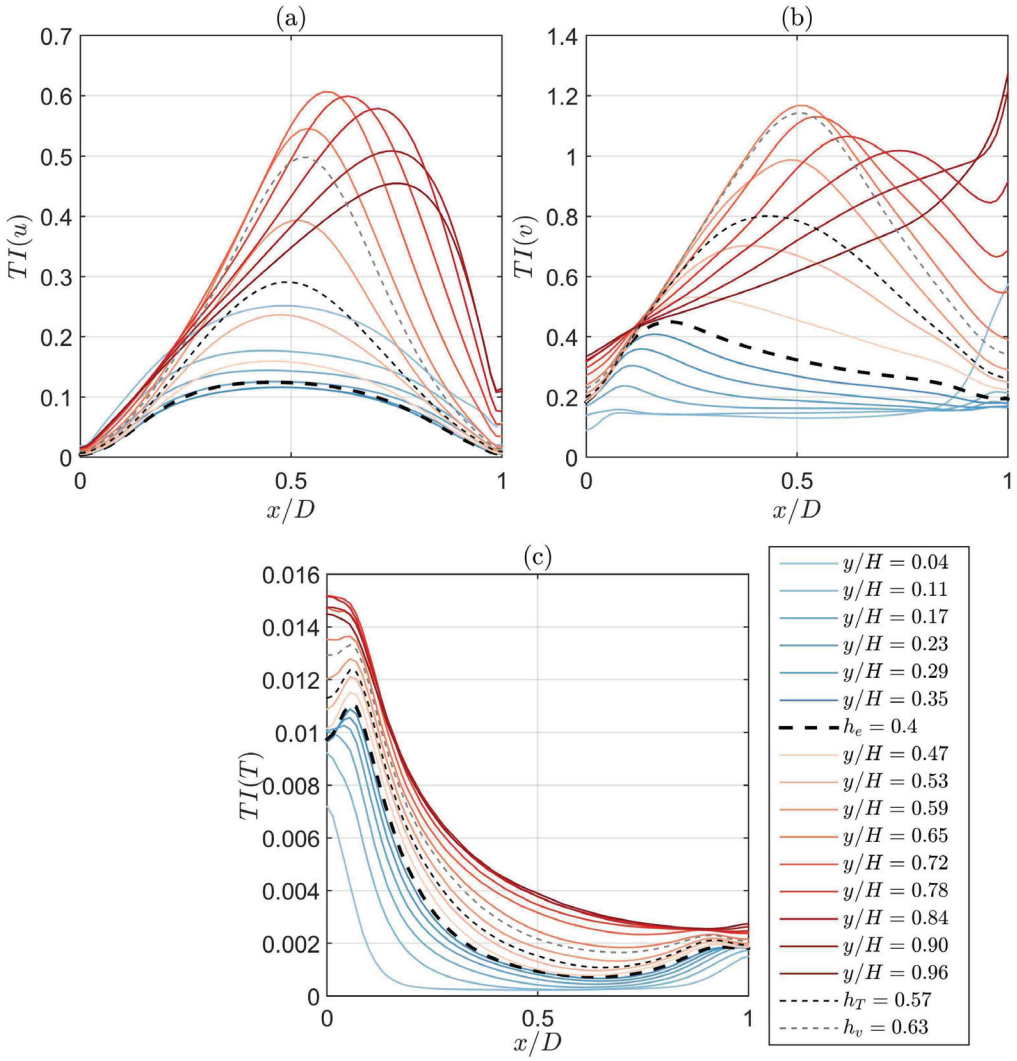

Fig. 5.8 Streamwise evolution of the turbulent intensity profiles at $z/W = 0.5$ at $Ra = 1.5 \times 10^{12}$ with 1.09 K/m, the thick black dashed line plots the TI at h_e, the thin black dashed line plots the TI at h_T and the thin gray dashed line plots the TI at h_v. (a) $TI(u)$, (b) $TI(v)$ and (c) $TI(T)$

h_e and h_c (defined in the previous chapter as the height at which the maximum near wall $v-\theta$ correlation was reached) indicates changes in the turbulent statistics. However no noticeable changes in the time-averaged quantities are observed at these heights. For that reason they are considered as early indicators of the transitional process and may indicate the beginning of the transition.

In the remainder of this study, only one indicator will be used. It is easier and more objective to define a height based on a local minimum or maximum such as h_T or h_v which can be clearly identified, compared to a changes of growth such as observed for $\left(\partial\overline{\theta}_{min}/\partial y\right)^*$, and $(\partial\overline{v}_{max}/\partial y)^*$ at h_e. For the present study, no special argument allows to settle whether h_T or h_v indicates best the transition region. However both experimental and numerical results are

Table 5.2 Summary of the transition indicators considered in this work

Indicator	Height of ...	Stage of transition
h_T	local maximum of $(\overline{\theta}_{wall})$	Advanced
h_v	maximum of $\overline{v}_{max}$	Advanced
h_e	changes of growth of $\overline{T}_{min}$ and $\overline{v}_{max}$	Early
h_c	maximum of $r_{v\theta,wall}$	Early

studied. Given that h_T is easier to obtained experimentally it will be retained as the transition indicator.

Now that the streamwise evolution of the time-averaged transitional flow has been described, the effect of the external thermal stratification on it will be studied.

5.4 Experimental and numerical investigation of the effect of positive δ_T on the velocity and temperature distributions and on the transition location.

PIV measurements were carried out in the inlet and outlet field of views, which are w1, $y/H \in [0;0.25]$ and w4, $y/H \in [0.75;1]$ (see figure 3.5). Since the size of the PIV camera field of view was limited, the measurement in these regions could not have been performed simultaneously. Therefore, between the experiments and at each heat input, the external thermal gradient δ_T and the reference temperature T_0 changed.

In the experiments T_0 varied depending on the day. The experimental reference temperatures which correspond to the selected cases studied here, are summarized in table 5.3.

Table 5.3 External thermal stratifications and reference temperature studied for the experimental and numerical cases under study

Ra	1.5×10^{12}		3.5×10^{12}	
y/H	w1	w4	w1	w4
$(\delta_T, T_0(^\circ C))$	(0.49, 21.0)	(0.90, 20.2)	(0.31, 19.3)	(0.78, 22.4)
	(0.83, 23.4)	(1.14, 21.1)	(0.72, 21.3)	(1.40, 17.4)
	(1.09, 23.0)		(1.33, 17.5)	

5.4.1 Temperature distributions

Wall temperature

The time-averaged temperature distributions at the heated wall, $\overline{\theta}_{wall}$ at $z/W = 0.5$ are plotted in figure 5.9 and figure 5.10 for the two Rayleigh numbers of $Ra = 1.5 \times 10^{12}$ and $Ra = 3.5 \times 10^{12}$ and various external thermal stratifications.

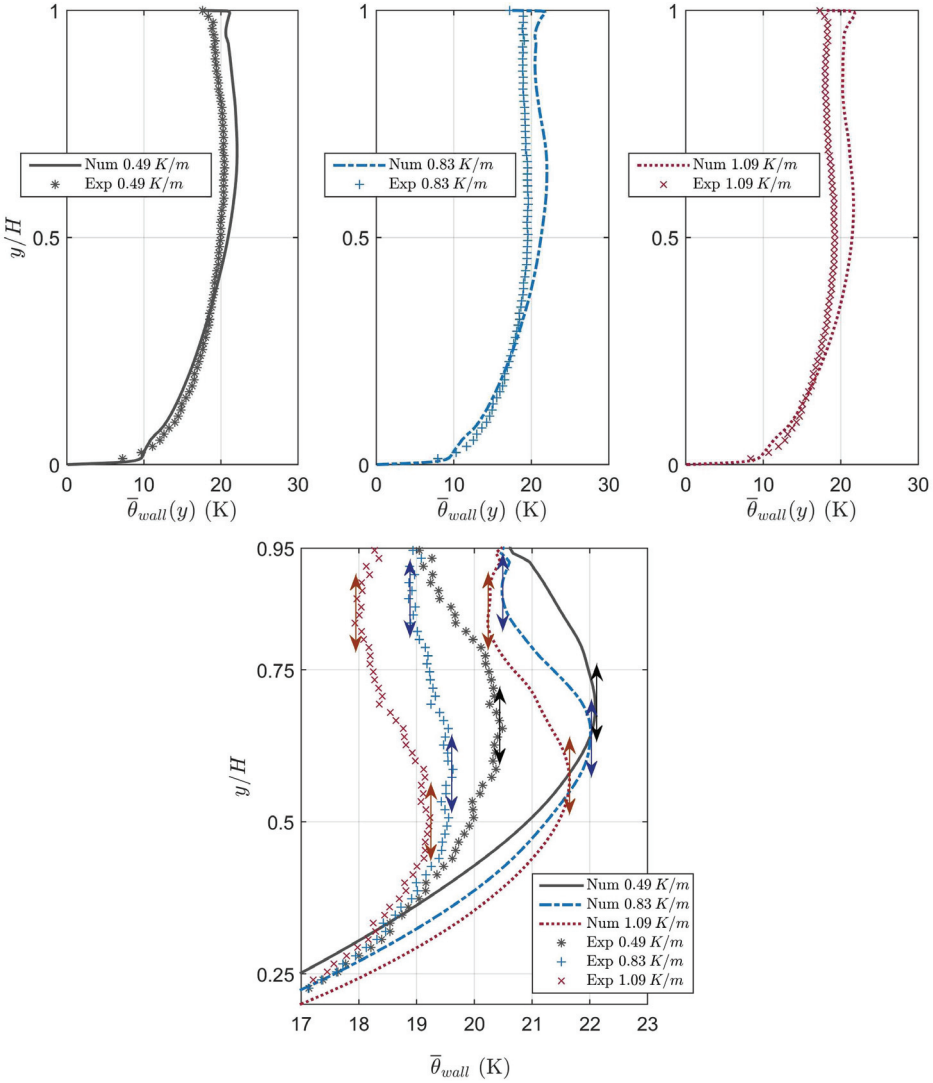

Fig. 5.9 (Top) Temperature distribution at the wall at $Ra = 1.5 \times 10^{12}$, from left to right $\delta_T = 0.49K/m$, $\delta_T = 0.83K/m$, $\delta_T = 1.09K/m$ (Bottom) Magnified views, double headed arrows indicate the local maxima and minima of temperature

In order to better observe the shape of the temperature distributions in the higher part of the channel, magnified views are plotted in figure 5.9. In all these cases, $\overline{\theta}_{wall}$ has a very high gradient in the first, lower, part of the channel but its slope decreases and the temperature finally reaches a local maximum at h_T.

In figure 5.9 at $Ra = 1.5 \times 10^{12}$, h_T is indicated by a tangential double arrow. At $\delta_T =$ 0.83 K/m and $\delta_T = 1.09$ K/m, the local minimum of temperature, which is above h_T, is also indicated by a tangential double arrow.

At $Ra = 1.5 \times 10^{12}$ in figure 5.9, the experimental temperatures are slightly under-estimated in the lower quarter of the channel, however, the data form the numerical simulations are slightly higher than the experimental results above that height. The differences between experimental and

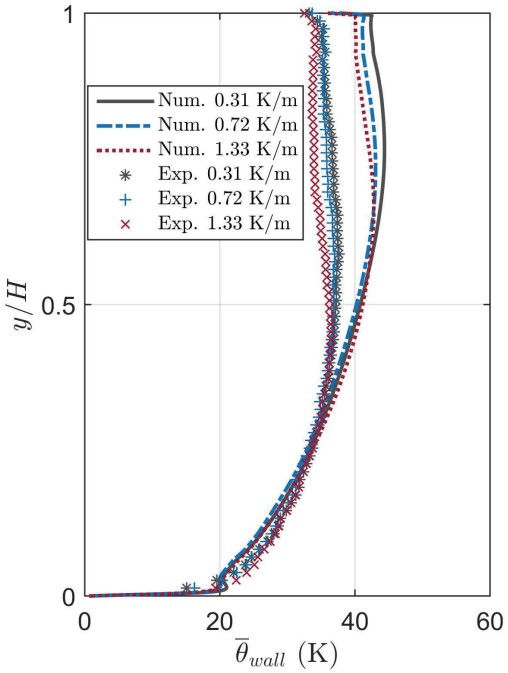

Fig. 5.10 Temperature distribution at the wall at $Ra = 3.5 \times 10^{12}$, from left to right $\delta_T = 0.50\ K/m$, $\delta_T = 0.72K/m$, $\delta_T = 1.33K/m$

numerical maximum temperatures reached at the wall are about 10 %. For each δ_T, the location of the local maximum of temperature is slightly higher in the numerical results. Regarding the local minimum of temperature observed at $\delta_T = 0.83$ K/m, $\delta_T = 1.09$ K/m, the locations are very well predicted numerically.

At $Ra = 3.5 \times 10^{12}$, the numerical and experimental temperature presented in figure 5.10 and the agreement between them is less satisfactory than at $Ra = 1.5 \times 10^{12}$. h_T is located higher in the numerical results than in the experimental data. The differences in the maximum temperature reaches 25% at $\delta_T = 0.50$ K/m. Moreover the local minimum, which appears in the experimental results at $\delta_T = 1.33$ K/m, does not appear on the corresponding numerical case.

However, it can be seen in figure 5.9 and 5.10 and detailed in table 5.4, in both the numerical and the experimental results, that the transition, indicated by h_T, moves lower in the channel as the external thermal stratification increases.

Outlet temperature

At $Ra = 1.5 \times 10^{12}$, the outlet time-averaged fluid temperatures, in the mid-section and at $\delta_T = 0.49$ K/m and $\delta_T = 1.09$ K/m are plotted in figure 5.11. As would be expected, the temperature is high near the hot wall, and quickly decreases in the wall-normal direction. The temperature in the bulk of the flow slowly decreases until it gets close to the inactive wall where it increases slightly because of the slight heating introduced to model the wall to wall radiation

Table 5.4 Location of the local maxima and minima of temperatures at the heated wall

Ra	δ_T	Case	h_T	y_{Tmin}/H
1.5×10^{12}	0.49	Exp	0.62	-
		Num	0.68	-
	0.83	Exp	0.61	0.87
		Num	0.63	0.84
	1.09	Exp	0.51	0.84
		Num	0.57	0.83
3.5×10^{12}	0.31	Exp	0.60	-
		Num	0.78	-
	0.72	Exp	0.57	-
		Num	0.70	-
	1.33	Exp	0.45	0.83
		Num	0.67	-

(see. 5.2.1). The temperature in the bulk region is three to five degrees higher than that at the inlet. This is in great part due to turbulent heat transfers and mixing. The difference of temperatures between the two cases plotted can be explained by the fact that transition had started lower in the channel in the case of $\delta_T = 1.09$ K/m than when $\delta_T = 0.49$ K/m. Consequently, turbulent transfers have also started lower in the channel and more heat was transferred to the bulk region. The maximum differences between the experimental and numerical results is approximately 0.5 K at $\delta_T = 1.09$ K/m.

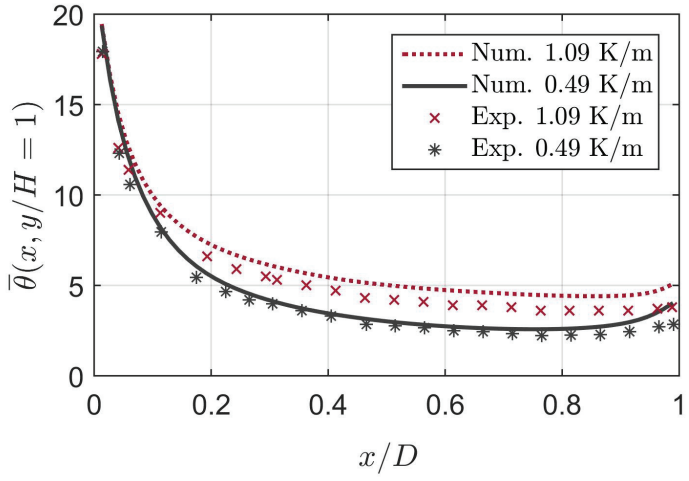

Fig. 5.11 Temperature profiles at the outlet at $Ra = 1.5 \times 10^{12}$ $\delta_T = 0.49K/m$, $\delta_T = 1.09K/m$

5.4.2 Velocity distributions

The time averaged velocity profiles are plotted in the centerplane $z/W = 0.5$, in the inlet and outlet regions.

In figure 5.12 the time-averaged streamwise velocities at $y/H = 0.25$ and $y/H = 0.90$, in the mid-section of the channel $z/W = 0.5$, are plotted for the two Rayleigh numbers under study and for various external thermal stratifications. At $y/H = 0.25$ the velocity profiles are all composed of a NCBL and a BR.

Regarding the impact of the external stratification, it can be observed that an increase of δ_T decreases the streamwise velocity. However the velocity profiles are not uniformly reduced. Indeed, the peak velocity is less affected by the external stratification than the velocity in the bulk region.

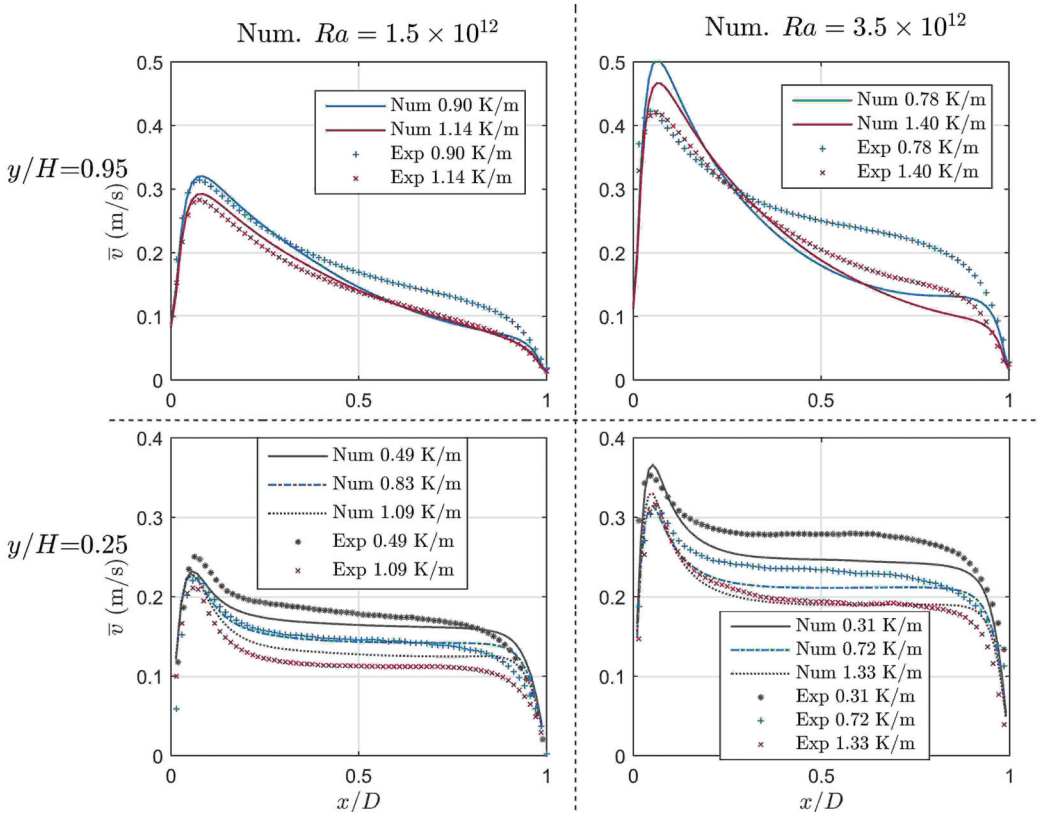

Fig. 5.12 Time averaged velocity profiles at (top) $y/H = 0.90$ and (bottom) $y/H = 0.25$, $z/W = 0.5$, symbols are used for the experimental data while lines are used for numerical results, left $Ra = 1.5 \times 10^{12}$, right $Ra = 3.5 \times 10^{12}$

At $y/H = 0.25$, $Ra = 1.5 \times 10^{12}$, the case of $\delta_T = 0.83$ K/m has the best experimental-numerical agreement whereas numerical results over-predict the velocity in the case of $\delta_T = 1.09$ K/m and under-predict it in the case of $\delta_T = 0.49$ K/m. Numerically, the peak velocity is almost not affected by the changes in the stratification. Experimentally, the peak velocity does not change between $\delta_T = 0.83$ K/m and $\delta_T = 1.09$ K/m but increase by 0.05 m/s at $\delta_T = 0.49$ K/m. The maximum experimental-numerical differences in the peak velocities is of 8% at $\delta_T = 0.49$ K/m and of 9% in the central bulk region at $\delta_T = 1.09$ K/m. Note that the differences are systematically more important close to the unheated wall which may be due to an overestimation of the heat transmitted from the unheated wall. At $Ra = 3.5 \times 10^{12}$, the peak

velocities are better predicted but not the bulk velocity. In this case, $\delta_T = 1.33$ K/m is the better predicted by the numerical model whereas the velocity profiles for the two lower stratifications are under-predicted. The maximum differences in the peak velocities is of 3% at $\delta_T = 0.50$ K/m and of 10% in the central bulk region at $\delta_T = 1.33$ K/m.

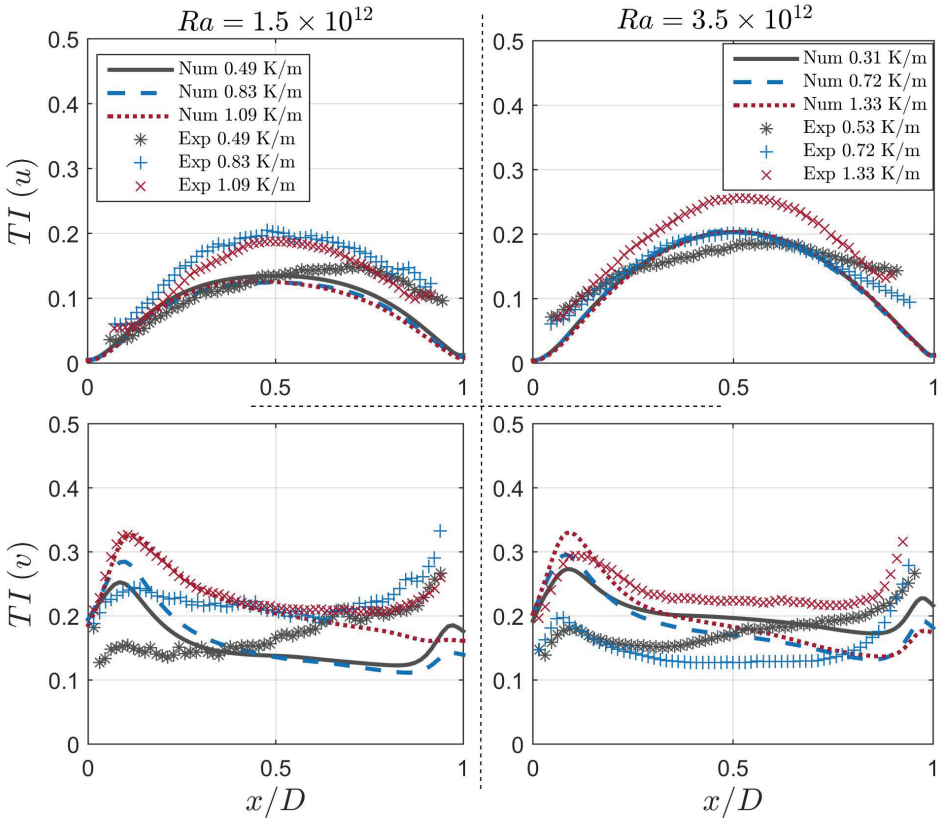

Fig. 5.13 Turbulent intensities at y/H=0.25 experimental and numerical

Regarding the velocity profiles in the upper part of the channel, the experimental-numerical agreement is excellent at $Ra = 1.5 \times 10^{12}$ for $\delta_T = 1.14$ K/m with maximum differences below 5%. Regarding the case of $\delta_T = 0.90$ K/m the velocity profiles agree very well between $x/D \in [0;0.4]$.

At $Ra = 3.5 \times 10^{12}$, the experimental velocity is numerically over-predicted close to the heated wall while it is under-predicted for $x/D > 0.3$. One of the main sources of the experimental-numerical differences in the velocity profiles is due to the difference of the transition location previously observed, as may be seen in table 5.4 and figure 5.10. Indeed, after the transition, the velocity peak is expected to decrease while the velocity in the bulk region increases.

The turbulent intensity of u and v, are plotted at $y/H = 0.25$ in figure 5.13. The turbulent intensity remains in the range of 10 to 25% in the bulk region and can reach 33% at $Ra = 1.5 \times 10^{12}$, for $\delta_T = 1.09$ K/m. $TI(u)$ is higher in the bulk region while $TI(v)$ reaches local peaks close to the walls. The agreements are qualitatively good for $TI(u)$ despite differences

in the amplitudes. However, these differences mostly remains within the uncertainties range. Regarding $TI(v)$ agreements are particularly good at $Ra = 1.5 \times 10^{12}$, $\delta_T = 1.09$ K/m between $x/D \in [0;0.5]$.

It is important to note that in this section, rather than the ability of the numerical model to exactly predict the quantities of the flow, its ability to capture the effect of the external thermal gradient on the time-averaged velocities and temperatures distributions as well as on the transitional behaviour is important.

Thus two main conclusions emerged from the experimental and numerical results. First, it was shown that as the external thermal stratification increases, h_T decreased and thus, the boundary layer transition, was moved lower in the channel. It was also observed that as δ_T increases, the velocity in the BR was reduced than the velocity in the NCBL.

At first glance these two effects may seem contradictory. Indeed the transition to turbulence is often related to velocity, and a decrease in the velocity would result in a delayed transition to turbulence. However the opposite is observed here and an explanation is proposed in the following section.

5.4.3 Displacement of the transition in a channel flow with various δ_T

In natural convection flow induced by a vertical hot surfaces, the transitional processes to turbulent flow remain an open question. However it has been observed in different studies that for the same heating configuration (same heat flux or same temperature), the flow induced by a hot vertical plate becomes turbulent at a lower location than the flow induced in a vertical channel. Miyamoto et al. (1986) showed that, for a same injected heat flux of 104 W/m^2, h_T was located up to twice as high in the case of a vertical channel flow than in the case of vertical plate flow. In the LES numerical investigation of Kogawa et al. (2016) in which the walls were heated at uniform temperature it could be observed that turbulent structures were developing lower in the case of vertical plate than in vertical channel flow. In order to explain this difference, Kogawa et al. (2016) observed that the velocity gradient between the velocity peak, in the NCBL, and the bulk velocity were higher in the case of the vertical plate flow than in the vertical channel flow. They concluded that the shear stresses induced were higher in the vertical plates configuration, resulting in an earlier transition. Other workers considered that shear stresses were one of the source of instability which could lead to turbulence(see e.g. (Daverat et al., 2017; Kogawa et al., 2016)).

Then these two points can be made:

1. As was seen in figure 5.6, in the present configuration the flow at the inlet resembles a plug flow but when approaching the transition height, evolves toward a flow, with a high velocity gradient, much more similar to a vertical plate natural convection flow. During

this topological change, shear stresses increase and the destabilization mechanisms proper to vertical plate flow could take place and lead to transition to turbulence.

2. In figure 5.12, it was observed that as the external thermal stratification increases, the velocity gradient between the NCBL and the BR was increased. As a consequence, in a stratified environment, the channel flow approaches the topology of a vertical plate flow at a lower level in the channel than in a non or less stratified environment.

Once all these points are established it is possible to explain displacement of the transition point. First, before transition occurs in the channel, the flow evolves from a plug flow at the inlet to a flow approaching the topology of a vertical plate flow. Given that transition to turbulence is triggered earlier in vertical plate flow than in channel flow, it is possible that as the channel flow approaches the vertical plate flow it becomes more subject to transition. Secondly, given that as the external thermal stratification increases, the channel flow approaches the topology of a vertical plate flow lower in the channel, it should also transit lower in the channel.

Note that other phenomena, not investigated here, may also contribute to the transition phenomena. Despite the fact that in the present configuration no permanent flow reversals were observed, an intermittent flow is present as was demonstrated bySanvicente et al. (2013), and may play a role in the destabilization processes. Jannot and Kunc (1998) also claim that the onset of transition in the case of natural convection over isothermal vertical plates, originates from the interaction between characteristic travelling wave within the boundary layer and the Brunt-Väisälä frequency, inherent to thermally stratified environment.

5.5 Extension to weak and negative thermal stratifications

In the following section the numerical model is used to investigate the flow changes in the cases of weak and negative stratifications. A weak thermal stratification, approaching δ_T=0 K/m, is very hard to establish experimentally especially in a room where the ambient temperature is not controlled. Due to its unstable character, a negative stratification of temperature is impossible to obtain in non-controlled laboratory conditions. However, it appears than in the atmosphere, negative and positive stratifications can be encountered. Flohn and Penndorf (1950) noted that within the first meters, negative stratifications could drop down to δ_T=-0.1 K/m.

In what follows, the effect of the external temperature stratification ranging from $\delta_T \in [-0.5; 1.4]$ K/m on the mass flow rate, the transition behavior and the maximum temperature at the wall are investigated.

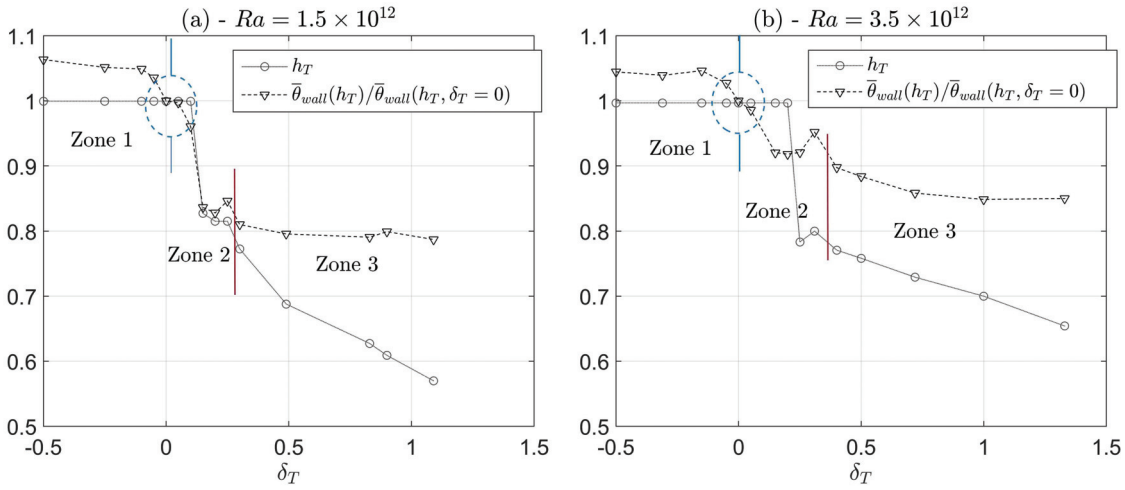

Fig. 5.14 Evolution of the transition height and maximum temperature at the wall for various δ_T at (a) $Ra = 1.5 \times 10^{12}$ and at (b) $Ra = 3.5 \times 10^{12}$

5.5.1 From laminar to transitional flow

h_T and $\overline{\theta}_{wall}(h_T)$ were plotted against δ_T for the cases of $Ra = 1.5 \times 10^{12}$ and $Ra = 3.5 \times 10^{12}$ in figure 5.14 (a) and (b). For visualization purposes $\overline{\theta}_{wall}(h_T)$ was scaled by $\overline{\theta}_{wall}(h_T, \delta_T = 0K/m)$.

The evolution of h_T and $\overline{\theta}_{wall}(h_T)$ with δ_T is rather complex. However for the two heat inputs, three zones can be defined in which h_T and $\overline{\theta}_{wall}(h_T)$ have a similar behaviour against δ_T. The first zone corresponds to negative and weak stratifications. Its upper limit is difficult to determine, and to that extent has been indicated by an ellipse. In this zone, h_T is at the top of the channel, at y/H=1 and $\overline{\theta}_{wall}(h_T)$ remains almost constant with a slight decrease for stratifications approaching 0 K/m and above. As δ_T increases above zero, the second zone is encountered, one in which the flow behaviour drastically changes. h_T is displaced to considerably lower levels in the channel and $\overline{\theta}_{wall}(h_T)$ decreases significantly, by up to 25% at $Ra = 1.5 \times 10^{12}$. At both $Ra = 1.5 \times 10^{12}$ and $Ra = 3.5 \times 10^{12}$ there is a peak in h_T and $\overline{\theta}_{wall}(h_T)$ at the end of zone 2. This peak is used as the limit between zone 2 and zone 3. Finally, in zone 3 $\overline{\theta}_{wall}(h_T)$ changes are small and h_T seems to be displaced lower in the channel almost linearly.

Using the meaning given here to h_T, in zone 1, for negative and weak thermal stratifications, h_T is reached at the top of the channel, which implies that the flow did not go through transition or that at least, the transitional process is only at its early stages. As a consequence in zone 1, the natural convection boundary layer flow will be considered laminar and this zone called the Laminar zone. In zone 2, the rapid changes in the location of h_T and $\overline{\theta}_{wall}(h_T)$ suggests that the flow configuration is changing from a flow without transition to a transitional flow. Thus, this configuration will be called the Connecting zone. Finally, in zone 3 the flow is transitional

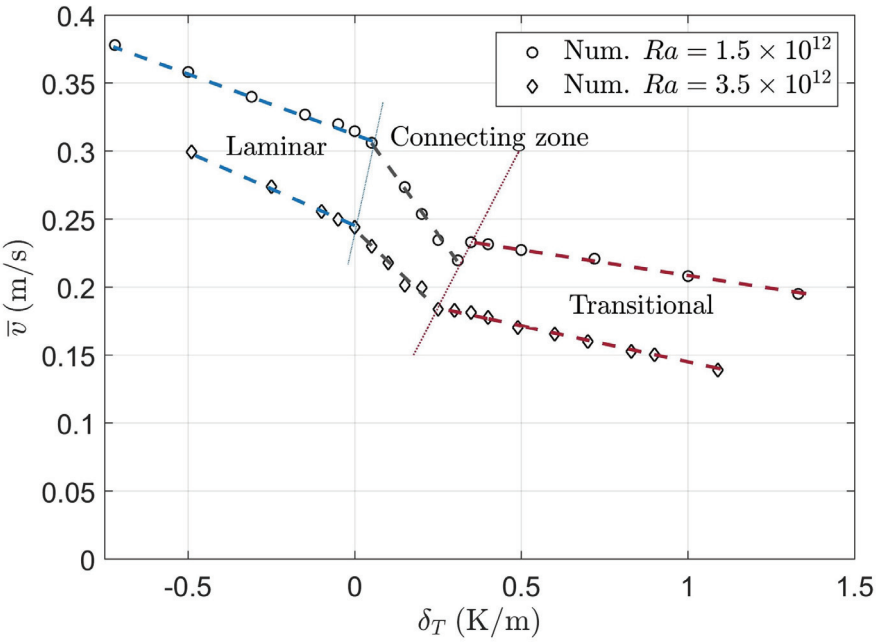

Fig. 5.15 Time and spaced averaged inlet velocities as a function of the external thermal stratification

and the changes in δ_T only alter h_T and $\overline{\theta}_{wall}(h_T)$ in a more predictable way. This zone is then referred to as the Transitional zone.

In figure 5.15, the time and spaced averaged inlet velocities, obtained from the numerical results have been plotted against δ_T. The averaged inlet velocity decreases as the external thermal stratification increases. Moreover, for each Rayleigh number, its evolution can be decomposed in three different regions, delimited here by dotted lines and which are characterized by different sensitivity to δ_T. The dashed lines were plotted to help visualize the different trends. The three regions identified coincide with the tree regions observed in figure 5.14 and their names were reported in figure 5.15. Note that in figure 5.15, it is easier to determine the limit between the laminar zone and the connecting zone based on velocity changes. This limit will be set at approximately δ_T=0.05 K/m at $Ra = 3.5 \times 10^{12}$ and δ_T=0 K/m at $Ra = 1.5 \times 10^{12}$.

There is a variation of almost 100% in the inlet velocities when δ_T changes from -0.5 to 1.4 K/m. Since in the past δ_T was not modelled in numerical studies the experimental and numerical data could not be made to match when thermal stratification was present during the experimental measurements.

The changes in the mass flow rate and h_T that are observed in the connecting zone are extremely interesting. Indeed, they suggest that, for the same heat input and for rather small variations of external thermal stratification of 0.2-0.3 K/m, the flow goes from a laminar regime to a transitional regime. Moreover, in the connecting zone, the mass flow rate changes by up to 25% and the maximum temperature by 10 to 20%. A detailed study of the mechanisms that take

place in these cases could provide many answers on the onset of transition to turbulence in these type of flows.

5.5.2 Time-averaged velocity and wall temperatures for various δ_T

The time-averaged wall temperatures for negative and positive δ_T, for the two heat fluxes have been plotted in figure 5.16. Three set of colors were used. Blue colors are used for wall temperature in the laminar zone, dashed grey lines are used for the connecting zone and the red lines are used for the transitional zone. The wall temperature shapes for the transitional zone have already been described in the previous sections. However regarding the wall temperatures for the laminar zone, the shape is increasing up to the top of the channel which is typical of laminar natural convection flow. Some slight changes are observed in the very top of the channel which may be due to exit effect as were already reported in many studies (see e.g. (Lau, 2013; Sanvicente et al., 2013)). It is also seen that in the bottom part of the channel there is a temperature peak. This is due to the separation which occurs at the leading edge. In this area, a local recirculation is created which induces a local rise of temperature. This phenomenon have already been observed experimentally and numerically (see e.g. (Vareilles, 2007)). It can be noted that for the laminar zone, the wall temperature rises as δ_T decreases. This could be in part due to the fact that, when there is a negative thermal stratification, the air below the entrance of the channel is at a higher temperature than T_0. Consequently, as the external thermal stratification decreases, the temperature of the air entrained inside the channel increases which slightly heats up the channel. In the connecting zone, the wall temperature profiles progressively evolve from a profile of a laminar channel flow to this of a transitional regime.

Time-averaged velocity profiles in the mid section and at y/H=0.25 and y/H=0.50 have been plotted in figure 5.17. The profiles are similar to those previously described with variation in the BR and NCBL velocities. Note that at $\delta_T = -0.25$ K/m $\delta_T = -0.49$ K/m, the maximum velocity is only slightly higher than the velocity in the bulk of the flow.

Contrary to the velocity profiles of the transitional configuration for which the BR is more affected by the changes in δ_T than the BL region, it is not the case for the velocity profiles of the connecting and the laminar zones.

It is interesting to note that the velocity profiles for δ_T=0.25 and δ_T=0.3 at y/H=0.25 and y/H=0.50 are nearly the same whereas the wall temperature tends to indicate that there is a change in the flow configuration as was previously observed (see figure 5.14).

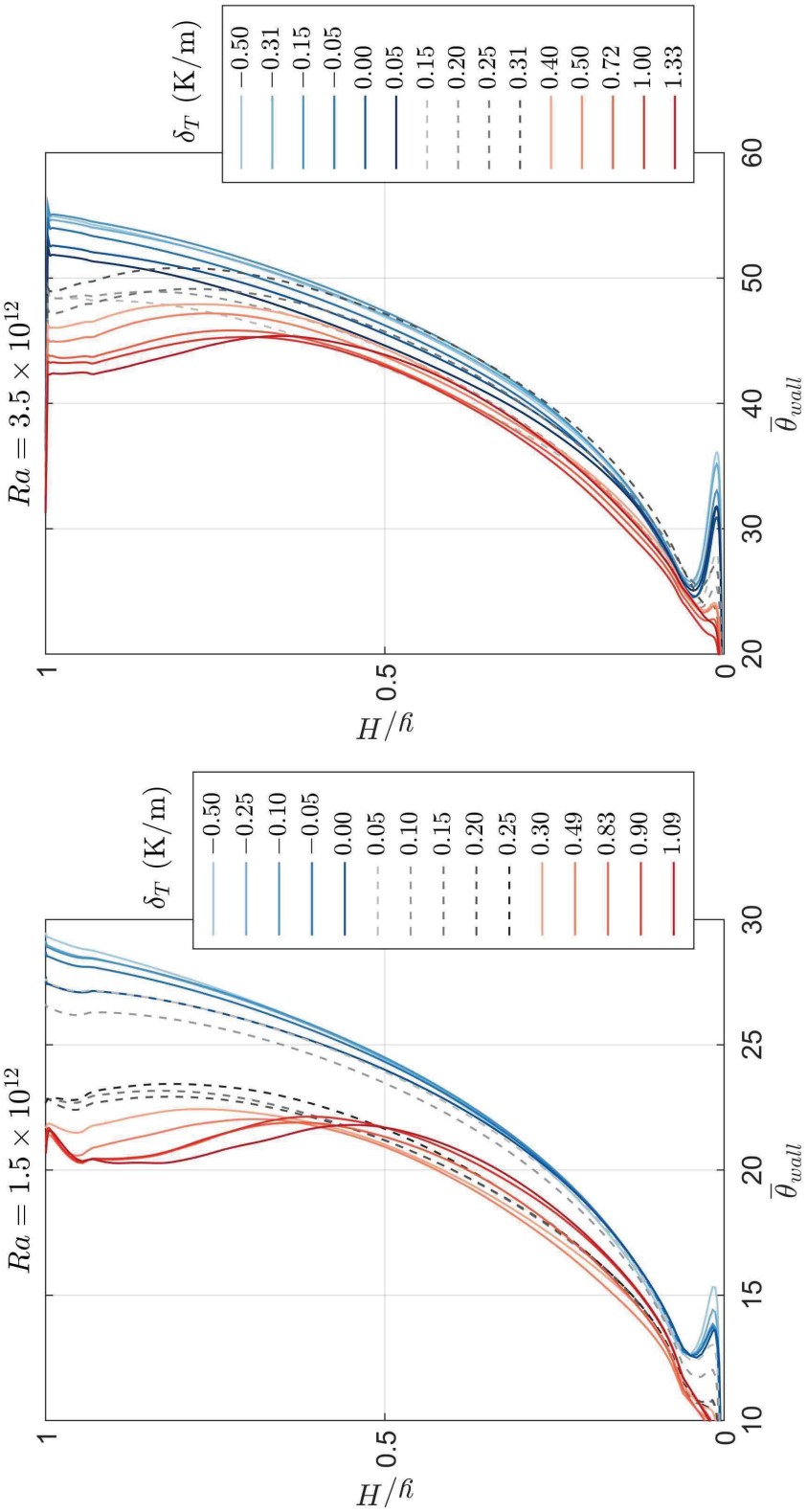

Fig. 5.16 Time-averaged wall-temperature in the mid-section at z/W=0.5 for various external thermal stratification and for the Rayleigh numbers, $Ra = 1.5 \times 10^{12}$ and $Ra = 3.5 \times 10^{12}$.

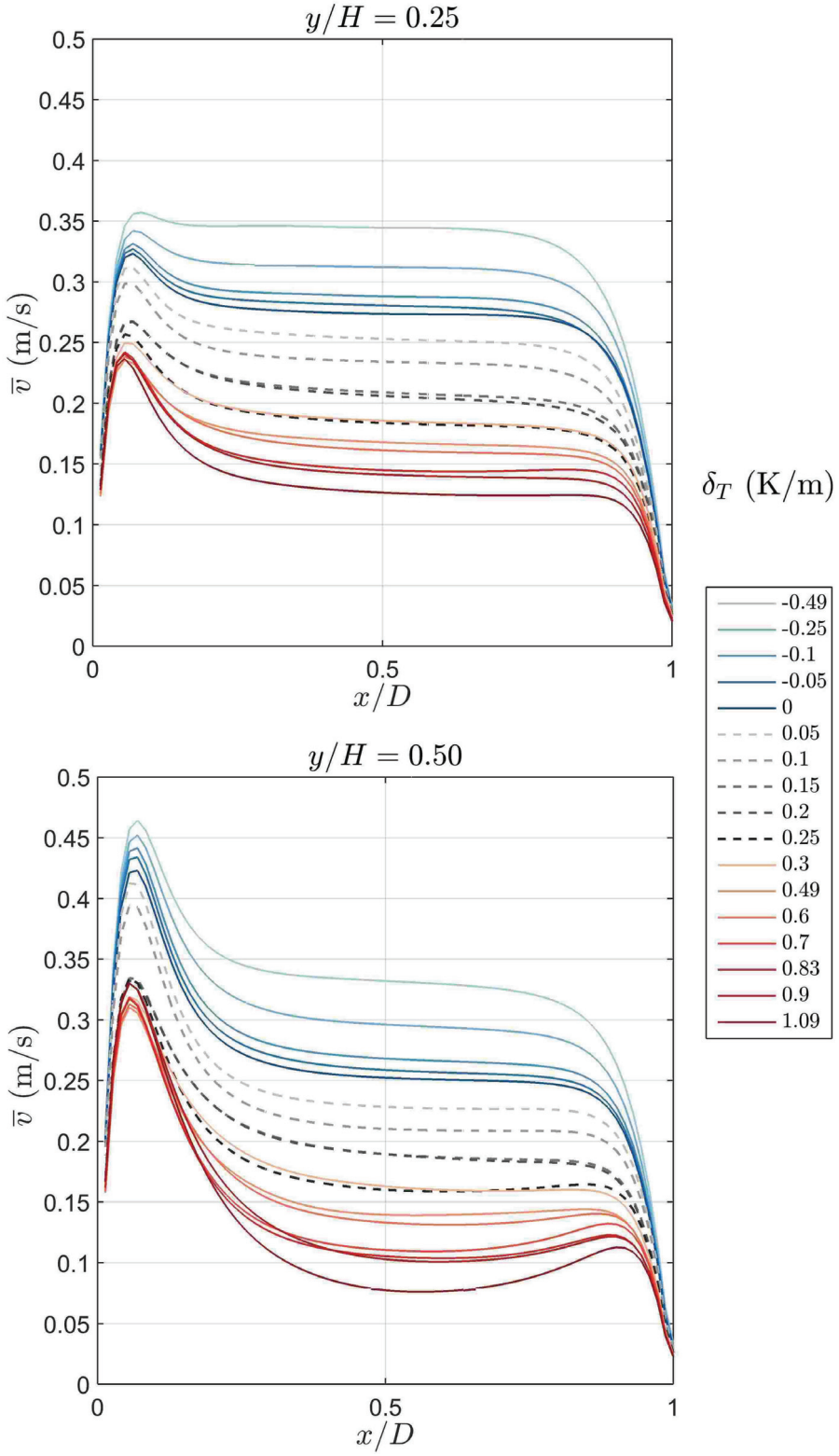

Fig. 5.17 Time-averaged velocity in the mid-section at z/W=0.5 and at heigths y/H=0.25, y/H=0.5 for various external thermal stratification at $Ra = 1.5 \times 10^{12}$.

5.6 Discussion of some results from the literature

5.6.1 Wall temperature distributions for similar configuration

The effects of the external thermal stratification on the temperature distribution presented above may help to explain some differences that were already presented in the literature. One example is presented in figure 5.18. In this figure the time-averaged wall temperature for two configurations have been plotted. The configuration of Ménézo et al. (2007) corresponds to a channel, 1.9 m high, 0.7 m wide and 0.1 m depth, the first 40 cm of the channel were not heated so that only 1.5 m of the channel total height was heated. The configuration of Vareilles (2007) corresponds to the present configuration. In the first half of the channel the two distributions are relatively similar, however in the case of Ménézo et al. (2007), h_T is located around the half of the heated part of the channel whereas it is located at the very top of the channel in the cases of Vareilles (2007). Given that the experiments were conducted on two different channels and in two different laboratories, there could be many reasons for this difference to occur. One of them could be attributed to be the presence of 40 cm of adiabatic section in the cases of Ménézo et al. (2007). However, the aim of an adiabatic extension at the inlet is to reduce the inlet disturbances by calming the flow before it enters the heated area. In that case it would be expected for the transition to be shifted at an higher level in the channel which is not the case. This difference could also be explained by considering the presence of a strong external thermal stratification for the measurements of Ménézo et al. (2007). Precise measurement of the external thermal stratification were not available for the tests of Vareilles (2007) and Ménézo et al. (2007). It was mentioned that the two channels were located in large rooms with high ceiling. However, in order to reduce the effect of the external disturbances within the room, Ménézo et al. (2007) placed heavy curtains around the channel which may have lead to a local strong external thermal gradient.

Based on the numerical observations made in the previous section, the measurements of Vareilles (2007) may have been carried out place in weakly stratified room and consequently the flow was whether in the laminar configuration or in the connecting zone. However the results of Ménézo et al. (2007) could have been obtained in a strongly stratified ambient which would explain why the flow is in the transitional configuration.

5.7 Partial conclusion

A transitional natural convection channel flow has been studied experimentally and numerically. The case of two Rayleigh numbers of $Ra = 1.5 \times 10^{12}$ and $Ra = 3.5 \times 10^{12}$ were investigated. Experimentally PIV and thermocouples were used for the velocity and temperature measurements, and the external thermal stratification was not controlled. Numerically, LES methodology

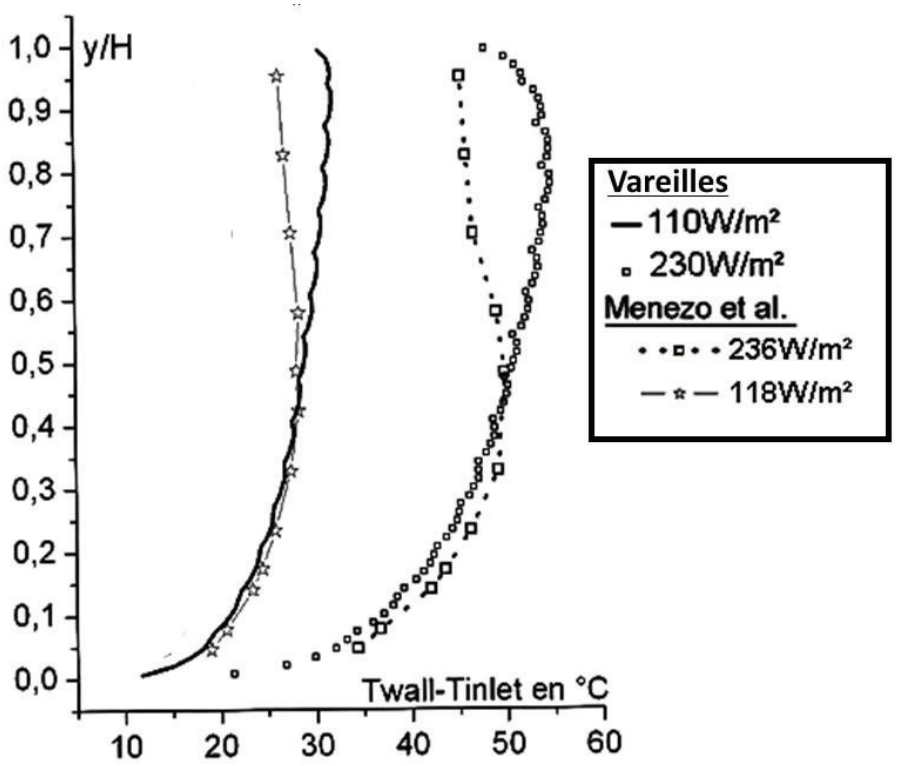

Fig. 5.18 Temperature profiles for two similar channel and heating configurations. This figure uses the data of Ménézo et al. (2007) and Vareilles (2007).

with the Vreman SGS model were used. In order to mimic the environmental noise inherent to the experimental measurements in the laboratory, inlet velocity disturbances were introduced. To model the experimental ambient temperature stratification, a stratification of temperature and pressure was applied at the open boundaries.

The numerical results were first used to better characterize the transition phenomenon by comparing different indicators of transition, namely h_T, height at which the maximum temperature occurs on the heated wall, h_v height at which the maximum velocity near the heated wall occurs and h_e, a newly defined indicator which is based on the changes in the variation of the minimum temperature in the bulk region and changes in the growth of the maximum velocity near the heated wall. This last indicators seems to be relevant for predicting changes in the velocity and thermal turbulent intensity profiles.

There is good qualitative agreement between the experimental and numerical results regarding the time averaged velocities in the inlet and outlet regions of the channel for different value of the external thermal stratification. Similarly time-averaged temperatures at the heated wall and at the outlet are also well modelled. Finally, the effect of the external thermal stratification on the transitional behaviour of the flow is also well captured numerically. It was observed, experimentally and numerically, that an increase in the external thermal stratification induces:

1. a decrease of the mass flow rate. However the peak velocity, near the heated wall is less impacted than the bulk flow velocities.

2. a displacement of the location of the transition to a lower level in the channel.

This last point is explained by the fact that, as the external thermal stratification increases, the significant increase in the gradient between the maximum velocity near the heated wall and the bulk velocity occurs lower in the channel. This produces larger shear stresses, in lower regions of the channel, moving the transition at a lower location.

The numerical model is then used to study the cases of weak and negative stratification which are difficult to obtain in a laboratory but are common in the atmosphere. Three flow regimes were identified depending on the external thermal stratification:, the laminar regime for negative and very weak stratifications, the connecting regime in which the flow changes from a laminar flow to a transitional flow, and finally the transitional configuration for which transition to turbulence occurs within the channel.

Chapter 6

Theoretical model for the prediction natural convective mass flow rate in a thermally stratified environment

In order to limit repeatability issues and to take into account the effect of the external thermal stratification, it is necessary to be able to predict its impact on the flow. In this chapter a simple one-dimensional theory is developed in order to predict the impact of the external thermal stratification on the mass flow rate. It is then validated against the authors experimental and numerical data, for negative and positive stratifications. Data from the literature are also used. The theoretical and experimental results of this chapter has been published in Thebault et al. (2018).

Contents

6.1 Introduction

As was showed in the previous chapter the changes in the ambient temperature distribution modify the flow behaviour and notably the time averaged velocities. Attempts at using dimensional analysis to provide a relationship of non-dimensional parameters to predict the impact of the external thermal stratification proved unsuccessful. As a consequence a one-dimensional theory was developed in an attempt to obtain better understanding of the phenomenon and allow all the available data to collapse on a single curve.

In this theory the net heat injected in the channel is a key parameter. As a consequence rather than using the Rayleigh numbers, the case will be referred as the 100 W, the 230 W and the 500 W cases. A summary of the cases and the correspondence between the Rayleigh number and the heat inputs is presented in 3.1.

6.2 Theoretical considerations

This theory is based on the following assumptions:

1. The flow induced by natural convection is established and in a steady state,

2. The channel is flowing full and the flow is considered to be one-dimensional and ascendant,

3. The vertical channel is embedded in a stagnant atmosphere far-field, with a vertical constant positive temperature gradient δ_T (K/m), in the ascending y-direction.

Similarly to the previous chapter, a linear distribution of temperature is considered,

$$T_a(y) = T_0 + y\delta_T \tag{6.1}$$

at the inlet height ($y = 0$) in the far-field, $T_a = T_0$.

The average temperature distribution in the mid-plane ($y/W = 0.5$) of the present apparatus and the notation used below are presented in figure 6.1. The background colour, from white to red represents a simplification of the temperature distribution patterns in a two-dimensional plane of the channel. The red rectangle represents the heated wall whilst white rectangles represent adiabatic walls; black arrows approximately indicate flow pattern.

6.2.1 Definition of the local temperatures at the open-boundaries of the channel and their relations in the buoyant vertical channel flow

Let $T_{(f,in)}$ (K) be the temperature of the fluid entering the channel and $T_{(s,in)}$ (K) the temperature outside the channel, in the immediate neighbourhood of the inlet of the channel. The temperature and the density of the fluid exiting the channel will be denoted $T_{(f,out)}$ (K) and $\rho_{(f,out)}$ (kg/m^3) respectively. $T_{(s,out)}$ (K) and $\rho_{(s,out)}$ (kg/m^3) are respectively the temperature and the density of the fluid, outside the channel, in the immediate surrounding of the outlet of the channel, but not of the exiting fluid flow.

Due to the heat input inside the channel, an upward directed flow is generated with a mass flow rate $\dot{m}$ (kg/s).

At the inlet boundary of the channel, if heat conduction and diffusion are considered to be negligible so that it can be assumed that

$$T_{(f,in)} \simeq T_{(s,in)}. \tag{6.2}$$

Regarding the outlet, since the motion which results from buoyancy force is ascending and one dimensional, the density of the fluid exiting the channel $\rho_{(f,out)}$ is lower than that of the fluid in the vicinity of the outlet, outside the channel, $\rho_{(s,out)}$ so that

$$\rho_{(f,out)} \leq \rho_{(s,out)}. \tag{6.3}$$

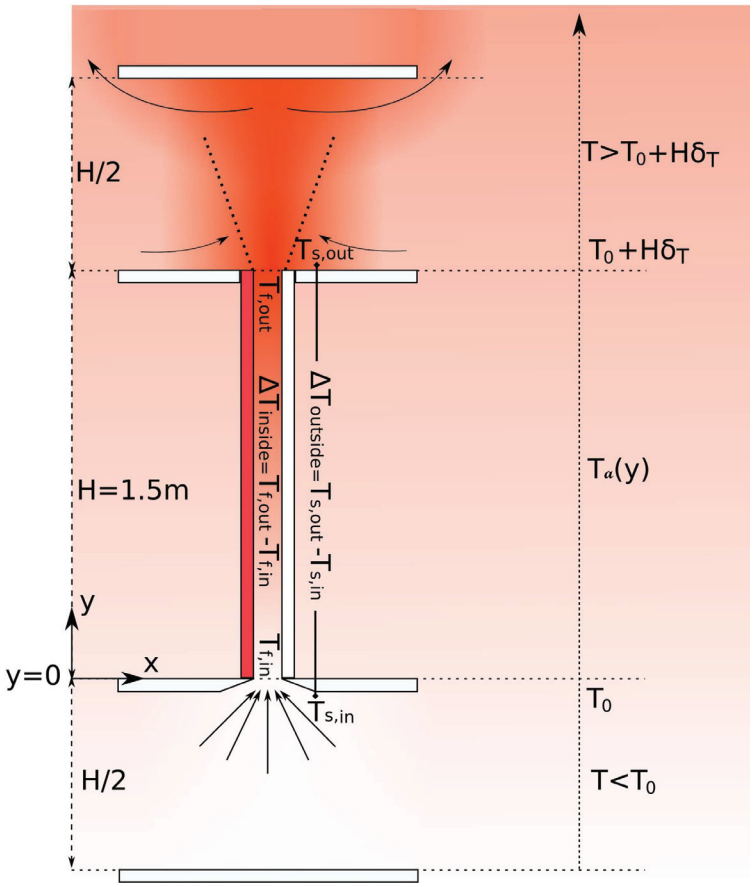

Fig. 6.1 Schematic diagram of the mid-plane flow in the apparatus and its associated simplified temperature distribution represented by the background colour. The plain black arrows approximately indicate flow pattern and the red rectangle represents the heated wall whilst white rectangles are adiabatic walls.

Considering now the Boussinesq approximation, which validity domain had been discussed amongst others by Gray and Giorgini (1976) $\rho(\mathrm{kg/m^3})$ the density of the fluid at a temperature T (K) can be expressed as

$$\rho = \rho_0(1 - b(T - T_0)). \tag{6.4}$$

Where ρ_0 ($\mathrm{kg/m^3}$) is the reference density of the fluid taken at T_0, In that context equation (6.3) can be expressed as the temperature difference

$$T_{(f,out)} \geq T_{(s,out)}. \tag{6.5}$$

Defining ΔT_{inside} (K), the temperature difference between the fluid exiting and the fluid entering the channel, and $\Delta T_{outside}$ (K), the temperature drop, in the immediate surrounding region outside the channel, between the top and the bottom of the channel, then by definition

$$\Delta T_{inside} = T_{(f,out)} - T_{(f,in)}, \text{ and } \Delta T_{outside} = T_{(s,out)} - T_{(s,in)} \tag{6.6}$$

From equation (6.2) and equation (6.5), it follows that an inherent consequence when an upward flow occurs in this configuration is that

$$\Delta T_{inside} \geq \Delta T_{outside}. \tag{6.7}$$

Therefore the inside temperature difference ΔT_{inside} can be written as

$$\Delta T_{inside} = \Delta T_{outside} + \Delta T_{eff}, \tag{6.8}$$

with ΔT_{eff} corresponding to the effective temperature rise. By definition,

$$\Delta T_{eff} \geq 0 \tag{6.9}$$

6.2.2 The temperatures in the outside vicinity of the open boundaries of the channel, and their dependence on the far field conditions in a linearly stratified ambient environment

In order to estimate the boundary conditions at the open ends of the channel, the far-field conditions have been usually used. In that case, the temperature drop in the outside vicinity of the open-boundaries, $\Delta T_{outside}$, defined in the previous section, is equal to $H\delta_T$, the temperature drop in the far-field ambient over the height of the channel. However, the choice of the inlet and outlet boundary conditions currently remains an open question. Indeed, it has been showed in numerous numerical studies (Dalbert et al., 1981; Desrayaud et al., 2013; Garnier, 2014; Zoubir,

2014) that using far-field conditions leads to an overestimate of the induced mass flow rate, compared with the one calculated from experimental results.

An alternative approach is proposed in this section for the case of a thermally stratified ambient atmosphere. To that extent inlet and outlet entrainment regions are introduced, outside the channel, in the vicinities of the open-boundaries. These bottom and top regions, the temperature of which are respectively $T_{(s,in)}$ and $T_{(s,out)}$, link the channel open-boundaries and the far-field conditions.

Considering the I-type geometry, defined by Manca et al. (1994), of the experimental device figure 3.1, the horizontal walls on each side of the channel inlet constraint the fluid in the inlet entrainment region to be entrained from levels lower than the entrance. Therefore the average temperature of the fluid in that region $T_{(s,in)}$ is lower or at most equal than that occurring in the far-field at the level of the channel entry T_0 so that if

$$\Delta T_{inlet} = T_{(s,in)} - T_0. \tag{6.10}$$

Then

$$\Delta T_{inlet} \leq 0. \tag{6.11}$$

With ΔT_{inlet} (K), the temperature difference between the inlet entrainment region and the far-field temperature at the level of the inlet.

Similarly at the outlet, the fluid in the entrainment region is entrained from levels higher than the outlet so that $T_{(s,out)}$ is higher or at least equal to the temperature far-field at the same height. If ΔT_{outlet} denotes the excess in temperature of the entrained fluid over the temperature pertaining at the same level as the outlet of the channel so that

$$\Delta T_{outlet} = T_{(s,out)} - (T_0 + H\delta_T). \tag{6.12}$$

Then

$$\Delta T_{oulet} \geq 0. \tag{6.13}$$

Therefore by substituting equations (6.10) and 6.12 in the expression of $\Delta T_{outside}$, equation 6.6 becomes

$$\Delta T_{outside} = \Delta T_{outlet} - \Delta T_{inlet} + H\delta_T, \tag{6.14}$$

with equations (6.11) and 6.13 giving

$$\Delta T_{outlet} - \Delta T_{inlet} \geq 0. \tag{6.15}$$

The temperature $T_{(s,in)}$ results from a mixing of fluid entrained at levels between the floor and the inlet height. As a first approximation, suppose that $T_{(s,in)}$ is equal to the temperature, far

field, at mid height between the floor and the inlet of the channel resulting in

$$T_{(s,in)} \simeq T_0 - \frac{1}{4} H \delta_T, \tag{6.16}$$

and

$$\Delta T_{inlet} \simeq -\frac{1}{4} H \delta_T. \tag{6.17}$$

Similarly at the outlet, because of the horizontal walls, the entrained fluid arriving from regions above the exit would be warmer than the far-field ambient fluid at the level of the channel outlet. Further, because of the semi-confined configuration stemming from the presence of the artificial ceiling, $T_{(s,out)}$ is assumed to correspond to the temperature, in the ambient, at the level half way between outlet and the artificial ceiling, namely so that

$$T_{(s,out)} \simeq T_0 + H \delta_T + \frac{1}{4} H \delta_T, \tag{6.18}$$

and

$$\Delta T_{outlet} \simeq \frac{1}{4} H \delta_T. \tag{6.19}$$

It follows that under these simple assumptions,

$$\Delta T_{outlet} - \Delta T_{inlet} \simeq \frac{1}{2} H \delta_T, \tag{6.20}$$

and consequently $\Delta T_{outside}$ can be estimated as

$$\Delta T_{outside} \simeq \frac{3}{2} H \delta_T. \tag{6.21}$$

The assessment for ΔT_{inlet} and ΔT_{outlet} proposed in this subsection is based on the geometric characteristics of the studied channel. Note that these assessments are specific to this channel configuration and would require new evaluation in the case of different channel geometries.

The estimates made in the present section are not valid when there is no heat input *i.e.* no flow inside the channel, as in that particular case, there are no entrainment region at the open boundaries and consequently the temperature distribution inside the channel is the same as the far-field ambient temperature distribution.

6.2.3 Reference case of a non-stratified ambient

In order to obtain the analytic relation between the mass flow rate and the external thermal stratification, the case of a non-stratified ambient, $\delta_T = 0$, is first considered and taken as the reference case.

The energy conservation is first used in order to obtain the energy balance of this flow configuration. In a real natural convection vertical channel flow, the energy balance is extremely difficult to perform and strong assumptions needs to be used in order to obtain an estimate of the energy budget. In appendix C, the details of the energy balance and the hypothesis made for that flow configuration are presented. It falls that the energy transfer rate inside the channel can be estimated as

$$Q = \dot{m}_{ref} C_p \Delta T_{ref}, \tag{6.22}$$

With $\dot{m}_{ref} = \dot{m}(\delta_T = 0)$ and $\Delta T_{ref} = \Delta T_{inside}(\delta_T = 0)$ being respectively the mass flow rate and the internal temperature rise through the channel when there is no stratification in the ambient. In that case, the operating point $(\dot{m}_{ref}, \Delta T_{ref})$ of the channel results from the balance between the stack effect inside the channel, the pressure drop between the top and the bottom of the channel and the viscous friction at the wall. This operating point can be estimated experimentally, numerically or by using analytical models by Brinkworth (2000); Olsson (2004); Sandberg and Moshfegh (2002) or He et al. (2016).

In this non-stratified case, equation (6.21) gives $\Delta T_{outside}(\delta_T = 0) = 0$ and consequently equation (6.8) leads to

$$\Delta T_{eff}(\delta_T = 0) = \Delta T_{inside}(\delta_T = 0) = \Delta T_{ref} \tag{6.23}$$

6.2.4 Case of a stratified ambient

Considering now a positive stratification, $\delta_T \geq 0$. For the same net heat input Q injected in the channel, the first law of thermodynamic leads now to

$$Q = \dot{m} C_p \Delta T_{inside}. \tag{6.24}$$

By substituting equation (6.14) in equation (6.8) it falls

$$\Delta T_{inside} = \Delta T_{eff} + H\delta_T + \Delta T_{outlet} - \Delta T_{inlet}. \tag{6.25}$$

For small δ_T, which corresponds to weakly stratified environment, ΔT_{eff} can be expressed using a Taylor development so that

$$\Delta T_{eff}(\delta_T) = \Delta T_{eff}(\delta_T = 0) + \Delta T'_{eff}(\delta_T = 0)\delta_T + O\left(\delta_T^2\right) \tag{6.26}$$

Where $\Delta T'_{eff}$ is the first derivative of ΔT_{eff} with respect to δ_T. Substituting equation equation (6.23) in equation equation (6.26) and factorising by ΔT_{ref}, equation (6.26) can be written as

$$\Delta T_{eff}(\delta_T) = \Delta T_{ref}(1 + h(\delta_T)) \tag{6.27}$$

with the limit of $h(\delta_T)$ being 0 as δ_T approaches 0. By substituting equation (6.27) in equation (6.25) and equation (6.25) in equation equation (6.24) it follows that

$$Q = \dot{m}C_p\left[\Delta T_{ref}(1+h(\delta_T)) + H\delta_T + \Delta T_{outlet} - \Delta T_{inlet}\right] \tag{6.28}$$

Replacing Q by its expression in the case of a non-stratified ambient equation (6.22) and simplifying by C_p yields to

$$\dot{m}_{ref}\Delta T_{ref} = \dot{m}\left[\Delta T_{ref}(1+h(\delta_T)) + H\delta_T + \Delta T_{outlet} - \Delta T_{inlet}\right] \tag{6.29}$$

Which can be rearranged as follows

$$\frac{\dot{m}}{\dot{m}_{ref}} = \frac{1}{1+h(\delta_T)+\frac{H\delta_T+\Delta T_{outlet}-\Delta T_{inlet}}{\Delta T_{ref}}} \tag{6.30}$$

At this stage the limit case when $h(\delta_T) \simeq 0$ is considered. This case is valid for small enough external thermal gradients. In that case equation (6.30) can be written as

$$\frac{\dot{m}}{\dot{m}_{ref}} \simeq \frac{1}{1+S_T}, \tag{6.31}$$

in which S_T is,

$$S_T = \frac{H\delta_T + \Delta T_{outlet} - \Delta T_{inlet}}{\Delta T_{ref}}. \tag{6.32}$$

The non-dimensional stratification parameter S_T represents the ratio of the external temperature increase between the open-boundaries of the channel in a stratified atmosphere, to the average internal temperature rise of the air flowing in the channel when the external atmosphere is at a uniform temperature.

6.3 Experimental validation

The theory developed in section 6.3 led to a non-dimensional formula that relates the mass flow rate to the external temperature gradient. However the evaluation of parameters ΔT_{inlet}, ΔT_{outlet} and $\dot{m}_{ref}$ is still to be addressed. Experimental data were collected either from measurements made by the authors in an air channel or from experimental data obtained Daverat et al. (2011) in water channel heated on both sides was studied.

6.3.1 Experimental mass flow rates

The average mass flow rate in the air channel can be estimated, on the assumption that the flow is two-dimensional, using the time-averaged velocity and temperature profiles measured at the

inlet in the center-plane ($z/W = 0.5$). This may lead to a slight error of the mass flow rate as three-dimensional effects have been neglected.

In figure 6.2 the time-averaged mass flow rate, $\dot{m}$ (kg/s), is plotted as a function of the external temperature gradient, δ_T, for the three cases studied. Each point corresponds to the mass flow rate time-averaged over one measurement period (15 min). The associated error bars, calculated from the experimental uncertainties are plotted for each measurement. It is clear from figure 6.2 that the mass flow rate is a function of the external temperature gradient. Where possible, a linear curve of best fit had been plotted so as to highlight the relationship.

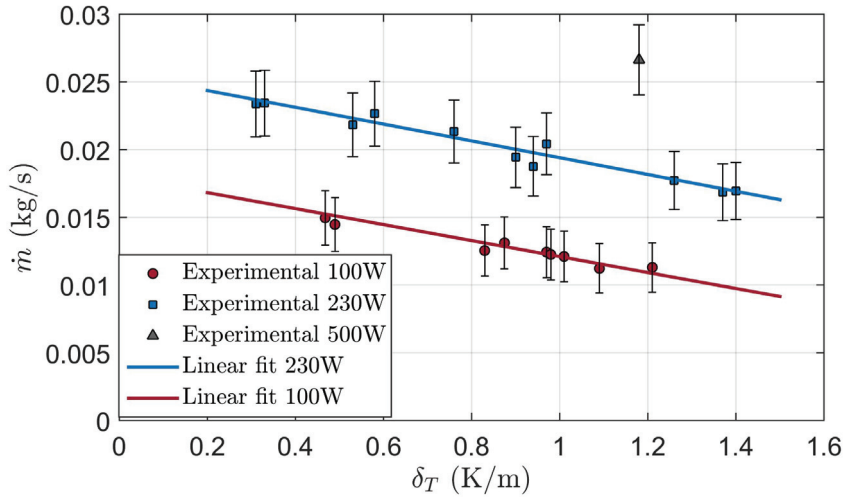

Fig. 6.2 Time-averaged mass flow rate, $\dot{m}$ against the thermal gradient within the room δ_T, for three different injected powers of Q_t=100, 230 and 500 W, and their associated error bars. The linear curve of best fit has been plotted as dashed line for the cases 100 W and 230 W respectively

It can be seen in figure 6.3 that the maximum wall-temperature h_T is located significantly lower than y/H=1 for each cases which means that the flow is in the transitional configuration as defined in section 5.5.1.

6.3.2 Experimental evaluation of ΔT_{inlet}, ΔT_{outlet} and m_{ref}

Present configuration: Air channel 100 W and 230 W cases

In the experimental apparatus presented in figure 3.1 thermocouples had been installed, as mentioned in section 3.2, at the inlet and at the edge of the outlet, in the mid plane $y/W = 0.5$. Therefore the temperature of the entrained fluid at the inlet had been measured as well as the temperature of the air entrained by the column of air exiting the channel, so that ΔT_{inlet} and ΔT_{outlet} could be evaluated. As the external temperature stratification δ_T increased, ΔT_{inlet} and ΔT_{outlet} respectively decreased and increased. They were evaluated from the slopes of the linear regressions of equations (6.10) and 6.12. The results are presented in table 6.1 and show good

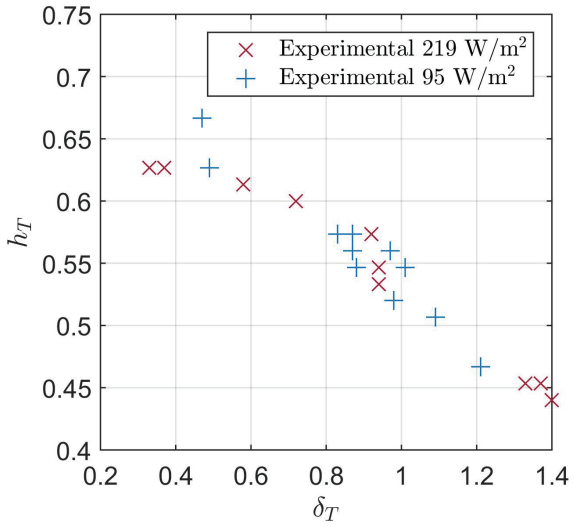

Fig. 6.3 Evolution of h_T for the various δ_T under study in the experimental cases

agreement with the assessments given by equation (6.17) and equation (6.19) in section 6.2.2. Note that ΔT_{inlet} is a linear function of δ_T in its literal algebra sense i.e. an extrapolation of T_{inlet} to $\delta_T = 0$ yields T_0. The

Table 6.1 Experimental ΔT_{inlet},ΔT_{outlet}, for the two data set 100 W and 230 W

Case	Exp. ΔT_{inlet} (K)	Exp. ΔT_{outlet} (K)
100 W	$-0.24H\delta_T$	$0.32H\delta_T$
230 W	$-0.25H\delta_T$	$0.37H\delta_T$

Since a non-stratified atmosphere is very hard to establish in a laboratory, the authors, could not directly measure $\dot{m}_{ref}$. A first approach would be to calculate the intercept of the linear curves of best fit plotted in figure 6.2. However, since extrapolation is also dangerous, another way is to rewrite equation (6.31) as

$$\dot{m}_{ref} = \frac{\dot{m}}{1 - \frac{\dot{m}C_p(H\delta_T + \Delta T_{outlet} - \Delta T_{inlet})}{Q}}. \tag{6.33}$$

The solution of equation (6.33) can be obtained for any set of $(Q, \dot{m}, \delta_T)$ using either the expressions of ΔT_{inlet} and ΔT_{outlet} available in table 6.1 or the coefficient assumed in section 6.2.2. Because whichever set is used, the values are similar, with a difference of less than 2% in the value of $\dot{m}_{ref}$, in what follows, the coefficients assumed in section 6.2.2 will be used. At a given heat input Q the $\dot{m}_{ref}$ obtained for different set of $(\dot{m}, \delta_T)$ were not exactly the same. As a result the average and standard deviation σ were calculated and since, as may be seen in table 6.2, σ, is quite small, the values of $\dot{m}_{ref}$ in table 6.2 are used in the remainder of the chapter.

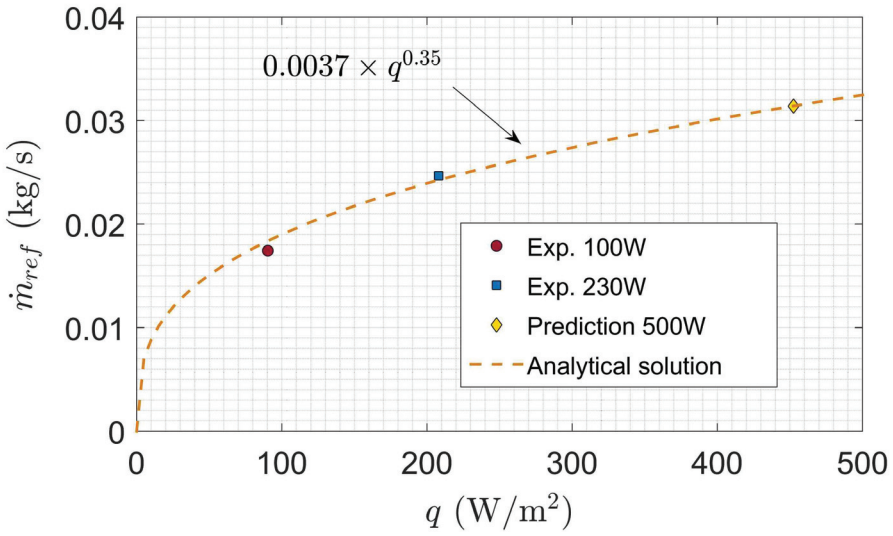

Fig. 6.4 The mass flow rate in an isothermal atmosphere plotted against the heat flux for the cases 100 W and 230 W. This figure also shows the correlation calculated from these cases and the prediction for 500 W

Table 6.2 $\dot{m}_{ref}$ and σ for the two data set 100 W and 230 W

Case	$\dot{m}_{ref}$ (kg/s)	σ (kg/s)
100 W	0.0174	0.0006
230 W	0.0246	0.0014

Present configuration: Air channel 500 W

Only one measurement was available for the 500 W case, so that $\dot{m}_{ref}$ could not be calculated as was done above. As a consequence a correlation was used instead. It is commonly accepted that $\dot{m}_{ref}$ varies as a power of the net heat flux (see e.g. (Moshfegh and Sandberg, 1996)) so that $\dot{m}_{ref}$ q^{ζ} in which q (W/m^2) is the heat flux associated to the net heat input Q and ζ is a coefficient that depends on the Rayleigh number. Khanal and Lei (2015) proposed that $\zeta = 0.35$ for $Ra > 10^{11}$.

Regarding the range of investigated Rayleigh numbers in table 3.1, it is thus assumed a constant $\zeta = 0.35$. In figure 6.4 is plotted $\dot{m}_{ref}$ as a function of net heat flux for 100 W, 230 W and 500 W obtained from the correlation $\dot{m}_{ref} = 0.0037 q^{0.35}$. Since this correlation fits the experimentally estimated values of $\dot{m}_{ref}$ well for 100 W and 230 W cases, the value of $\dot{m}_{ref}$ for the 500 W will therefore be used.

Configuration of Daverat et al. (2011): Water channel

The experiments of Daverat et al. (2011) were carried out in a water channel, uniformly heated on both sides. The channel is 0.6 m height for 0.23 m wide, the two walls being 0.05 m apart and is located in a water tank of dimensions $1.50 \times 0.63 \times 0.23$ m^3. The net heat flux supplied to the channel was 190 W/m^2 and the corresponding Rayleigh number is $Ra = 2.9 \times 10^4$. The ratio between the water tank height and the water channel height is similar to the ratio between the artificial ceiling height and the channel height of the present channel (see section 3.2), as a consequence, the same values of ΔT_{inlet} and ΔT_{outlet} have been evaluated. They provide a measure of the mass flow rate $\dot{m}_{ref}$ for a uniform temperature distribution outside the channel.

6.3.3 Prediction of the non-dimensional mass flow rate

Experimental results for the cases obtained in the air channel 100 W, 230 W and 500 W as well as the experimental data of Daverat et al. (2011) obtained in the water channel have been plotted in figure 6.5.

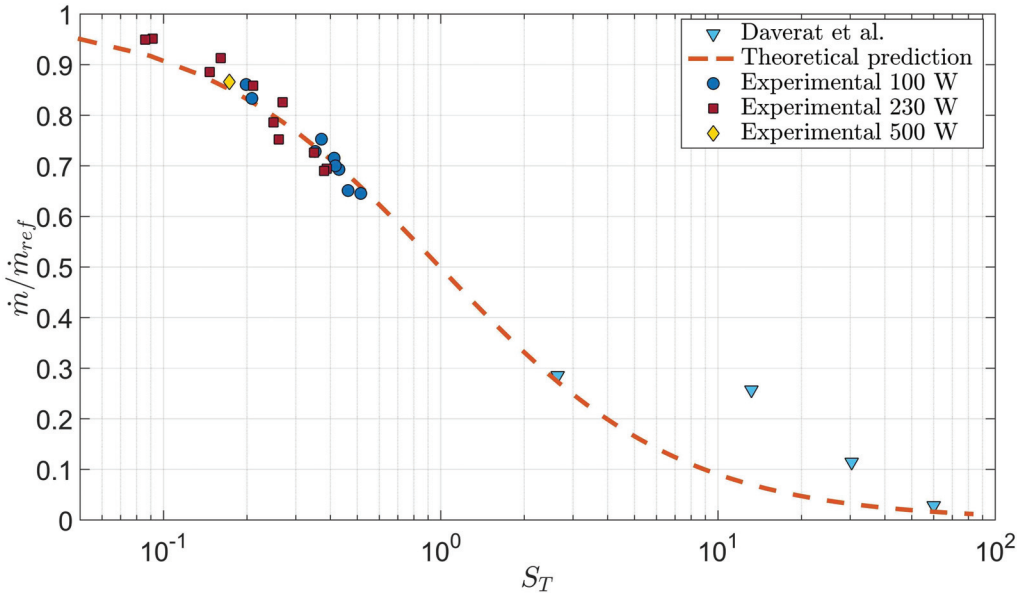

Fig. 6.5 Non-dimensional mass flow rate as a function of the non-dimensional stratification parameter S_T

The data closely cluster around the curve obtained from equation (6.31). The experimental results for the air channel, obtained in this work, are in excellent agreement with the theoretical prediction with a maximum relative deviation of less than 5%. The maximum relative uncertainties, calculated from the experimental uncertainties, are around 12% on the ratio $\dot{m}/\dot{m}_{ref}$ and around 5% on the stratification parameter S_T. There is also an excellent agreement with the first experimental data point obtained in the water channel by Daverat et al. (2011) for $S_T = 2.6$

which represents a stratification parameter five times higher than that obtained in the air channel. However the next two experimental points obtained in the water channel cannot be accurately predicted. This can be explained from the fact that, past a certain level of stratification, the water channel is not flowing full, as can be seen in Daverat et al. (2011). Instead, two separate boundary layer flows develop independently on each wall of the channel with an important quasi-stagnant region in the middle of the channel. In these conditions the channel flow cannot be considered as 1-D and the model developed in section 6.2 in its present form is not suitable. In that specific case it would have been possible to derive a similar model as the one developed in section 6.2 by evaluating the temperature of the fluid feeding the boundary layer flows, from the temperature distribution in the quasi-stagnant zone. However this would require additional temperature data which is not provided by Daverat et al. (2011).

Thus the proposed approximate analysis allows all the available experimental results, of the dependence of the mass flow rate induced by natural convection in a heated open channel on the external thermal gradient to be represented by a single curve.

6.4 Numerical validation including negative stratification

In this section, the theory developed above is compared to numerically generated data. The numerical cases are the same as those presented in the previous chapter and therefore include cases of weak and negative thermal stratification.

In the numerical results, ΔT_{out} and ΔT_{in} are found to vary linearly with $H\delta_T$ and their values have been reported in table 6.3. Another important parameter of the predictive model is the evaluation of $\dot{m}_{ref}$ which corresponds to the mass flow rate in the channel when there is no stratification. In the experiments presented above, it was not possible to obtain an experimental evaluation of $\dot{m}_{ref}$ because the stratification was always positive, as a consequence its value was obtained by extrapolation of the experimental data.

However, as can be noted in figure6.3 the experimental flow was always in a transitional regime as was defined in section 5.5.1. Considering now the numerically obtained mass flow rate plotted in figure6.6 in issue is raised considering the evaluation of $\dot{m}_{ref}$. Indeed, the $\dot{m}_{ref}$ that can be calculated from an extrapolation of the mass flow rates of the transitional configuration does not correspond to the $\dot{m}_{ref}$ obtained numerically for $\delta_T = 0$.

Table 6.3 Parameters of the theoretical model

	Laminar configuration			Transitional configuration		
Case	ΔT_{inlet}	ΔT_{outlet}	$\dot{m}_{ref}$	ΔT_{in}	ΔT_{out}	$\dot{m}_{ref}$
100 W	$-0.21H\delta_T$	$0.07H\delta_T$	0.0205	$-0.21H\delta_T$	$0.28H\delta_T$	0.0167
230 W	$-0.23H\delta_T$	$0.10H\delta_T$	0.0264	$-0.23H\delta_T$	$0.27H\delta_T$	0.0210

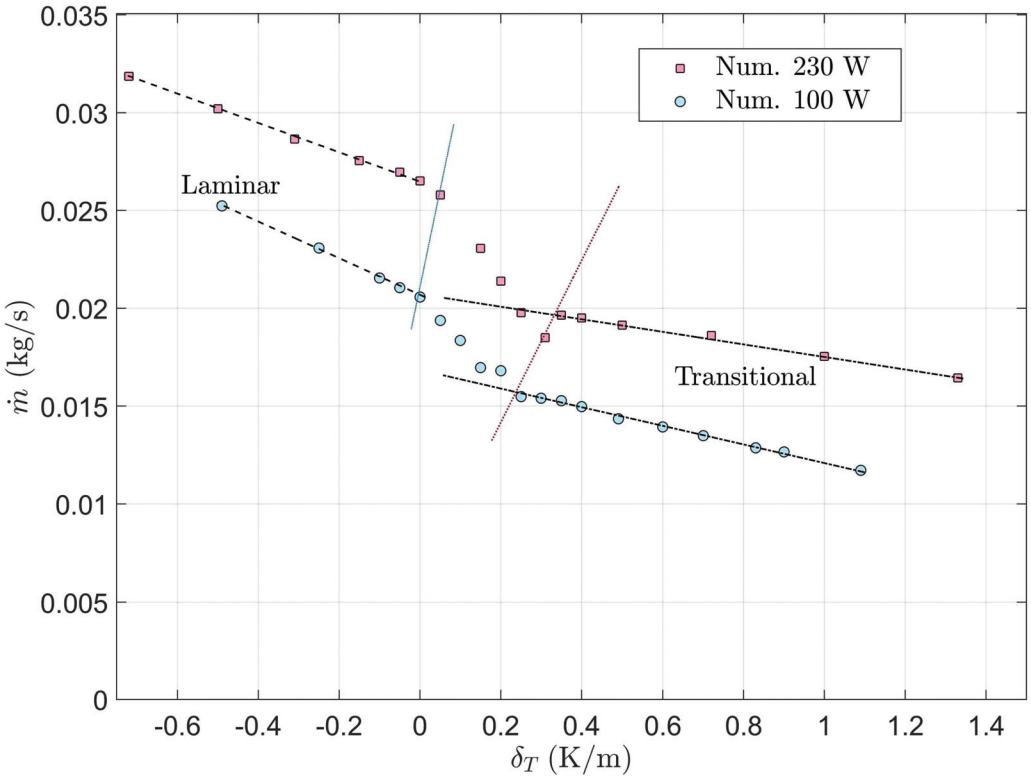

Fig. 6.6 Time averaged numerically obtained mass flow rates as a function of the external thermal stratification

Because the theory developed in section 6.2 did not include potential changes in the flow configuration, two different $\dot{m}_{ref}$ are considered here depending on whether the flow is in the laminar or the transitional configuration. The reference mass flow rate for the laminar flow configurations, $\dot{m}_{ref,lam}$, corresponds to the value obtained numerically at $\delta_T = 0$ K/m. The reference mass flow rate for the transitional configuration $\dot{m}_{ref,tran}$, is evaluated similarly to what was done for the experimental configuration in section. Finally, the data points in the connecting configuration were disregarded in what follows as neither $\dot{m}_{ref,lam}$ nor $\dot{m}_{ref,tran}$ yielded a good result. This was expected as probably complex transitional phenomena would be likely to appear for this configuration and would strongly alter the flow behaviour.

The non-dimensional mass flow rates scaled by $\dot{m}_{ref,lam}$ or $\dot{m}_{ref,tran}$ have been plotted against S_T in figure 6.7. The experimental data were reported as well. As can be seen, the theoretical model predicts precisely the mass flow rates for the laminar and transitional configurations with differences below 1%.

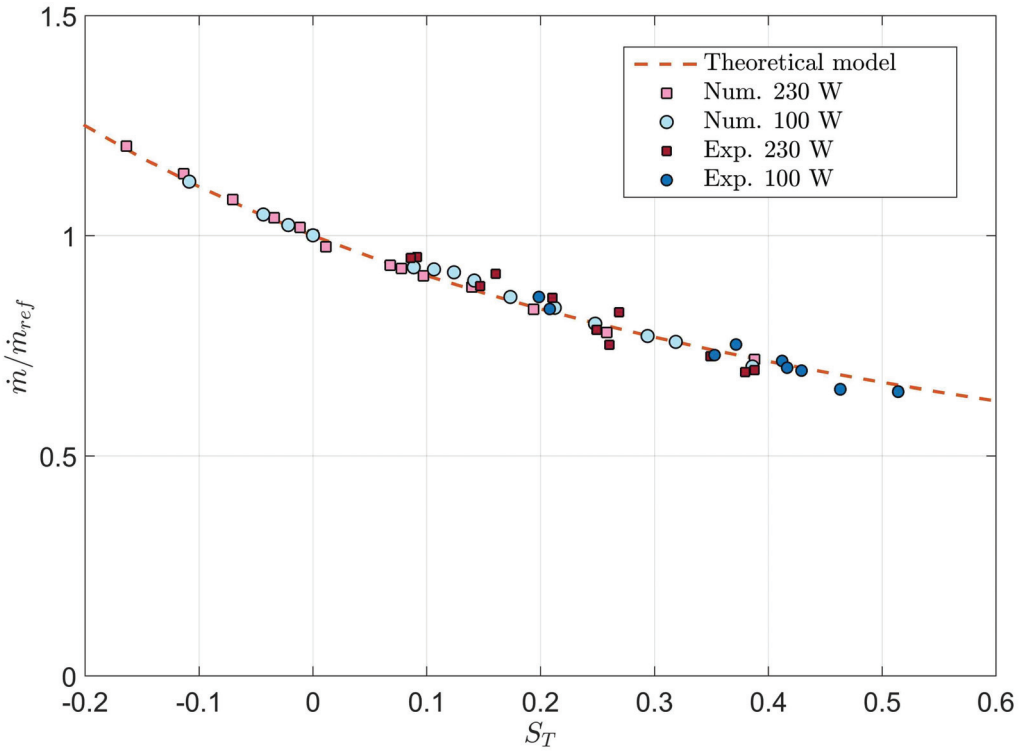

Fig. 6.7 Non-dimensional mass flow rated plotted against the stratification parameter S_T. Pink squares - Numerical 230 W, Light Blue circles Numerical - 100 W, Red squares - Experimental 230 W, Dark Blue circles Experimental - 100 W, the orange dotted lines plots the analytical solution

6.5 Discussion

6.5.1 Sensitivity of the induced mass flow rate to the external temperature gradient

The sensitivity of the mass flow rate to the injected power, and more commonly to the Rayleigh number can be investigated by doing a basic sensitivity analysis. As discussed in section 6.3.2, the mass flow rate evolves as a power of the Rayleigh number, so that

$$\dot{m}_{ref} \simeq K_1 Ra^{\zeta}. \tag{6.34}$$

Despite that ζ is varying as a function of the Rayleigh number, ζ remains between 0 and 1. Given that the Rayleigh number is directly proportional to the net heat flux, equation (6.31) can be rewritten as

$$\dot{m} = \frac{K_1 Ra^{\zeta}}{1 + K_2 \frac{H\delta_T + \Delta T_{outlet} - \Delta T_{inlet}}{Ra^{1-\zeta}}}, \tag{6.35}$$

where

$$K_2 = \frac{C_p K_1 g b D^4}{A_h a \nu \kappa}, \tag{6.36}$$

A_h (m^2) being the heated area. K_1 and K_2 are positive constant depending on the fluid properties and the channel geometry.

It can be seen from equation (6.35) that as the Rayleigh number increases, the external temperature gradient has a lower influence on the mass flow rate. This remark is consistent with the intuitive thought that, for a given fluid and channel geometry, the mass flow rate is relatively less affected by the external temperature distribution when the injected power increases.

6.5.2 Toward better analytical models

This work contributes to reducing the uncertainty usually attributed to experimental repeatability errors as one source of potential discrepancies has been clearly identified and quantified. This chapter may help explaining some inadequacies found in the literature between experimental measurements and numerically generated or analytically obtained results. This could be the case for the work of Chen et al. (2003) where they noted significant differences between the analytically predicted and the experimentally measured mass flow rate. In their work, the channel dimensions and injected powers are quite similar to those in the present study. However the room ceiling is 2.7 m lower. Consequently it is possible that stronger vertical temperature gradients occurred, inducing a decrease of the mass flow rate. Despite that the external temperature stratification was not reported by them, this analysis becomes even more credible when Chen et al. (2003) noticed that the differences between analytically expected results and experimental data drastically reduce as the channel is inclined. Indeed as the channel is inclined, the external temperature drop at the channel open boundaries decreases as well, reducing its impact on the mass flow rate.

In figure 6.8 mass flow rates are plotted against the heat flux injected in the channel. The two sets of blue dots corresponds to the data reported by Chen et al. (2003). The dark blue set corresponds to their analytical prediction while the light blue dots corresponds to the mass flow rates experimentally measured. It can be seen that there is a significant differences. Now considering an external thermal stratification of δ_T=1.5 K/m, which corresponds to the highest stratification observed in the present work, the difference between the experimental and analytical results drastically reduces. An almost perfect agreement is reached for δ_T=2.5 K/m. This last stratification level may seem high and is 1 K highest than any δ_T observed in the present configuration, but given the relatively low ceiling height, almost twice as low as the ceiling in the present study, it may be possible for strong δ_T to occur in the study of Chen et al. (2003).

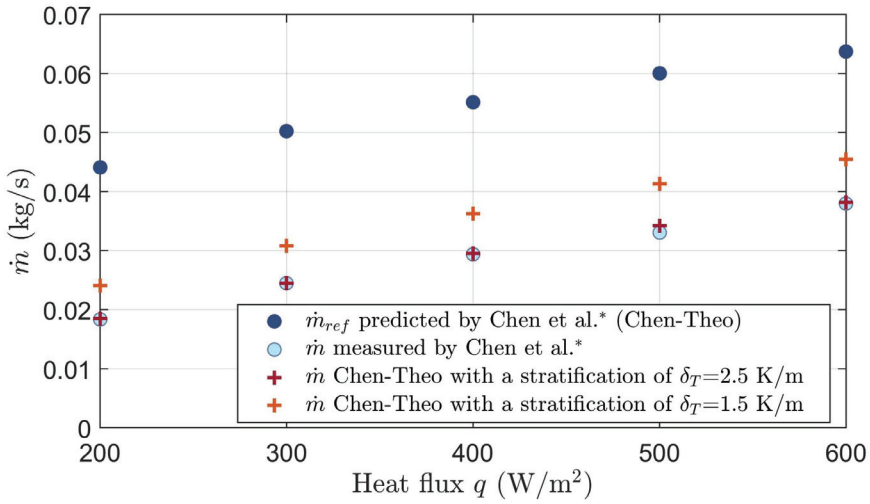

Fig. 6.8 Experimental and analytical results of Chen et al. (2003) as well as their analytical results considering various external thermal stratification.

6.6 Partial conclusion

In this chapter, the impact of the external temperature stratification on the mass flow rate induced in a vertical uniformly heated channel was investigated experimentally numerically and theoretically.

In order to obtain a non-dimensional relation, to collapse on a single curve the results obtained at different injected powers and different external temperature gradients, a steady one-dimensional theory has been developed. This theoretical model is in excellent agreement with experimental data collected on an air channel, as well as some data, from the literature, obtained in a water channel. It can also predict very accurately the mass flow rates numerically obtained for negative and positive stratifications.

More specifically, this model provides a way to estimate the impact of the external temperature gradient on the mass flow rate which, as a consequence, reduces the inadequacies observed between experimental measurements and analytically or numerically generated results. It therefore removes one of the potential sources of difference, usually neglected by the numericists. It demonstrates also that experimentalists have to provide additional information on the external thermal gradient while performing measurements on natural convection in vertical channels.

Moreover, despite the fact that the one-dimensional steady model has been developed without including the Prandtl or Rayleigh numbers, the agreement between the experimental and theoretical results, for various fluids, seems to suggest that these do not need to be included in the analysis as long as the channel is flowing full.

Chapter 7

Conclusion and perspectives

7.1 Conclusion

An experimental and a numerical investigation has been performed on a spatially developing transitional natural convection channel flow in a vertical open-ended channel heated on one side. The research is focused on two phenomena: the first on the intermittent coherent structures generated as the flow develops, partly as the result of disturbances ingested into the channel from the surroundings and the second on the effects that thermal gradients in the laboratory have on the flow in the channel.

The effect of the disturbances, occurring naturally within the laboratory was modelled numerically. These disturbances drastically change the time-averaged as well as the intermittent flow behaviour. Moreover, whereas transition is not observed when there are no perturbations once the perturbation is introduced the transition is triggered within the channel. Another consequence of the introduction of a disturbance in the flow is the increased number of intermittent structures which play a great role in the heat transfer.

A numerical three-dimensional transitional flow was simulated and the study of the intermittent structures generated by the flow was carried out using Proper Orthogonal Decomposition and Spectral Proper Orthogonal Decomposition. It is shown that SPOD is a powerful tool to extract spatio-temporal modes, the most energetic of which are classified, based on their frequency content, into two great families: the low-frequency (LF) and the mid-frequency (MF) modes. These families appear to have two distinct behaviours. The LF-modes represent long correlated thermal-velocity streamwise streaks, which do not influence much the turbulent heat transfer growth rate at the wall. The MF-modes are drastically different and appear in the transitional region. They represent staggered structures which sometimes have a characteristic v-shape. These modes play a role in the growth of the turbulent heat transfer rate within the transitional region.

These two characteristic types of structures are similar, in shapes and in role, to the structures that are observed in the by-pass transition in forced convection. Thus, despite the fact that the flow is driven by entirely different mechanisms from forced convection, the ingestion of external disturbances into the flow, results in a natural convection type of by-pass transition.

Experimentally, the local maximum of temperature reached at the heated wall, referred here as h_T has commonly been used as an indicator of transition. Since in the numerical solutions velocity fields are available and it is instabilities in the velocity field which drive turbulence, it should also be possible to define criteria, other than the maximum temperature on the heated wall, as indicators of transition. One possibility studied was the height at which the maximum near wall velocity is reached. This indicator was referred to as h_v. At levels higher than h_T and h_v, strong changes in the time averaged velocity and temperature distributions are observed. These indicators indicates advanced stages in the transition.

Other indicators that suggest early stages of the transition, based on the turbulence characteristics were identified. The height h_e indicates the level at which the growth of the maximum velocity at the wall starts to decrease and the height at which the minimum temperature in the bulk of the channel starts to considerably increase. These indicators may not be a pointer to changes in the time averaged velocity and temperature fields within the channel. However it proved able to capture the changes in the turbulent intensity developments. Another indicator h_c was defined as the height at which the correlation between the near wall streamwise velocity and temperature reaches its maximum. These indicators indicates early stages in the transition.

Since the environment in the laboratory was not controlled in addition to flow disturbances ingested into the channel, the external thermal gradient was another factor which needed to be taken into consideration. A numerical, experimental and theoretical investigation was then carried out to demonstrate that the hitherto neglected thermal stratification in the environment outside the channel is a major parameter which significantly impacts the flow.

It is shown that an increase of the external positive upward thermal gradient provokes a decrease of the mass flow rate and a displacement of the transition location to a lower region of the channel. Whereas rise in the magnitude of a negative upward external thermal gradient causes an increase in the mass flow rate. Numerically the changes in the mass flow rate reach nearly 100% between a stratification of -0.5 K/m and 1 K/m. In the numerical investigations it is observed that for weak enough and negative stratifications, transition does not occur any more within the channel, and as a consequence the maximum temperature at the hot wall increases by up to 20%. Experimentally only a change in stratification by 1 K/m yields a change in the mass flow rate by 35%. It is now clear that thermal stratification explains, at least in part, the difficulties experienced in achieving repeatability in experimental mass flow rates under supposedly identical conditions.

A non-dimensional theoretical model is then proposed to predict the impact of the external thermal stratification on the induced mass flow rate. There is excellent agreement between the

theory and the experimental results and numerical data with positive upward external thermal gradients. The model also accurately predicts numerical results for negative upward thermal gradients.

7.2 Future Works

Transitional natural convection flow is a very complex flow, and the present dissertation provided some answers as to the impact of the surroundings on the flow as well as on the knowledge of the flow itself. It also opened the scope for different perspectives listed below.

- **Characterisation of various inlet velocity disturbances and their impact:** Unless the whole environment of the channel is to be modelled, the inlet conditions and particularly the inlet velocity disturbances must be better characterized by performing a detailed experimental studies of their nature. Experimentally, two or three dimensional velocity measurements as well as thermal measurements would provide better knowledge of these structures. The variation in the inlet flows from one laboratory to another need to be evaluated, since numerically these structures need to be properly modelled so that the flow behaviour can be accurately determined.

- **Three-dimensional characterisation of the experimental flow structures:** It was numerically shown that the structures observed are highly three-dimensional. For this reason, the uses of stereo PIV, holographic PIV or at least two-dimensional PIV measurements performed in plans parallel to the heated wall would allow a very valuable source of information regarding the structures observed experimentally. It could confirm the nature of the transition and allow a better agreement between numerical generated and experimentally visualised structures.

- **Control of the flow and the heat transfers:** Now that some of the structures which play a role in the transition and in the turbulent heat transfer in the channel have been identified, better control of these structures, would enhance the heat transfer at the hot wall. To that end active or passive disturbance method could be implemented.

- **Non-dimensional analysis:** The numerical/experimental comparisons are not quantitatively perfect and one way to considerably improve them is to develop a proper scaling analysis of the transitional spatially developing natural convection flow in the channel. Amongst others, a non-dimensional analysis could confirm if the numerically and experimentally observed structures are of the same nature.

- **Reduced order model:** As mentioned in the introduction, decomposition methods such as POD are also the first steps in order to build reduced-order-model. These models could provide more efficient models of such flow for integration in building simulation tools.

It should be emphasized that unless thermal stratification in laboratory studies is controlled or at least measured at each occasion, thermal stratification will continue to be a confounding variable in all future work on natural convection in vertical open channels.

References

Abe, A. and Antonia, R. A. (2009). Near-wall similarity between velocity and scalar fluctuations in a turbulent channel flow. *Physics of Fluids*, 21:025109.

Abramov, A. G., Smirnov, E. M., and Goryachev, V. D. (2014). Temporal direct numerical simulation of transitional natural-convection boundary layer under conditions of considerable external turbulence effects. *Fluid Dynamics Research*, 46(4):041408.

Armfield, S., Patterson, J. C., and Lin, W. (2007). Scaling investigation of the natural convection boundary layer on an evenly heated plate. *International Journal of Heat and Mass Transfer*, 50(7-8):1592–1602.

Arndt, R. E., Long, D. F., and Glauser, M. N. (1997). The proper orthogonal decomposition of pressure fluctuations surrounding a turbulent jet. *Journal of Fluid Mechanics*, 340:1–33.

Atta, C. W. V. and Helland, K. N. (1980). Exploratory temperature-tagging measurements of turbulent spots in a heated laminar boundary layer. *Journal of Fluid Mechanics*, 100(2):243–255.

Aubry, N., Holmes, P., Lumley, J. L., and Stone, E. (1988). The dynamics of coherent structures in the wall region of a turbulent boundary layer. *Journal of Fluid Mechanics*, 192:115–173.

Auletta, A., Manca, O., Morrone, B., and Naso, V. (2001). Heat transfer enhancement by the chimney effect in a vertical isoflux channel. *International Journal of Heat and Mass Transfer*, 44(22):4345–4357.

Aung, W. (1972). Fully developed laminar free convection between vertical plates heated asymmetrically. *International Journal of Heat and Mass Transfer*, 15(8):1577–1580.

Aung, W., Fletcher, L., and Sernas, V. (1972). Developing laminar free convection between vertical flat plates with asymmetric heating. *International Journal of Heat and Mass Transfer*, 15(11):2293–2308.

Bailon-Cuba, J. and Schumacher, J. (2011). Low-dimensional model of turbulent rayleigh-bénard convection in a cartesian cell with square domain. *Physics of Fluids*, 23(7):077101.

Bar-Cohen, A. and Rohsenow, W. (1984). Thermally optimum spacing of vertical, natural convection cooled, parallel plates. *Journal of Heat Transfer*, 106(1):116–123.

Berkooz, G., Holmes, P., and Lumley, J. L. (1993). The proper orthogonal decomposition in the analysis of turbulent flows. *Annual review of fluid mechanics*, 25(1):539–575.

Bloem, J. (2008). Evaluation of a pv-integrated building application in a well-controlled outdoor test environment. *Building and Environment*, 43:205–216.

Bodoia, J. and Osterle, J. (1962). The development of free convection between heated vertical plates. *Journal of Heat Transfer*, 84(1):40–43.

Borgers, T. and Akbari, H. (1984). Free convective turbulent flow within the trombe wall channel. *Solar Energy*, 33(3-4):253–264.

Brady, P. (2013). Interaction between turbulent natural convection in a channel and the surroundings. In *8th Australian Natural Convection Workshop*.

Brangeon, B., Joubert, P., and Bastide, A. (2015). Influence of the dynamic boundary conditions on natural convection in an asymmetrically heated channel. *International Journal of Thermal Sciences*, 95:64–72.

Brinkworth, B. J. (2000). Estimation of flow and heat transfer for the design of pv cooling ducts. *Solar Energy*, 69:413–420.

Brinkworth, B. J. and Sandberg, M. (2006). Design procedure for cooling ducts to minimise efficiency loss due to temperature rise in pv arrays. *Solar Energy*, 80:89–103.

Campo, A., Manca, O., and Morrone, B. (1999). Numerical analysis of partially heated vertical parallel plates in natural convective cooling. *Numerical Heat Transfer: Part A: Applications*, 36(2):129–151.

Cantwell, B. J. (1981). Organized motion in turbulent flow. *Annual Review of Fluid Mechanics*, 13(1):457–515.

Carpenter, J., Briggs, D., and Sernas, V. (1976). Combined radiation and developing laminar free convection between vertical flat plates with asymmetric heating. *Journal of Heat Transfer*, 98(1):95–100.

Cheesewright, R. (1967). Natural convection from a plane, vertical surface in non-isothermal surroundings. *International Journal of Heat and Mass Transfer*, 10:1847–1859.

Chen, C.-H. P. and Blackwelder, R. F. (1978). Large-scale motion in a turbulent boundary layer - a study using temperature contamination. *Journal of Fluid Mechanics*, 89:1–31.

Chen, Z., Bandopadhayay, P., Halldorsson, J., Byrjalsen, C., Heiselberg, P., and Li, Y. (2003). An experimental investigation of a solar chimney model with uniform wall heat flux. *Building and Environment*, 38:893–906.

Chinesta, F., Keunings, R., and Leygue, A. (2014). In *The Proper Generalized Decomposition for Advanced Numerical Simulations*. Springer International Publishing.

Chong, M. S., Perry, A. E., and Cantwell, B. J. (1990). A general classification of three-dimensional flow fields. *Physics of Fluids A: Fluid Dynamics*, 2(5):765–777.

Dalbert, A., Penot, F., and Peube, J. (1981). Convection naturelle laminaire dans un canal vertical chauffé à flux constant. *International Journal of Heat and Mass Transfer*, 24:1463–1473.

Daverat, C. (2012). *Etude expérimentale de la convection naturelle en canal vertical à flux de chaleur imposé: application au rafraîchissement passif de composants actifs de l'enveloppe des bâtiments*. PhD thesis, Lyon, INSA.

Daverat, C., Li, Y., Pabiou, H., Ménézo, C., and Xin, S. (2017). Transition to turbulent heat transfer in heated vertical channel - experimental analysis. *International Journal of Thermal Sciences*, 111:321–329.

Daverat, C., Pabiou, H., Bouia, H., Xin, S., and Ménézo, C. (2011). Convection naturelle dans un canal vertical en eau avec chauffage pariétal : influence de la stratification. In *20ième Congrès Français de Mécanique*, number 20, pages 162–167. Presses universitaires de Franche-Comté.

Daverat, C., Pabiou, H., Ménézo, C., Bouia, H., and Xin, S. (2013). Experimental investigation of turbulent natural convection in a vertical water channel with symmetric heating: Flow and heat transfer. *Experimental Thermal and Fluid Science*, 44:182–193.

Desrayaud, G., Chénier, E., Joulin, A., Bastide, A., Brangeon, B., Caltagirone, J., Cherif, Y., Eymard, R., Garnier, C., Giroux-Julien, S., Harnane, Y., Joubert, P., Laaroussi, N., Lassue, S., Quéré, P. L., Li, R., Saury, D., Sergent, A., Xin, S., and Zoubir, A. (2013). Benchmark solutions for natural convection flows in vertical channels submitted to different open boundary conditions. *International Journal of Thermal Sciences*, 72:18 – 33.

Desthieux, G., Carneiro, C., Camponovo, R., Ineichen, P., Morello, E., Boulmier, A., Abdennadher, N., Dervey, S., and Ellert, C. (2018). Solar energy potential assessment on rooftops and facades in large built environments based on lidar data, image processing, and cloud computing. methodological background, application, and validation in geneva (solar cadaster). *Frontiers in Built Environment*, 4:14.

Dupont, F., Ternat, F., Samot, S., and Blonbou, R. (2013). Two-dimension experimental study of the reverse flow in a free convection channel with active walls differentially heated. *Experimental Thermal and Fluid Science*, 47:150–157.

Elenbaas, W. (1942). The dissipation of heat by free convection the inner surface of vertical tubes of different shapes of cross-section. *Physica*, 9(8):865–874.

Enerdata (2018). Global energy trends, 2018 edition. a step backward for the energy transition?

Fedorov, A. G. and Viskanta, R. (1997). Turbulent natural convection heat transfer in an asymmetrically heated, vertical parallel-plate channel. *International Journal of Heat and Mass Transfer*, 40:3849–3860.

Ferahta, F., Bougoul, S., Médale, M., and Abid, C. (2012). Influence of the air gap layer thickness on heat transfer between the glass cover and the absorber of a solar collector. *Fluid Dynamics & Materials Processing*, 8(3):339–351.

Flohn, H. and Penndorf, R. (1950). The stratification of the atmosphere (i). *Bulletin of the American Meteorological Society*, 31:71–78.

Fossa, M., Ménézo, C., and Leonardi, E. (2008). Experimental natural convection on vertical surfaces for building integrated photovoltaic (bipv) applications. *Experimental Thermal and Fluid Science*, 32:980–990.

Garnier, C. (2014). *Modélisation numérique des écoulements ouverts de convection naturelle au sein d'un canal vertical asymétriquement chauffé*. Phd thesis, Université Pierre et Marie Curie.

George, W. K. (2017). A 50-year retrospective and the future. In *Whither Turbulence and Big Data in the 21st Century?*, pages 13–43. Springer, Cham.

Giroux-Julien, S., Ménézo, C., Vareilles, J., Pabiou, H., Fossa, M., and Leonardi, E. (2009). Natural convection in a nonuniformly heated channel with application to photovoltaic facades. *Computational Thermal Sciences: An International Journal*, 1(3).

Glauser, M. N. and George, W. K. (1987). Orthogonal decomposition of the axisymmetric jet mixing layer including azimuthal dependence. In *Advances in Turbulence*. Springer, Berlin, Heidelberg.

Gray, D. D. and Giorgini, A. (1976). The validity of the boussinesq approximation for liquids and gases. *International Journal of Heat and Mass Transfer*, 19:545–551.

Gresho, P. M. (1991). Incompressible fluid dynamics: some fundamental formulation issues. *Annual review of fluid mechanics*, 23(1):413–453.

Haaf, W., Friedrich, K., Mayr, G., and Schlaich, J. (1983). Solar chimneys part i: Principle and construction of the pilot plant in manzanares. *International Journal of Solar Energy*, 2:3–20.

Hack, M. J. P. and Moin, P. (2018). Coherent instability in wall-bounded shear. *Journal of Fluid Mechanics*, 844:917–955.

Haller, G. (2005). An objective definition of a vortex. *Journal of Fluid Mechanics*, 525:1–26.

Hasan, N. and Sanghi, S. (2007). Proper orthogonal decomposition and low-dimensional modelling of thermally driven two-dimensional flow in a horizontal rotating cylinder. *Journal of Fluid Mechanics*, 573:265–295.

He, G., Zhang, J., and Hong, S. (2016). A new analytical model for airflow in solar chimneys based on thermal boundary layers. *Solar Energy*, 136:614–621.

Hemmer, C., Popa, C., Sergent, A., and Polidori, G. (2016). Heat and fluid flow in an uneven heated chimney. *International Journal of Thermal Sciences*, 107:220–229.

Hemmer, C., Saad, A., Popa, C., and Polidori, G. (2017). Early development of unsteady convective laminar flow in an inclined channel using cfd: Application to pv panels. *Solar Energy*, 146:221–229.

Holmén, V. (2012). Methods for vortex identification. *Master's Theses in Mathematical Sciences*.

Holmes, P., Lumley, J. L., and Berkooz, G. (1996). *Turbulence, Coherent Structures, Dynamical Systems and Symmetry*. Cambridge University Press.

Hunt, J. C., Wray, A., and Moin, P. (1988). Eddies, streams, and convergence zones in turbulent flows.

IAE (2017). *Renewables 2017: Analysis and Forecasts to 2022*. Market Report Series.

Jaluria, Y. and Gebhart, B. (1974a). On transition mechanisms in vertical natural convection flow. *Journal of Fluid Mechanics*, 66:309–337.

Jaluria, Y. and Gebhart, B. (1974b). Stability and transition of buoyancy-induced flows in a stratified medium. *Journal of Fluid Mechanics*, 66:593–612.

Jannot, M. and Kunc, T. (1998). Onset of transition to turbulence in natural convection with gas along a vertical isotherm plane. *International Journal of Heat and Mass Transfer*, 41:4327–4340.

Jeong, J. and Hussain, F. (1995). On the identification of a vortex. *Journal of Fluid Mechanics*, 285:69–94.

Jeong, J., Hussain, F., Schoppa, W., and Kim, J. (1997). Coherent structures near the wall in a turbulent channel flow. *Journal of Fluid Mechanics*, 332:185–214.

Jiménez, J. (2018). Coherent strutures in wall-bounded turbulence. *Journal of Fluid Mechanics*, 842:P1.

Jing, C.-J., Henry, D., Ben Hadid, H., and Imaishi, N. (2003). Low-order dynamical model for low-prandtl number fluid flow in a laterally heated cavity. *Physics of Fluids*, 15(8):2152–2162.

Katoh, Y., Miyamoto, M., Kurima, J., and Kaneyasu, S. (1991). Turbulent free convection heat transfer from vertical parallel plates : Effect of entrance bell-mouth shape. *JSME*, 34(4):496–501.

Khanal, R. and Lei, C. (2014). A scaling investigation of the laminar convective flow in a solar chimney for natural ventilation. *International Journal of Heat and Fluid Flow*, 45:98–108.

Khanal, R. and Lei, C. (2015). A numerical investigation of buoyancy induced turbulent air flow in an inclined passive wall solar chimney for natural ventilation. *Energy and Building*, 93:217–226.

Kheireddine, A., Sanda, M. H., Chaturvedi, S., and Mohieldin, T. (1997). Numerical prediction of pressure loss coefficient and induced mass flux for laminal natural convective flow in a vertical channel. *Energy*, 22(4):413–423.

Kim, J. and Moin, P. (1989). *Transport of Passive Scalars in a Turbulent Channel Flow*. Springer, Berlin, Heidelberg.

Klebanoff, P. S., Tidstrom, K. D., and Sargent, L. M. (1962). The three-dimensional nature of boundary-layer instability. *Journal of Fluid Mechanics*, 12:1–34.

Kline, S. J., Reynolds, W. C., Schraub, F. A., and Runstadler, P. W. (1967). The structure of turbulent boundary layers. *Journal of Fluid Mechanics*, 30(4):741–773.

Kogawa, T., Okajima, J., Komiya, A., Armfield, S., and Maruyama, S. (2016). Large eddy simulation of turbulent natural convection between symmetrically heated vertical parallel plates for water. *International Journal of Heat and Mass Transfer*, 101:870–877.

Kolář, V. (2007). Vortex identification: New requirements and limitations. *International Journal of Heat and Fluid Flow*, 28(4):638–652.

Lau, G. (2013). *Natural convection in building-integrated photovoltaic systems: A computational study*. Phd thesis, UNSW-Sydney.

Lau, G., Sanvicente, E., Yeoh, G., Timchenko, V., Fossa, M., Ménézo, C., and Giroux-Julien, S. (2012a). Modelling of natural convection in vertical and tilted photovoltaic applications. *Energy and Buildings*, 55:810–822.

Lau, G. E., Timchenko, V., Ménézo, C., Giroux-Julien, S., Fossa, M., Sanvicente, E., Reizes, J. A., and Yeoh, G. H. (2012b). Numerical and experimental investigation of unsteady natural convection in a vertical open-ended channel. *Computational Thermal Sciences: An International Journal*, 4(5).

Lau, G. E., Yeoh, G. H., Timchenko, V., and Reizes, J. A. (2011). Large-eddy simulation of turbulent natural convection in vertical parallel-plate channels. *Numerical Heat Transfer, Part B: Fundamentals*, 59(4):259–287.

Lau, G. E., Yeoh, G. H., Timchenko, V., and Reizes, J. A. (2012c). Application of dynamic global-coefficient subgrid-scale models to turbulent natural convection in an enclosed tall cavity. *Physics of Fluids*, 24(9):094105.

Lau, G. E., Yeoh, G. H., Timchenko, V., and Reizes, J. A. (2012d). Large-eddy simulation of natural convection in an asymmetrically-heated vertical parallel-plate channel: Assessment of subgrid-scale models. *Computers & Fluids*, 59:101–116.

Lesieur, M. (2008). Fourier analysis of homogeneous turbulence. In *Turbulence in Fluids: Fourth Revised and Enlarged Edition*, pages 155–185. Springer Netherlands.

Li, C., Tsubokura, M., Fu, W., Jansson, N., and Wang, W. (2015). Compressible direct numerical simulation with a hybrid boundary condition of transitional phenomena in natural convection. *International Journal of Heat and Mass Transfer*, 90:654–664.

Li, Y., Daverat, C., Pabiou, H., Ménézo, C., and Xin, S. (2017). Transition to turbulent heat transfer in heated vertical channel - scaling analysis. *International Journal of Thermal Sciences*, 112:199–210.

Li, Y., Pabiou, H., and Ménézo, C. (2018). Unsteady heated vertical channel flow in a cavity. *International Journal of Thermal Sciences*, 125:293–304.

Lumley, J. L. (1967). The structure of inhomogeneous turbulent flows. In *Atmospheric turbulence and radio wave propagation*, number 13, pages 166–167.

Lumley, J. L. and Poje, A. (1997). Low-dimensional models for flows with density fluctuations. *Physics of Fluids*, 9(7):2023–2031.

Manca, O., Morrone, B., and Naso, V. (1994). A numerical study of natural convection between symmetrically heated vertical parallel plates. In *XII Congresso Nazionale UIT*.

Manca, O., Musto, M., and Naso, V. (2003). Experimental analysis of asymmetrical isoflux channel-chimney systems. *International Journal of Thermal Sciences*, 42(9):837–846.

Ménézo, C., Fossa, M., and Leonardi, E. (2007). An experimental free cooling by natural convection of vertical sur-faces for building integrated photovoltaic (bipv) applications. *Thermal Issues in Emerging Technologies*, 7:4327–4340.

Miyamoto, M., Katoh, Y., Kurima, J., and Sasaki, H. (1986). Turbulent free convection heat transfer from vertical parallel plates. In *The Eighth International Heat Transfer Conference*, volume 4, pages 1593–1598. Hemisphere Publishing Corporation.

Moshfegh, B. and Sandberg, M. (1996). Investigation of fluid flow and heat transfer in a vertical channel heated from one side by pv elements, part i - numerical study. *Renewable Energy*, 8:3849–3860.

Nakao, K., Hattori, Y., and Suto, H. (2017). Numerical investigation of a spatially developing turbulent natural convection boundary layer along a vertical heated plate. *International Journal of Heat and Fluid Flow*, 63:128–138.

Nasri, Z., Laatar, A., and Balti, J. (2015). Natural convection enhancement in an asymmetrically heated channel-chimney system. *International Journal of Thermal Sciences*, 90:122–134.

Naylor, D., Floryan, J., and Tarasuk, J. (1991). A numerical study of developing free convection between isothermal vertical plates. *Journal of Heat Transfer*, 113(3):620–626.

negaWatt, A. (2015). *Manifeste negaWatt*. Actes Sud/Association negaWatt.

Ng, C. S., Ooi, A., Lohse, D., and Chung, D. (2017). Changes in the boundary-layer structure at the edge of the ultimate regime in vertical natural convection. *Journal of Fluid Mechanics*, 825:550–572.

Noack, B. R. (2016). From snapshots to modal expansions–bridging low residuals and pure frequencies. *Journal of Fluid Mechanics*, 802:1–4.

Olsson, C. (2004). Prediction of nusselt number and flow rate of buoyancy driven flow between vertical parallel plates. *Journal of Heat Transfer*, 126:97–104.

O'Meara, T. and Poulikakos, D. (1987). Experiments on the cooling by natural convection of an array of vertical heated plates with constant heat flux. *International Journal of Heat and Fluid Flow*, 8(4):313–319.

Ospir, D., Popa, C., Chereches, C., Polidori, G., and Fohanno, S. (2012). Flow visualization of natural convection in a vertical channel with asymmetric heating. *International Communications in Heat and Mass Transfer*, 39(4):486–493.

Pallares, J., Vernet, A., Ferre, J. A., and Grau, F. X. (2010). Turbulent large-scale structures in natural convection vertical channel flow. *International Journal of Heat and Mass Transfer*, 53(19):4168–4175.

Park, H. M., Sung, M. C., and Chung, J. S. (2004). Stabilization of rayleigh–bénard convection by means of mode reduction. *Proceedings of the Royal Society of London A: Mathematical, Physical and Engineering Sciences*, 460(2046):1807–1830.

Pearson, K. (1901). Liii. on lines and planes of closest fit to systems of points in space. *Philosophical Magazine Series 6*.

Peuportier, B. (2016). Energétique des bâtiments et simulation thermique.

Pirozzoli, S., Bernardini, M., and Orlandini, P. (2016). Passive scalars in turbulent channel flow at high reynolds number. *Journal of Fluid Mechanics*, 788:614–639.

Podvin, B. and Le Quéré, P. (2001). Low-order models for the flow in a differentially heated cavity. *Physics of Fluids*, 13(11):3204–3214.

Podvin, B. and Sergent, A. (2012). Proper orthogonal decomposition investigation of turbulent rayleigh-bénard convection in a rectangular cavity. *Physics of Fluids*, 24:105106.

Podvin, B. and Sergent, A. (2015). A large-scale investigation of wind reversal in a square rayleigh–bénard cell. *Journal of Fluid Mechanics*, 766:172–201.

Polidori, G., Fatnassi, S., Ben Maad, R., Fohanno, S., and Beaumont, F. (2015). Early-stage dynamics in the onset of free-convective reversal flow in an open-ended channel asymmetrically heated. *International Journal of Thermal Sciences*, 88:40–46.

Polidori, G., Popa, C., and Mai, T. H. (2003). Transient flow rate behaviour in an external natural convection boundary layer. *Mechanics Research Communications*, 30(6):615–621.

Quemener, O., Neveu, A., and Videcoq, E. (2007). A specific reduction method for the branch modal formulation: Application to a highly non-linear configuration. *International journal of thermal sciences*, 46(9):890–907.

Ramakrishna, K., Rubin, S., and Khosla, P. (1982). Laminar natural convection along vertical square ducts. *Numerical Heat Transfer, Part A Applications*, 5(1):59–79.

Ramalingom, D., Cocquet, P., and A., B. (2017). Numerical study of natural convection in asymmetrically heated channel considering thermal stratification and surface radiation. *Numerical Heat Transfer, Part A: Applications*, 72:681–696.

Ramalingom, D., Cocquet, P.-H., Maleck, R., and Bastide, A. (2018). A multi-objective optimization problem in natural convection for a vertical channel asymmetrically heated. working paper or preprint.

Rempfer, D. and Fasel, H. F. (1994). Evolution of three-dimensional coherent structures in a flat-plate boundary layer. *Journal of Fluid Mechanics*, 260:351–375.

Ribeiro, J. H. M. and Wolf, W. R. (2017). Identification of coherent structures in the flow past a naca0012 airfoil via proper orthogonal decomposition. *Physics of Fluids*, 29(8):085104.

Rohsenow, W. M., Hartnett, J. P., Cho, Y. I., et al. (1998). *Handbook of heat transfer*, volume 3. McGraw-Hill New York.

Saadon, S., Gaillard, L., Giroux-Julien, S., and Ménézo, C. (2016). Simulation study of a naturally-ventilated building integrated photovoltaic/thermal (bipv/t) envelope. *Renewable Energy*, 87:517–531.

Sandberg, M. and Moshfegh, B. (1996). Investigation of fluid flow and heat transfer in a vertical channel heated from one side by pv elements, part ii - experimental study. *Renewable Energy*, 8:254–258.

Sandberg, M. and Moshfegh, B. (2002). Buoyancy-induced air flow in photovoltaic facades: Effect of geometry of the air gap and location of solar cell modules. *Building and Environment*, 37:211–218.

Sanvicente, E. (2013). *Experimental investigation of thermal and fluid dynamical behavior of flows in open-ended channels: Application to Building Integrated Photovoltaic (BiPV) Systems*. Phd thesis, INSA de Lyon.

Sanvicente, E., Giroux-Julien, S., Ménézo, C., and Bouia, H. (2013). Transitional natural convection flow and heat transfer in an open channel. *International Journal of Thermal Sciences*, 63:87–104.

Sayadi, T., Hamman, C. W., and Moin, P. (2013). Direct numerical simulation of complete h-type and k-type transitions with implications for the dynamics of turbulent boundary layers. *Journal of Fluid Mechanics*, 724:480–509.

Sayadi, T., Schmid, P. J., Nichols, J. W., and Moin, P. (2014). Reduced-order representation of near-wall structures in the late transitional boundary layer. *Journal of Fluid Mechanics*, 748:278–301.

Schmid, P. J. (2010). Dynamic mode decomposition of numerical and experimental data. *Journal of Fluid Mechanics*, 656:5–28.

Sieber, M., Paschereit, C. O., and Oberleithner, K. (2016). Spectral proper orthogonal decomposition. *Journal of Fluid Mechanics*, 792:798–828.

Sieber, M., Paschereit, C. O., and Oberleithner, K. (2017). On the nature of spectral proper orthogonal decomposition and related modal decompositions. *arXiv:1712.08054*.

Sirovich, L. (1987). Turbulence and the dynamics of coherent structures. part i: Coherent structures. *Quarterly of applied mathematics*, 45:561–571.

Smagorinsky, J. (1963). General circulation experiments with the primitive equations: I. the basic experiment. *Monthly weather review*, 91(3):99–164.

Smirnov, A., Shi, S., and Celik, I. (2001). Random flow generation technique for large eddy simulations and particle-dynamics modeling. *Journal of Fluids Engineering*, 123:359–371.

Sparrow, E. and Azevedo, L. (1985). Vertical-channel natural convection spanning between the fully-developed limit and the single-plate boundary-layer limit. *International Journal of Heat and Mass Transfer*, 28(10):1847–1857.

Sparrow, E., Chrysler, G., and Azevedo, L. (1984). Observed flow reversals and measured-predicted nusselt numbers for natural convection in a one-sided heated vertical channel. *Journal of Heat Transfer*, 106(2):325–332.

Stöhr, M., Oberleithner, K., Sieber, M., Yin, Z., and Meier, W. (2017). Experimental study of transient mechanisms of bistable flame shape transitions in a swirl combustor. *Journal of Engineering for Gas Turbines and Power*, 140(1):011503.

Tabor, G. R. and Baba-Ahmadi, M. H. (2010). Inlet conditions for large eddy simulation: A review. *Computers & Fluids*, 39:553–567.

Taira, K., Brunton, S. L., Dawson, S. T. M., Rowley, C. W., Colonius, T., McKeon, B. J., Schmidt, O. T., Gordeyev, S., Theofilis, V., and Ukeiley, L. S. (2017). Modal analysis of fluid flows: An overview. *AIAA Journal*, 55(12):4013–4041.

Tanda, G. (1997). Natural convection heat transfer in vertical channels with and without transverse square ribs. *International journal of heat and mass transfer*, 40(9):2173–2185.

The New Climate Economy (2014). Better growth, better climate. *The Global Commission on the Economy and Climate*.

Thebault, M., Reizes, J., Giroux, S., Timchenko, V., and Ménézo, C. (2018). Impact of external temperature distribution on the convective mass flow rate in a vertical channel–a theoretical and experimental study. *International Journal of Heat and Mass Transfer*, 121:1264–1272.

Thielicke, W. and Stamhuis, E. (2014). Pivlab – towards user-friendly, affordable and accurate digital particle image velocimetry in matlab. *Journal of Open Research Software*, 2.

Tkachenko, O. A., Timchenko, V., Giroux-Julien, S., Ménézo, C., Yeoh, G. H., Reizes, J. A., Sanvicente, E., and Fossa, M. (2016). Numerical and experimental investigation of unsteady natural convection in a non-uniformly heated vertical open-ended channel. *International Journal of Thermal Sciences*, 99:9–25.

Tkachenko, S. (2018). *Coupling of radiation and natural convection in open-ended channel in application to building-integrated photovoltaic systems*. Phd thesis, UNSW-Sydney.

Towne, A., Schmidt, O. T., and Colonius, T. (2018). Spectral proper orthogonal decomposition and its relationship to dynamic mode decomposition and resolvent analysis. *Journal of Fluid Mechanics*, 847:821–867.

Vareilles, J. (2007). *Étude des transferts de chaleur dans un canal vertical différentiellement chauffé : application aux enveloppes photovoltaïques/thermiques*. Phd thesis, Université Claude Bernard Lyon 1.

Vreman, A. W. (2004). An eddy-viscosity subgrid-scale model for turbulent shear flow: Algebraic theory and applications. *Physics of Fluids*, 16(10):3670–3681.

Webb, B. and Hill, D. (1989). High rayleigh number laminar natural convection in an asymmetrically heated vertical channel. *Journal of Heat Transfer*, 111(3):649–656.

Wu, X. and Moin, P. (2009). Direct numerical simulation of turbulence in a nominally zero-pressure-gradient flat-plate boundary layer. *Journal of Fluid Mechanics*, 630:5–41.

Wu, X. and Moin, P. (2010). Transitional and turbulent boundary layer with heat transfer. *Physics of Fluids*, 22(8):085105.

Wu, X., Moin, P., Wallace, J., Skarda, J., Lozano-Durán, A., and Hickey, J.-P. (2017). Transitional–turbulent spots and turbulent–turbulent spots in boundary layers. *Proceedings of the National Academy of Sciences*, 114(27):E5292–E5299.

Yilmaz, T. and Fraser, S. M. (2007). Turbulent natural convection in a vertical parallel-plate channel with asymmetric heating. *International Journal of Heat and Mass Transfer*, 50:2612–2623.

Yilmaz, T. and Gilchrist, A. (2007). Temperature and velocity field characteristics of turbulent natural convection in a vertical parallel-plate channel with asymmetric heating. *Heat and Mass Transfer*, 43:707–719.

Zaki, T. A. (2013). From streaks to spots and on to turbulence: Exploring the dynamics of boundary layer transition. *Flow, Turbulence and Combustion*, 91:451–473.

Zhao, Y., Lei, C., and Patterson, J. C. (2013). Transition of natural convection boundary layers - a revisit by bicoherence analysis. *Journal of Fluid Mechanics*, 58:147–155.

Zhao, Y., Lei, C., and Patterson, J. C. (2017). The k-type and h-type transitions of natural convection boundary layers. *Journal of Fluid Mechanics*, 824:352–387.

Zoubir, A. (2014). *Étude des transferts thermo-convectifs dans un canal semi-ouvert : Application aux façades type double-peau*. Phd thesis, INSA de Lyon.

Appendix A

Impact of the acoustic disturbance?

A.1 Experimental acoustic disturbance

A.1.1 Acoustic perturbation device and perturbation frequencies

In order to introduce a perturbation, the choice of an acoustic perturbation has been made. Despite acoustic waves propagate at the speed of sound, locally the particles in the ambient fluid oscillate at a much lower velocity in the propagation direction because of the succession of compression and depression. This velocity called the particle velocity can be directly obtained from the local pressure variation of the acoustic waves. Except for some cases with high frequency waves, the sound wave cannot generate a motion on its own in the way that a particle in motion will not see its overall displacements changed by the presence of an acoustic wave. To that extent an acoustic perturbation could be considered as non-intrusive.

Acoustic perturbations are generated by an 80 watt 8 Ohms loudspeaker bandwidth of [50 Hz – 20 000 Hz]. Because of the organisation of the set of lenses it has not been possible to directly positioned the speaker vertically immediately below the entrance. To that extent it was placed below the heated wall and centred in the z-direction so that the mid plane perturbation stays in 2D. The speaker is tilted so that the acoustic perturbation directly enters the channel. A scheme and a picture of the speaker position are presented in figures A.1a and A.1b respectively.

The signal is generated through a Matlab algorithm that enables many different shapes of sinusoidal signals. A microphone allows to estimate the sound pressure amplitude and consequently the particle velocity amplitude through the relation.

$$\Delta P = c\rho\Delta U \tag{A.1}$$

where c (m/s) is the acoustic wave celerity in air, ρ (kg/m^3) is the air density, ΔP (Pa) is the sound pressure and ΔU (m/s) the particle velocity. Moreover an accelerometer has been placed on one of the channel wall to evaluate the impact of the acoustic perturbation on the channel

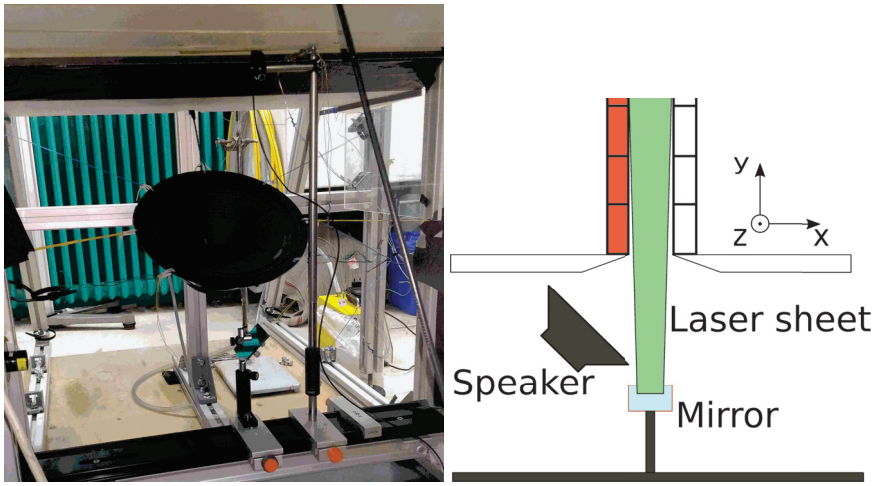

(a) Speaker picture (b) Scheme below the channel

Fig. A.1 Acoustic device location and representation

vibrations. The amplitude of the perturbation is measured by a microphone and the maximum particle velocity is estimated around 0.01 m/s which corresponds to a perturbation of the inlet velocity ranging between 5 to 10%, depending on the heat input.

Given that the frequency of interests previously identified by Sanvicente et al. (2013) and confirmed in this work, are below 1 Hz, it is not possible to generate, sinusoidal wave with such low frequencies. To that extent, low frequencies are generated by pulses. These pulses are constituted of a 60 Hz signal emitted during a short period at the frequency required. Two pulses emitted at 1 Hz are illustrated in figure A.2. Note that in this figure, only for visualisation purposes, the signal that constitute the pulses is emitted at 25 Hz. Moreover other type of signal has been generated. To that extent a white noise have been generated at the inlet of the channel. Different frequency peak could have been observed, amongst them a frequency at 74 Hz, 118 Hz and 134 Hz. The frequency at 74 Hz is characteristic of a strong vibration of the channel observed on the accelerometer. The frequencies of 118 Hz and 134 Hz corresponds to acoustic resonant frequency of the channel itself and are strongly amplified within the channel (organ pipe principle).

A.1.2 Summary of the cases studied

In section A.1 the experimental cases have been summarised. 'NC' refers to measurements made without perturbations (NC stands for Natural Case), 'Pulse' refers to the case with an acoustic pulse, finally 'SW' refers to Standing Waves which corresponds to the frequencies 74 Hz, 118 Hz, 134 Hz. All the results represents around 5 TB of data and around 24 h of video. To that extent Matlab routines and sub-routines to systematically post-process and post-treat the data.

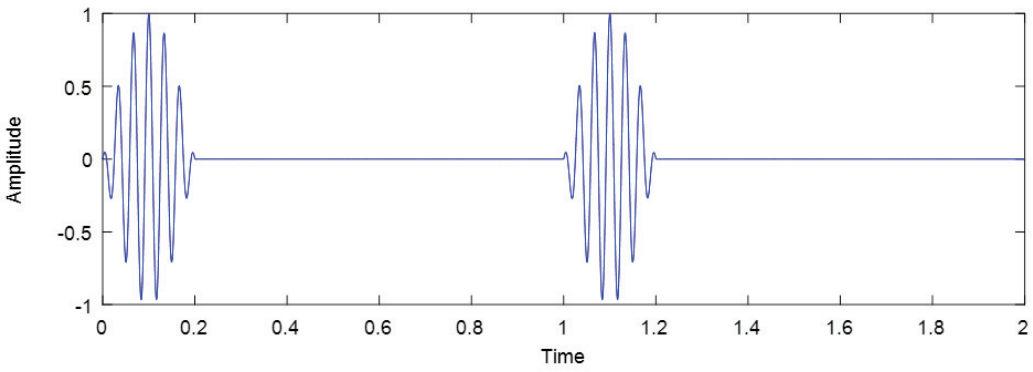

Fig. A.2 Representation of an acoustic pulse

Table A.1 Summary of the experimental measurements

Ra	1.5×10^{12}	3.5×10^{12}	7.5×10^{12}
w1	NC, Pulses, SW	NC, Pulses, SW	NC
w2		NC, Pulses	
w3		NC	
w4	NC, Pulses, SW	NC, Pulses, SW	NC
Number of test	40	40	5

As mentioned above, numerous test were made for different disturbance frequencies in order to investigate its effect on the flow. To limit repeatability issues as much measurements as possible were carried during each session. To that extent settings were the same and the evolution of the room ambient conditions was small (see section 3.2.4). Measurements are carried in the afternoon and in the evening. Once the settings are ready different measurements are done at different frequencies and a measurement is done in the natural case which stands as the reference case.

A.2 Effect of the pulsed disturbance on the entrance flow development

The inlet region is of great importance for the flow development as any structures instabilities or phenomenon developing there may impact the whole channel flow. In the measurements it was observed that sometimes, instabilities of type Kelvin-Helmholtz were developing from the leading edge of the unheated wall. One such instability can be observed on an instantaneous 2D plot of the streamwise velocity in figure A.3. This instability develops because of the entrance effect which induce a separation of the streamline. Then this instability breaks apart into vortices which are convected toward the heated wall. This instability may develop because of the edge effect at the entrance and the shear that develops between the high velocity bulk flow and the

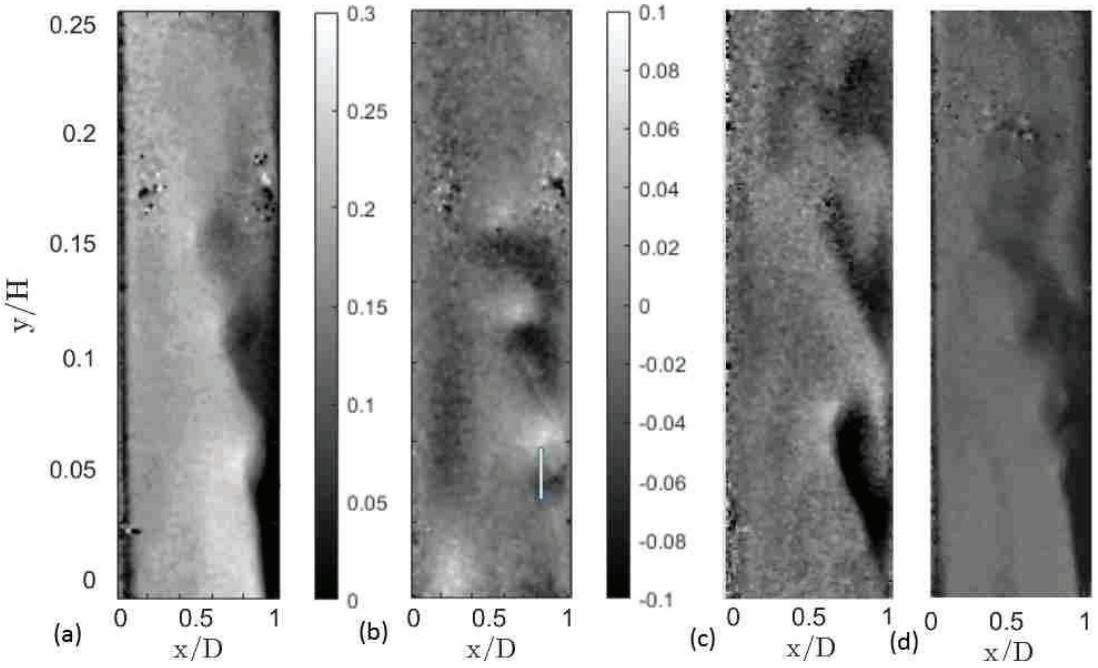

Fig. A.3 Instantaneous captions of the velocity fields (a) streamwise velocity at time t_1 (b) wall-normal velocity at time t_1 (c) streamwise velocity at time t_2 (d) streamwise velocity at time t_3. The color scheme of plots (c) and (d) is the same as for (a).

low velocity region near the unheated wall. The frequency content of the time evolution of the wall-normal velocity, plotted near the unheated wall on a segment between $y/H = 0.04$ and $y/H = 0.06$ at $x/D = 0.8$ is plotted in figure A.4. The frequency spectrum is broad in low frequencies and different peaks can be identified. The peak frequency is reached at 0.44 Hz, moreover harmonics of this frequency are observed. During the same afternoon a measurement was carried with a disturbance frequency of 0.45 Hz.

The 5th first streamwise POD modes of the flow, measured in w1, are plotted in the natural case figure A.5 and in the case disturbed at 0.45 Hz figure A.6. The mean flow has been removed and consequently the first mode represents the main slow variations of the flow around the mean flow. For both cases, Modes 2 and 3 reflects the initial wall-normal flapping. This wall-normal

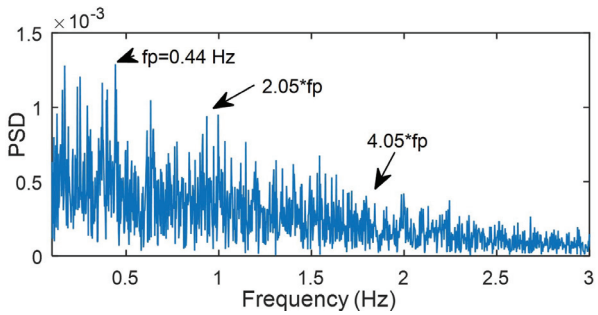

Fig. A.4 Temporal evolution of the wall-normal velocity between $y/H = 0.04$ and $y/H = 0.06$ at $x/D = 0.8$.

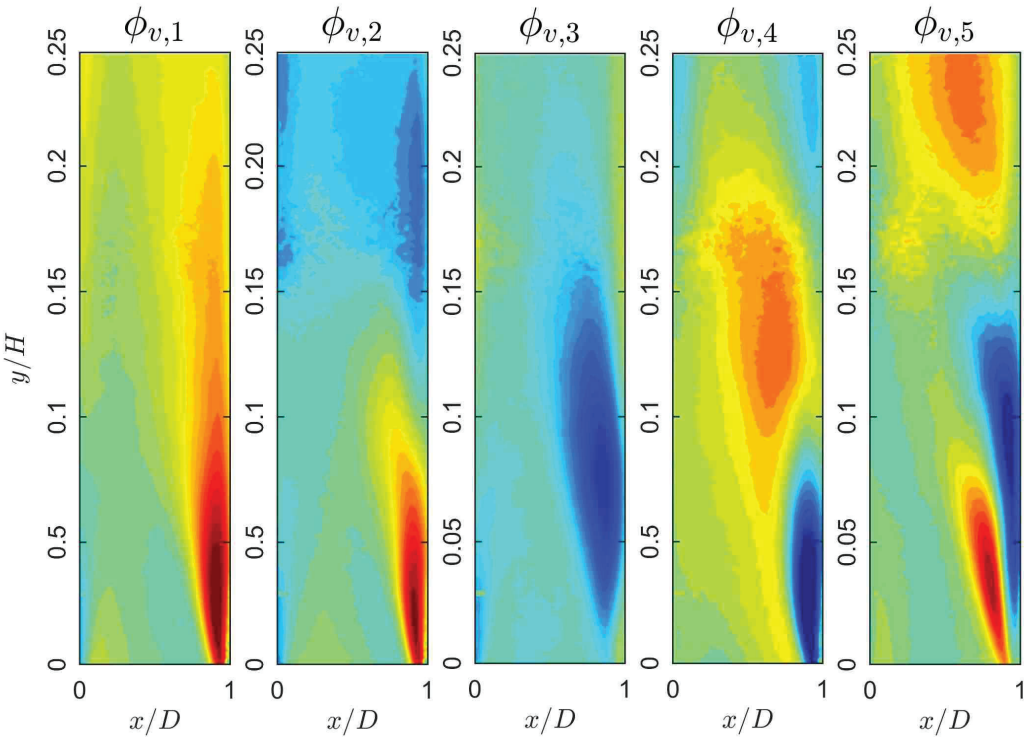

Fig. A.5 POD spatial modes 1 to 5 of the inlet flow measured in w1, natural case.

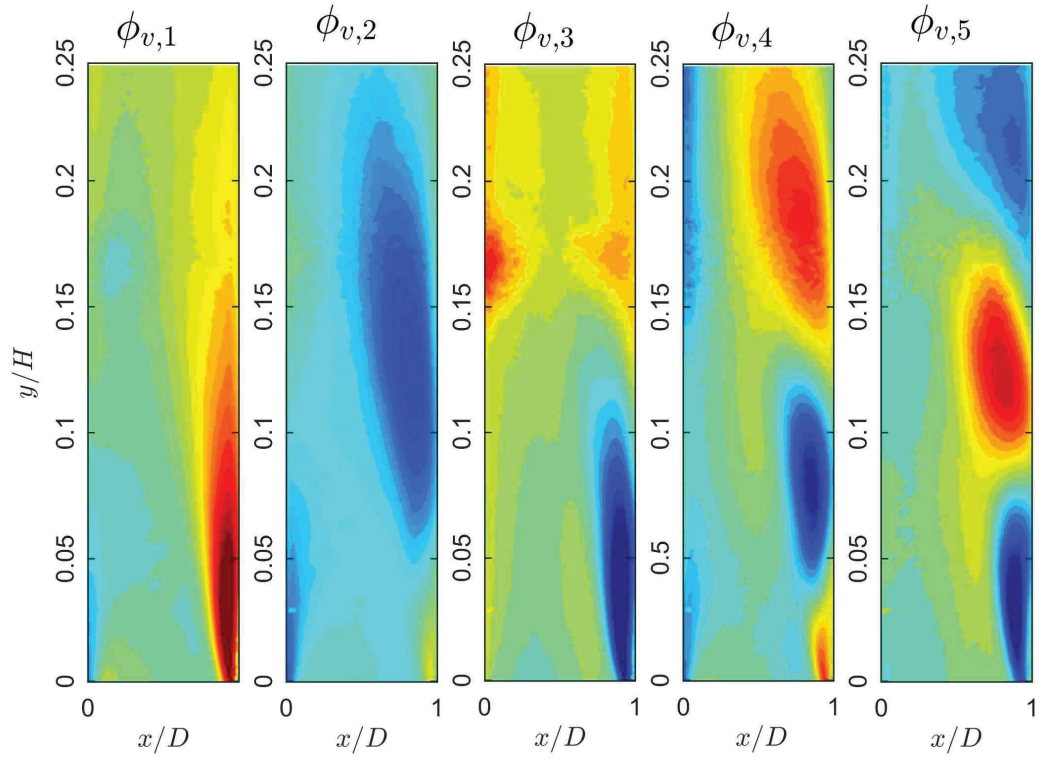

Fig. A.6 POD spatial modes 1 to 5 of the inlet flow measured in w1, 0.45 Hz.

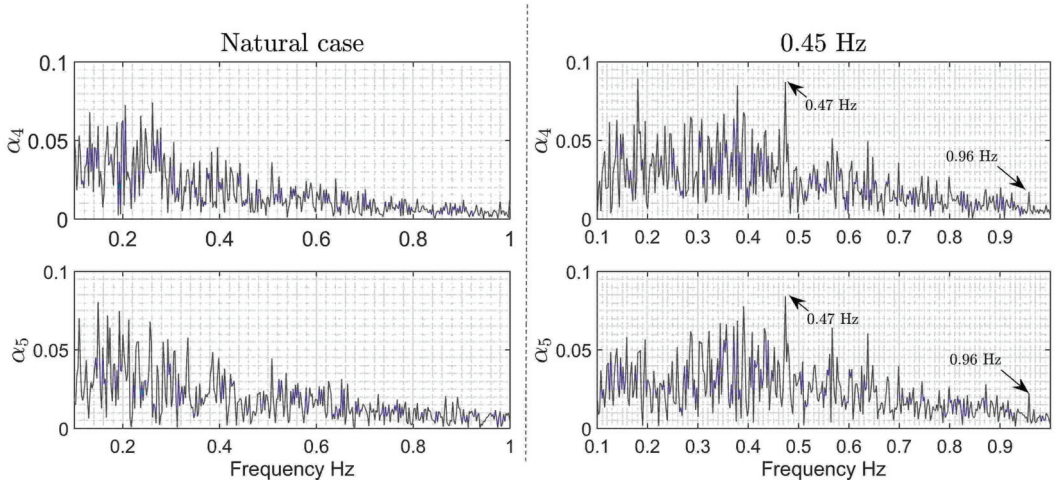

Fig. A.7 Frequency content of the POD modes 4 and 5 in the natural case and at 0.45 Hz.

flapping sometimes leads to spanwise oscillations associated with streamwise travelling waves as observed in figure A.3. This phenomenon is in part represented by the combined contribution of the modes 4 and 5 which contain a phase change in the streamwise direction. It can be noted that when the 0.45 Hz disturbance is introduced figure A.6 the modes are better defined which suggests that the instability is regularized in time. In figure A.7 the frequency content of the temporal coefficient of the modes 4 and 5 at 0.45 Hz case. By definition POD modes are not necessarily linked to eigenfrequencies. However, if an energetic structure linked to a specific frequency occurs in the flow, this frequency should be found in the associated mode frequency spectrum. For the 0.45 Hz case, there is a clear peak at 0.47 Hz for the modes 4 and 5. Moreover a harmonic at 0.96 Hz is seen which gives more credit to this eigenfrequency. However, in the natural case the peak is not as pronounced which suggest that the instability is weaker, and its decomposition is distributed among a larger range of modes.

The changes in the time averaged velocities that can be observed in figure A.8 are significantly smaller than those induced by the external thermal stratification. These changes are even below the uncertainty of the PIV measurements.

From this plots it has been concluded that, despite interesting results obtained with acoustic controlled disturbance, one of the major challenge to address before being able to carefully study the effect of a controlled disturbance in experimental conditions is to work on sources of repeatability issues, and particularly on the effect of the external thermal gradient which is addressed in chapters 5 and 6.

A.3 Effect of a standing waves

The effect of different standing waves was also investigated. In figure A.9, three plots of the time-averaged velocity obtained in the case of a undisturbed flow (0 Hz) and a flow disturbed

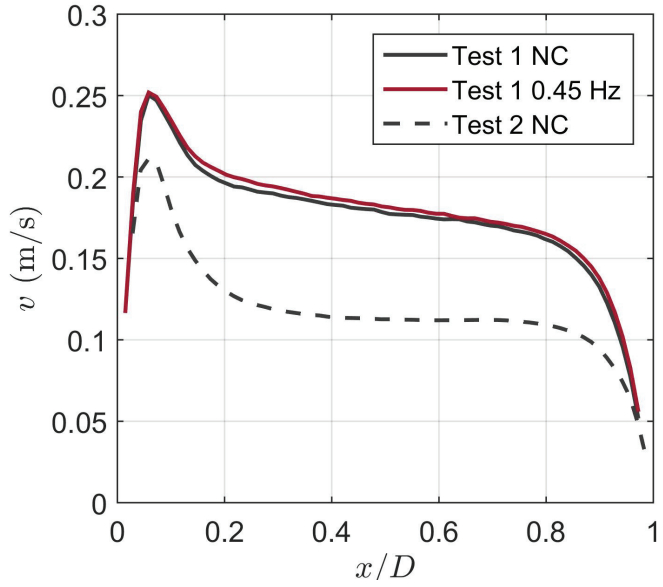

Fig. A.8 Temporal evolution of the wall-normal velocity between $y/H = 0.04$ and $y/H = 0.06$ at $x/D = 0.8$.

with a standing wave (74 Hz) are plotted for two heat input and two height. In figure A.9 (a) and (b), the 74 Hz case has a different distribution than the 0 Hz case with a higher peak velocity and a lower velocity near the unheated wall. In figure A.9 (c) the velocity at 74 Hz is lower than at 0 Hz, however the velocity distribution is also different with a more pronounced velocity peak. It remains hard to give a firm conclusion on the effect of the standing wave given that these changes are small and may be the consequences of other external factors.

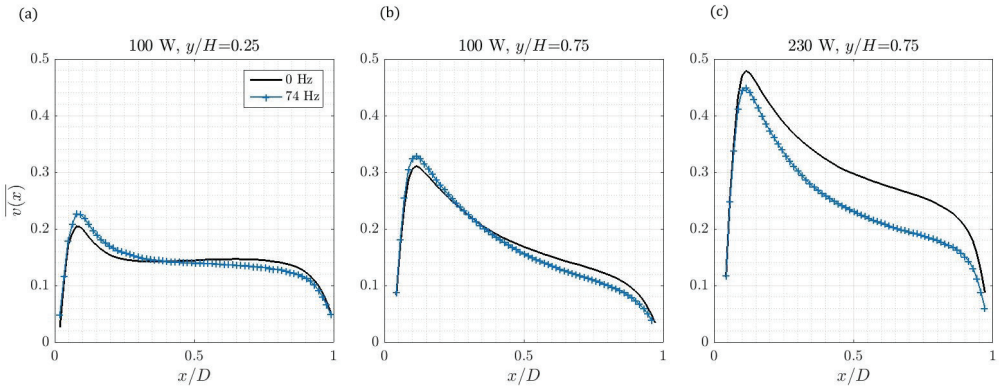

Fig. A.9 Time averaged velocity profiles without perturbation and with a perturbation at 74 Hz. (a) 100 W y/H=0.25, (b) 100 W y/H=0.75, (c) 230 W y/H=0.75.

Appendix B

Observations on the external velocity disturbances on the flow behaviour

This section discusses some observations that were made experimentally and numerically regarding the impact of the surroundings of the channel on the flow developing in the channel and particularly the impact of external structures of the flow.

In the present case, recordings of the velocity at the entrance region of the channel were carried out for a Rayleigh number of $Ra = 3.5 \times 10^{12}$ which corresponds to a heat input of 230 W. In this sequence, it can be observed that in addition to a mean ambient noise, large coherent structures are entrained within the channel.

Figure B.1 depicts instantaneous velocities obtained by PIV. Velocities were measured in the inlet region of the channel in w1. Different types of environmental perturbations are illustrated: a large coherent velocity structure which is entrained into the channel is observed in figure B.1 (a) and (b) between $y/H = 0$ and $y/H = 0.07$. As it can be seen on the wall-normal component figure B.1 (b) this large structure is vortical. The channel starts at y/H=0 therefore it is clear that this structure was not generated within the channel and comes from outside the channel.

In the literature no referenced work studied the effect of convective external flow structures on the channel flow. However a work was carried few years ago at UNSW by Peter Brady and John Reizes (Brady, 2013) in which they performed a two-dimensional LES modelling[1] of a symmetrically heated channel contained in a cavity. Their channel dimensions were similar to those of the channel under study. The ambient air is isothermal and still at the beginning of the simulation and a total heat flux of 100 W/m^2 is injected. The total simulated time is of 1000 s. A buoyant jet starts to oscillate at the exit of the channel as can be seen in figure B.2 (a). This jet also creates large convective structures which progressively populate the whole cavity as

[1] No details on the numerical methods used by Peter Brady and John Reizes are provided as only the qualitative results are of interest here.

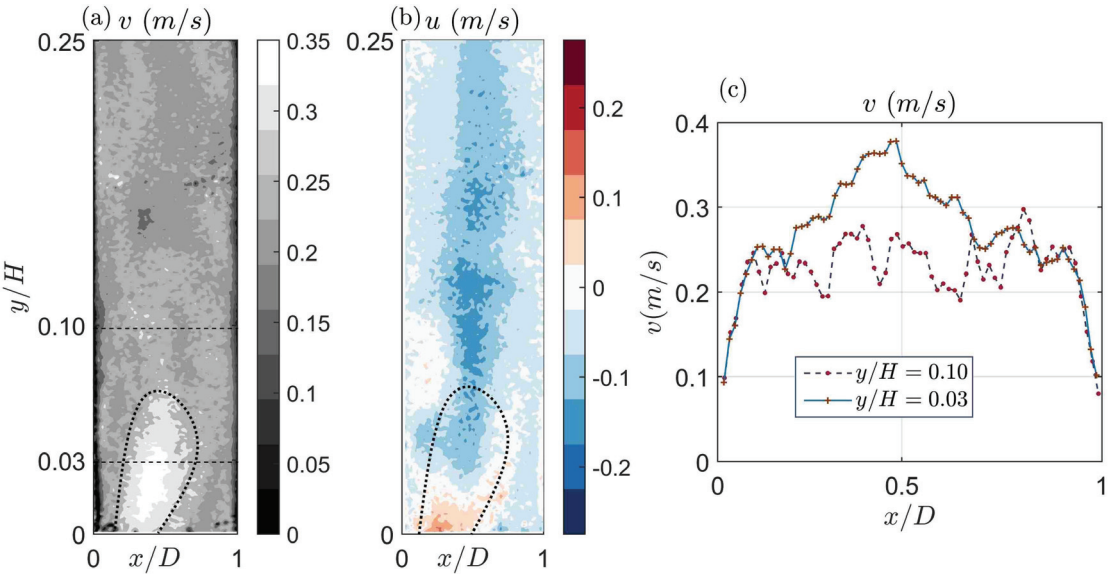

Fig. B.1 Instantaneous snapshots of the (a) streamwise v and (b) wall-normal u velocities obtained PIV measurements in the bottom part of the channel, between $y/H = 0$ and $y/H = 0.25$. The dashed lines in (a) indicates the heights at which v is plotted in (c). The dotted line in (a) and (b) depict the contours of the external velocity structure entering the channel.

depicted in B.2 (b). As time goes by, these structures travel lower in the room and approach the channel entrance. At one point they start to be intermittently entrained in the channel and each time they enter the channel they considerably disturb the flow behaviour within the channel. A magnified view of the effect of these large external structures is presented in figure B.3. At t=858 s and t=861 s one of these structures identified by an ellipse marker is entrained inside the channel. Then, at t=863 s and t=864 s (figure B.3) the flow appear to be significantly disturbed and modified and especially in the middle and to part of the channel. Another of these structures, indicated by a dotted line ellipse is then entrained in the channel.

These large coherent structures need to be carefully studied since they generate intermittency. The large convective structures observed numerically may be similar to those observed experimentally in figure B.1. Unfortunately the PIV field of view size does not allow to follow the structures and their effect on the flow higher in the channel. But as was previously observed by Sanvicente (2013) and mentioned in section 4.9.1, the flow sometimes has strongly unsteady and apparently disorganised behaviour. This strongly disturbed flow is likely to have complex characteristics, and therefore, the results of the modal decomposition performed in 5 could be greatly altered if such structures were simulated. Finally the understanding of these structures is necessary in order to be able to numerically model the boundary conditions of such channel.

(a)

(b)

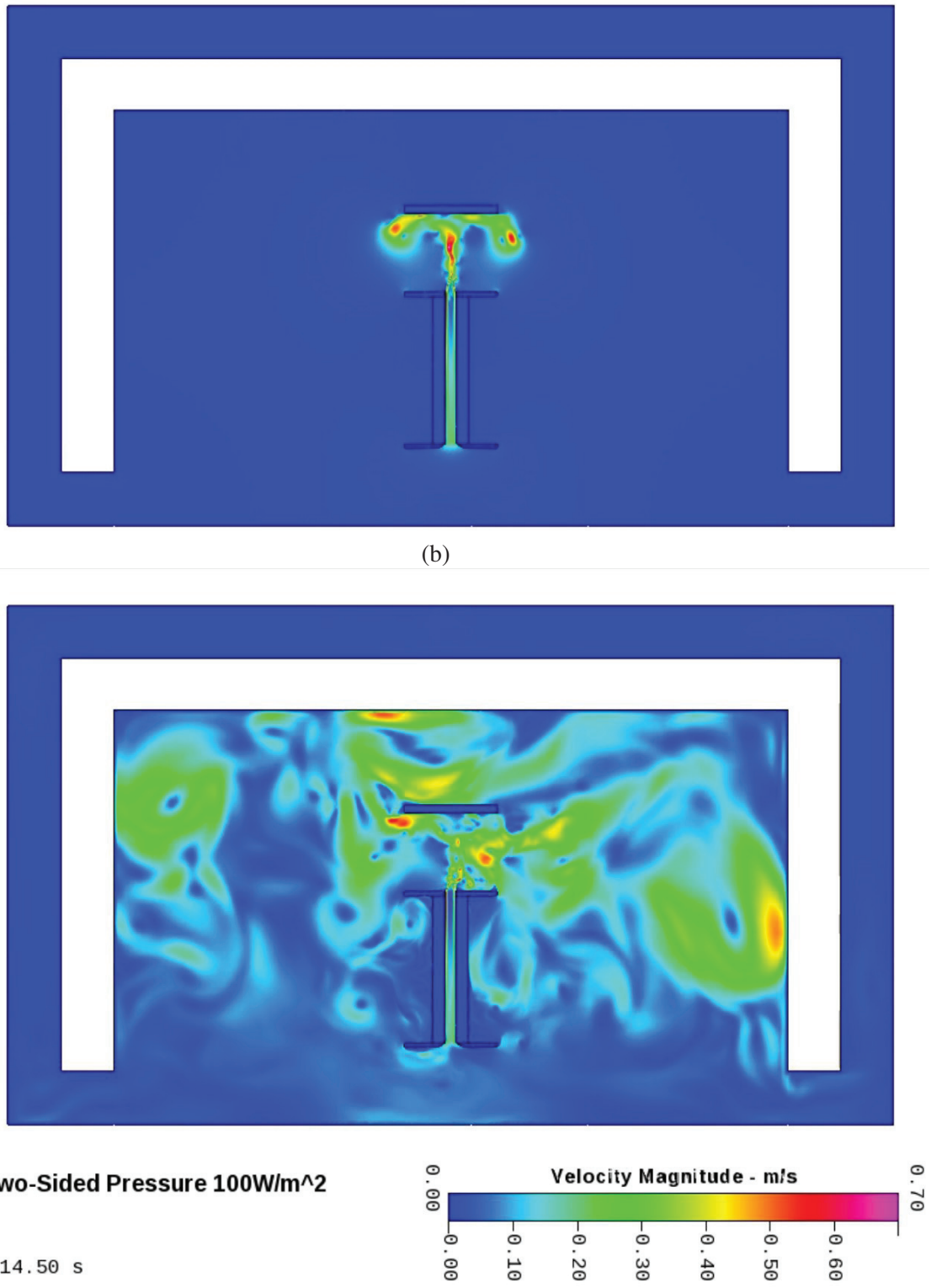

Fig. B.2 Two-dimensionnal LES modelling of a channel contained within a cavity at time (a) t=9.6 s and (b) at t=314.5 s. (Credit P.Brady and J.Reizes)

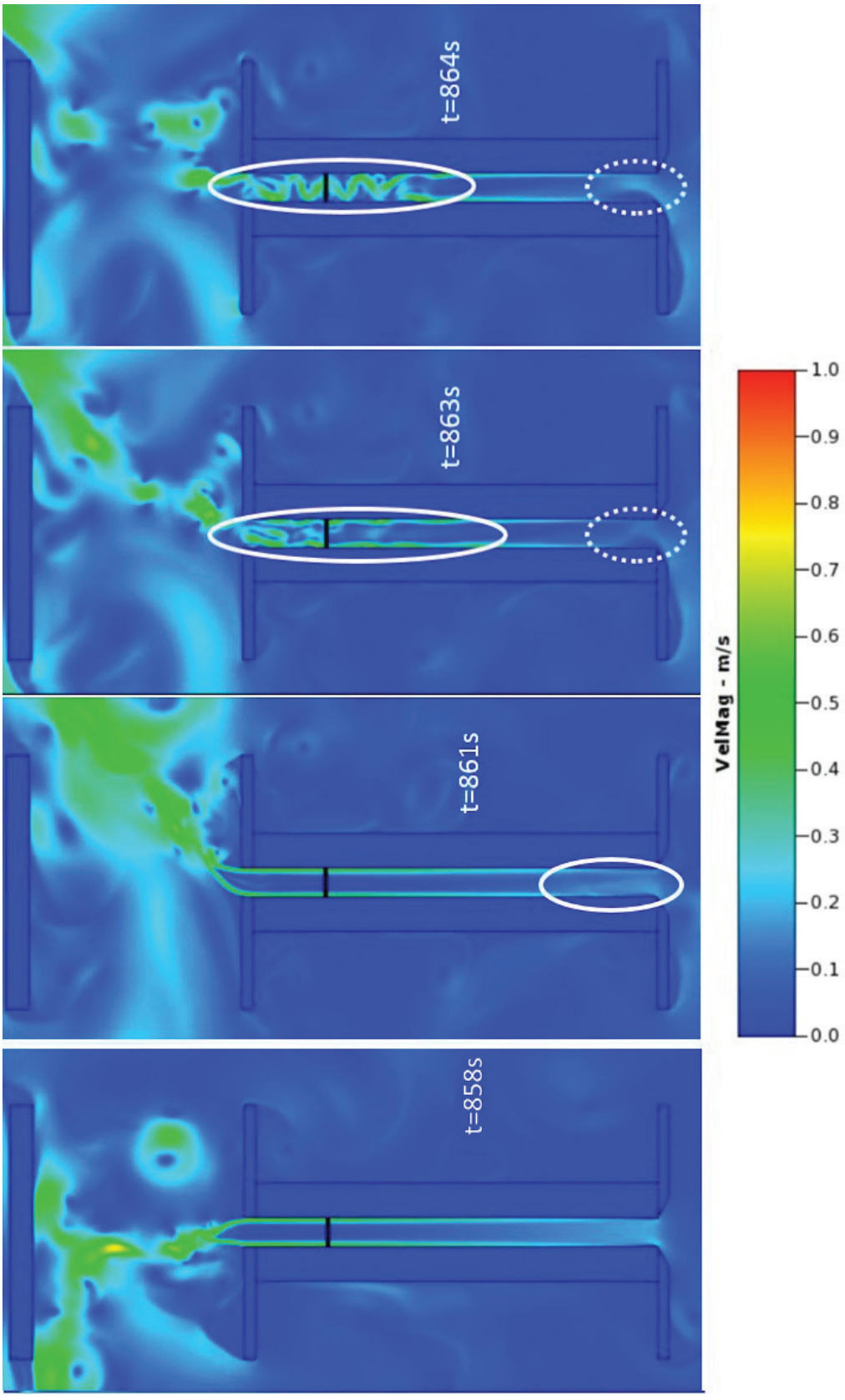

Fig. B.3 Development of the large convective structures within the room and tracking of the effect of one of them. The white ellipse indicates one of this large convective structures entrained in the channel and its effect on the flow behaviour. The dotted line ellipse shows another external convective structures which is being entrained in the channel.(Credit P.Brady and J.Reizes)

Appendix C

Energy budget of a vertical channel heated at constant heat flux

In this appendix, a discussion is carried out about the energy balance in the channel. It starts from the fundamental principles of thermodynamics and uses hypothesis in order to justify the simple energy balance commonly used in vertical channel configuration.

C.1 Theoretical energy budget of a Newtonian fluid

Let consider an infinitesimal fluid volume for which the 1^{st} principal of thermodynamic is applied. The energy conservation law in a fluid lead to:

Energy conservation

$$d\dot{E}_c + d\dot{E}_h + d\dot{W} = 0 \tag{C.1}$$

Where

$d\dot{E}_c$ is the rate of change of energy inside the volume,

$d\dot{E}_h$ is the heat added to the element,

$d\dot{W}$ is the rate of work done on the element due to body and surface forces

Assuming a Newtonian fluid the equation C.1 becomes

$$\frac{\partial}{\partial t}\left(\rho e^0\right) + \frac{\partial}{\partial x_i}\left(\rho u_i e^0\right) + \frac{\partial \varepsilon_i}{\partial x_i} + S = \frac{\partial}{\partial x_j}\left(u_i \tau_{ij}\right) - \frac{\partial}{\partial x_i}\left(u_i P\right) + \rho u_i f_i \tag{C.2}$$

Where ρ is the density of the fluid, e^0 is the total energy of the fluid, P is the static pressure, ε_i the energy transport through molecular diffusion at the frontier of the element in the $i-th$ direction (diffusion/conduction), τ_{ij} the shear stresses, f_i the volumetric forces (gravity, magnetic field etc) and S the source term, (the amount of thermal energy added by unity of mass for examples: radiation, exothermic reaction, nuclear reaction).

C.2 One-dimensional steady approach

C.2.1 Hypothesis

Equation C.2 is general to all Newtonian fluid parcel. In what follow, the specific case of a vertical channel flow induced by natural convection is considered. The idea of this short study is to grasp some understanding of the energy balance in such flow and therefore, hypothesis are made in order to simplify the problem.

1. The flow is considered one-dimensional and flowing in the vertical y-direction. As was discussed in chapter 5, this hypothesis is strong. Moreover it is not realistic as was observed in chapter 4 figure 5.6. However this remains the simplest assumption possible and have been used in many analytical models.
2. The flow is steady viz, $\partial/\partial t = 0$,
3. The working fluid is dry air and thus considered as non-participative and non-reactive, therefore there are no source term within the fluid viz $S = 0$,
4. Molecular diffusion is considered neglectible at the fluid interface. At the heated wall(s) when integrated on the whole channel this term corresponds to the net injected heat.
5. it is assumed that the power distribution is uniform at the heated wall(s) and therefore

$$\frac{\partial \varepsilon_i}{\partial x_i}(x = x_{wall}) = -q, \tag{C.3}$$

   otherwise

$$\frac{\partial \varepsilon_i}{\partial x_i}(x \neq x_{wall}) = 0 \tag{C.4}$$

   q is here the heat flux.
6. e^0 is the total energy and

$$e^0 = e + \frac{1}{2}U^2 \tag{C.5}$$

   where e is the internal energy and $\frac{1}{2}U^2$ is the kinetic energy. The assumption is made that $e = C_p T$.
7. The only volumetric force considered is the gravity.

C.2.2 Simplified one-dimensional energy balance

This set of hypothesis leads to the following formulation of the velocity,

$$\mathbf{u} = (0, v(y), 0) \tag{C.6}$$

and the continuity equation yields

$$\rho v(y) = constant = \frac{\dot{m}}{D} \tag{C.7}$$

where $\dot{m}$ is the mass flow rate and D the area of an horizontal section of the channel.

These equations, when substituted in equation C.2 with the above mentioned hypothesis leads to

$$\frac{\dot{m}}{D}\frac{\partial}{\partial y}(e^0) + \frac{\partial}{\partial y}(vP) + \frac{\partial \varepsilon}{\partial y} = \frac{\partial}{\partial y}((v\tau_{yy}) - \frac{\dot{m}}{D}g \tag{C.8}$$

Integrating in the x-direction between x=0 and x=D, then integrating between the inlet and outlet of the channel it becomes

$$\dot{m}\left((e^0)_{out} - (e^0)_{in}\right) + \left((vP)_{out} - (vP)_{in}\right)D = -V_D - \dot{m}gH + qA_h \tag{C.9}$$

where A_h is the heated area and V_D is the viscous dissipation due to the shear stresses, this term includes the pressure drop due to the change of diameter at the inlet and the outlet as well as the regular losses by friction at the wall. By replacing e^0 by its expression in equation C.5,

$$\underbrace{\dot{m}\left[(C_pT)_{out} - (C_pT)_{in}\right]}_{1} + \underbrace{\frac{1}{2}\dot{m}\left[(v^2)_{out} - (v^2)_{in}\right]}_{2} + \underbrace{\left[(vP)_{out} - (vP)_{in}\right]D}_{3} = -V_D - \dot{m}gH + qA_h \tag{C.10}$$

This relation corresponds to the one-dimensional steady-state energy budget of a vertical channel. In this case the only sources of energy is the heat injected at the wall. The first term of equation C.10 is the main term. It corresponds to the difference between the heat convected out of the channel relatively to the heat that the fluid convect inside the channel at the inlet. The temperature variation in such system do not induce any noticeable changes of C_p, which can thus be assumed constant.

The second term stands for the amount of energy converted into kinetic energy. In the case of a steady state, the increase in velocity between the inlet and the outlet, which results from the fluid expansion, is very low. For the present configuration, $\dot{m} \sim 10^{-2}$ and $v^2 \sim 10^{-2}$ so that this term is of the order of magnitude of 10^{-4} W which is neglectible compared to the power injected.

The third term is the work of the pressure forces at the top and bottom open boundaries. Given that the pressure distribution in the channel is extremely hard to determine, this term is difficult to apprehend. As a first approximation, $P_{out} - P_{in}$ can be evaluated as having the same order of magnitude as the static pressure difference far from the channel, considering the velocity changes between the inlet and the outlet neglectible, and substituting by the mass flow

rate equation C.7 then

$$[(vP)_{out} - (vP)_{in}]D \sim -\rho g H v_{in} D = -\dot{m} g H \tag{C.11}$$

These hypothesis allow to show that the work of the pressure forces at the open surfaces $[(vP)_{out} - (vP)_{in}]D$ can be expected to be, at least to some extent, compensated by the work of the gravity forces. In these conditions, these two terms cancel in equation C.10. However, as was mentioned in chapters 2 and 6, the inlet and outlet conditions are not equal to the far-field conditions and a proper investigation is necessary to evaluate more precisely the contribution of this term.

Finally the viscous dissipation is expected to be low in this low-velocity flow and consequently V_D is assumed neglectible.

By assuming all these hypothesis, the simplified energy balance used in chapter 6 can be obtained

$$\dot{m} C_p \left(T_{out} - T_{in}\right) = q A_h \tag{C.12}$$